University of Sussex

Cryogenic ion trapping for next generation quantum technologies

Darren C. S. De Motte

Submitted for the degree of Doctor of Philosophy
University of Sussex, Brighton, United Kingdom
September 2015

Declaration

I hereby declare that this thesis has not been and will not be submitted in whole or in part to another University for the award of any other degree.

Signature:

Darren C. S. De Motte

UNIVERSITY OF SUSSEX

Darren C. S. De Motte, Doctor of Philosophy

Cryogenic Ion Trapping for Next Generation Quantum Technologies

For Mum.

Abstract

Quantum technology has made great strides in the last two decades with trapped ions demonstrating all the necessary building blocks for a quantum computer. While these proof of principle experiments have been demonstrated, it still remains a challenging task to scale these experiments down to smaller systems. In this thesis I describe the development of technology towards scalable cryogenic ion trapping and quantum hybrid systems.

I first discuss the fundamentals of ion trapping along with the demonstration of ion trapping on a novel surface electrode ion trap with a ring shaped architecture. I then present the development of a cryogenic vacuum system for ion trapping at $\sim$4 K, which utilizes a closed cycle Gifford McMahon cryocooler with a helium gas buffered ultra-low vibration interface to mechanically decouple a ultra-high vacuum system. Ancillary technologies are also presented, including a novel in-vacuum superconducting rf resonator, low power dissipation ceramic based atomic source oven and an adaptable in-vacuum permanent magnet system for long-wavelength based quantum logic.

The design and fabrication of microfabricated surface ion traps toward quantum hybrid technologies are then presented. A superconducting ion trap with an integrated high quality factor microwave cavity and vertical ion shuttling capabilities is described. The experimental demonstration of the cavity is also presented with quality factors of Q$\sim$6 000 and Q$\sim$15 000 for superconducting niobium nitride and gold based cavities respectively, which are the highest demonstrated for microwave cavities integrated within ion trapping electrode architectures. An ion trap with a multipole electrode geometry is then presented, which is capable of trapping a large number of ions simultaneously. The homogeneity of five individual linear trapping regions are optimized and the design for the principle axis rotation of each linear region is presented. An overview of microfabrication techniques used for fabricating surface electrode ion traps is then presented. This includes the detailed microfabrication procedure for ion traps designed within this thesis.

A scheme for the integration of ion trapping and superconducting qubit systems as a step towards the realization of a quantum hybrid system is then presented. This scheme addresses two key difficulties in realizing such a system; a combined microfabricated ion trap and superconducting qubit architecture, and the experimental infrastructure to facilitate both technologies. Solutions that can be immediately implemented using current technology are presented. Finally, as a step towards scalability and hybrid quantum systems, the interaction between a single ion and a microwaves field produced from an on chip microwave cavity is explored. The interaction is described for the high-Q microwave cavity designed in this thesis and a $^{171}Yb^{+}$ ion. A description of the observable transmission from the cavity is described and it is shown that the presence of a single ion can indeed be observed in the emission spectrum of high-Q microwave cavity even in the weak coupling regime.

Acknowledgements

General Acknowledgements

The last four years would not have been possible without the help and support of the people around me. Firstly, I would like to thank my supervisor, Prof. Winfried Hensinger, for giving me the opportunity to undertake a DPhil within his highly motivated research group and on such an exciting project. His enthusiasm and drive is unparalleled and I have learned a great deal from him throughout the years. I would also like to thank my second supervisor Dr. Barry Garraway for his valuable advice and guidance.

A huge thank goes to all my fellow PhD students and post docs. Dr. Gouri Giri joined the group shortly after I arrived and worked with me on the cryogenic system for two years. His knowledge, patience and openness was a pleasure to work with and I am extremely grateful for all he has done.

I would also like to thank Anton Grounds who began working on the cryogenic system during my final years and has helped me greatly throughout. He has made a considerable contribution to the project while making the experimentally complex seem rather trivial. Dr. Bjoern Lektisch has also provided me with great help throughout my PhD with his microfabrication expertise for which I am very grateful. I have been asking him questions since the first day of my PhD to my last days, and he has always had the time to answer them all.

David Murgia and Tomas Navickas arrived two years after I began and have contributed greatly to the experimental setup of the cryogenic system. I couldn't have asked more from them, in or out of the lab (except that they had joined me two years earlier). My thanks also goes to Dr. Seb Weidt, who has helped me tremendously with his advice throughout my PhD as a colleague and as a friend.

Dr. James Siverns, Dr. Robin Sterling and Dr. Jim McLoughlin were in the final stages of their PhD when I joined the group. I consider myself lucky to have worked along side them in the group and I am very thankful for their experience filled help and advice.

My sincerest thanks go Andrea Rodriguez Blanco. I am enormously grateful and indebted to her for her continuing help and support throughout my final year.

My thanks also goes out to Dr. Marcus Hughes, Dr. Kimberley Lake, Eamon Standing, Joe Randall, Weikang Fan, Anna Webb, Ethan Potter, Adrian Parra, Dr. Simon Webster, Dr. Altaf Nizamani, Mark Davies, Alasdair Price, Louis Williams, who have all helped me greatly. I wish you all the best for the future. I would also like to thank all those at the University of Sussex outside of the lab that have help me greatly. I will always appreciate the help given by all those at the engineering and science workshop, who were capable of deciphering my drawings and bringing them to reality.

A big thank you also go out to my family and friends who have always helped and encouraged me. A PhD would be impossible without the support of your closest friends, and for that I would like to thank Kieran Ayres and James Lepoittevin for your enduring support, your enthusiastic interest and the countless escapes you provided to the real world. You helped more than you may know. A heartfelt thank you also goes to Hannah Fosbraey.

Finally, I want to give my deepest thanks to my mother. Without her endless support and encouragement none of this would be possible; I cannot thank you enough.

Detailed Acknowledgements

As I started my PhD with an empty laboratory, the work presented in this thesis would not have been possible if it was not for the grateful contributions from my colleagues. Here, I acknowledge their contribution.

Chapter 3: Experimental setup

The experimental setup was performed primarily with Dr. Gouri Giri, along with the help of David Murgia, Tomas Navickas and Dr. Seb Weidt. The room temperature vacuum system used within this chapter was designed and built by Dr. Marcus Hughes and Dr. Seb Weidt. The optical imaging system for the room temperature vacuum system was also designed and built by Dr. Marcus Hughes.

Chapter 4: Cryogenic vacuum system

Initial testing of a Gifford McMahon cryocooler was performed by myself with the help of Richard Hendricks at the Centre for Cold Matter Research, Imperial College London. The cryogenic system was assembled by myself and Dr. Gouri Giri, who also helped to

characterize the operation of the cryogenic system. The in-vacuum rf resonator was designed and tested by myself with Dr. Gouri Giri and Anton Grounds. The initial design for a ceramic based atomic source oven was developed by Dr. Bjoërn Lektisch.

Chapter 5: Surface electrode ion traps

The surface electrode ion traps presented were design by myself with the help of Dr. Bjoërn Lektisch and Dr. Gouri Giri. Dr. Gouri Giri performed the preliminary simulations of the microwave cavity. Myself and Dr. James Siverns performed the computational optimization of the flat multipole ion trap.

Chapter 6: Microfabrication

The microfabrication of the surface electrode ion traps designed in chapter 5 was performed by Dr. Bjoërn Lektisch. The cleaning procedure for the gold ion traps was developed by David Murgia.

Chapter 7: Integrating ion trapping and superconducting qubit systems

The microfabricated ion trap for coupling to superconducting circuits was designed by myself and Anton Grounds. The scheme for ion trapping in a dilution fridge was performed by myself, Matus Rehák, Anton Grounds and Dr. Gouri Giri. The theoretical foundation describing the challenges and solutions involved was performed by myself and Andrea Rodriguez Blanco.

Chapter 8: Detecting trapped ions with a microwave CPW

The simulation of the magnetic field of the cavity was performed by Anton Grounds. The theoretical calculations for the cavity and ion interaction were performed by myself, Andrea Rodriguez Blanco and Anton Grounds, with the valuable guidance from Klaus Mølmer.

Publications

Journal publications

Scheme for integrating ion trap and superconducting qubit systems,
D. De Motte, A. Grounds, M. Rehák, A. Rodriguez Blanco, B. Lekitsch, G. S. Giri, P. Neilinger, G. Oelsner, E. Il'ichev, M. Grajcar, W. K. Hensinger.,
(In preparation)

Conference contributions - *Posters*

Towards quantum hybrid systems: Vertical shuttling ion trap with a high Q microwave resonator in a cryogenic environment,
D. De Motte, G. S. Giri, B. Lekitsch and W. K. Hensinger.
Poster at the Advances in Photonics of Quantum Computing, Memory, and Communication VI Conference 2012, 4-7 February 2012, at San Francisco, USA.

Scalable Ion Quantum Technology,
K. Lake, B. Lekitsch, R. C. Sterling, M. D. Hughes, J. D. Siverns, J. J. McLoughlin, S. Weidt, D. De Motte, S.C.Webster, G.S Giri, A H. Nizamani, P. Srinivasan, H. Rattanasonti, Jessica Maclean, C. Mellor, M. Kraft and W. K. Hensinger.
Poster at the European Conference on Trapped ions (ECTI) 2012, 9-14 September 2012, at Obergurgl, Austria.

Cryogenic ion trapping: Integrated high Q microwave resonator ion chips and ion trap architectures for quantum technologies and quantum hybrid systems,
D. De Motte, G. S. Giri, B. Lekitsch and W. K. Hensinger.
Poster at the 21st International Conference on Laser Spectroscopy - ICOLS 2013, 9-14 June 2013, at Berkeley, California, USA.

Cryogenic ion trapping: Integrated high Q microwave resonator ion chips and ion trap architectures for quantum technologies and quantum hybrid systems,
D. De Motte, G. S. Giri, B. Lekitsch and W. K. Hensinger.
Poster at the Techniques for Trapped Ions Ion Tech 2 COST-IOTA Workshop, 23-25 October 2013, at Paris, France.

Cryogenic ion trapping: Integrated high Q microwave resonator ion chips and ion trap architectures for quatum technologies and quantum hybrid systems,
D. De Motte, G. S. Giri, B. Lekitsch and W. K. Hensinger.
Poster at IQsim13 2013 - 1st International Workshop on Quantum Simulation with Trapped Ions, 16-19 December 2013, at Brighton, UK.

Ion storage ring on a chip and advanced microfabricated ion traps with integrated current carrying wires for quantum information and simulation,
M. D. Hughes, B. Lekitsch, J. O. Maclean, S. Weidt, G. S. Giri, T. Navickas, D. De Motte, D. F. Murgia, J. Randall, R. C. Sterling, I. Sari, M. Kraft, C. J. Mellor and W. K. Hensinger.
Poster at IQsim13 2013 - 1st International Workshop on Quantum Simulation with Trapped Ions, 16-19 December 2013, at Brighton, UK.

Cryogenic ion trapping: Integrated high Q microwave resonator ion chips and ion trap architectures for quantum technologies and quantum hybrid systems,
D. De Motte, G. S. Giri, B. Lekitsch and W. K. Hensinger.
Poster at IARPA meeting, 28th January 2014, at San Francisco, USA.

Cryogenic ion trapping and technology development for quantum simulation, computing and hybrid systems,
D. De Motte, G. S. Giri, B. Lekitsch, A. Grounds, M. Rehák, D. F. Murgia, T. Navickas and W. K. Hensinger.
Poster at the European Conference on Trapped ions (ECTI) 2014, 15-19 September 2014, at Schloss Waldhausen, Germany.

Microfabricated ion traps for quantum information and simulation,
B. Lekitsch, M. D. Hughes, R. C. Sterling, H. Rattanasonti, S. Weidt, K. Lake, P. Srinivasan, S. C. Webster, J. O. Maclean, G. S. Giri, T. Navickas, D. De Motte, D. F. Murgia,

J. Randall, M. Kraft, C. Mellor, and W. K. Hensinger.
Poster at the European Conference on Trapped ions (ECTI) 2014, 15-19 September 2014, at Schloss Waldhausen, Germany.

Cryogenic ion trapping and technology development for quantum simulation, computing and hybrid systems,
D. De Motte, G. S. Giri, B. Lekitsch, A. Grounds, M. Rehák, D. F. Murgia, T. Navickas and W. K. Hensinger.
Poster at IOP Topical Research Meeting on Hybrid Quantum Systems, 16-18 December 2014, at the National College for Teaching and Leadership, Nottingham, UK.

Microfabricated ion traps for quantum information and simulation,
B. Lekitsch, M. D. Hughes, R. C. Sterling, H. Rattanasonti, S. Weidt, K. Lake, P. Srinivasan, S. C. Webster, J. O. Maclean, G. S. Giri, T. Navickas, D. De Motte, D. F. Murgia, M. Kraft, C. Mellor, and W. K. Hensinger.
Poster at IOP Topical Research Meeting on Hybrid Quantum Systems, 16-18 December 2014, at the National College for Teaching and Leadership, Nottingham, UK.

Cryogenic ion trapping and technology development for quantum simulation, computing and hybrid systems,
D. De Motte, G. S. Giri, B. Lekitsch and W. K. Hensinger.
Poster at IARPA MQCO meeting, 3rd Feburary 2015, at New York, USA.

Microfabricated ion traps for quantum information and simulation,
B. Lekitsch, M. D. Hughes, R. C. Sterling, H. Rattanasonti, S. Weidt, K. Lake, P. Srinivasan, S. C. Webster, J. O. Maclean, G. S. Giri, T. Navickas, D. De Motte, D. F. Murgia, M. Kraft, C. Mellor, and W. K. Hensinger.
Poster at IARPA MQCO meeting, 3rd Feburary 2015, at New York, USA.

Scalable cryogenic and microwave systems for the creation of high fidelity quantum gates,
A. Grounds, A. Parra, D. De Motte, G. S. Giri, B. Lekitsch, M. Rehák, D. F. Murgia, W. Fan, E. D. Standing, E. Potter, S. Weidt and W. K. Hensinger.
Poster at Quantum, Atomic, Molecular and Plasma Physics (QuAMP) Conference 2015, 1-4 September 2015, at the University of Sussex, Brighton, UK.

Conference contributions - *Presentations*

Ion Trap Tools For Realizing an Integrated Quantum Hybrid System,

D. De Motte and G. S. Giri.

Presentation at the Integrated Quantum Information Technology (iQIT) Meeting, 16-17 April 2012, at the Leibniz-Institut für Photonische Technologien e.V., Jena, Germany.

Optimal electrode geometries for vertical ion shuttling and development of a cryogenic set up,

D. De Motte and G. S. Giri.

Presentation at the Integrated Quantum Information Technology (iQIT) Meeting, 27-28 October 2012, at the University of Salerno, Italy.

IQIT Report: Development of specialized ion traps and cryogenic system,

D. De Motte.

Presentation at the Integrated Quantum Information Technology (iQIT) Meeting, 21-23 April 2013, at Comenius University, Bratislava, Slovakia.

Development of specialized ion traps and cryogenic system,

D. De Motte and B. Lekitsch.

Presentation at the Integrated Quantum Information Technology (iQIT) Meeting, 28-29 April 2014, at Billund (hosted by Aarhus University), Denmark.

Development of specialized ion traps and cryogenic system,

D. De Motte and A. Grounds.

Presentation at the Integrated Quantum Information Technology (iQIT) Meeting, 27-28 October 2014, at the University of Sussex, Brighton, UK.

Contents

List of Tables

List of Figures

Chapter 1

Introduction

Throughout history mankind has strived to develop new technology to help it understand the world we live in, and to continually improve our quality of life. This has been epitomized in the 20^{th} century with the age of the computer, which has brought about arguably the greatest technological revolution in history. While the modern computer as we know it has been a relatively recent invention, the history of computing stretches further back in time, over 2500 years, to the abacus, which still shares the same principles as modern computers to make repeated calculations faster than the human brain.

The development of the first mechanical calculator came into being only in 1642 at the hands of French scientist and philosopher Blaise Pascal. The calculator was formed from simple interlocking cogs, but was capable of performing fundamental arithmetic calculations. The first concept for a truly computational machine came soon afterwards in the 1800's from the Charles Babbage, now regarded as one of the "fathers of computing". Babbage designed what is now known as the Babbage difference engine. For the first time history, a machine was capable of taking an input, storing information, processing the information and providing an output, demonstrating the fundamental mechanisms by which all modern computers operate. As well as these ground breaking experimental demonstrations, another pioneer of the modern computer, Alan Turing, described the theoretical computer known as the Turing machine [32], which formed the blueprint for modern digital computers.

Large scale computers began emerging in the 1940's and quickly became limited by the technology at the time, which was chained to vacuum tubes, a key active component in classical computing. To develop computers an order of magnitude greater at the time would have required millions tubes for each computer. A major breakthrough in the miniaturization of computers came from John Bardeen, Walter Brattain and William

Shockley at Bell laboratories, who developed a replacement for the vacuum tube known as the transistor, which signalled the dawn of the semi-conductor age. In the 1960's Jack Kilby took the transistor to the next step in scalability and established the integrated circuit, which allowed the fabrication of millions of transistors within a single chip and brought us to the modern age of computing.

1.1 Quantum computing

The turn of the 20^{th} century also brought the quantum revolution, and it wasn't long until the potential of bringing the quantum and computing worlds together was realized. Richard Feynman was the first to lay the principles for quantum computing [33] and famously claimed that

> "*Nature isn't classical...and if you want to make a simulation of Nature, you'd better make it quantum mechanical*".

This echoed the idea at the time that to simulate the behaviour of elementary particles, quantum mechanics was required. It was argued that as nature was based on the laws of quantum mechanics, it could only be fully simulated through quantum mechanical means, which would also bring us to the true limit of computational efficiency.

The foundation of the quantum computers strength stems from the quantum bit, known as the 'qubit'. Unlike the binary nature of the classical computer bit, which can take the form of '0' or '1', the qubit can take the values $|0\rangle$ and $|1\rangle$, which can also be a normalized superposition of these basis vectors. This superposition gives the quantum computer its power, with the qubits possessing an infinite amount of superposition states. This allows a quantum computer with N qubits to be in a superposition of 2^{N} states, where as a classical computer can only occupy one of the 2^{N} states at any given time. While the measurement of the quantum system will result in the collapse of the superposition and produce a single output, the process can be repeated a number of times to give the probability of the system in a given state.

Following Feynman's work, David Deutsch described the first universal quantum computer [34]. Deutsch introduced the analogue to logic gates found in classical computers with quantum gate operations. These included entangling gates, where the entanglement of qubits meant that they could no longer be treated individually. Instead, operations on individual qubits resulted in changes to entangled qubits, leading to faster parallel quantum computing.

In the 1990's, the development of quantum algorithms placed the power of the quantum computer on display. Grover's search algorithm [35], reduced the number of search iterations for a sample size of N to $\sqrt{N}$, compared with classical computer which are limited to $N/2$. Shor's algorithm [36] demonstrated the speed up in factoring large numbers. This highlighted an area of modern computing that would be revolutionized as the most common method of encrypting sensitive material, such as financial information, relies on the infeasibility of factoring the product of two large numbers. Shor's algorithm presents the possibility of a quantum computer breaking such encryptions in a short amount of time and as such has grabbed the attention of defence agencies such as the NSA [37], as well as major technology companies such as Google [38], IBM [39] and Microsoft [40].

While the advancement of quantum technologies over recent decades has led to the realization of qubits in various physical systems, such as molecules [41], neutral atoms [42], superconducting qubits [43], quantum dots [44], nitrogen vacancy centres [45] and photons [46], this thesis focuses on trapped ions [47]. Quantum gates for quantum computing with cold trapped ions was first proposed by Cirac and Zoller [48] and was initially demonstrated in 1995 by Monroe *et al.* [49]. Later in 2003, Schmidt-Kaler *et al.* [50] demonstrated the full scheme using a string of ions. While some qubit types possess strengths over others, the ion offers a number of benefits that meet a set of requirements outlined by DiVincenzo [51], known as the DiVincenzo criteria.

The DiVincenzo criteria

The DiVincenzo criteria were set out by David DiVincenzo in 1995 as the necessary and sufficient criteria for the successful implementation of a quantum information processor [51]. These criteria can be given as

1. A scalable physical system with well characterized qubits
2. Reliable state preparation
3. Universal set of quantum gates
4. Qubit-specific measurement
5. Long coherence times

Two additional criteria can also be included for quantum communication, which are

5. Interconversion of stationary and flying qubits

6. Transmit flying qubits between distant locations

Most of these criteria have already been demonstrated with trapped ions; initialization of qubits [52], a set of universal quantum gates [53, 54], the detection of states [55], long coherence times [56, 57], and a scalable architecture to host a large number of qubits [17, 58, 59].

Surface electrode ion traps

As with the semiconductor revolution in classical computers, the equivalent challenges towards a scalable trapped ion quantum computer are being tackled with microfabrication technology [47, 60–64]. Early ion traps possessed macroscopic hand made structures on the scale of centimetres. The development of microfabrication technology now allows the deposition of conductive and insulating layers on the micron scale to form ion traps. This new generation of ion traps allows for features on the scale of microns allowing for finer control of the ion and the ability to create far more complex geometries [65]. Such architecture also offer the possibility for large parallel gate executions, with several trapping zones on a single chip for performing multiple tasks. Each trapping zone can contain a number of dc and rf electrodes to generate confining potentials far easier than traps formed from macroscopic elements.

Cryogenic ion trapping

Cryogenic ion trapping systems with surface electrode ion traps have already been demonstrated [66] and provide a number of benefits over room temperature systems. As well as obtaining ultra-high vacuum pressures more readily in cryogenic environments, suppression of heating rates in cryogenic surface electrode ion traps [16], as well as traps utilizing superconducting materials for trap electrodes [67] have been demonstrated. The demonstration of superconducting ion traps has also opened the possibilities for integrating trapped ions with superconducting devices, with a number of proposals for the integration of trapped ions and superconducting circuits being presented [68–70].

1.2 Thesis outline

Chapter 2: I begin by outlining the fundamental principles underlining the operation of radio frequency Paul traps and describe how specific isotopes of ytterbium can be used as an ion for quantum information experiments.

Chapter 3: The experimental setup, including lasers, laser stabilisation, the operation of ultra-high vacuum systems at room temperature and optical imaging setups are then discussed. This includes demonstration of ion trapping on an ion trap with a novel ring based electrode architecture.

Chapter 4: This chapter outlines all work related to the development of a cryogenic vacuum system for ion trapping at $\sim$4 K, as well as an in depth discussion on the benefits of the cryogenic regime for trapped ions. This includes a description of the cryocooler, the vacuum system and ancillary technologies such as rf and dc electronics, atomic sources and mounting schemes. The chapter concludes with a description and characterization of the operation of the cryogenic system.

Chapter 5: After the cryogenic system has been described, the design and simulation of microfabricated surface ion trap technologies toward hybrid quantum technologies are described. This includes a superconducting ion trap with a high quality factor microwave cavity and vertical ion shuttling capabilities. An ion trap with a multipole electrode geometry is then presented, which is capable of trapping a large number of ions simultaneously.

Chapter 6: An overview of microfabrication techniques used for fabricating surface electrode ion traps is then given. This includes the detailed microfabrication procedure for ion traps, including those designed in chapter 5, using a gold based electrode process and a superconducting niobium nitride based electrode process. The results of the fabrication are then presented.

Chapter 7: Here, an experimental design for integration of ion trapping and superconducting qubit systems as a step towards the realization of a quantum hybrid system is presented. The chapter addresses two key difficulties in realizing such a system; a combined microfabricated ion trap and superconducting qubit architecture, and the experimental infrastructure to facilitate both technologies and presents solutions that can be implemented using current technology.

Chapter 8: As a step towards scalability and hybrid quantum systems, the final chapter explores the interaction of ions with a microwaves field produced from an on chip microwave cavity. The interaction between a single trapped ion and the high-Q microwave cavity designed in chapter 5 is presented with a description of the observable transmission from the cavity due to the interaction.

Chapter 2

Ion traps and the Yb^+ ion

The work presented in this thesis is based upon the radio frequency (rf) Paul trap, also known as the quadrupole ion trap. The trap was first developed by Wolfgang Paul in the late 1950's with the goal of confining ionized atoms for long periods of time for experiments in the field of mass spectrometry. The concept was taken forward in 1978 by Wineland *et al.* [71] and Neuhauser *et al.* [72] who both independently demonstrated laser cooling of trapped Mg^+ and Ba^+ ions respectively. Paul traps are now used in a wide range of fields including atomic clocks [73–75], frequency standards [76,77], quantum electrodynamics [78] and quantum information and computing [48, 79–84].

This chapter will outlines the electromagnetic principles required to understand the operation of the rf quadrupole ion trap. It highlights important aspects such as ion trap dynamics 2.1.1, motion of the ion 2.1.2 and how the electrical potential of arbitrary ion trap geometries can be simulated 2.2. This chapter also introduces the Yb^+ ion 2.4 and discusses its usefulness in quantum information technology and its manipulation via Doppler cooling. The energy level structure for even numbered isotopes 2.4.2 and the more complex odd numbered isotopes 2.4.3 are also presented with a scheme to address all possible transitions for a closed cooling cycle.

2.1 Radio frequency Paul traps

2.1.1 Ion trap dynamics

The purpose of a Paul trap is to use time-varying electric fields combined with static fields to confine a charged particle in three dimensional free space. To confine an ion or any point charge, a stable equilibrium cannot be created solely with static electric fields. This is more commonly known as Earnshaw's theorem. For a particle to be held in this manner,

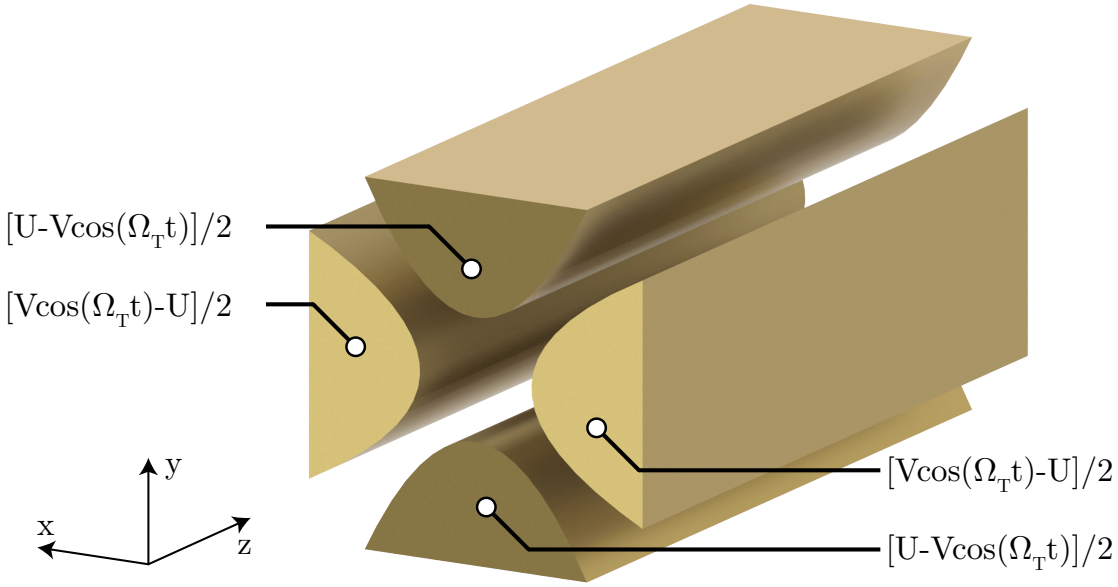

Figure 2.1: Paul trap with a hyperbolic electrode geometry. All electrodes possess an oscillating voltage at a frequency of ω_T, with two opposite electrodes oscillating π out of phase.

all electric field lines would need to be directed towards the trapping position, resulting in a negative divergence of the field. From Gauss's law we know that the divergence of the electric field must be zero in free space $\nabla \cdot \vec{E} = 0$, which forbids this possibility. As $\vec{E}(\vec{r}) = \nabla\phi(\vec{r})$, where $\phi(\vec{r})$ is an electrical potential, this satisfies Laplace's equation which is given by

$$\nabla^2\phi(x, y, z) = 0, \tag{2.1}$$

where $\phi(x, y, z)$ is the three dimensional electric potential.

To understand how a stable trapping potential is formed, we can first consider a linear Paul ion trap with hyperbolic electrodes (figure 2.1), which produces a quadrupole potential in the radial axis. The potential takes the form of a saddle, where in one radial axis the ion will feel a force towards the centre and in the other radial axis it will feel a force outwards from the centre (figure 2.2). By reversing the polarity of the potential the shape of the saddle will also invert. A stable trapping field can then be created by replacing the static voltages with oscillating voltages. As the voltage oscillates, an effective pseudopotential is created that confines the ion in the radial axes. As the force acting on the ion is proportional to the gradient of the potential, the oscillation will result in the ion moving towards the centre of the field where the gradient is zero.

For the Paul trap shown in figure 2.1, all four electrodes possess a voltage oscillating at a frequency of ω_T, with two opposite electrodes oscillating π out of phase. This time

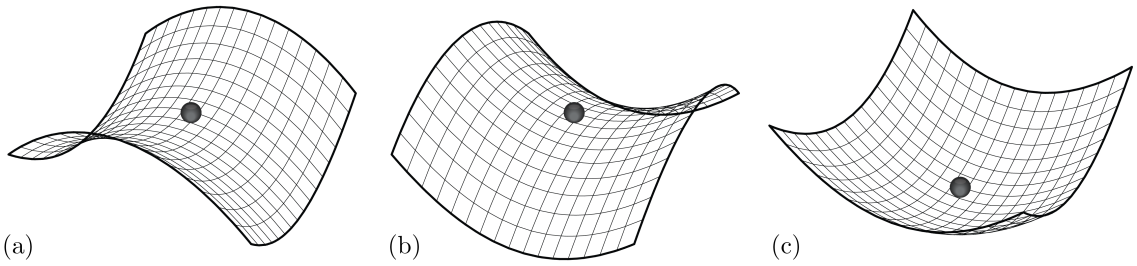

Figure 2.2: (a) Saddle potential created from an rf Paul trap with a hyperbolic electrode geometry. (b) The saddle potential after a π phase shift in the applied voltage. (c) The resultant pseudopotential formed from an oscillating voltage applied to the trap electrodes.

dependant pondermotive pseudopotential can be given as

$$\phi_p(x, y, t) = [U - V\cos(\Omega_T t)]\left(\frac{x^2 - y^2}{2r_0^2}\right), \tag{2.2}$$

where r_0 is the ion-electrode distance, V is the amplitude of the oscillating voltage, U is a static offset voltage and Ω_T is the drive frequency of the oscillating voltage. This in itself does not produce a complete trapping potential, with confinement restricted only to the two radial axes. To achieve complete three dimensional confinement, static voltage end cap electrodes are required for confinement in the axial direction.

The work presented in this thesis focuses on the development of surface electrode ion traps, the electrode geometry is limited to a single plane 2.3. Two parallel planar electrodes are capable of producing a confining pseudopotential in the radial axes with the application of an oscillating voltage (figure 2.4. Total confinement can also be achieved by using just two opposite outer static voltage electrodes or a single centre segmented electrode. Static voltage control electrodes also provide several additional functions such as ion shuttling and micromotion compensation.

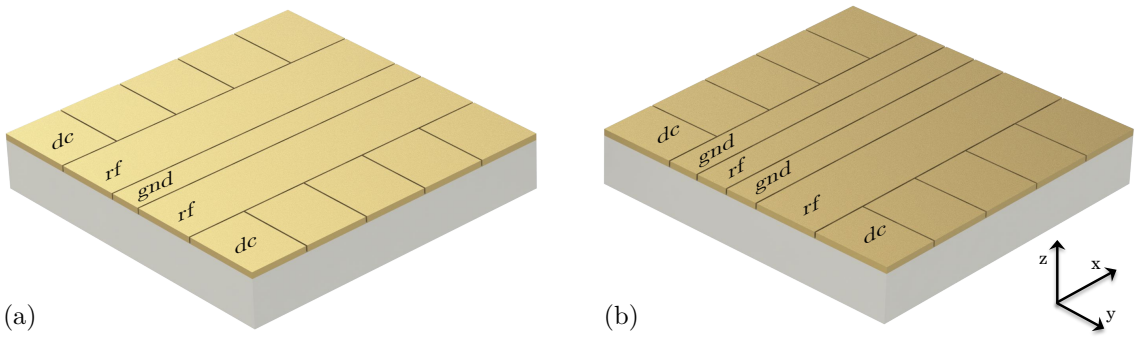

Figure 2.3: (a) Surface electrode ion trap with a symmetric electrodes geometry and (b) an asymmetric rf electrode geometry for principal axis rotation.

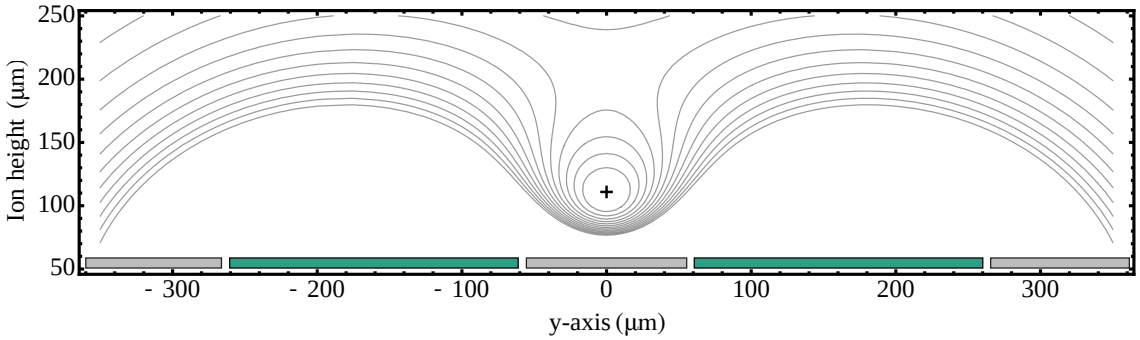

Figure 2.4: Pseudopotential created from a surface electrode ion trap. The planar electrode geometry creates a confining pseudopotential in the radial axes using two parallel rf electrodes. Static voltage end cap electrodes provide complete three dimensional confinement.

2.1.2 Equations of motion

The motion of the ion in a trapping potential is an important dynamic that must be understood and can be described using two methods. I will begin by describing a method that gives a good approximation and I will then go on to a more comprehensive description of the ions motion using the Mathieu equations.

The first method for describing the dynamics of the ions motion is known as the pseudopotential approximation. This method allows the rf potential to be treated in terms of electrostatics alone, allowing for a much simpler analysis of arbitrary electrode geometries. The approximation is performed by considering the time averaged force the ion experiences in an inhomogeneous field over one oscillation. If we take an rf voltage equal to $V\cos(\Omega_T t)$, this gives us a pseudopotential approximation of [85]

$$\psi = \frac{e^2}{4m\Omega_T^2}|\nabla V(x,y,z)|^2, \tag{2.3}$$

where m is the mass of the ion and $\nabla V(x,y,z)$ is the gradient of the potential. The motion of the ion in the pseudopotential can now be described in terms of the secular harmonic motion, where $q_i/2 \equiv \sqrt{2}\omega_i/\Omega_T \ll 1$. The secular frequency is given by

$$\omega_i^2 = \frac{e^2}{4m^2\Omega_T^2}\frac{\partial^2}{\partial i}\left(|\nabla V(x,y,z)|^2\right). \tag{2.4}$$

The dynamics of an ion in an rf Paul trap can also be described using the Mathieu equation, which gives a complete solution. Using the potential given in equation 2.2, the motion of the ion can be shown as

$$\frac{\partial^2 x}{\partial t^2} = -\left(\frac{e}{m}\right)\frac{\partial \phi_p(x,y,t)}{\partial x} = -\frac{e}{mr_0^2}\left[U - V\cos(\Omega_T t)\right]x, \tag{2.5}$$

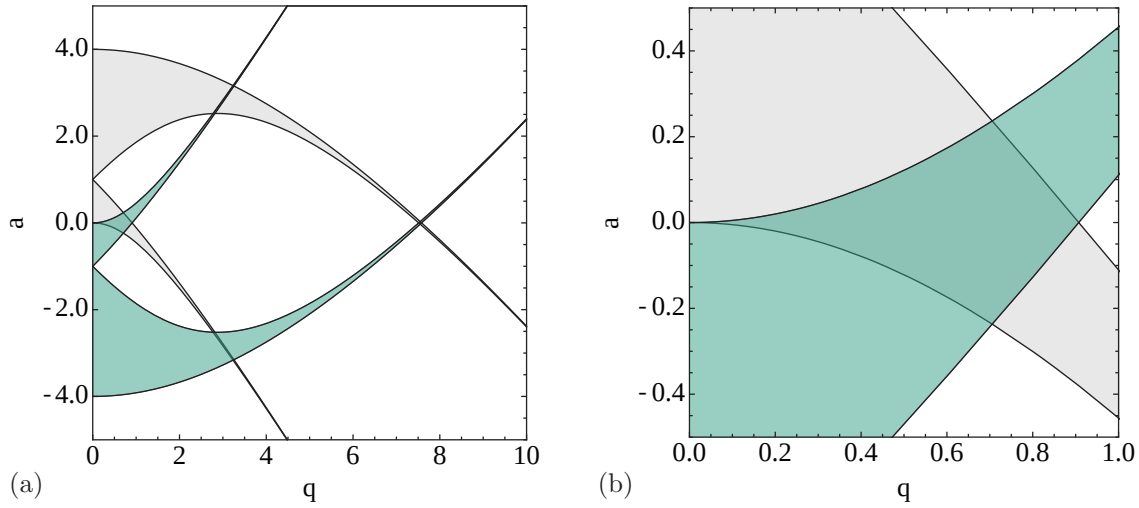

Figure 2.5: (a) Stability regions for which the motion of the ion is stable. (b) Highlights the overlapping region where the ion in stable in both the x and y axes.

$$\frac{\partial^2 y}{\partial t^2} = -\left(\frac{e}{m}\right)\frac{\partial \phi_p(x,y,t)}{\partial y} = \frac{e}{mr_0^2}\left[U - V\cos(\Omega_T t)\right] y, \tag{2.6}$$

$$\frac{\partial^2 z}{\partial t^2} = -\left(\frac{e}{m}\right)\frac{\partial \phi_p(x,y,t)}{\partial z} = 0. \tag{2.7}$$

We can now see more clearly from equation 2.7 that there is no confinement along the axial z axis. By making the following substitutions

$$a = \frac{4eU}{mr_0^2\Omega_T^2} \qquad q = \frac{2eV}{mr_0^2\Omega_T^2} \qquad \zeta = \frac{\Omega_T t}{2}, \tag{2.8}$$

equations 2.5 and 2.6 can then be written in the form of the Mathieu equation, which are given as

$$\frac{\partial^2 x}{\partial \zeta^2} = -\left[a - 2q\cos(2\zeta)\right] x = 0, \tag{2.9}$$

$$\frac{\partial^2 y}{\partial \zeta^2} = \left[a - 2q\cos(2\zeta)\right] y = 0. \tag{2.10}$$

The Mathieu equations produced give a periodic result due to the cosine term. Solutions to the equations can be found by using the Floquet theorem, which gives rise to values of a and q. Stability regions for the ion in the radial x and y axes can then be found, which are dependant on the a and q parameters, which are in turn dependant on parameters such as the voltage amplitude and drive frequency. For the ion to be stable in both axes, an overlapping region of stability must be used, thus ensuring that a and q parameters have

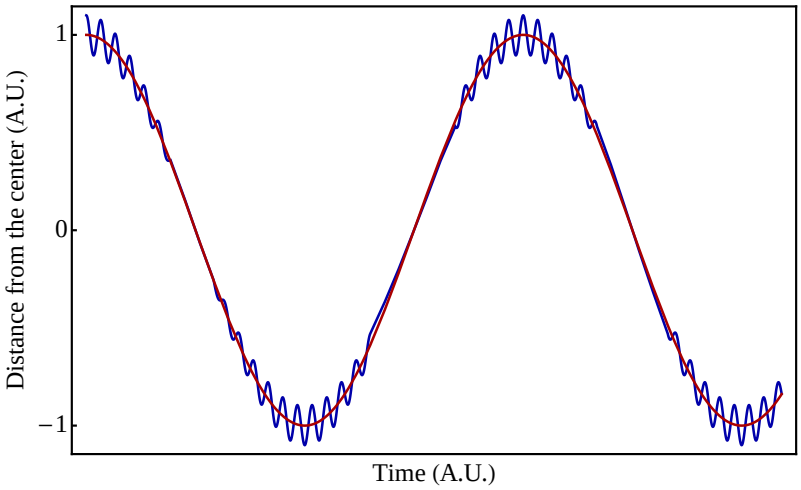

Figure 2.6: The motion of the ion as given in equation 2.11, showing the large amplitude low frequency secular motion and a small amplitude high frequency micromotion for $q = 0.1$ and $a = 0$.

stable motions in both axes (figure 2.5). In most ion trap experiments, the overlapping region with a small values for a and q are used. For a stable trapping potential in both the x and y axes, values of $a \sim 0$ and $q \lesssim 0.7$ are commonly chosen.

2.1.3 Micromotion

When we solve the Mathieu equations using the Floquet theorem [86] for the overlapping stability region of $a = 0$ and $q \ll 1$, the motion of the ion in the x-axis can then be given as

$$x(t) = \kappa \cos(\nu_x t) \left[1 + \frac{q_x}{2} \cos(\Omega_T t)\right]. \tag{2.11}$$

We can see that the ions motion is a combination of a large amplitude low frequency secular motion and a small amplitude high frequency micromotion. This can be seen clearly in figure 2.6. The high frequency oscillation that is superimposed on the secular frequency corresponds to the frequency of the confining potentials drive frequency and is known as micromotion. Micromotion can be divided into two forms; an intrinsic form and an extrinsic form. Intrinsic micromotion results from the ion being driven away from the potential nil due to its secular frequency. Extrinsic micromotion originates from the ion experiencing a net static electric field resulting in an offset in the ions position from the rf nil. This offset can have various sources such as non symmetric electrodes, fabrication imperfections in the trap or random charge build up on dielectric surfaces.

While micromotion can be useful [87, 88], it is in general undesirable. It can result in reduced trapped ion life times, broadened atomic transition line widths and second order Doppler shifts. While intrinsic micromotion cannot be compensated for, extrinsic micromotion can be compensated by using additional static voltage electrodes to bring the

ion to the rf nil. We can see the effect this would have in figure 2.6 where the amplitude of the extrinsic micromotion is minimal at zero displacement and maximum at the largest displacement from the rf nil. Micromotion can also be a result of phase mismatch between opposing rf electrodes in more complex electrode geometries.

2.2 Simulating ion traps

2.2.1 Analytical calculations

Before a trap can be fabricated, potential designs are first simulated to determine if they meet initial requirements. Analytical and numerical simulations can be performed to determine several key parameters for each ion trap. The trap depth, which is the height of the potential barrier confining the ion in each axis, can be quickly determined for arbitrary combinations of voltages and drive frequencies. Secular frequencies can also be determined and with the inclusion of static electrode voltages can be used to determine exact voltages for adiabatic ion transport. Stability parameters a and q can also be determined to identify stable trapping regions for a given drive voltage and frequency.

Analytical calculations are a useful tool for initial calculations of trap geometries, allowing the quick determination of approximate parameters. While the electrostatics of simple geometries can be solved easily through analytical calculations, complex geometries can be difficult to effectively model. Fortunately, work performed by House *et al.* [89] allows for approximate analytical functions to be determined for arbitrary surface electrode ion trap geometries. This allows for the electrostatic potential of complex geometries to be solved quickly using analytical methods. The function describing the electrostatic potential for an arbitrary geometry is given by [89]

$$\begin{aligned}\phi_i(x,y,z) = \frac{V}{2\pi}\Bigg\{ &\arctan\left[\frac{(x_2-x)(z_2-z)}{y\sqrt{y^2+(x_2-2)^2(z_2-z)^2}}\right] - \arctan\left[\frac{(x_1-x)(z_2-z)}{y\sqrt{y^2+(x_1-2)^2(z_2-z)^2}}\right] \\ &-\arctan\left[\frac{(x_2-x)(z_1-z)}{y\sqrt{y^2+(x_2-2)^2(z_1-z)^2}}\right] + \arctan\left[\frac{(x_1-x)(z_1-z)}{y\sqrt{y^2+(x_1-2)^2(z_1-z)^2}}\right]\Bigg\},\end{aligned} \tag{2.12}$$

where ϕ_i is the potential created by a rectangular electrode and V is the voltage applied to the electrode with dimensions of $x = x_2 - x_1$ and $y = y_2 - y_1$.

To form a generalized analytical solution for arbitrary geometries, the model makes a number of assumptions. Firstly, it treats all electrodes as stretching out to infinity in

the x and y plane. The model also assumes that all electrodes lay on a single plane of $z = 0$, where z is the axis perpendicular to the surface of the electrodes. Finally, the model assumes infinitely small gaps between electrodes, allowing the application of differing voltages on individual electrodes, but not treating the gaps between electrodes. This model is therefore more commonly known as the gapless plane approximation.

For most linear ion trapping regions, this analytical calculation holds for initial approximations. However, it should be noted that for more complex regions such as junctions or regions with varying electrode widths, this approximation does not hold. The gapless plane approximation can therefore only be applied when the gap size is significantly smaller than the electrode size [90].

Basis functions

Until now, the solution for the electrostatic potential of only a single electrode has been discussed. However, for a complete ion trap geometry we must consider the electrostatic potential from all electrodes simultaneously. To do this we can use the basis function technique. This allows us to treat the combined field as a linear combination of $\phi_i(x, y, z)$ for all electrodes. The proof of this principle is given in [91] and will be described here.

The electric potential of an arbitrarily distributed charge configuration on a surface with Dirichlet boundary conditions can be given as [91]

$$\Phi\left(\vec{x}\right) = \frac{1}{4\pi\epsilon_0}\int_V \rho\left(x'\right) G\left(\vec{x},\vec{x}\,'\right) d^3\vec{x}\,' - \frac{1}{4\pi}\oint_S \Phi\left(\vec{x}\,'\right)\frac{\partial G\left(\vec{x},\vec{x}\,'\right)}{\partial n'} da'. \tag{2.13}$$

The first integral describes the volumes interior, where $G(\vec{x},\vec{x}\,')$ is the Green function and $\rho(\vec{x}\,')$ is the charge within the volume. When the charge within the volume is zero $\rho(\vec{x}\,') = 0$, the first term vanishes leaving only the second integral, which is the integral over the surface of the electrode. This is multiplied by the normal derivative of the Green function, where S is the surface and n is the normal to the surface.

The total potential of the trap, given as the sum of the potential for each individual electrode with all other electrodes held at ground can be given as

$$\Phi\left(\vec{x}\,'\right) = \sum_i \Phi_i\left(\vec{x}\,'\right). \tag{2.14}$$

Therefore, by using equation 2.13, we can write the total trap potential as

$$\Phi\left(\vec{x}\right) = -\frac{1}{4\pi}\sum_i \oint_{S_i} \Phi_i\left(\vec{x}\,'\right)\frac{\partial G_i\left(\vec{x},\vec{x}\,'\right)}{\partial n_i'} da'. \tag{2.15}$$

As the voltage for each electrode is constant, equation 2.15 can be given as the sum of the voltage V_i multiplied by the surface integral of the i^{th} electrode in the trap

$$\Phi\left(\vec{x}\right) = \sum_i \frac{-V_i}{4\pi}\left(\oint_{S'} \frac{\partial G\left(\vec{x},\vec{x}\,'\right)}{\partial n'}\partial a'\right)_i = \sum_i V_i \Theta_i, \tag{2.16}$$

where the basis function for the electrostatic potential of the i^{th} electrode Θ_i is held at 1 V and is given as

$$\Theta_i = -\frac{1}{4\pi}\oint_{S'} \frac{\partial G\left(\vec{x},\vec{x}\,'\right)}{\partial n'}\partial a'. \tag{2.17}$$

As solutions of Laplace's equations, the basis functions are valid for static potentials. However, basis functions can also be used to describe the pseudopotential created by oscillating voltages for rf Paul traps. This is due to the wavelengths at typical drive frequencies of $1 - 100$ MHz being $\approx 10^{-1}$ m, which are much greater than the trap dimensions of 10^{-3} m. Any changes in the trap potential can therefore be considered uniform across the trap. We can then introduce the time dependence of the rf voltage by treating the voltage on each electrode V_i as a functions of time. This allows for the quasi-static analytical calculation of the electric pseudopotential.

2.2.2 Numerical simulations

Numerical simulations allow for more accurate results for arbitrary electrode geometries and determine the pseudopotential in three dimensional space. Numerical simulations can be performed using two different methods known as finite element method (FEM) and boundary element method (BEM). These methods are both capable of producing full three dimensional potentials above the trap structure.

FEM acts by laying a mesh throughout the desired volume of interest to be simulated, which for an ion trap applies to the electrodes and ground plane structures. The mesh is formed of triangles or quadrilaterals that serve as discrete subdomains, or 'elements', and are connected at discrete points called nodes via vertices (figure 2.7b). An iterative process then finds a solution to Laplace's equation under the Dirichlet boundary conditions between the nodes, giving a potential at each node. The total electric field across the whole surface is produced by summing the results at each individual node.

The BEM method reduces the dimensionality of the physical model to be simulated by one. For two dimensional models, BEM applies one dimensional elements on the outline of the model. Similarly for three dimensional models, such as our electrodes, it applies two

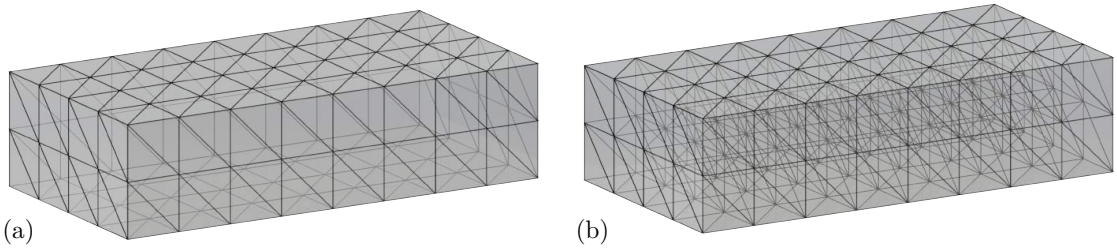

Figure 2.7: (a) A mesh formed using a boundary element method (BEM) on the surface of an object and (b) a finite element method (FEM) throughout the area of interest.

dimensional elements on the surface of the model. The BEM simulates the electric field inside a volume by creating a charge distribution on the boundary of the volume. The field calculations are performed by using the integral equation of Laplace's form, which results in only surface integrals [92].

In this thesis a program called BEMsolver, which uses the BEM technique, was used to simulate the ion traps [93]. BEMSolver acts particularly well for large open spaces as the field calculations are based on integrating over boundary sources where all the important model structures for ion traps are located. Such integration provides a smoothing effect that the differential method in FEM can force with smoothing functions. The reduced dimensionality also helps to significantly reduce processing time when generating large and complex electromagnetic fields. BEMSolver is based on a CERN tool called ROOT, which reads in the electrode structures from a .dxf file, which in this thesis were created using AutoCAD.

To obtain the potential of the complete trap, the basis function technique is used in the same manner as the analytical calculations. Each electrode is numerically simulated with an applied voltage of 1 V, with all other electrodes held at ground. The total potential is then obtained by summing over all basis functions. Each basis function can then be multiplied by the required voltage to generate the necessary field.

2.3 Motional states of the ion

The pseudopotential generated by the ion trap can be approximated as a three dimensional harmonic potential well. This applies for ions with low motional energy and assuming their three directions of motion are uncoupled. If we consider the ion motion in one axis, the Hamiltonian describing the system can be given as

$$H = \hbar\omega \left(a^{\dagger} a + \frac{1}{2} \right) \tag{2.18}$$

where ω is the secular frequency in the given direction and $a^\dagger$ and a are the raising and lowering operators respectively, which can be given as $a^\dagger|n\rangle = \sqrt{n+1}|n+1\rangle$ and $a|n\rangle = \sqrt{n}|n-1\rangle$.

When an ion moves up or down one motional level, it gains or loses one motional quanta of kinetic energy $\pm\hbar\omega$. For most quantum gates with trapped ions, the ion must be within the Lambe-Dicke regime, where the ion's wave function spread is much less than that of the wavelength of the interacting field.

The original proposal for quantum gates required the ion to be in it's ground state of motional energy [48], however, more robust schemes have since been developed to utilize so called 'hot' ions for quantum gates [94]. The description of the ion as a quantum mechanical harmonic oscillator can help in understanding how we can lower and raise the motional quanta of the ions motions.

2.3.1 Doppler cooling

For most applications, ions must to be cooled to a low level of motional quanta. In general, this cooling is done with lasers using a Doppler cooling technique. For a simplified two level system, when a photon emitted from a laser interacts with an ion's atomic dipole transition equal to the photon energy, the photon will be absorbed. This gives the ion a momentum kick of $p = \hbar k$, where k is the laser wave vector. When the system returns to its original ground state, the photon is emitted in a random direction. The momentum kicks associated with the photon emission average to zero after many photon absorption-emission cycles. The net momentum transfer is therefore be in a single direction [95].

In practice the lasers are detuned to the red (frequency reduced) to take into account the shift in wavelength at the ions rest frame. When the ion moves towards the laser it experiences a Doppler shift towards the resonant frequency, resulting in more absorption/scattering events and the reduction in the ions energy. Less scattering events will occur when the ions motion reduces and when it is travelling in the opposite direction of the laser beam. This results in the ion being gradually damped and not heated by the laser. The rate at which the atom absorbs and re-emits a photon is known as the scattering rate γ_p and can be given as [96]

$$\gamma_p = \frac{s_0\Gamma/2}{1 + s_0 + (2\Delta_{eff}/\Gamma)^2} \tag{2.19}$$

where Γ is the linewidth of the transition, $s_0 = I/I_s$ is the saturation parameter with laser intensity I and saturation intensity I_s of the particular transition at wavelength λ and

lifetime $\tau = 1/\Gamma$, and $\Delta_{eff} = \Delta + \Delta_D$ is the effective detuning. The detuning of the laser from the transition frequency can be given as $\Delta = \omega_L - \omega_{eg}$. The Doppler shift of the ion moving in the opposite direction of the laser beam propagation at a velocity v can be given as $\Delta_D = -kv$. The saturation intensity can also be given as

$$I_s = \frac{\pi hc}{3\tau\lambda^3}. \tag{2.20}$$

The average force of photon scattering due to the atom receiving a momentum kick $p = \hbar k$ can be given as [96]

$$F = \hbar k \gamma_p = \frac{\hbar k s_0 \Gamma/2}{1 + s_0 + (2(\Delta_{eff} =)/\Gamma)^2}. \tag{2.21}$$

We can also describe the temperature of the ion in terms of its velocity as $m\vec{v}^{\,2}/2 = k_B T/2$, which gives

$$T = \frac{m\vec{v}^{\,2}}{k_B}, \tag{2.22}$$

where for $s \gg 1$ gives a Doppler cooling temperature of [97]

$$T = \frac{m\hbar\Gamma^2}{8m\Delta k_B}\left[1 + \left(\frac{2\Delta}{\Gamma}\right)^2\right]. \tag{2.23}$$

For efficient cooling, the laser should have a detuning of $\Gamma/2$, which puts a limit on the lowest kinetic energy of the ion given by

$$k_B T = \frac{\hbar\Gamma}{2}, \tag{2.24}$$

where k_B is the Boltzmann constant and T is temperature. For $^{171}\mathrm{Yb}^+$ with a natural line width of $\Gamma/2 = 19.6\,\mathrm{MHz}$, the lowest temperature achievable with Doppler cooling is $470\,\mu\mathrm{K}$. Doppler cooling can typically only achieve a cooling to an average motional energy state of $\overline{n} > 1$. For cooling to the motional ground state of an ion, resolved sideband cooling using stimulated Raman transitions are required. This is traditionally performed using lasers [6] and has recently been demonstrated using rf radiation [24].

For efficient ion cooling, the k-vector of the laser needs a component in all three directions of the ions motion. This can be achieved by rotating the ions principal axes of motion. The rotation can be performed by the use of asymmetries in the rf electrode geometry or from static voltages from control electrodes. The angle of rotation can be obtained from the Hessian Matrix of the electric field and describes the linear transformation

Isotope	Nuclear spin	Natural abundance %	Enriched abundance %
^{168}Yb	0	0.135	13-24
^{170}Yb	0	3.03	> 78
^{171}Yb	1/2	14.31	> 95
^{172}Yb	0	21.82	> 97
^{173}Yb	5/2	16.13	> 92
^{174}Yb	0	31.84	> 98
^{176}Yb	0	12.73	> 96

Table 2.1: Table showing naturally occurring stable Yb isotopes with their nuclear spin and natural abundance. For experiments which require only one particular isotope, a enriched Yb sample can be obtained. The commonly available abundance of enriched samples for different Yb isotopes is also shown [1].

of the electric potential.

2.4 The Yb^+ ion

Quantum information technology with trapped ions require the atoms used to meet a very specific criteria. One major requirement is that the atom must be easily ionized such that they can interact with the confining electrical potentials. The ion must then posses a single outer electron to perform Doppler cooling and quantum information tasks. For this reason group 2 periodic elements, known as alkali earth elements, are chosen. These elements offer two outer electrons allowing the atom to be ionized while leaving behind an hydrogenic ion. The use of these elements including Be, Mg, Ca, Sr and Ba, as well some transition metals such as Cd and Yb, which have the same outer electronic structure have been demonstrated in experiments towards quantum technology.

The work carried out in this thesis is based upon Yb^+ ions as it offers several desirable features for quantum information technology. The Yb^+ ions energy level structure has optical transitions that are within or very close to the optical spectrum between 369 nm and 935 nm. These transitions are easily accessible by commercially available diode lasers. Yb also has 7 naturally occurring stable isotopes, which are shown in table 2.1, where enriched samples can be obtained for experiments that only require a single isotope.

In this thesis we are primarily concerned with $^{174}Yb^+$ and $^{171}Yb^+$ ions. Even numbered isotope do not have any nuclear spin and hence no hyperfine structure. This makes it ideal for initial trapping and experimentation. $^{174}Yb^+$ is chosen for this task due to its naturally high abundance. With no hyperfine structure even numbered Yb atoms are not

Isotope	Transition wavelength $^1S_0 \leftrightarrow {}^1P_1$ (nm)
$^{171}Yb^+$	398.91051(6)
$^{171}Yb^+$	398.91070(6)
$^{171}Yb^+$	398.91083(6)
$^{171}Yb^+$	398.92224(6)
$^{171}Yb^+$	398.91144(6)

Table 2.2: Table showing the wavelengths for the $^1S_0 \leftrightarrow {}^1P_1$ transition.

suited for quantum information technology and so we turn to the odd numbered Yb atoms. $^{171}Yb^+$ and $^{173}Yb^+$ both have non zero nuclear spins resulting in a hyperfine structure. $^{171}Yb^+$ is chosen as the odd numbered isotope as the spin 1/2 nucleus provides a simple energy level structure with a hyperfine doublet that can be used for the $|0\rangle$ and $|1\rangle$ qubit states.

2.4.1 Photoionisation

To trap Yb we must first remove an outer valence electron to give it a net charge, which then allows it to interact with a confining electrical potential. This ionisation process can be performed via two different methods; electron impact ionisation and photoionisation. Electron impact ionisation is a technique where energetic electrons are used to ionize a diffuse atomic source. The interaction is in the form of electron collisions, which cause the ejection of bound electrons. While this technique is experimentally simpler to implement as it relies on thermionically emitted electrons, it can lead to a relatively large accumulation of excess charge on the trapping electrodes resulting in the perturbation of the confining potential.

Photoionisation on the other hand, while being more complex to experimentally implement, has many benefits over electron impact ionisation and is the method used for the work presented in this thesis. The process operates by exciting the outer valence electron with a photon of sufficient energy to liberate it into the electronic continuum. This allows for isotope selective ionisation by tuning the laser to the desired frequency (table 2.2). Photoionisation also offers more efficient ionisation rates [98], which allows for the reduction in atomic beam flux when loading, thereby reducing the charge build up and atomic coating on electrodes.

The partial energy diagram for neutral Yb is given in figure 2.8, where we can see that there are multiple methods to ionize Yb. The first ionization method is to address

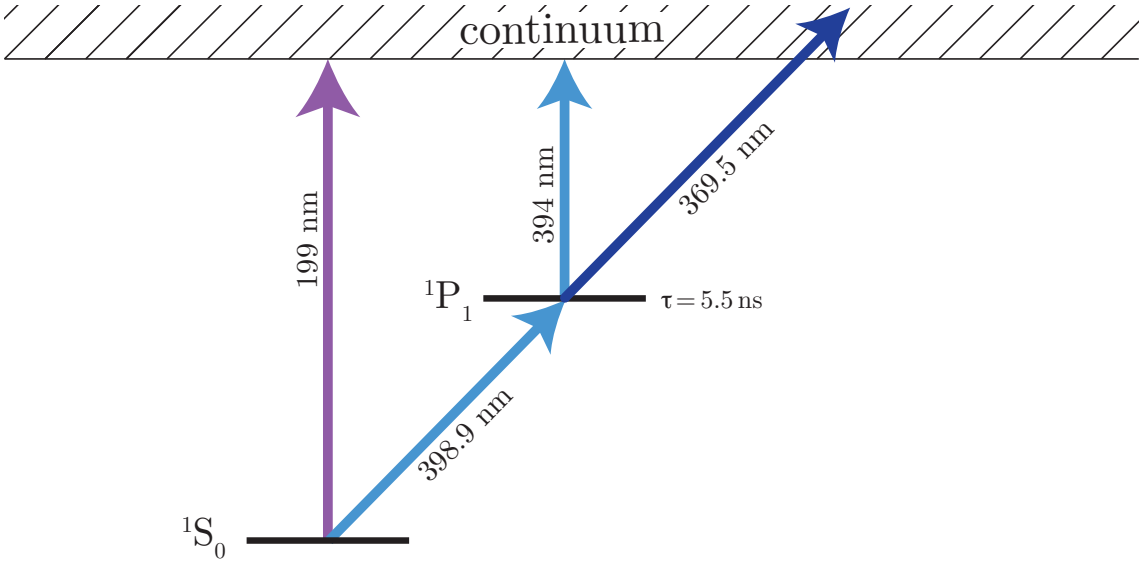

Figure 2.8: The partial energy diagram for a Yb atom showing a single photon and a two photon photoionisation process.

the transition with a single 199 nm laser. While this is a simpler direct transition, this method does not allow individual addressing of different isotopes for selective ionisation. Furthermore, as this transition is in the deep UV it also requires an expensive laser setup to produce the desired wavelength. Another ionisation method is to use a two photon process. Firstly, this requires a laser at a wavelength of 398.9 nm, corresponding to the $^1S_0 \leftrightarrow {}^1P_1$ transition for neutral Yb atoms. A second laser is then required at 394 nm for the ion to reach the ionisation continuum. The process can be simplified by using the Doppler cooling laser at 369.5 nm as the second laser for the two photon ionisation process, which removes the requirement of an additional laser. The saturation intensity of the first ionisation step is $I_{sat} = 60\,\mathrm{mW/cm^2}$ and a beam focused to a diameter of 50 μm will saturate the transition with 1.5 μW of power.

Depending on the relative angle between the atomic beam and the laser, a correction in laser wavelength is required. The change in frequency δf can be given as

$$\delta f = \frac{f}{c} \times v\cos(\theta), \tag{2.25}$$

where θ is the angle between the atomic beam flux and the laser beam, and v is the average velocity of the atomic flux. The average velocity for ohmically evaporated ytterbium is $260 \pm 20\,\mathrm{ms^{-1}}$ [99].

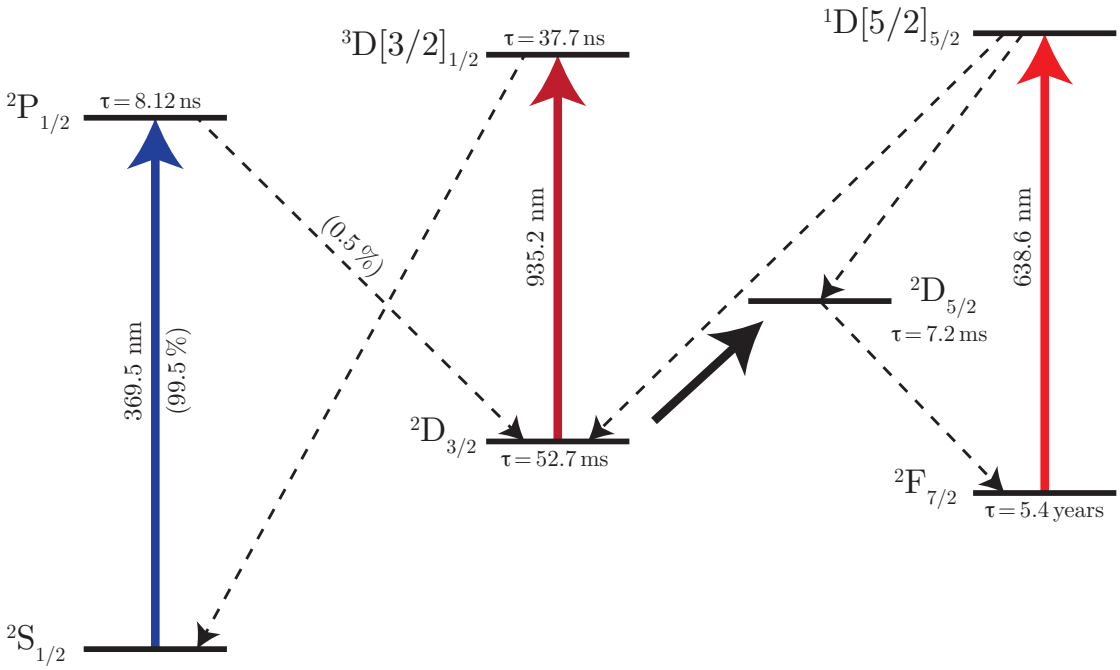

Figure 2.9: The energy level diagram for ^{174}Yb. This diagram shows the transitions that are driven (solid lines) and the decay transitions (dashed lines).

2.4.2 Energy level structure for $^{174}Yb^+$

The energy level structure for $^{174}Yb^+$ can be found in figure 2.9. The structure is common to all isotopes of Yb with the only variation being the exact transition wavelengths between the states. The odd numbered isotopes have a non-zero spin nucleus and also have a hyperfine structure, which is discussed later in section 2.4.3.

After the Yb atom has been ionised, the strong $^2S_{1/2} \leftrightarrow {}^2P_{1/2}$ dipole transition with a linewidth of $\Gamma/2\pi = 19.6\,\text{MHz}$ is used for Doppler cooling and fluorescence detection. This is not a closed cycle and the ion has a 0.5% chance of decaying from the $^2P_{1/2}$ state into the $^2D_{3/2}$ state. To depopulate this state, a laser at 935 nm is required to address the $^2D_{3/2} \leftrightarrow {}^3D[3/2]_{1/2}$ transition from which the ion will decay back into the $^2S_{1/2}$ state. In the $^2D_{3/2}$ state there is a small probability that the ion will decay into the $^2D_{5/2}$ state and then into the $^2F_{7/2}$ state. This transition is much rarer and primarily due to collisions with background gases. For normal operating conditions of 10^{-12} mbar, this transition occurs once every few hours. To depopulate this state, a laser at 638.6 nm can be used, which pumps the ion into the $^1D[5/2]_{5/2}$ state which decays into the $^2D_{3/2}$, which then returns back into the Doppler cooling cycle $^2S_{1/2} \leftrightarrow {}^2P_{1/2}$. In summary, with the use of a 369.5 nm, 935.2 nm and 638.6 nm laser, a closed loop cooling cycle can be created for even numbered Yb ions.

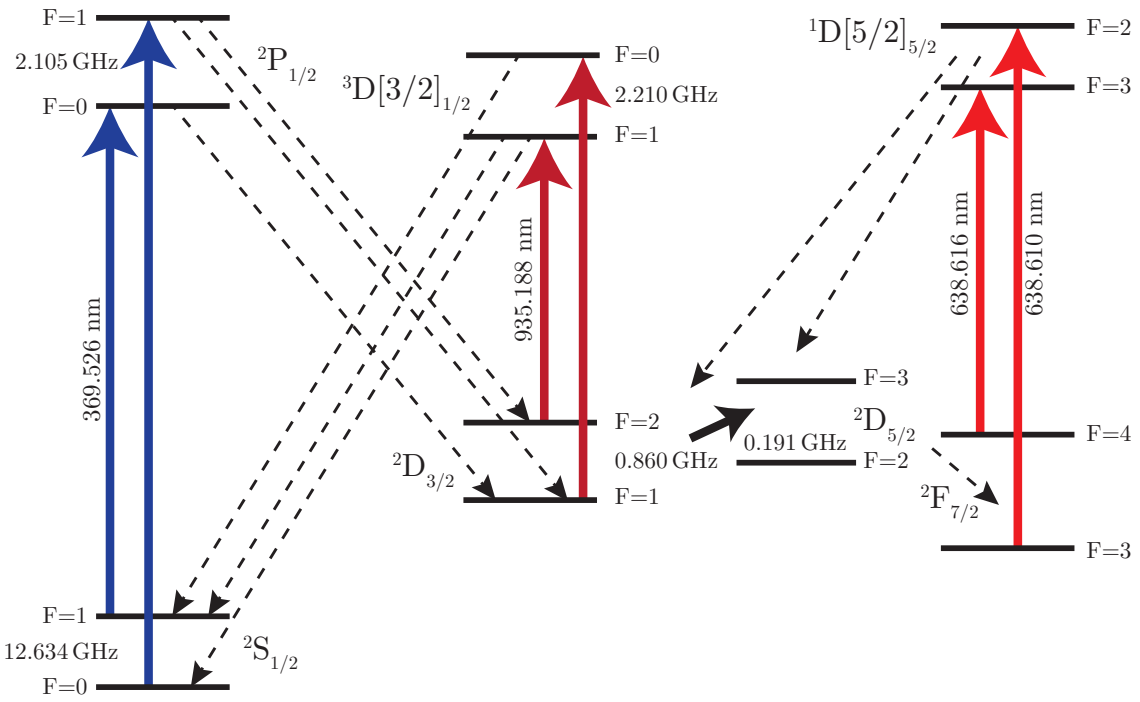

Figure 2.10: The energy level diagram for $^{171}Yb^+$. This diagram shows the hyperfine splitting as a result of the spin half nucleus with driven transitions (solid lines) and the decay transitions (dashed lines).

2.4.3 Energy level structure for $^{171}Yb^+$

The energy level structure for odd numbered Yb ions are more complicated due to their non zero nuclear spin, which results in hyperfine splitting. The energy level structure for $^{171}Yb^+$ showing its hyperfine splitting due to its spin half nucleus (I = 1/2) is given in figure 2.10. The ground state hyperfine splitting of the $^2S_{1/2}$ level makes the ideal qubit with the states $^2S_{1/2}|F=0, m_f=0\rangle$ and $^2S_{1/2}|F=1, m_f=0\rangle$ acting as the states $|0\rangle$ and $|1\rangle$. These clock states are separated by 12.6 GHz.

For state preparation of the ion in the ground state, we optically pump into the $^2S_{1/2}|F=0\rangle$ state using light resonant to the transition $^2S_{1/2}|F=1\rangle \leftrightarrow^2 P_{1/2}|F=1\rangle$ by using a laser at 369 nm and the first sideband at 2.1 GHz produced by an electro-optic modulator (EOM). The ion can then decay into the $^2D_{3/2}|F=1\rangle$ and $^2D_{3/2}|F=2\rangle$ states. To pump the population back into the desired state, a laser at 935 nm resonant with the transition $^2D_{3/2}|F=1\rangle \leftrightarrow^2 D[3/2]_{1/2}|F=0\rangle$ is applied with a first order 3 GHz sidebands. This can be performed by either using an EOM or a power broadened laser at 935 nm able to pump from $^2D_{3/2}|F=2\rangle \leftrightarrow^2 D[3/2]_{1/2}|F=1\rangle$.

To detect if the ion is in the $|0\rangle$ or $|1\rangle$ state, we can use a florescence technique. If the ion was prepared in the $|1\rangle$ state, we can collect the fluorescence from the $^2P_{1/2}|F=0\rangle$ state using a laser resonant with the $^2S_{1/2}|F=1\rangle \leftrightarrow^2 P_{1/2}|F=0\rangle$ and the corresponding

lasers at 935 nm and 638 nm to form a closed cooling cycle. This state is known as the 'bright state'.

If the ion was prepared in the state $|0\rangle$, the closed cooling cycle described above cannot drive the transition $^2S_{1/2}|F=0\rangle \leftrightarrow^2 P_{1/2}|F=0\rangle$ as it is a forbidden transition. Due to off resonant coupling between the $^2P_{1/2}|F=0\rangle$ and $^2P_{1/2}|F=1\rangle$ states, the ion can decay into the $^2S_{1/2}|F=0\rangle$ state. To drive the ion into the $^2P_{1/2}|F=1\rangle$ state we can apply a detuning of 14.7 GHz on the 369.5 nm laser, which corresponds to this transition. The 935 nm laser also has sidebands added, with the difference between the $^2D_{3/2}|F=2\rangle \leftrightarrow {}^3D[3/2]_{1/2}|F=1\rangle$ transition and the $^2D_{3/2}|F=1\rangle \leftrightarrow {}^3D[3/2]_{1/2}|F=0\rangle$ transition being 3.08 GHz. To depopulate the $^2F_{7/2}$ state, light at 638.610 nm and 638.616 nm is used by scanning between these two wavelengths. By keeping the 369 nm laser with a low saturation parameter ($s_0 \leq 1$), we can avoid the off resonant coupling of $^2S_{1/2}|F=0\rangle \leftrightarrow^2 P_{1/2}|F=1\rangle$. This population in the state $|0\rangle$ is therefore known as the 'dark state', where no photons are collected.

Chapter 3

Experimental setup

This chapter briefly outlines the experimental setup used for experiments described in this thesis. This includes lasers (section 3.1), laser stabilization (section 3.2), optical setups (section3.3), a room temperature vacuum system (section 3.4) and imaging (section 3.5). A description of ion trap operation in a room temperature vacuum system is also given (section 3.6).

3.1 Lasers

3.1.1 External cavity diode lasers (ECDL)

Laser diodes are capable of producing coherent radiation by electrically pumping a forward-biased PN junction formed in a direct-band gap semiconductor [100]. To generate light at 399 nm, 935 nm and 638 nm, tuneable external cavity diode lasers in a Littrow configuration are used. Figure 3.2 shows a schematic diagram of an ECDL in Littrow configuration, which consists of a laser diode, an aspheric lens and a diffraction grating. Figure 3.2 shows a picture of the ECDL setup used for the 399 nm laser.

Light emitted from the laser diode in an EDCL setup passes through an aspheric lens, which possess a surface curvature that collimates the light and minimizes spherical aberration. The collimated beam then hits a diffraction grating that acts as the wavelength selective element, which can tune the lasers wavelength. It does this by acting as a mirror that reflects the first-order diffracted beam back to the laser diode as optical feedback, while the zeroth-order is reflected as the output beam. The wavelength of the output beam is dependent on the angle between the incident laser beam and the grating (Littrow angle θ). Therefore, by changing the Littrow angle the output wavelength can also be tuned. The relation between the Littrow angle and the wavelength of the laser is given as

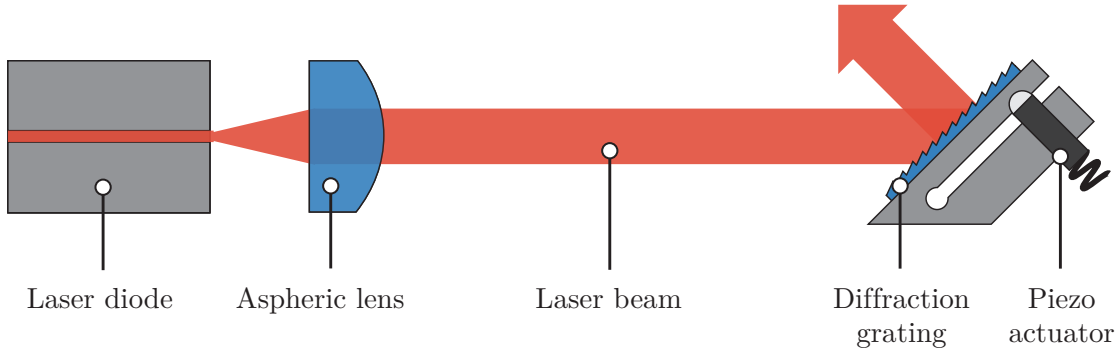

Figure 3.1: Schematic diagram of an ECDL in Littrow configuration. The Schematic shows the positions of the laser diode, aspheric lens, diffraction grating, piezo actuator and beam path.

$$d \sin \theta = n\lambda \tag{3.1}$$

where d is the distance between grooves on the diffraction grating, n is the beam order number and λ is the wavelength of the beam. The angle of the grating, and hence the wavelength, can be remotely controlled using a piezo (Piezomechanik PSt 150/4/5 bS) attached to the back of the grating mount. While the Littrow configuration has the benefit of providing high efficiency and power, variations in the output wavelength and Littrow angle result in an angular displacement of the output beam which can affect the optical alignment of the experiment. However, misalignments can be easily corrected. The ECDL in Littrow configuration is also subject to mode-hopping, a solution to which is described later in section 3.2.

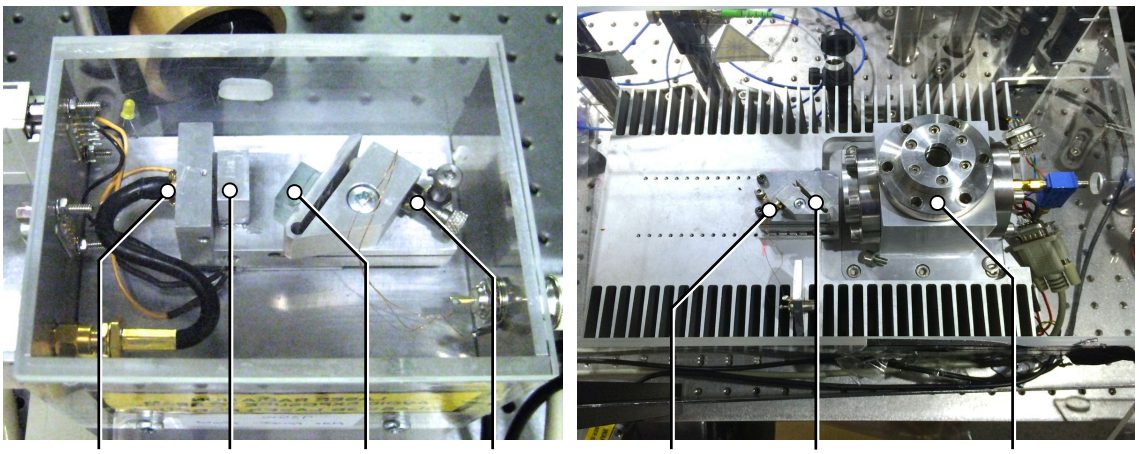

Figure 3.2: (a) The 399 nm ECDL and (b) 369 nm ECDL (ColdLase) used for experiments in Littrow configuration.

399 nm laser

The 399 nm ECDL uses a Sanyo laser diode (DL-4146-301S), a Thorlabs aspheric lens (A390TM-A) and a Thorlabs diffraction grating (GH13-24V). The laser is operated at an output power of 2 mW, measured prior to external optics.

935 nm laser

The 935 nm ECDL uses a Roithner laser diode (RLT940-100GS), a Thorlabs aspheric lens (C330TM-B) and a Thorlabs diffraction grating (GH13-1210). The laser is operated at an output power of 15 mW, measured prior to external optics.

638 nm laser

The 638 nm ECDL uses a Sanyo laser diode (DL-6148-030), a Thorlabs aspheric lens (A390TM-B) and a Thorlabs diffraction grating (GH13-24V). The laser is operated at an output power of 17 mW, measured prior to external optics.

3.1.2 ColdLase 369 nm laser

Two independent laser systems are used to provide light at 369 nm for the Doppler cooling transition. The first laser used is the ColdLase system, which was built in-house and used for experiments described in section 3.6. The ColdLase system is based on an ECDL setup in Littrow configuration as described in section 3.1.1 and is shown in figure 3.2. A 375 nm laser diode (Nichia NDU1113E) and cooled to sub-zero temperatures to reach an emitted wavelength of 369 nm. An aspheric lens (Thorlabs A390TM-A) is mounted with the laser diode within an enclosure (figure 3.2) and a diffraction grating is positioned outside of the enclosure. Both the enclosure and the diffraction grating are mounted on a large heat sink as one mechanism for heat dissipation. The systems is also actively cooled using a two stage thermoelectric cooler (TE Tech te-2-(127-127)-1.3) and the temperature of the system is measured using a thermistor (Farnell AD592ANZ). As the enclosure containing the diode and lens is not hermitically sealed, it is prone to forming condensation. A 'Molecular Sieve' (Baltimore Innovations BIL-10127-WSG) is therefore used within the enclosure to absorb moisture and is capable of absorbing up to 20% of its own weight in moisture. During operation the laser is operated at an output power of 2 mW.

M Squared 369 nm laser

The second laser used for 369 nm is the frequency doubled M Squared system (figure 3.3 which is divided into seven separate module stages. The first stage consists of a solid state pump laser that is used to generate 12 W at 532 nm. The second stage is a pump optics module, which includes a pair of manually adjustable mirrors to steer the pump beam from the pump to the next module (SolTis). The third stage is the SolTis (1000 PSX-R) module, which contains a Ti Sapphire cavity that takes the input pump beam at 532 nm and outputs at 739 nm. The module also contains an etalon which can be used to lock the 739 nm at this stage. The fourth stage is a pick-off module. Here, 30 mW of 739 nm is picked off from the main beam and fed out of the module, allowing the beam to be coupled into an optical fibre that leads to the wavemeter. The fifth stage is an electro-optic modulator (EOM) that can be used to control the power, phase and polarization of the beam using an electrical control signal. The EOM also allows the setup to generate sidebands for future experiments. The sixth stage is a beam steering stage which includes a pair of adjustable mirrors for beam alignment and a focusing lens. The final stage is the ECD-X (ECD 369) resonant frequency doubler module. At this stage the 739 nm beam is converted to 369 nm through a second harmonic generation technique using an LBO crystal. The frequency can also be locked internally at this stage using a Hänsch-Couillaud technique [101]. The final output power after the ECD-X stage is ∼1.4 W.

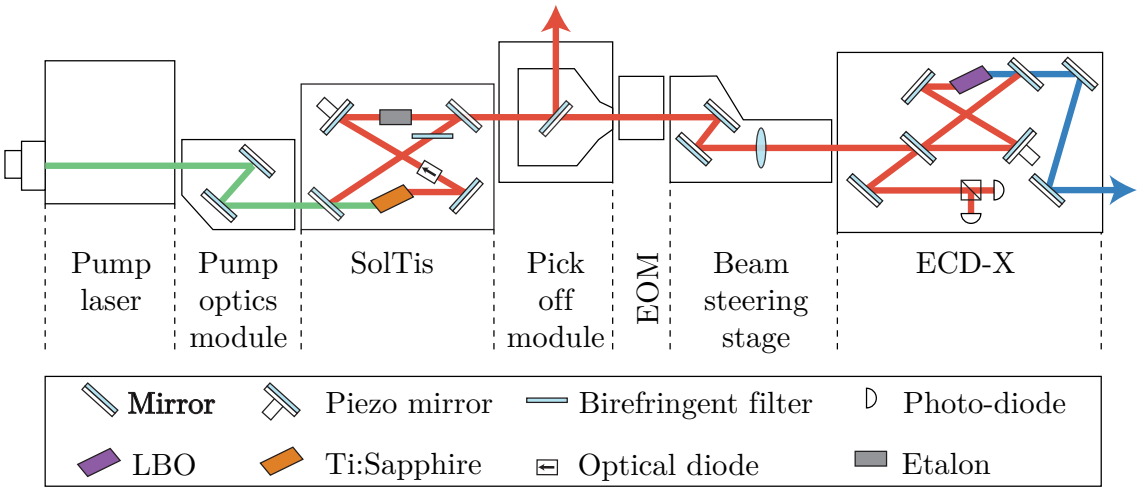

Figure 3.3: Schematic diagram of the M Squared laser showing the seven module stages used for generating 369 nm.

3.2 Laser stabilisation

Laser wavelengths can be extremely sensitive to variations in current, temperature and in changes to their cavity length. To stabilize the wavelengths there are several passive and active techniques that can be implemented. The temperature of lasers built in-house are passively stabilized by placing each laser within two boxes to help decrease the effects of changes in temperature. Each laser is also connected to its own temperature control unit to help maintain the temperature to within 0.01 K. Each box, except for the Cold-Lase system, is also covered internally in multi-density foam to dampen the transfer of acoustic energy and mitigate any variations in cavity length. On the other hand, active frequency stabilization is performed using various laser locking techniques. For all experiments described in this thesis, lasers were either wavemeter locked or left unlocked. For completeness, a reference laser lock and transfer cavity lock are also described in this section as the techniques which are already employed in the lab and will eventually be included for the lasers described in section 3.1.

3.2.1 Wavemeter lock

The 399 nm, 935 nm and ColdLase lasers were all locked using a wavemeter (High Finesse WS7). The M Squared laser was stable to within 80 MHz over an hour and did not require being externally locked for initial trapping purposes. To lock the wavelengths using the wavemeter, a quartz plate is used to pick off 10% of the laser beam which is then coupled into an optical fibres and sent to the wavemeter. The fibre passes through a multi-channel switcher which switches between all input fibres, allowing for all fibre wavelengths to be displayed simultaneously. To maintain a fast update rate sufficient power should be coupled into each fibre, allowing for the exposure time on each channel to be minimized. The measured wavelength is sent to the experimental computer which runs a LabVIEW locking program where a desired wavelength can be set. The locking program compares the desired wavelength and the wavemeter input and generates a feedback signal proportional to the wavelength difference. The signal is sent via an analogue output card (National Instruments PCI-6722) to the ECDLs piezo, described in section 3.1.1, and brings the measured wavelength to the set point. The wavemeter provides an absolute frequency stability of ± 60 MHz and ± 120 MHz below 370 nm.

3.2.2 780 nm reference laser lock

To provide better frequency stability than a wavemeter lock <20 MHz, a reference laser [102] can be used to lock lasers against. The reference laser is locked to an atomic transition within Rubidium (Rb) providing a frequency stable laser with <1 MHz over one hour. Other lasers can then be locked to the stable reference laser and it reference frequency can also be used to calibrate the wavemeter. The system consists of an ECDL setup with a laser diode (Thorlabs GH0781JA2C), aspheric lens (Thorlabs GH0781JA2C) and diffraction grating (Thorlabs GR13-185) that produces an output power of 80 mW. The laser is locked to the $^2S_{1/2} \leftrightarrow ^2P_{3/2}$ D_2 transition within Rb^{87} which has a natural linewidth of $\Gamma/2\pi = 6$ MHz (figure 3.4). Due to the kinetic energy of the Rb within the vapour cell, the transition is Doppler broadened to ~ 500 MHz. To produce a Doppler free absorption spectrum two counter propagating beams known as the pump and probe, with powers of 1.3 mW and 0.1 mW respectively, are passed through the Rb vapour cell and are detected using two photodiodes (Hammatsu Si PIN photodiode S5972). The pump beam saturates the transition while the probe beam displays the peaks within the absorption spectrum. Subtracting the two absorption signals provides a Doppler free absorption spectrum. A proportional integration controller (PI) is used on the lock-in amplifier output and the results are sent to a piezo controller that locks the laser to the absorption line.

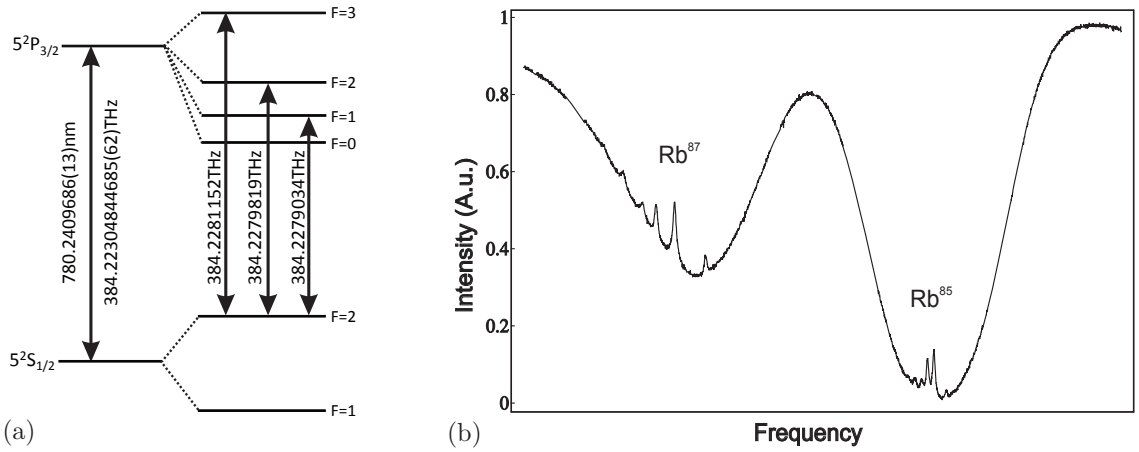

Figure 3.4: (a) Hyperfine structure, including the $^2S_{1/2} \leftrightarrow ^2P_{3/2}$ D_2 transition within Rb^{87}, used to as a reference for locking. (b) Saturation absorption signal.

3.2.3 Dual wavelength cavity lock

For future experiments the M Squared 369 nm laser can be locked using a dual wavelength cavity lock. To perform the lock two Fabrey-Pérot confocal cavities with high reflectivity coatings at the desired wavelength are used. Polarizing beam splitters are used to combine

739 nm from the M Squared laser pick-off module with the 780 nm reference laser in one cavity. The 780 nm beam is first aligned through an AOM in double-pass configuration, which shifts the frequency of the beam corresponding to the frequency applied. The 780 nmbeam is then tuned into resonance with the cavity and the cavity length is then locked using a PID controller. The output laser signals from the cavity are collected using individual photodiodes. A side fringe lock is then used to lock the 739 nmbeam with the cavity length. This process can also be performed for the 399 nm and 935 nm lasers.

3.3 Optical setup

In this section two optical setups are described. Both setups were present on the same table, however, they were implemented at different stages of the experiment. The first setup shown was used for the room temperature vacuum system described in section 3.4 and the second setup shown was used for the cryogenic system described in section 4.

3.4 Vacuum systems

Ion trapping experiments naturally require an ultra high vacuum (UHV) environment to prevent unwanted collisions between the ion and surrounding particles. To achieve this, a vacuum chamber capable of reaching pressures down to 10^{-12} torr was developed. Figure 3.6 shows the fully assembled vacuum system used for experiments described in section 3.6. The central chamber that contains the ion trap consists of a spherical octagon (Kimball Physics PN MCF600-SphOct-F2C8) and a weldable cluster (Kimball Physics PN MCF450-Weld-E1C4).

3.4.1 Electrical connections

Within the centre of the octagon, the surface electrode ion trap is attached to a 208 pin chip carrier (Global Chip Materials PGA10047002) as shown in figure 3.7. The chip carrier is inserted into a two-piece PEEK mounting bracket that holds gold plated pin receptacles (Mill-Max 0672-1-15-15-30-27-10-0). The pins are connected to Kapton coated ribbon cables (Allectra 380-D50FXPR-500) which lead to a 2×50 pin D-sub feedthrough (K.J.Lesker IFDGG501056A). The central mounting bracket (figure 3.7) also incorporates two ohmically heated atomic source ovens that provide a Yb flux towards the ion trap. The oven itself is formed from a Yb wire inserted within a 20 mm long 0.0650" diameter stainless steel tube that is crimped at one end. One oven contain natural Yb (Goodfellow

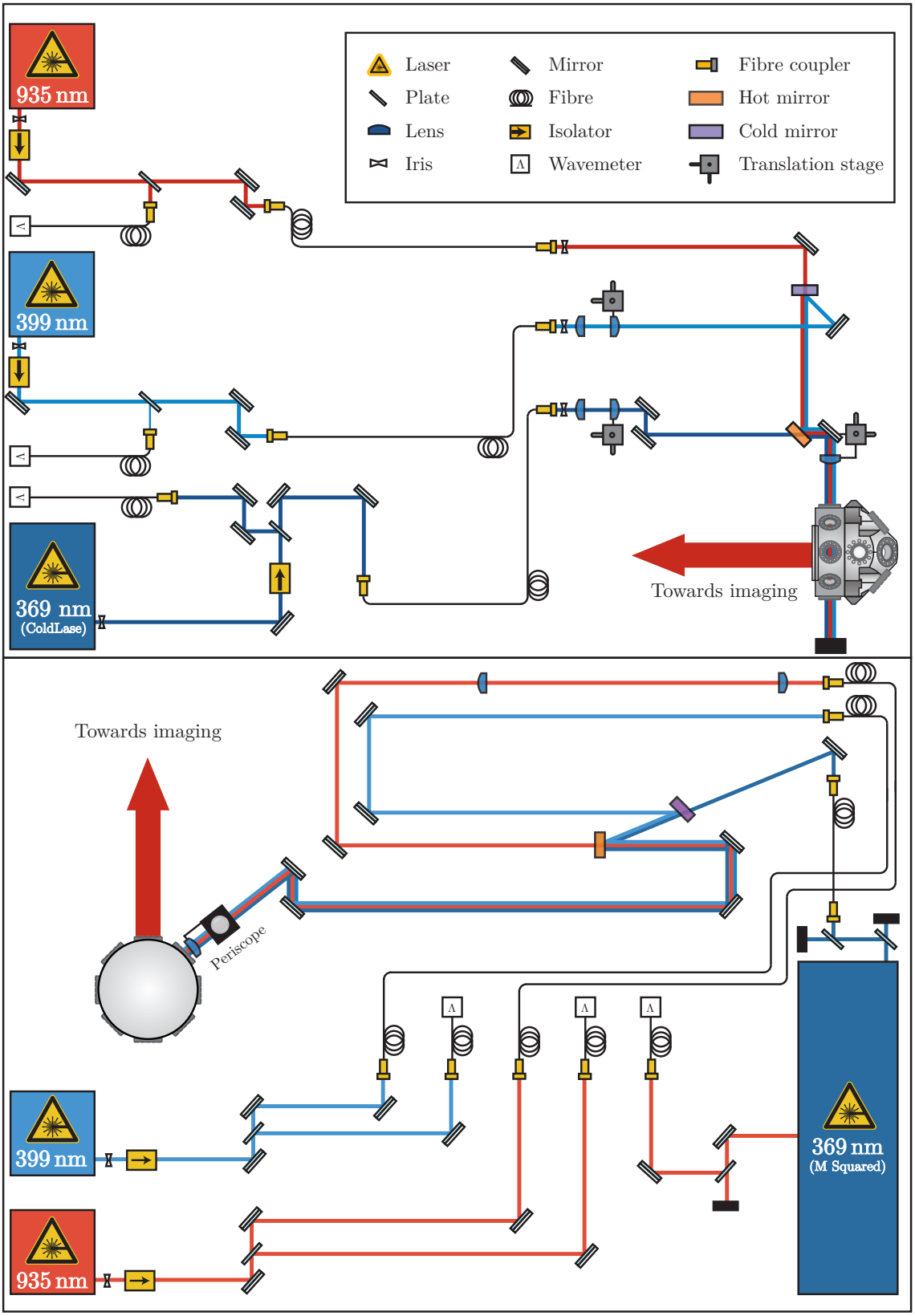

Figure 3.5: Optical setups showing the beam paths from the lasers to the room temperature vacuum system (top) and cryogenic vacuum system (bottom).

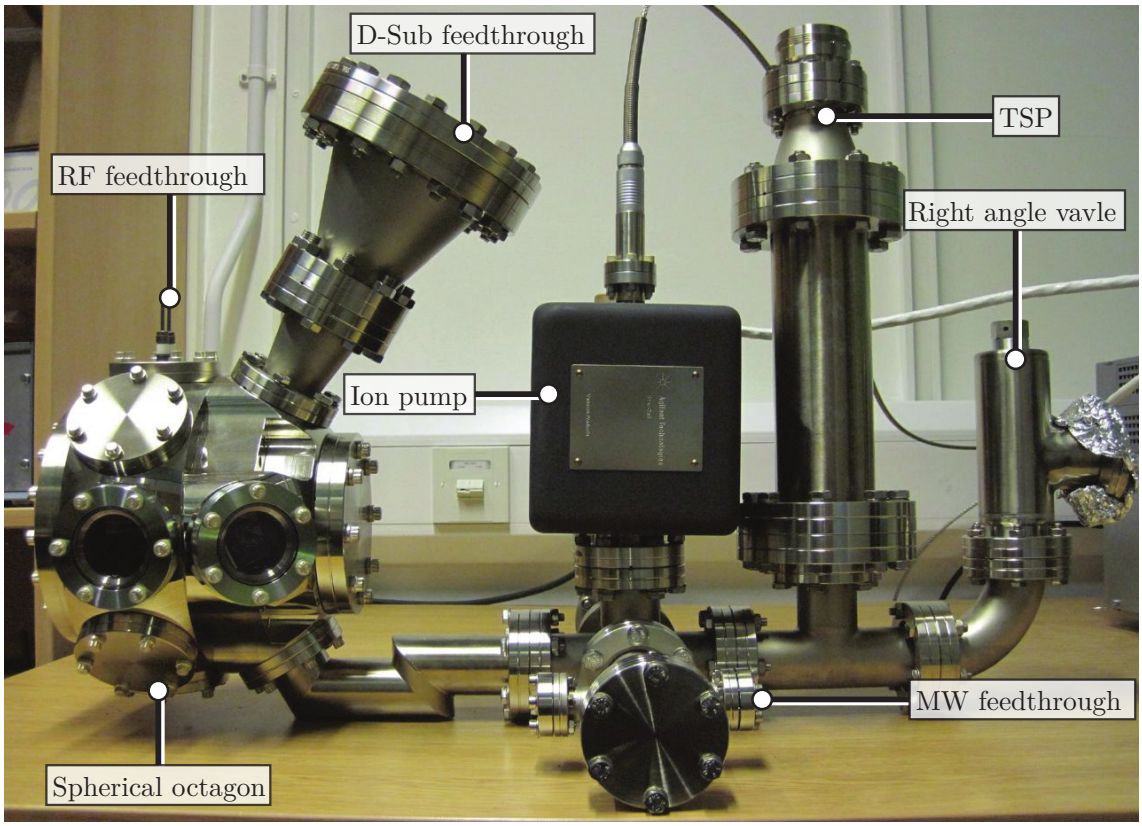

Figure 3.6: Room temperature vacuum system used for experiments described in section 3.6.

GO0196) and the other oven contains 90% enriched ^{171}Yb (Oak Ridge National Laboratory OA0036). The ovens are operated by applying a current of 5-10 A via a six pin 2.75" electrical feedthrough (K.J.Lesker EFT0265063). The oven is capable of reaching temperatures up to 400°C after a few minutes which is sufficient to evaporate Yb. The rf voltage to create the pseudopotential is supplied to the trap via a helical resonator (section 3.4.3) attached to a high voltage two pin 2.75" feedthrough (Allectra 264-24CU5K-2-C40).

3.4.2 Attaining vacuum pressures

A turbo molecular pump (TMP) (Pfeiffer TSH 071 E) is used to bring the system from atmospheric pressure down to 10^{-7} torr and is attached via a right angle valve (K.J.Lesker VZCR40R). Once the system reaches $10^{-7} - 10^{-8}$ torr an ion pump (Varian StarCell 9191145) can be used to bring the pressure down to $10^{-9} - 10^{-12}$ torr. After the system goes below 10^{-6} torr an ion gauge (Varian 9715015) can be used to measure the pressure of the system. A system opened to atmospheric pressure will not be capable of directly attaining a pressure down to 10^{-12} torr using this process. To remove any contaminants that may have entered the vacuum chamber, the system can be baked at 200°C for two

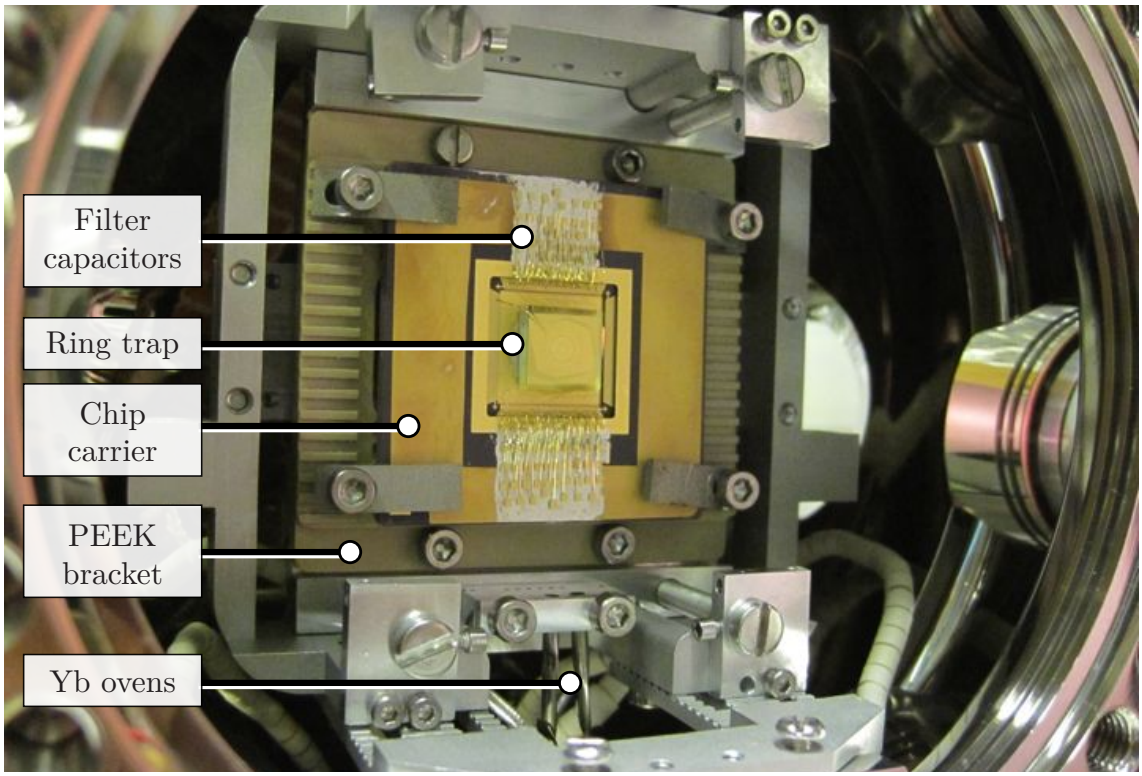

Figure 3.7: Close up image of the surface electrode trap within the octagon of the room temperature vacuum system.

weeks. During this process, only the TMP and a secondary external ion pump are used to pump the system [103]. After the baking process a titanium sublimation pump (TSP) (Varian 9160050) is operated to reduce the pressure further. By periodically applying a current of 46 A to a filament within the TSP, the titanium begins to sublimate and coat the surrounding nipple walls in a thin layer of clean titanium. The sublimated titanium reacts with the particles within the system to form stable products that stick to the coated walls. The angle valve can then be closed and the system pumped solely by the internal ion pump which can bring the pressure down to 10^{-12} torr. Figure 3.8 shows the vacuum system on the optical table during active use.

3.4.3 Helical resonator

To produce a confining pseudopotential, an rf voltage must be applied to the trap. The rf voltage must have a relatively small bandwidth such that it filters out any unwanted noise which could otherwise lead to heating of the ion [104]. It should also be capable of supplying sufficiently high voltages to produce the required trap depth for the ions. Impedance matching between the rf voltage source and the trap must also be taken into account as unwanted reflections can result in reflected power damaging equipment. The

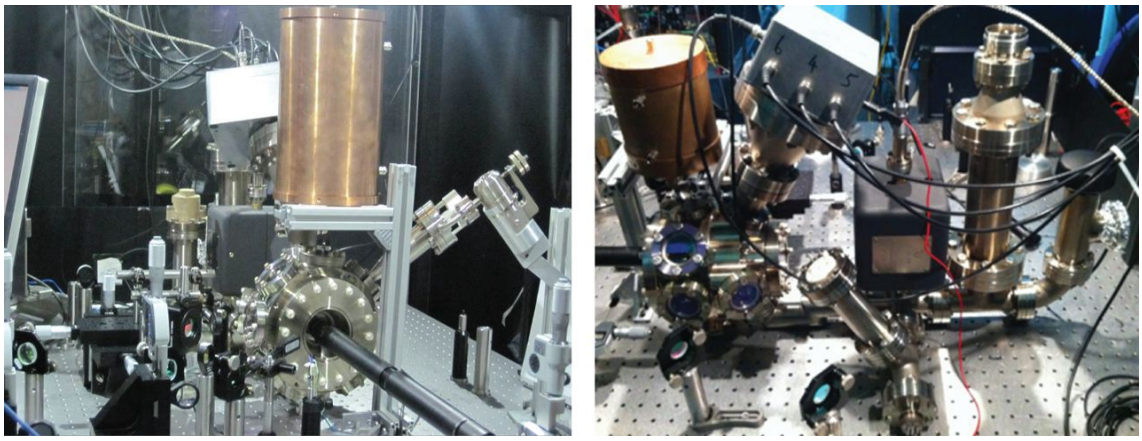

Figure 3.8: Images showing the room temperature vacuum system during operation with all electrical connections include the rf helical resonator described in section 3.4.3.

bandwidth, high voltage and impedance matching requirements can all be met by the use of a helical resonator. Figure 3.9 shows a schematic diagram of the rf system.

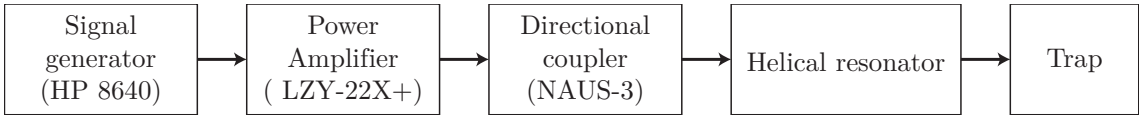

Figure 3.9: Schematic diagram for the rf signal delivery setup to the trap.

The rf signal is supplied to the resonator using a signal generator (HP 8640B) and passes through an amplifier (Mini-Circuits LZY-22X+) which amplifies the signal by 43 dB. The signal then passes through a directional power meter (Rhode & Schwarz NAUS-3) which measures any reflections. This signal then goes to the helical resonator which is composed of an antennae coil, a pick up coil and an enclosing cylindrical copper shield (figure 3.10).

The oscillating voltage in the antennae coil generates an oscillating magnetic field which in turn induces an oscillating voltage on the pick up coil which is electrically connected to the ion trap via internal coax cables, PCB tracks and wire bonds. The length of the pick up coil L is precisely constructed such that $L = \lambda/4$ which leads to maximum coupling. Frequencies that are not resonant with the pick up coil are reflected. The impedance matching is performed by adjusting the geometry of the antennae coil and observing the reflected power on the directional power meter. Using this method a coupling of $> 95\%$ can be achieved. The peak rf voltage V_{rf} is given by

$$V_{rf} = \kappa\sqrt{2PQ} \tag{3.2}$$

where κ is the traps geometrical factor, P is the power applied to the resonator from the amplifier and Q is the quality factor of the resonator. The quality factor of the resonator

can be described as the ratio of energy stored in the resonator and the energy dissipated and is given as

$$Q = \frac{\text{Energy stored}}{\text{Energy dissipated}} = \frac{f_0}{\Delta f} = \frac{f_0}{f_+ - f_-} = \frac{1}{2\pi f_0 RC} \tag{3.3}$$

where Δf is equal to $f_+ - f_-$ which is the -3 dB bandwidth, and R and C are the resistance and capacitance respectively of the resonant circuit. The resonant frequency f_0 of the circuit is given by

$$f_0 = \frac{1}{2\pi\sqrt{LC}}. \tag{3.4}$$

where L is the inductance of the resonant circuit. Figure 3.10 shows an exterior and interior view of the resonator. Table 3.1 shows the parameters of the resonator used in section 3.6. A full description of the design of the helical resonator is given in [105].

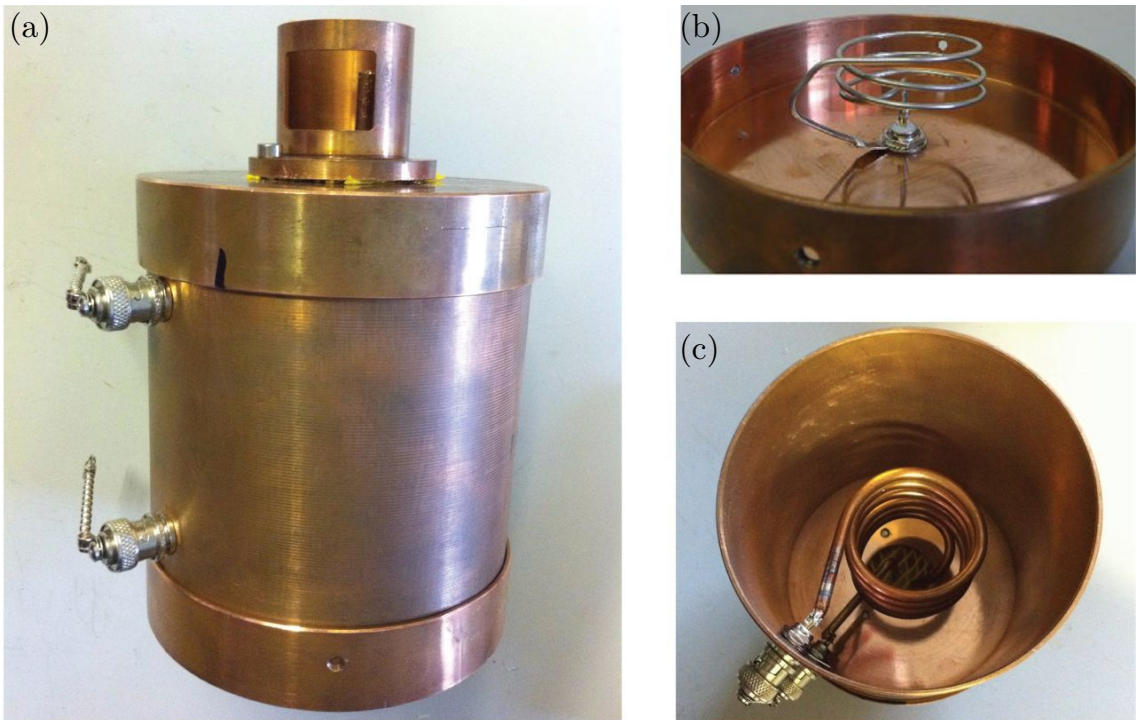

Figure 3.10: (a) Assembled helical resonator, (b) helical resonator cap with antennae coil and (c) helical resonator ground shield and pick-up coil.

3.5 Imaging system

An imaging system was designed and developed to detect ion fluorescence from the Doppler cooling transition $^2S_{1/2} \leftrightarrow {}^2P_{1/2}$ at 369 nm. The system was designed to be used for the cryogenic system described in chapter 4 and to be capable of easily switching between

Shield Diameter, D [mm]	145(2)
Shield length, B [mm]	250(2)
Coil Diameter, d [mm]	62(3)
Coil Length, b [mm]	130(5)
Coil diameter, d_0 [mm]	3.6(1)
Winding pitch, τ [mm]	7.7(2)
Number of turns, N	17.0(5)
Resonant frequency with trap load, f_0 [MHz]	13.6(1)
Q with trap load	136(20)

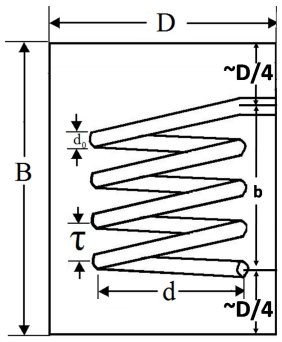

Table 3.1: Design specifications for the resonator used in section 3.6.

a charged coupled device (CCD) (Andor Luca R DL-604M) and a photomultiplier tube (PMT) (Hamamatsu H8259-01) using a motorized flipper mirror (Newport 8892-K) after passing through a bandpass filter (Semrock FF01-370136) that transmits >94% of light at 369 nm. A separate imaging system was used for the room temperature vacuum system described in section 3.6 and was designed and developed by Marcus Hughes [106]. The combined imaging setup for both systems is given in figure 3.11.

3.5.1 Cryogenic system imaging

The first optical element from the cryogenic vacuum system is a custom objective composed of five individual lenses (Sill Optics S6ASS2245) [107]. The lens system is designed to image through 8 mm of fused silica (vacuum chamber windows), optimized for collimation, has a large numerical aperture (NA) of 0.4, a focal length of 40 mm and possess AR-coating for 369 nm on all lenses. Figure 3.12 shows a schematic diagram of the lens system including three fused silica windows used in the cryogenic vacuum system totalling 8 mm in thickness. Using the given NA the optical resolution of the system is calculated as $r = 0.61\lambda/NA = 0.52\,\mu$m. The design was independently simulated using OSLO[1] and the light confined to the central airy disc, known as the relative irradiance, was shown to be 99.59% (figure 3.12).

The collimated light is then reflected off a broadband dielectric mirror (Thorlabs BB2-E01) mounted on a right angle kinematic cage block (Thorlabs KCB2) which sends the beam path parallel to the surface of the optical table. The next optical element is a plano-convex lens with a focal length of 500 mm (Thorlabs LA4782-UV). Since the objective lens produces a collimated beam, this allow the distance between the objective and the first lens to be arbitrary and dependant only on the final position of the CCD and PMT. If

[1] http : //www.lambdares.com/software products/oslo

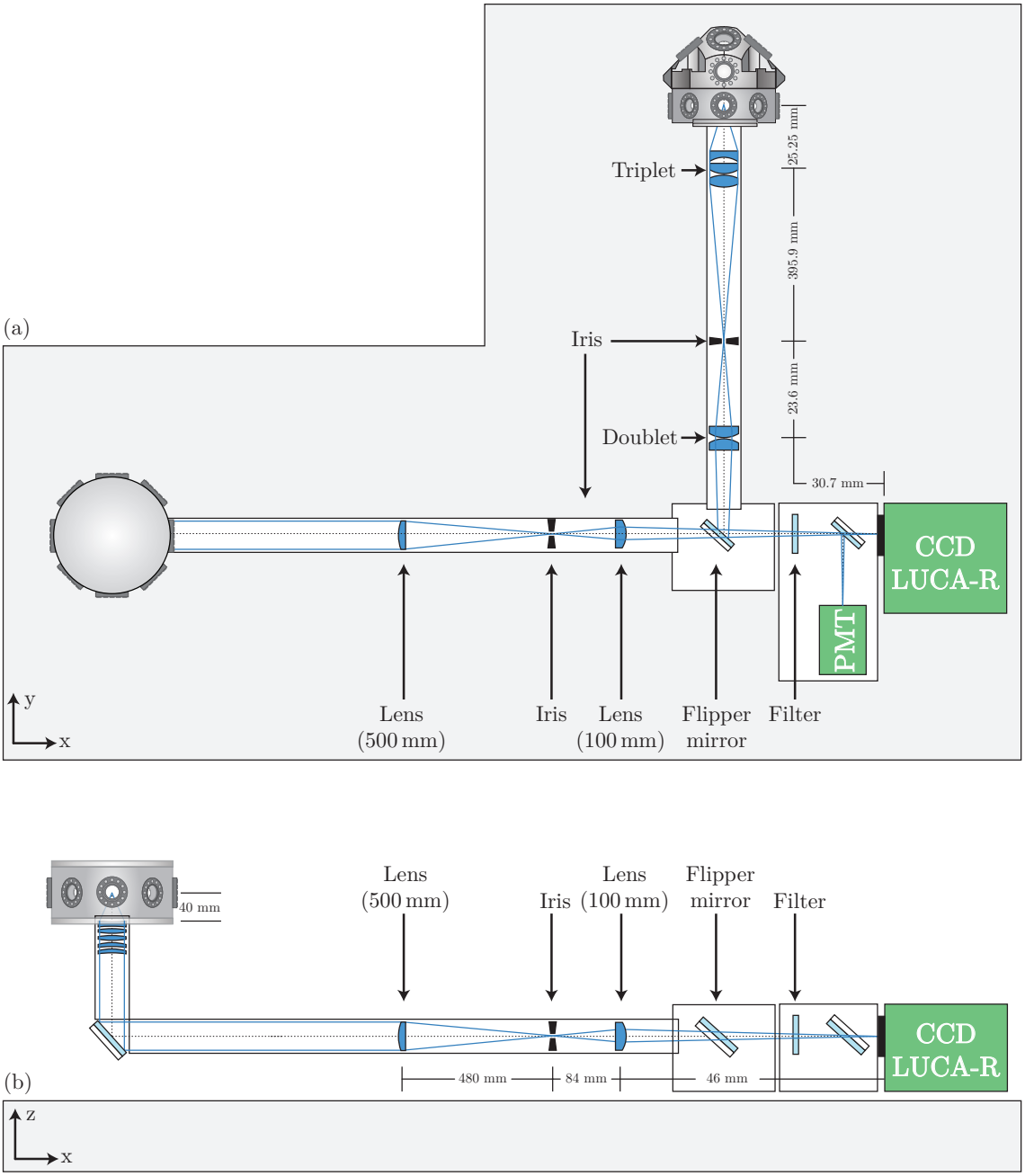

Figure 3.11: Imaging system for the room temperature and cryogenic vacuum system. The top image shows the optical table in a top-down view and the bottom image shows the optical table in a side-on view.

the combination of the objective and first lens could be treated as a thin lens system, the magnification could be calculated using

$$M = \frac{f}{f - d_0} \tag{3.5}$$

where f is the focal length and d_0 is the object distance. This would provide a magnification of 12.5. However, as the system is more complex the lens configuration was simulated in OSLO and found to have a magnification M_{OBJ} of 12.1.

The final lens used is another plano-convex lens with a 100 mm focal length (Thorlabs LA4545-UV). The object distance for the 100 mm lens is determined by the total magnification required. If the diffraction limited size of an ion (0.52 μm) is to be scaled to cover a five by five pixel area, where each pixel is 8 μm, then an overall magnification M_{TOTAL} of 77.45 is required. This requires the final lens to have a magnification M_2 of 6.40 resulting in an object distance of 84 mm and an image distance of 46 mm.

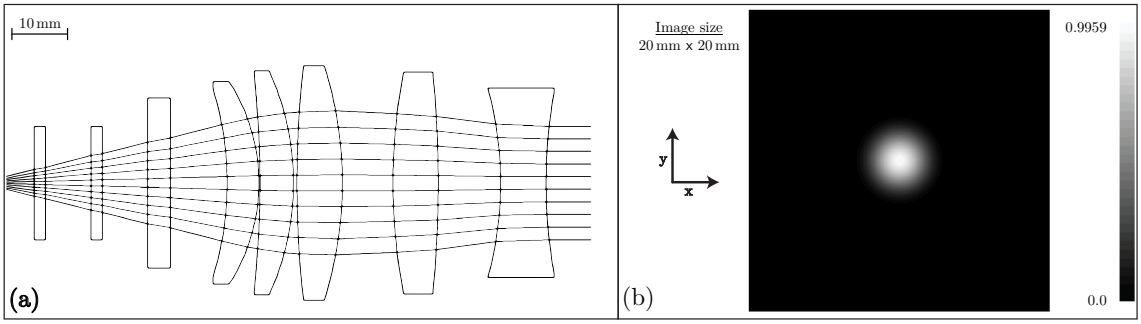

Figure 3.12: (a) Light ray diagram of the cryogenic objective lens system including three fused silica windows simulated in OSLO. (b) Point spread function for after the lens system.

3.5.2 Room temperature system imaging

The first optical component for the room temperature system is an objective composed of three individual lenses (Special Optics 54-17-29-369) and was also designed to image through 8 mm of fused silica. This objective is designed to be 23.54 mm from the ion and to produce an image at a distance of 549.7 mm with a relative irradiance of 75.8%. The magnification of the triplet system M_{OBJ} is 23.4. The next element is a doublet system which consists of two plano convex lens. The position of the doublet lenses can again be determined by first determining the total magnification required to scale the diffraction limited ion, in this case 1.13 μm, across a given number of pixels. The combined focal length of the doublet is given as

$$f_D = \frac{f_1 f_2}{f_1 + f_2} \tag{3.6}$$

where f_1 and f_2 are the focal lengths of the two lens. The resultant magnification of the doublet is given as $M_D = d_i/d_o$, where d_i and d_o are the image and object distances respectively.

3.5.3 Comparison of cryogenic and room temperature imaging systems

The objective lens systems

There are several key difference between the cryogenic and room temperature imaging systems that make them more suited for their specific application. The most significant design feature for both systems is the imaging objective. The room temperature objective (Special Optics 54-17-29-369) possess a relatively small working distance of 23.54 mm, increasing the collection of photons by being closer to the ion trap. The cryogenic system on the other hand is limited by the increased distance between the ion trap and the outer surface of the imaging window, which is due to the radiation shields within the vacuum chamber. However, the cryogenic systems objective (Sill Optics S6ASS2245) possess a higher numerical aperture of 0.40 compared with room temperature system's objective of 0.31. This is due to the larger diameter of 40 mm for the cryogenic objective compared with 15 mm for the room temperature objective.

Another key difference between the two systems is that the cryogenic objective was designed to collimate the output light, where as the room temperature objective was designed to focus the light. While both objectives can in theory collimate and focus the output beam by varying the working distance, both lens systems have been designed and optimized to minimize spherical and chromatic aberration at their specified working distances. The collimated light produced by the cryogenic objective is extremely beneficial as it allows an arbitrary distance between the objective and the CCD and PMT as described in section 3.5.1. In figure 3.11b we can see that the distance between the objective and the two lens system, where the beam is collimated, can be varied to meet any limitations in space in the experimental environment. It should be noted that while the cryogenic objective performs significantly better than the room temperature system and offers a larger working distance, the cryogenic objective is a more complex lens arrangement with 5 individual lenses compared with the 3 lenses from the room temperature system. The cryogenic objective is also more expensive by a factor of $\sim$10 and is a custom built arrangement compared with the 'off the shelf' room temperature objective.

The 'doublet' lens systems

The other key difference between the two systems is the two lens 'doublet' systems after the objective. Both doublets are utilized to provide further magnification of the ion, however, they differ in their arrangement to take into account their respective objective lens systems. The room temperature doublet is formed of a compact two lens system, which must focus the light from the objective to the CCD within a total ion-CCD distance of $\sim$700 mm. The ion-CCD distance for the cryogenic system is >2000 mm, which allows more space for the imaging optics. While compact achromatic doublet lens are designed to eliminate chromatic and spherical aberrations inherent in single lenses, the compact doublet in the room temperature system is formed from two separate plano-convex lenses with a non-achromatic configuration. The doublet systems from both systems can therefore be considered as similar systems with differing lens focal lengths and separations.

For the cryogenic imaging system, two plano-convex lens were chosen instead of achromatic lenses for two reasons. Firstly, the imaging system does not suffer from chromatic aberration as it only detects the single wavelength at 369 nm from ion fluorescence. Secondly, the spherical aberration was found to be negligible for both imaging systems. Spherical aberration occurs when light passes through lenses with spherical surfaces, at different distances from the central optic axis. The light entering at different points focuses the output rays at different distances. This cannot be accounted for by using the lens equation as this assumes all rays are paraxial, which are rays close to the optic axis, and also assumes ideal lenses. The effects of spherical aberration can be reduced by selecting lenses with less curved surfaces (larger radius of curvature) and therefore larger focal lengths. For the cryogenic doublet it was ensured that the spherical aberration would be minimized by using lenses with relatively large focal lengths of 500 mm and 100 mm.

Figure 3.13a and 3.13b show the motivation for the selection of the 500 mm and 100 mm lenses. Figure 3.13a shows the variation in relative irradiance as a function of the focal length for the first lens in the doublet. Selecting a 500 mm plano-convex lens maintains a relative irradiance >0.98 while keeping the focal length as small for the practical purposes. The second lens is chosen to maintain a high relative irradiance at the final image, while keeping a small focal length and allowing for a variation in the final magnification by varying the position of the second lens. Figure 3.13b shows the relative irradiance through the complete imaging system as a function of the doublets magnification. By simply changing the position of the final lens, the magnification of the imaging system can be varied by a factor of $2 - 13$ while maintaining a relative irradiance of >95%.

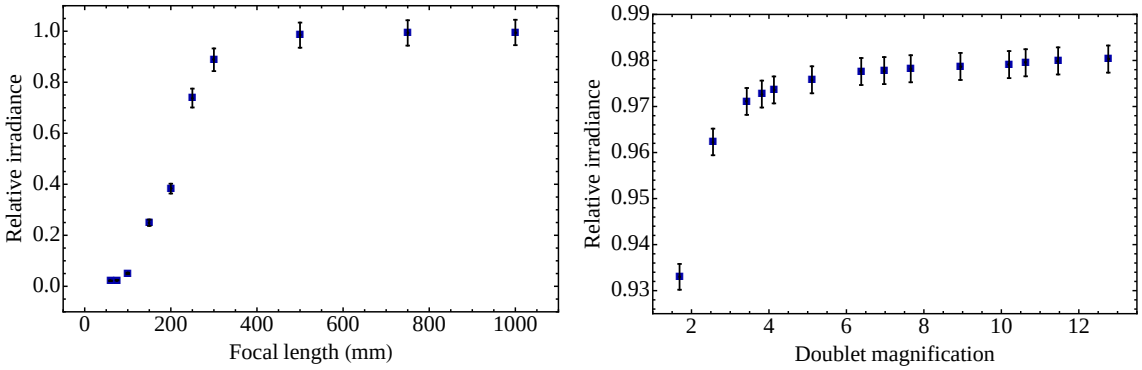

(a) (b)

Figure 3.13: (a) The variation in relative irradiance as a function of the focal length for the first lens in the doublet. Larger focal length lenses with less curved surfaces provide a higher relative irradiance due to the reduction in spherical aberration. (b) Relative irradiance through the complete imaging system as a function of the doublets magnification. Both sets of data are simulated using OLSO - TracePro.

3.6 Ring trap

The experiments performed in this section were done using a microfabricated ion trap [106] fabricated using microelectromechanical systems (MEMS) techniques, such as those described in chapter 6. The geometry of the trap possess a ring shaped architecture, where a continuous circular trapping region allows for a string of ions to be confined in a ring above the trapping structure (figure 3.14). The ring structure has a radius of 1690 μm and produces a fixed ion height of 245 μm. A confined ion chain should exhibit periodic boundary conditions with homogenous ion-ion spacing, opening up the possibility of studying physical systems such as the homogeneous Kibble-Zurek mechanism [108], Hawking radiation [109] and space-time crystals [110].

The trap was fabricated on a 500 μm thick fused quartz wafer with a surface roughness of < 2 nm and a high optical transmission. To allow for voltages to be applied to isolated central electrodes, buried wires are incorporated into the trap architecture. The buried wires and surface electrodes are formed from layers of gold deposited by thermal evaporation and electroplating respectively. Further details of the fabrication procedure and trap architecture can be found in [106].

3.6.1 Trap operation

The trap was mounted on an aluminium block and then onto a ceramic chip carrier using a conductive silver epoxy (EPO-TEK H21). The trap electrodes were electrically connected to the chip carrier bond pads using a wedge wirebonder (Kulicke & Soffa 4523A) with

gold wire (Coining 4828). The chip capacitance was measured to be $22 \pm 2\,\mathrm{pF}$. To ensure rf grounding a low pass filter was included for all dc electrodes. A 620 pF capacitor was attached to the chip carrier and wire bonded to the static electrodes with a $1\,\mathrm{k}\Omega$ resistors connected in series. The chip was mounted within the room temperature UHV vacuum system at a pressure of $4.0\times10^{-11}\,\mathrm{mbar}$. The helical resonator provided a $> 90\%$ coupling between the rf amplifier and chip at resonant frequency ($\Omega/2\pi = 13.6\,\mathrm{MHz}$) with $Q = 136$. Atomic ovens containing natural ytterbium were ohmically heated to produce a flux of atoms parallel to the trap surface. The atoms were resonantly ionised using the two-colour photoionization process and laser cooling process described in section 2, with ion fluorescence imaged onto an electron multiplied CCD array.

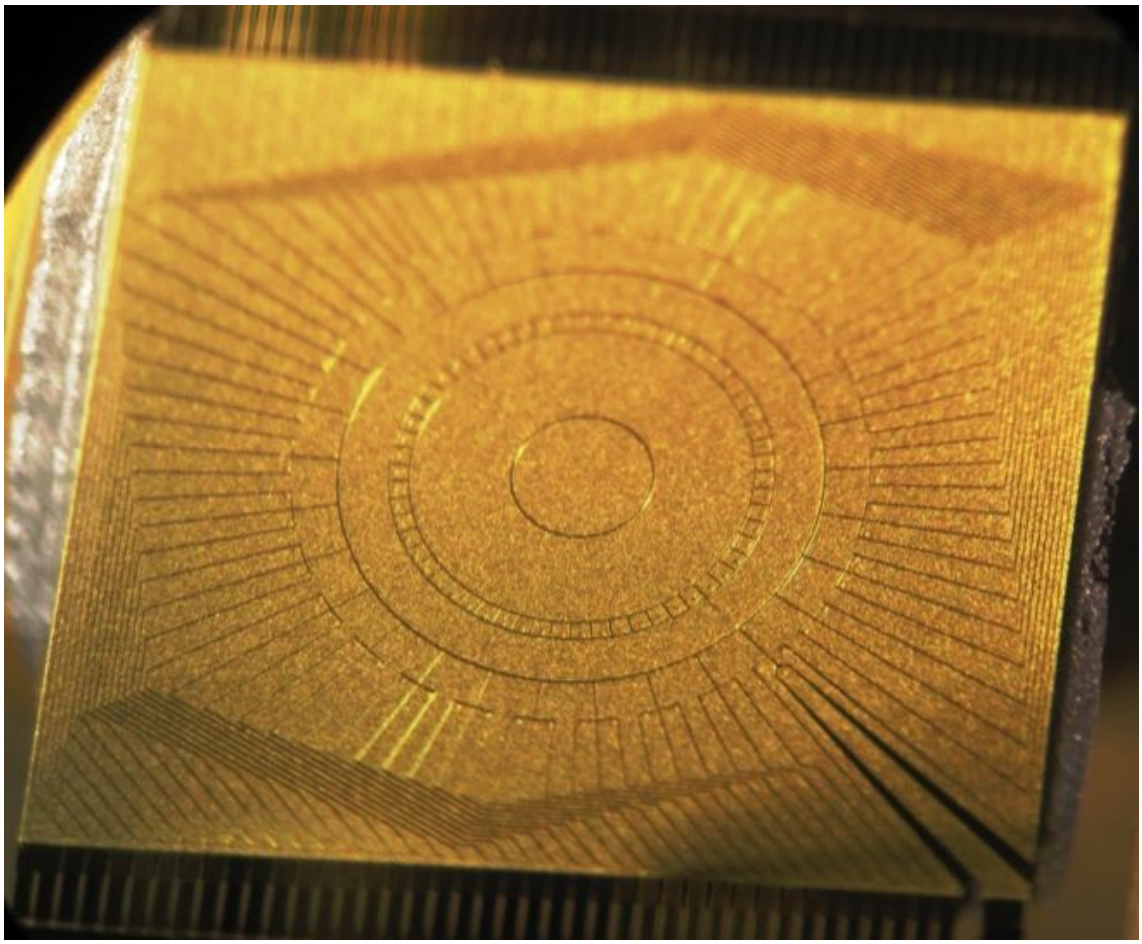

Figure 3.14: Surface electrode gold ring trap. The ring architecture has a radius of $1690\,\mu\mathrm{m}$, producing an ion height of $245\,\mu\mathrm{m}$.

^{174}Yb ions were trapped by applying an rf voltage $V_0 = 190\,\mathrm{V}$ at a frequency $\Omega/2\pi = 13.6\,\mathrm{MHz}$ and at a ion-electrode distance of $245\,\mu\mathrm{m}$. Using these results, numerical simulations of the trap predict a trap depth of 0.1 eV. The ion secular frequency along the principle axes are calculated to be $\omega_{x,y}/2\pi, \omega_z/2\pi = (720, 210)\,\mathrm{kHz}$ respectively for a single

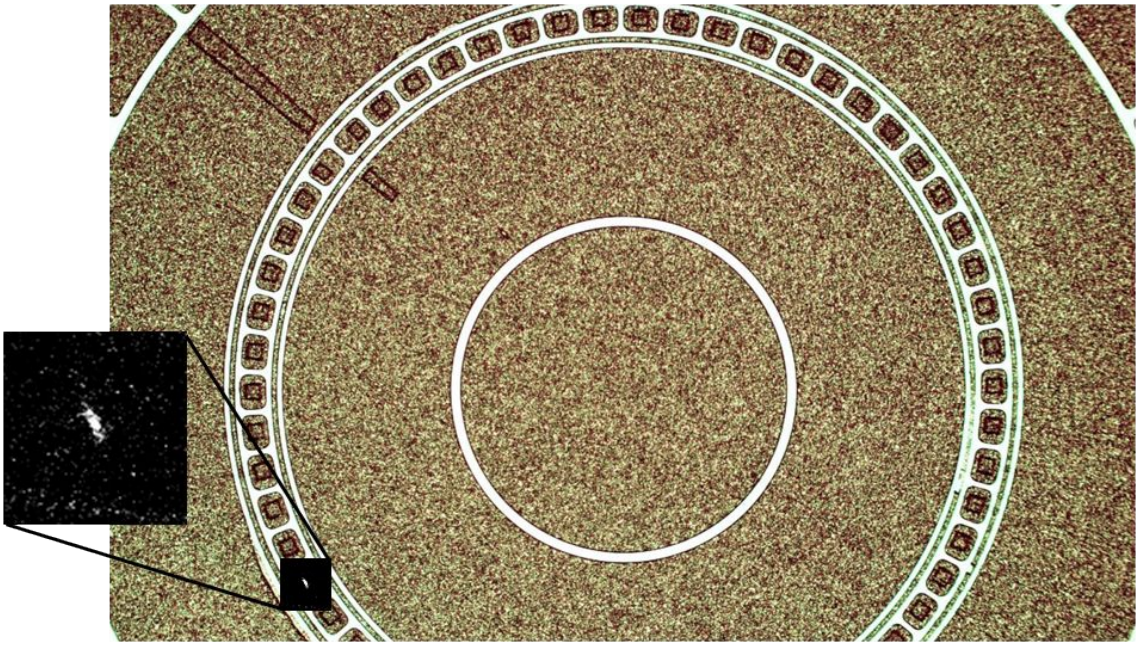

Figure 3.15: An image of a single trapped $^{174}Yb^{+}$ ion. The area imaged by the imaging system is marked with a black square using on an image taken using an optical microscope.

trapped ion trapped at the location given in figure 3.15.

3.6.2 Voltage breakdown

To achieve large trap depths, large rf and dc voltages are required. Due to the smaller distances between electrodes on microfabricated traps compared with macroscopic traps, the maximum voltage that can be applied is smaller due to electrical breakdown. To increase theses tolerances, it is important to understand that during breakdown most of the current will flow through the surface material separating the two electrodes. By carefully choosing the surface material and its composition, an increased breakdown voltage can be achieved. The dielectric layer structure described and tested in [63] (where voltages up to 1000 V can be applied to increase the trap depth) was used for microfabrication of the ring trap. The structure is composed of alternating layers of Si_3N_4 and SiO_2, which are applied using plasma enhanced chemical vapour deposition (PECVD). The choice of PECVD over other methods is due to the ability to use it at lower temperatures, reducing the stress on the chip. The etching of this material is performed via Inductively Coupled Plasma (ICP) etching, which exposes the underlying rf electrode layer for further structure development and the ability to integrate vertical interconnects (VIAs), allowing the use of centre segmented electrodes.

Electrical flashover measurements were performed on a separate trap with a Y-junction electrode architecture that was fabricated on the same wafer. The chip was attached to a

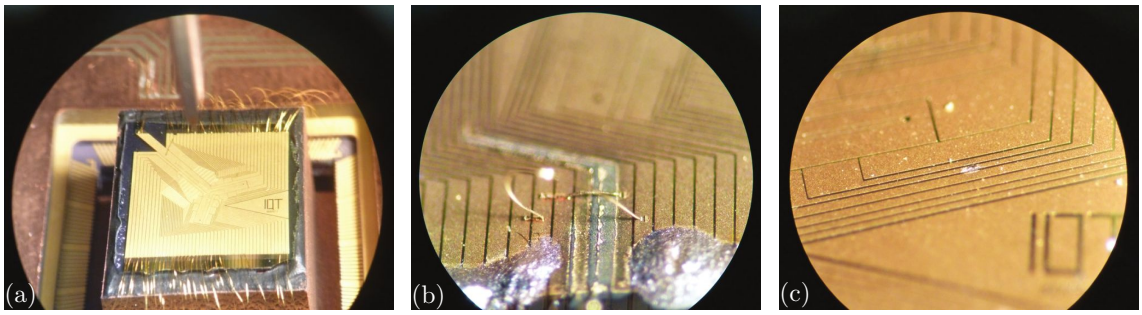

Figure 3.16: (a) Y-junction surface electrode trap used for breakdown measurements. (b) dc breakdown across two electrodes at $\sim 2000\,\mathrm{V}$. (c) rf breakdown across two electrodes at $\sim 360\,\mathrm{V}$.

copper block using an eclectically insulating epoxy (Stycast 2850 FT) and then to a 208 pin ceramic chip carrier. The chip was operated in the same vacuum system in high vacuum at $10^{-7}\,\mathrm{mbar}$. The rf voltage was provided by connecting a helical coil resonator to the vacuum feedthrough. This provided $> 90\%$ coupling between the rf amplifier and chip at a resonant frequency of $34.5 \pm 0.2\,\mathrm{MHz}$with $Q = 62.5 \pm 10$. The rf and dc was steadily increased individually until breakdown was observed. Figure 3.16 shows the Y-junction trap before and after rf and dc breakdown. The mean flashover voltages were measured to be $V_{dc} = 2000 \pm 100\,\mathrm{V}$ and $V_{rf} = 360 \pm 20\,\mathrm{V}$.

It should be noted that the breakdown voltages were obtained from a single data point for each measurement. From the fabrication process of the chip [106] we would expect to see breakdown results in excess of $\sim 1000\,\mathrm{V}$ for both rf and dc [111]. However, the voltages were applied to dissimilar electrodes which could account for the variation in breakdown voltages. The dc and rf voltages were applied to the electrodes that would have been used during trap operation to provide a realistic voltage limit when trapping. The dc electrode possessed a minimum separation of $10\,\mu\mathrm{m}$ between itself and its nearest neighbouring electrode. However, the rf electrode possessed a minimum separation of $4\,\mu\mathrm{m}$ at the position the breakdown occurred. Another source of the lower rf breakdown voltage may be related to the position of a buried electrode directly below the breakdown position. The presence of the conductive buried electrode will increase the electric field density at this position, increasing the probability of breakdown at that location.

Chapter 4

Cryogenic vacuum system

The science of cryogenics describes materials at very low temperatures. The temperature regime for cryogenics is the region where permanent gases such as oxygen, nitrogen, hydrogen, and helium begin to liquefy. This chapter discusses the motivations driving the use of cryogenic systems for ion trapping (section 4.1), the different types of cooling systems (section 4.2 and 4.3), the vacuum chamber (section 4.5), ancillary technologies (sections 4.7-4.11) and the operation of the cryostat (section 4.12).

4.1 Cryogenic ion trapping

There are several benefits that drive the implementation of cryogenic environments for ion trapping. This section describes some of those key benefits which includes cryopumping (section 4.1.1), reduction in ion heating rates (section 4.2) and the utilization of superconductivity (section 4.1.3).

4.1.1 Cryopumping

One of the most significant benefits of using a cryogenic system is its ability to perform cryopumping. Cryopumping is the process of reducing background gas pressure in a vacuum system by using surfaces cooled to cryogenic temperatures. While room temperature systems require weeks of baking and pumping as described in section 3, a cryopumped system can reach the UHV regime in a matter of hours. This has a powerful impact on turn around times for opening vacuum systems and resuming experiments, from typically $\sim$3 weeks to less than a day. A cryogenic environment can also help reduce the pressure beyond the usual limits of 10^{-12} mbar for room temperature systems resulting in fewer collisions between background gases and trapped ions, leading to increased ion lifetimes. The

cryopumping process operates via three separate mechanisms known as cryocondensation, cryosorption and cryotrapping.

Cryocondensation

Cryocondensation operates by creating a cold surface to condense gases. The minimum attainable pressure is determined by the saturation pressure at the temperature of the cold surfaces. For most gases, cryocoolers are capable of achieving temperatures below their triple point. At this point the saturation and sublimation curves become the same and gas particles undergo a direct phase transition from a gaseous to solid state. Figure 4.1 shows the sublimation curves for common atmospheric gases. At a temperature of $\sim 100\,\mathrm{K}$ water and all hydrocarbons condense. The majority of the remaining atmospheric gases condense at $\sim 20\,\mathrm{K}$, while hydrogen isotopes and neon condense at $\sim 4\,\mathrm{K}$.

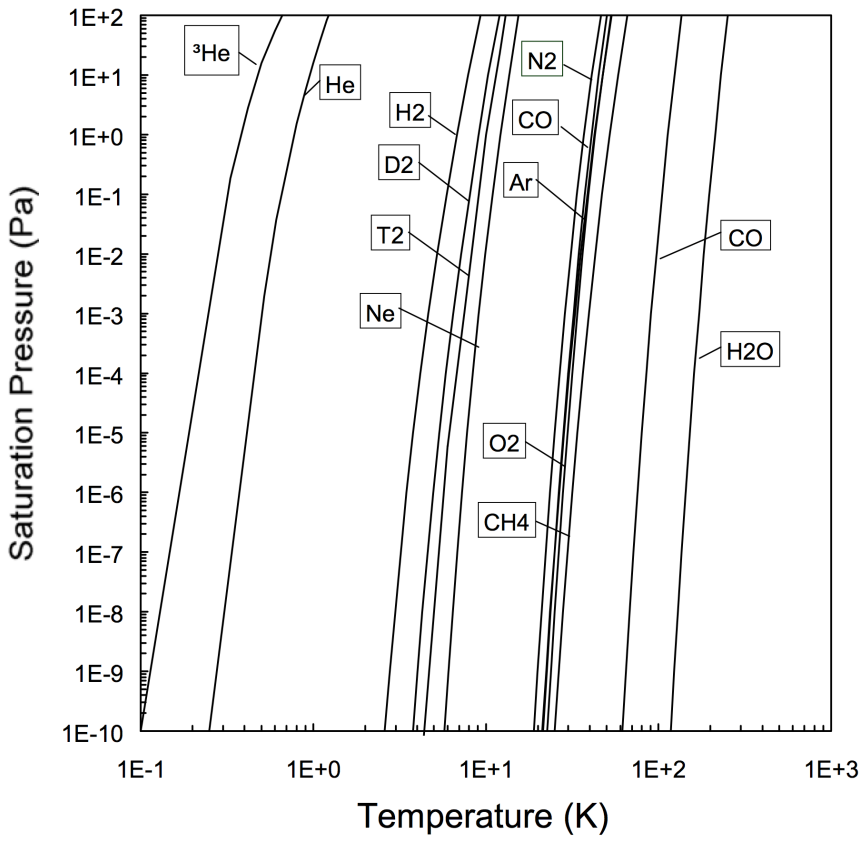

Figure 4.1: Saturation curves for common atmospheric gases [3].

Cryosorption

The cryosorption processes occurs as gas particles strike cold surfaces and lose enough of their incident kinetic energy such that they stay attached to the cold surface via weak

intermolecular forces. This process is subtly different to cryocondensation as it relies on dispersion forces between the gases and cold surfaces rather that between just the gases in a cryocondensed state. As such the equilibrium pressure of adsorbed gases are much higher than the saturation pressure for cryocondensates. However, cryosorption is a vital cryopumping mechanism as it allows the pumping of gases, such as helium and hydrogen, that are difficult to condense with most cryostats.

Cryotrapping

Cryotrapping occurs when gases condense on cold surfaces and in turn function as a cold porous surface that can trap more particles. The increase in a cold surface area within the system will also increase the probability of particles striking a cold surface to reduce the background pressure. This mechanism can be artificially accelerated by the introduction of dedicated getter material within the system, such as activated charcoal. Cryotrapping can also be useful for pumping non-condensable gases by introducing a condensable gas whose crystallite surfaces adsorb the non-condensable gas molecules.

Material selection

The mechanical properties of materials used within the cryostat are important. Some solids can become brittle at low temperatures and break after a number of cooling cycles. Throughout the development of the cryostat, materials that are well characterized at low temperatures were chosen (e.g. copper, steel, brass, PEEK, Macor) [112, 113]. Materials without any data were tested first by performing a complete cooling cycle and examining the material afterwards for any signs of stress or fractures. In contrast to the restrictions on some materials, at low temperatures ($\sim$4 K) there are significantly lower levels outgassing due to the temperature of the materials. This allows a wider variety of materials to be used in the system that are not UHV compatible at room temperature (e.g. tin-lead (PbSn) solder).

4.1.2 Ion heating

For multi qubit operations the control of the motional state of the ions required. The original proposal for the CNOT gate by Cirac and Zoller [79] required the ions to be cooled to their motional ground state. Later proposals, despite no longer requiring ground state cooling [53, 94, 114–117] are still limited by the ions heating rates.

Johnson-Nyquist noise

Johnson-Nyquist noise (also known as Johnson noise) is the thermal agitation of charge carriers within conductors. This temperature dependant statistical fluctuation of electric charge exists in all conductors, and results in a random variation in potential between the ends of the conductor [118]. The fluctuations emerge from finite electrical resistances in the conductor and external circuitry. Resistive ion trap electrodes result in thermal fluctuations and become a fundamental limit for ion heating [4, 119].

The induced voltage amplitude is equivalent to the sum of normal modes energies of electrical oscillation along a transmission line connected with a resistor at each end [120]. The spectral density, $S_V(\omega)$, of such voltage fluctuations in a resistive element is given by [120]

$$S_V(\omega) = 4k_B T R(\omega) \tag{4.1}$$

where T is the temperature of the element and $R(\omega)$ is the real part of the complex impedance $Z(\omega)$. The voltage fluctuations result in perturbations in the ions confining electrical potential, where the heating of the ion is inversely proportional to the ion-electrode distance. Turchette *et al.* [4] showed that the power of the electric field noise should scale with an ion-electrode distance as $d^{-\alpha}$, where the scaling exponent is given by $\alpha = 2$. As the fluctuations are thermally dependant, reducing the temperature of the trap electrodes can therefore minimize perturbations in the pseudopotential.

Anomalous heating

In most ion traps the primary source of heating originates from an unknown source known as anomalous heating. Cooling ion trap electrodes from 300 K to 150 K has shown to decrease ion heating rates by an order of magnitude [5], however, this is still two orders of magnitude above the expected limit from Johnson noise alone [121]. This thermal dependency suggests one potential source of anomalous heating is due 'patch' potentials [122], which are thermally driven.

For an ideal electrical conductor the surface can be treated as an equipotential. This assumes a surface along a crystalline plane free of any impurities. Real surfaces however do not meet these requirements and possess polycrystalline structures, surface impurities, oxide layers and stresses. One proposed mechanism for the creation of patch potentials is via a static component that is attributed to the differences in work functions between different crystal facets and surface adsorbates [122, 123]. Different crystallographic planes

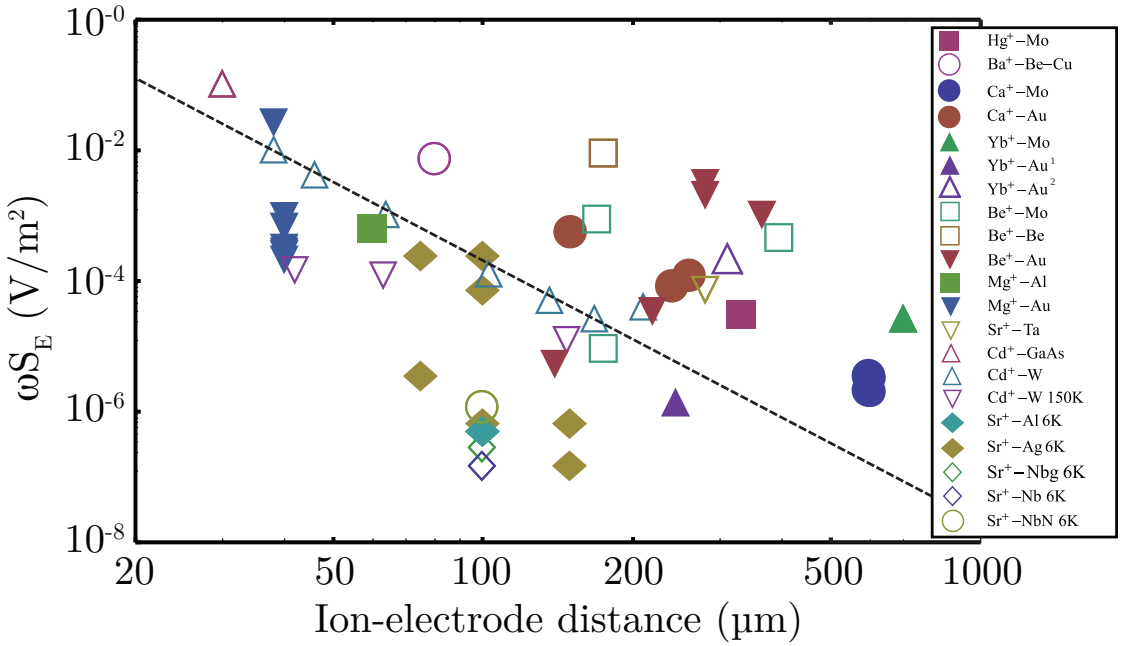

Figure 4.2: Published measurements of motional heating as a function of ion electrode distance. The spectral noise density multiplied with the secular frequency is plotted in order to scale out behaviour from different ion masses or different secular frequencies. A $1/d^4$ line was plotted with the data [4–23]. [1,2] Refer to the same ion trap in 2012 [23] and 2015 [24].

are known to have different work functions. For gold in the surface directions of $\langle 100 \rangle$, $\langle 110 \rangle$ and $\langle 111 \rangle$ the work functions are 5.47 eV, 5.37 eV and 5.31 eV respectively [124]. Contaminants and impurities also effectively create a surface dipole layer that changes the potential above the surface. When the different planes and surface contaminants with varying work functions are in contact, a current will flow until the chemical potential (Fermi energy) across both conductors becomes equal [125]. This leads to a net dipole distribution formed at the interface, giving rise to a contact potential between the two conductors equal to the difference in work functions [126].

A second mechanism attributes the source of patch potentials with a fluctuating component [4, 127] and is motivated by experimental evidence which demonstrates a $1/\omega$ frequency scaling [4, 5, 16]. To quantify the effect of electrical noise, the heating of the secular motion of the ion can be expressed as [104]

$$\dot{\bar{n}} = \frac{q^2}{4m\hbar\omega_m}\left(S_E(\omega_m) + \frac{\omega_m^2}{2\Omega_T^2}S_E(\Omega_T \pm \omega_m)\right) \tag{4.2}$$

where ω_m is the secular frequency for a given mode of the ion, Ω_T is the rf drive frequency and $S_E(\omega)$ is the power spectrum of the electric field noise which is defined by $S_E(\omega) = \int_{-\infty}^{\infty}\langle E(\tau)E(t+\tau)\rangle e^{i\omega\tau}d\tau$. The second term in equation 4.2 denotes the cross coupling

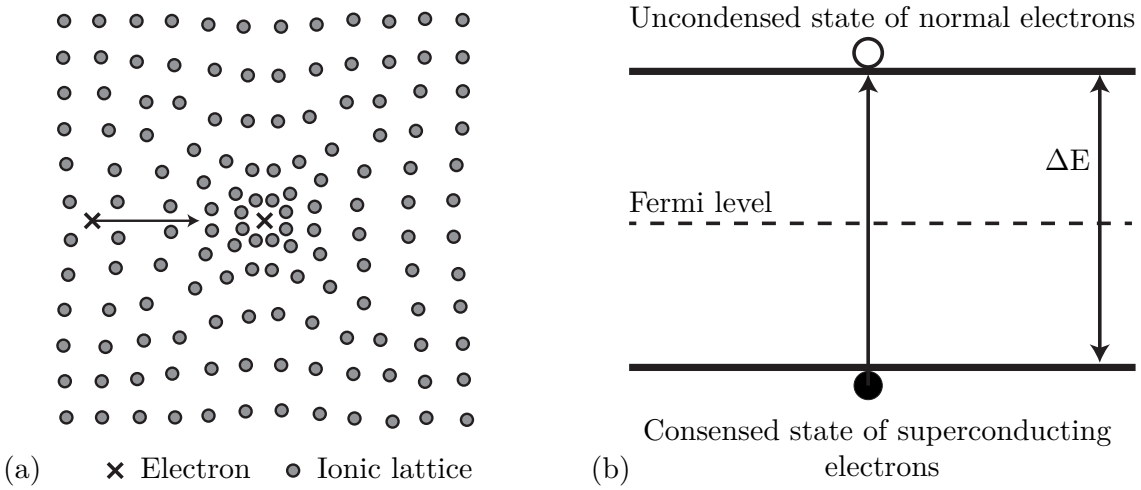

Figure 4.3: (a) Shows the ionic lattice with the ions attracted to an electron resulting in a small ionic displacements that creates a more positively charged region. (b) Energy gap of a superconductor centred about the Fermi energy.

between the noise and the rf drive frequency. This coupling has a negligible effect when $(\omega_k/\Omega)^2 >> 1$ [104]. This result means that axial motion can be neglected as axial confinement is primarily provided by dc endcap electrodes [128]. Turchette et al. [4] approximated this form of heating to have an ion-electrode dependence of d^{-4}.

Figure 4.2 shows combined results from previous measurements of motional heating as a function of ion electrode distance. The spectral noise density is multiplied with the secular frequency and is plotted in order to scale out behaviour from different ion masses or different secular frequencies. A $1/d^4$ line was plotted with the data. A controlled experiment has shown the scaling exponent as $\alpha = 3.5 \pm 0.1$ [5].

4.1.3 Superconductivity

Superconducting materials are those that exhibit zero electrical resistance below a given critical temperature (T_c). For experimental considerations, superconducting materials are divided into two categories, type 1 and type 2 superconductors. Type 1 superconductors transition to a superconducting state instantly at its critical temperature and are commonly formed from single element materials. Type 2 superconductors gradually enter a superconducting state at its T_c and are commonly formed from alloys which exhibit higher T_cs. Table 4.1 shows a selection of type 1 and 2 superconductors and their corresponding T_c.

For type 1 superconductors the sudden transition into a superconducting regime is a phase transition, which can be described by BCS theory [129]. The theory can be described by first considering current through non-superconducting metals, where electrons will flow

Material	Critical temperature (T_c)
Gallium	1.1 K
Aluminium	1.2 K
Indium	3.4 K
Tin	3.7 K
Mercury	4.2 K
Lead	7.2 K
Niobium	9.3 K
NbTi	10 K
NbN	15.7 K
MgB_2	39 K
Tl-Ba-Cu-oxide	125 K

Table 4.1: A selection of type 1 and 2 superconductors and their corresponding T_c.

through the ionic lattice of the metal making a number of collisions. Each collision results in dissipation of energy from the electron to the lattice which manifests itself as heat. This energy transfer process is characterised as the electrical resistance. In superconductors below their T_c, the electrons form bound pairs via phonon exchange known as Cooper pairs. The paired state of electrons have a lower energy than the Fermi energy and can therefore be considered as a bound pair. As the electrons move through the lattice the electrons and the ions within the lattice are attracted to each other. This can result in small ionic displacements that create more positively charged regions. This in turn attracts more electrons which are normally repelled from each other. The energy of the pairing interaction is relatively weak ($\sim 10^{-3}$ eV) and thermal energy can easily break the pairs. Given that $E = k_B T$ where $k_B \approx 10^{-4}$ eV/K, this gives an approximate temperature of ~ 10 K below which Cooper pairs can be bound. For type 2 conductors, despite significant research within the field [130–132], a conclusive theory has yet to be determined.

Cooper pair fluid has an energy spectrum, where an energy gap is equal to the difference between the energy of the electron in the normal states and superconducting in the superconducting state. This energy gap arises as a result of The interaction of the Cooper pairs to form a coherent state results in the creation of the energy gap, where the electrons in the superconducting state posses a lower energy than those in the normal state. If a minimum energy ΔE is given to both electrons, they will have sufficient energy to move across the gap, resulting the pair being spilt and scattered. At low current densities and temperatures ΔE is smaller than the thermal energy of the lattice and therefore scattering events are inhibited resulting in zero resistance.

The attainment of superconductivity within a cryogenic ion trapping system is another important benefit. Chapter 6 described surface electrode traps fabricated using the type 2 superconductor NbN. With no resistance on trap electrodes there is also no power dissipation ($P = I^2R$) resulting in a minimization of electrical fluctuations due to thermal effects. Zero resistance also allows for high quality superconducting resonators to be used. Chapter 5 describes high quality factor on chip microwave resonators used for near field ion interaction and section 4.9 describes the use of superconducting wire for high quality factor in-vacuum rf resonators. Chapter 7 also describes the benefits of superconductivity for ion trapping in terms of technology development for quantum hybrid systems using superconducting qubits and trapped ions [69].

4.2 Cryostats

To achieve cryogenic temperatures there are several approaches that can be taken, such as bath cryostats, continuous-flow cryocoolers, closed cycle cryocoolers and dilution fridges.

Bath cryostats

In principle, the simplest method of cooling a sample to cryogenic temperatures is by the use of a bath cryostat. Bath cryostats utilize a reservoir of liquid cryogen, usually liquid nitrogen or helium, to cool a contact surface to which a sample is attached. The benefits of this passive cooling system are a low capital cost with respect to active coolers, minimal to no vibration, effective cooling due to continuous cryogen cooling, and low acoustic noise. Bath cryostats have also been experimentally demonstrated as a sufficient cooling technology in the field of ion trapping [133–135]. Despite these benefits a major drawback to this method technique is the reliance on a liquid cryogen, which leads to a finite time between cryogen refills and high operating costs.

Continuous flow cryostats

A continuous flow cryostat is an active cooling system that operates in a similar way to bath cryostats, relying on a liquid cryogen to cool a sample stage. However, unlike bath cryostats, continuous flow cryostats provide a continuous flow of liquid cryogen from a storage Dewar to maintain the required temperature indefinitely. The cryogen flow can also be adjusted to provide rudimental temperature control using a PID controller. For relatively higher capital cost when compared to bath cryostats, flow cryostats are acoustically quiet and offer low levels of vibration ($< 10^{-10}\,\mathrm{m}$). Similar to bath cryostats,

the major disadvantage of a continuous flow system is the reliance on a liquid cryogen supply and the resulting high operating costs.

Closed cycle cryostats

Closed cycle cryostats operate by using a mechanical refrigeration system to cool helium gas, extract heat and recycle the gas. The primary benefit of the system is that the working gas vapour is contained in a 'closed cycle', removing the need for a continuous external supply of cryogen. Closed cycle systems can also operate indefinitely and have also been demonstrated in several ion trapping applications [28, 135–138].

Dilution refridgerators

Dilution fridges are another form of closed cycle system that utilizes both a closed cycle cryocooler for primary cooling and a ^{3}He/^{4}He mixture for a secondary cooling process. Using a combination of these two cooling processes, dilution fridges are one of the only methods of achieving temperatures below 0.3 K [139] and are capable of cooling down to temperatures of 2 mK [140]. Superconducting qubits, which require sub-Kelvin temperatures for alumina based technology, have already demonstrated large strides towards quantum computing [43, 141, 142] in dilution fridges. For ion trapping purposes however, the dilution fridge infrastructure is too large and too complex to be effectively incorporated into current ion trapping experimental architectures. Section 7 discusses these issues in more depth and proposes solutions that will allow ion trapping within dilution fridges for future applications.

Summary

For ion trapping applications, closed cycle cryocoolers offer the most cost effective solution for achieving temperatures down to 4 K. The typical size of closed cycle coolers (length $\simeq$ 100 cm, radius $\simeq$ 100 cm) also makes them sufficiently small enough to be integrated within existing ion trapping infrastructures and laboratories. Closed cycle systems are arguably becoming a standard method in the field [28, 135–138] and the work presented in this thesis makes use of a closed-cycled Gifford McMahon cryocooler.

4.3 Closed cycle cryocooler

The initial performance requirements for the cryocooler were the ability to cool a sample to $\sim$4 K, extract $>$1 W at 4 K and achieve a vibrational amplitude of $<$100 nm in all axes.

	Gifford McMahon	**Pulse tube**
Model	Sumitomo SHI RDK-415	Cryomech PT415
Cooling power at 2nd stage	1.5 W	1.5 W
Cooling power at 1st stage	35 W at 50 K	40 W at 45 K
Quoted base temperature	3.5 K	2.8 K
Measured base temperature [145, 146]	2.5 K	2.2 K
Cool down time	60 min	60 min
Vibration	10-100 μm	1-10 μm
Vibration w/ buffer gas interface	<15 nm	<15 nm
Maintenance interval (cryocooler)	10 000 hrs	20 000 hrs
Maintenance interval (compressor)	30 000 hrs	20 000 hrs

Table 4.2: Summary of key specifications for the Sumitomo RDK415 and Cryomech PT415.

For closed cycle cryocoolers there are two options, a Gifford McMahon (GM) cryocooler and a pulse tube cryocooler (PT). Both cryocooler types are capable of providing a cooling power of 1.5 W at 4 K. GM coolers utilize a moving displacer, usually with an integrated regenerator, and a compression and expansion space. PTs operate with the same thermal and pressure cycles as GM coolers but without the use of a displacer [143] resulting in a lower level of vibration. GM and PT coolers therefore possess a typically vibrational amplitude of ∼10-100 μm and ∼1-10 μm respectively. As both coolers do not meet the requirements for vibration, an additional 'low vibration interface' was developed in conjunction with ColdEdge Technologies to achieve low vibration levels independent of the cooler type chosen (section 4.4). The resultant vibration of the cooler-interface system for both GM and PT coolers is < 15 nm [144] and therefore both systems meet the vibration requirements. Table 4.2 shows the primary operating parameters for leading GM and PT cryocoolers available (figure 4.4). The performance of both coolers are almost identical and the final choice was based upon financial considerations. The GM cooler was chosen due to its lower capital costs ($\sim$ £22,000) compared with the PT cooler ($\sim$ £30,000).

4.3.1 The Gifford McMahon cryocooler

The Gifford McMahon cryocooler used is a Sumitomo RDK-415D2 (figure 4.4). Figure 4.5 shows the heat capacity map for the cooler which details the heating extraction for a given temperature, which can also be interpreted as the systems temperature for a given heat load. The cooling system is formed of two main components, the cold head (also known as the cold finger) and the compressor (figure 4.6). The cold head contains the expansion and compression space for the working gas, along with a regenerator and displacer. For most GM coolers the regenerator is incorporated into the displacer. The compressor supplies

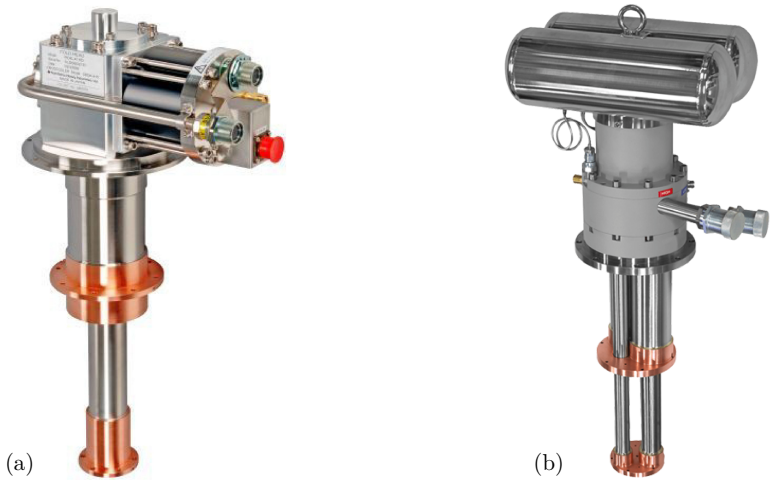

(a) (b)

Figure 4.4: An SHI-RDK 415D GM cooler (a) and a CryoMech PT415 PT cooler (b).

the cold head helium gas through a high and low pressure lines. A rotary valve connected on the cold head alternates between the two lines at a frequency of 1-2 Hz.

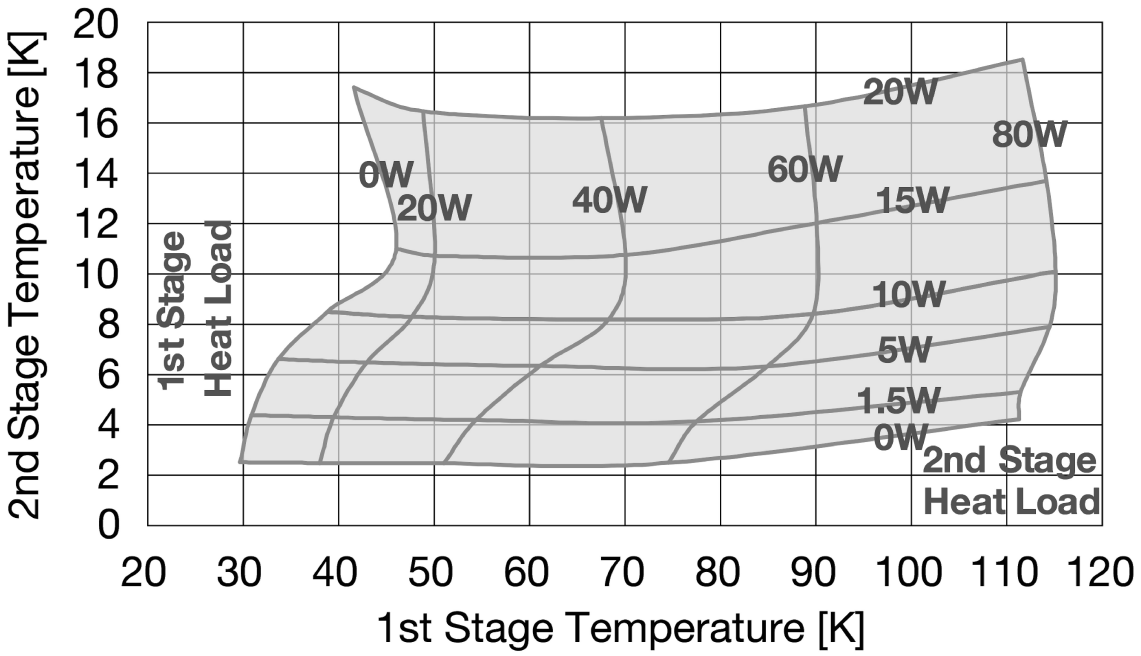

Figure 4.5: Heat capacity map for a SHI-RDK 415D GM cooler which gives the heat extraction for a given temperature and can also be interpreted as the systems temperature for a given heat load [25].

The cooling cycle of the cold head is a four stage process shown in figure 4.7. In the first stage, the cold head is connected to the high pressure line and the regenerator moves from the low temperature region to the ambient temperature region. As it does so the regenerator absorbs heat from the gas. In the second stage the rotary valve switches to the low pressure line. As the pressure is reduced some of the gas passes through the regenerator and goes towards the compressor. The expansion of gas in the cold head is

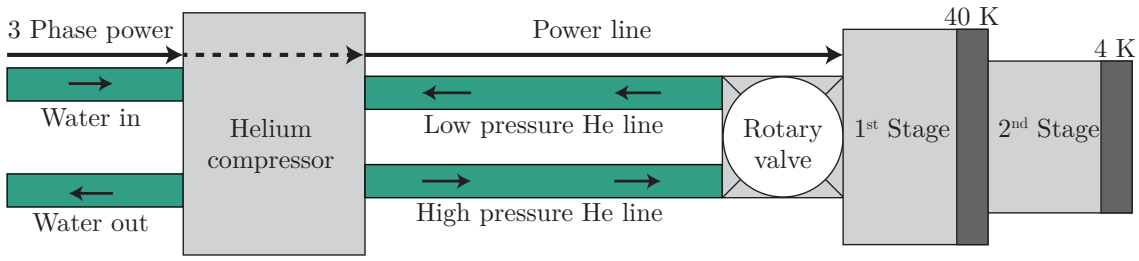

Figure 4.6: Schematic diagram of the cooler system consisting of the compressor and cold head.

isothermal and therefore heat is absorbed from the cooling stage. In the third stage the regenerator moves towards the cold region forcing the cooled gas to absorb the heat from the regenerator. Finally, in the fourth stage the rotary valve switches back to the high pressure line and the cycle starts again.

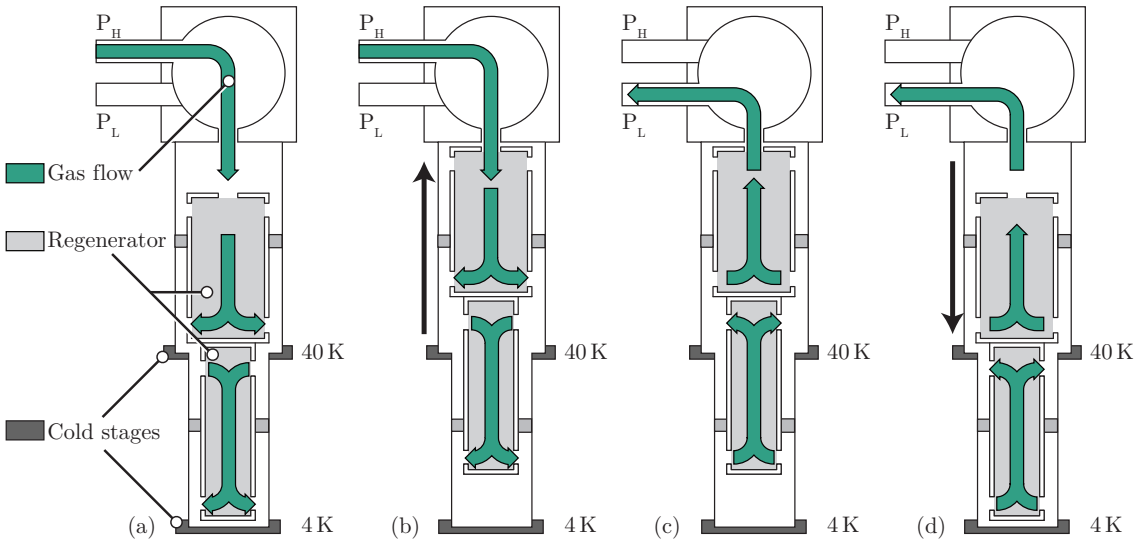

Figure 4.7: The four stage (1)-(4) cooling cycle for a two stage GM cryocooler showing the movement of the displacer and regenerator and the two cold stages.

4.3.2 Magnetic field noise

There are several sources of oscillating magnetic fields that emanate from GM and PT cryocoolers. A clear understanding of the magnetic noise is important in determining any effects on the magnetic field sensitive states in the ground state hyperfine manifold of ^{171}Yb. The predominant source of these oscillating fields originates from an AC motor which drives a rotary valve between the compressor and cold head and is present in both GM and PT coolers. The motor used is a 3 phase synchronous motor operating at AC 200 V at 50 Hz. For the GM cryocooler the motor is located directly on top of the cold head which is approximately 50 cm away from the position of an ion trap.

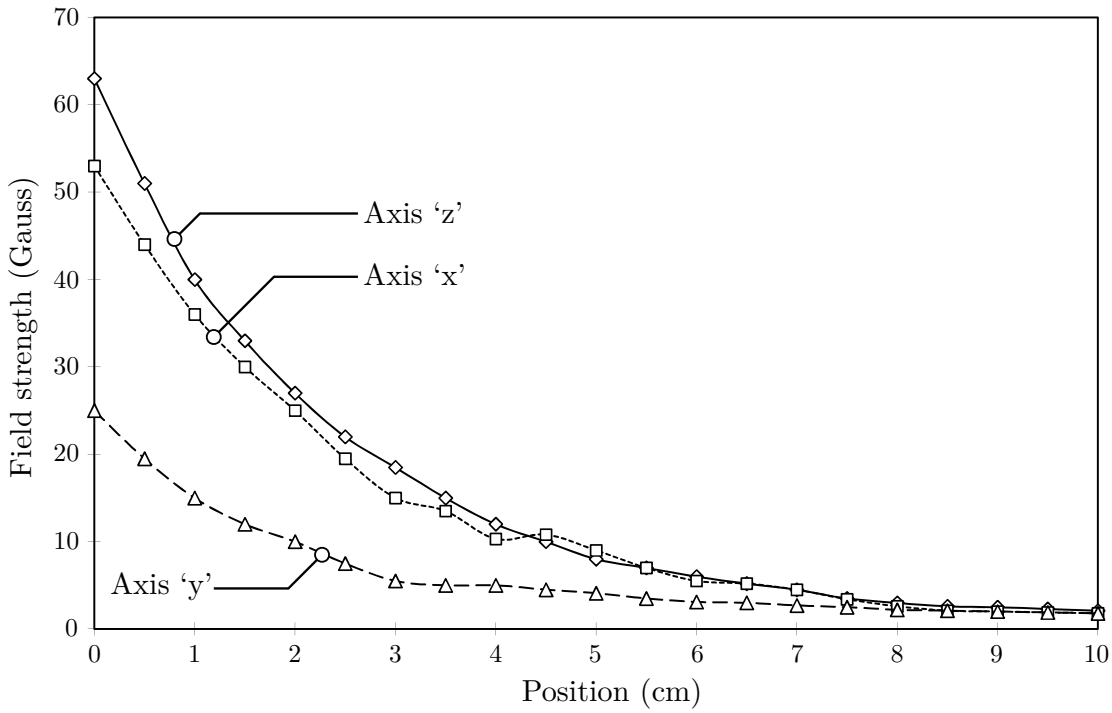

Figure 4.8: External magnetic field noise for the RDK 415D GM cryocooler [26].

Figure 4.8 shows the absolute magnetic field from the GM valve motor to a maximum position of 10 cm. Axis 'z' is our primary consideration as this is in the direction from the cold head to the trap. Extrapolation of the magnetic field to the ions position becomes difficult as the data in figure 4.8 also includes elements of external magnetic fields. Compensating for the Earth's magnetic field gives a magnetic field amplitude of (3 ± 2) mG at 50 Hz, corresponding to a small Zeeman splitting of ~ 8 kHz between the ± 1 mF levels in the $2S_{1/2}|F = 1\rangle$ state. To make an empirical measurement of this noise, a SHI RDK415 cooler was tested at the Centre for Cold Matter Research, Imperial College London. To measure the absolute magnetic field contribution of the cooler, a magnetometer was used to measure the magnetic field strength in three axes at the position of the ion trap (figure 4.9). The field was measured with the cooler on and off to eliminate background fields. Table 4.3 shows the results to be low ($\sim$mG) and therefore negligible.

Axis	Cooler off (mG)	Cooler on (mG)
X	0.00 ± 0.10	1.20 ± 0.40
Y	0.00 ± 0.05	0.35 ± 0.10
Z	0.00 ± 0.10	2.10 ± 0.70

Table 4.3: The magnetic field noise of a SHI-RDK 415D GM cryocooler in three axes at the position of the ion trap measured at the Centre for Cold Matter Research, Imperial College London.

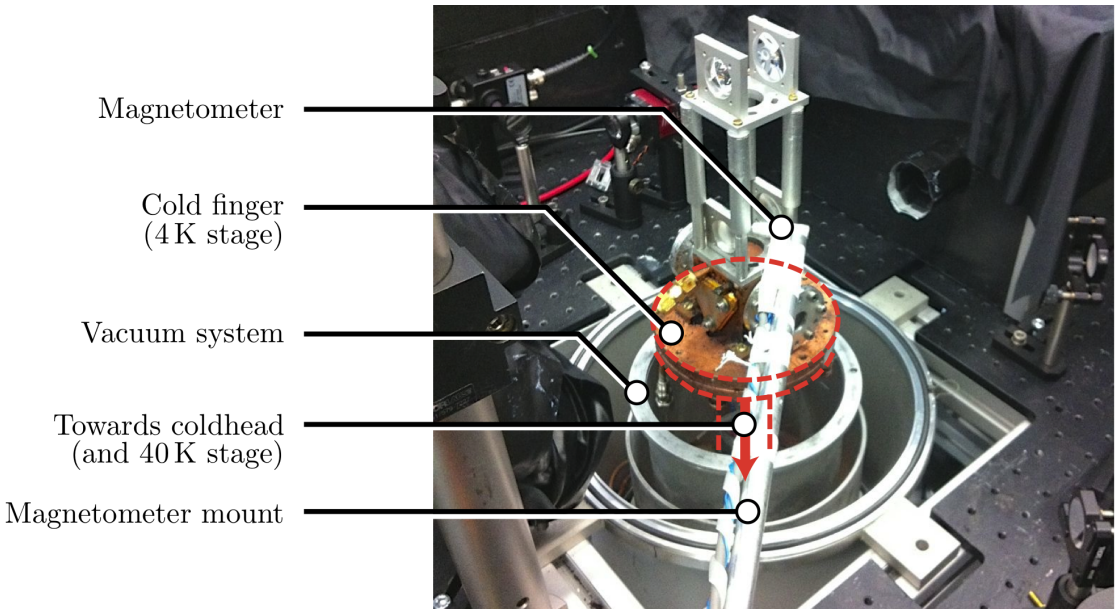

Figure 4.9: A magnetometer was used to measure the magnetic field strength of an SHI-RDK 415D GM cryocooler in three axes at the potential position of the ion trap.

4.4 Ultra low vibration interface (ULVI)

Ideally, an ion trap cooled to cryogenic temperatures should not be subject to any motion as a result of the cooling process. For closed cycle cryocoolers with a level of vibration in the 10's of microns it is necessary to reduce the transmitted vibration from the cryocooler to the ion trap. This can be accomplished by decoupling the cryocooler and sample through several approaches. One common technique to form a thermal bridge with the use of a semi-rigid physical contact such as a soft copper braid [147]. Alternatively a fully mechanically decoupled connection can also be created using a condensed liquid helium interface or a circulating helium buffer gas [135].

While a copper braid will reduce vibration and provide a direct highly thermally conductive copper path between cooler and sample, it will also transfer a higher amplitude of vibration to the sample than a liquid or gas interface [147]. Liquid interfaces require the ability to condense helium and use this as a reservoir to cool the sample. This can be beneficial as by forming a reservoir the cryocooler can be then turned off and the system can be used free from vibration. This is the same principle as using a bath cryostat but with the use of a closed cycle cryocooler to recondense the helium buffer gas in-situ. However, to cool a sample using a reservoir alone will impose a strict time constraint before the helium evaporates and the sample begins to heat. This adds a further level of experimental difficulty and uncertainty to longer experiments.

4.4.1 He gas buffer

The work in this thesis uses a helium buffer gas to extract heat from the sample as the cooling system offers continuous cooling with a significantly reduced level of vibration down to ∼nm. The efficiency of heat exchange using a gas interface is 20% lower than a physical connection, however, for the RDK-415D cryocooler this still offers a substantial 1.2 W of cooling at 4 K. The interface used is a custom designed 'Ultra Low Vibration Interface' (ULVI) from ColdEdge Technologies (figure 4.10).

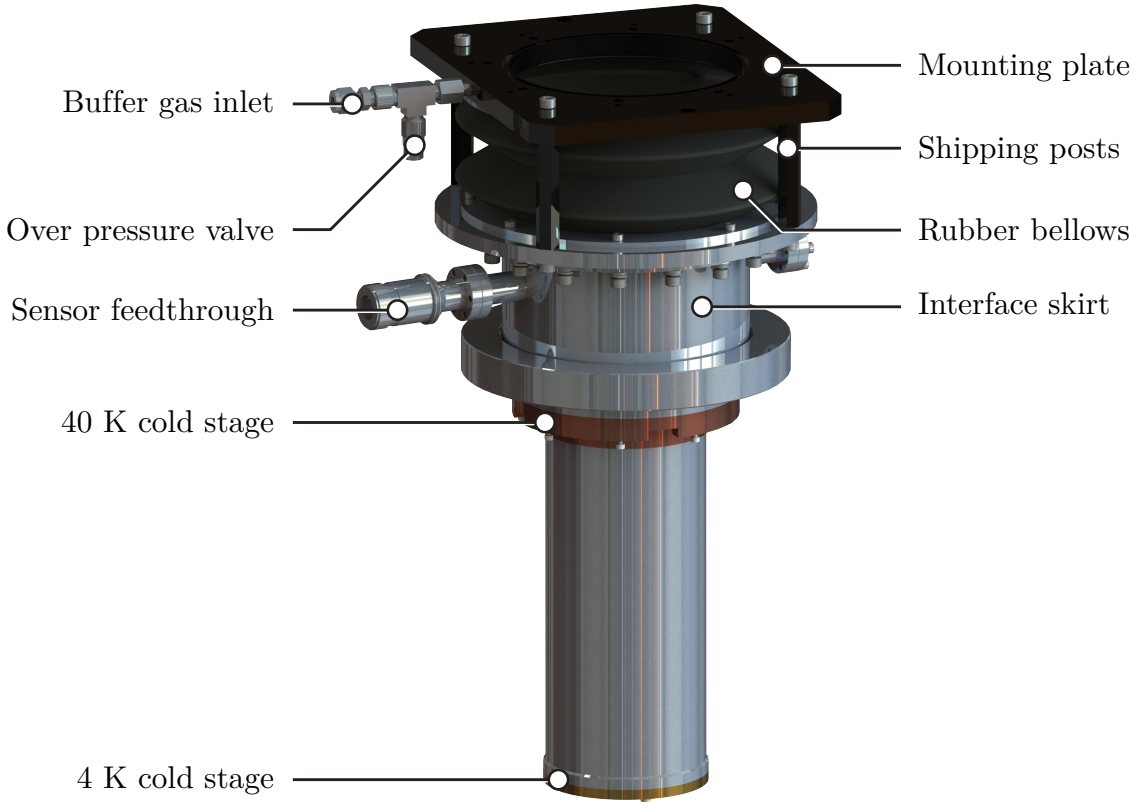

Figure 4.10: The 'ultra low vibration' interface uses a helium buffer gas to reduce the transmitted vibration from the cooler to the sample by three orders of magnitude.

The interface operates as a sealed shroud over the cryocooler. The region in between the cooler and the interface can then be filled with high purity helium buffer gas. For the interface used this is recommended to be at least CP grade helium (99.995% purity). This ensures optimum performance and avoids any unwanted contaminants freezing within this region. The interface can then be attached to an open flange on the vacuum system to close the system. Figure 4.11 shows how the cooler and interface are non-mechanically linked, the area in which the buffer gas occupies and how the vacuum chamber is attached to the interface. To ensure the cryocooler is mechanically decoupled, it is mounted independently from the vacuum system and optical table and only connected via flexible rubber bellows.

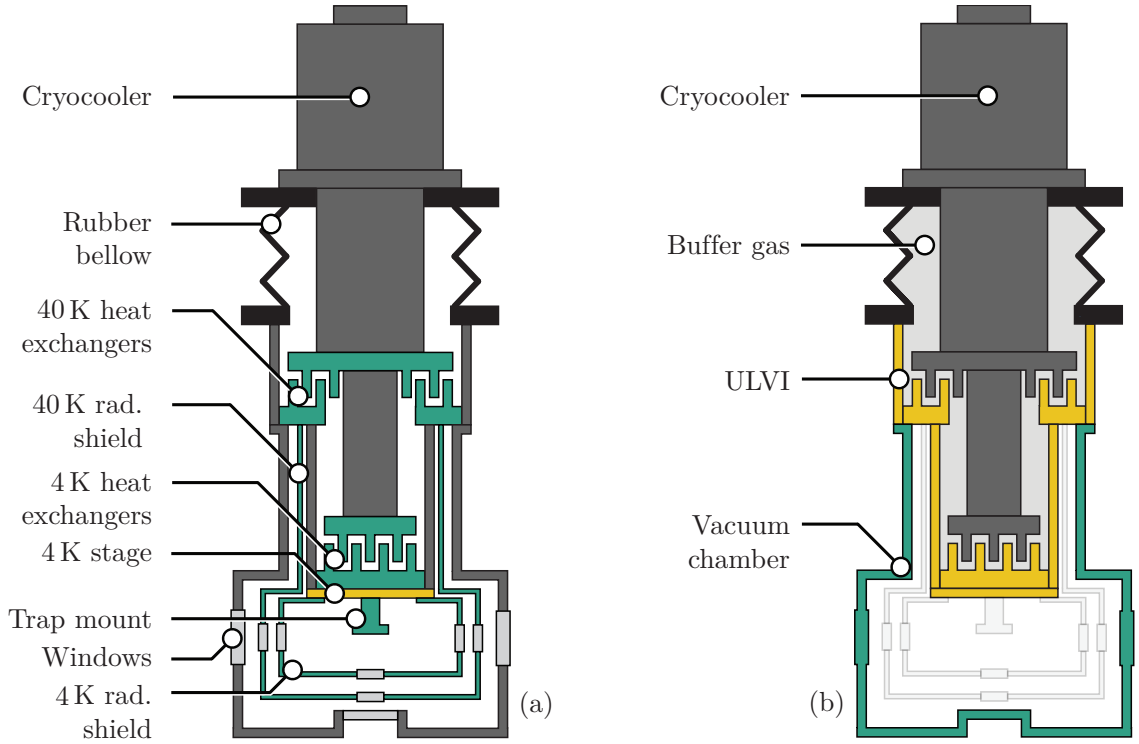

Figure 4.11: (a) Schematic diagram of the cryogenic system with (b) a simplified diagram showing the cryocooler, interface, vacuum system and area occupied by the helium buffer gas.

For convenience the cryocooler is mounted on the existing optical table over hang.

The heat transfer between the cryocooler and the interface takes place in between heat exchangers at the two cold stages of the cryocooler. At both heat exchanger regions the buffer gas is cooled by the cryocoolers heat exchangers which in turn cools the heat exchangers attached to the interface. To make the buffer gas cooling process more efficient, the heat exchangers are formed from concentric copper rings that are attached to the first and second cooling stage on the cryocooler (figure 4.12a) as well as the corresponding locations on the interior of the interface (figure 4.12b). The heat exchangers increase the surface area at the cooling stages allowing the gas to be cooled more efficiently.

4.4.2 Sample stage

The sample stage is located on the second cooling stage of the interface. The stage has been gold coated (figure 4.13) to prevent oxidization and to provide a highly thermally conductive surface. Attached to the ULVI are two silicon diode temperature sensors (Lakeshore DT-670B-CO) and a resistive heater (Lakeshore HTR-25), which are all connected to a temperature control unit (Cryocon 24C). One temperature sensor is mounted firmly into a recessed section on the side of a second stage. This sensor is attached via a piece of indium

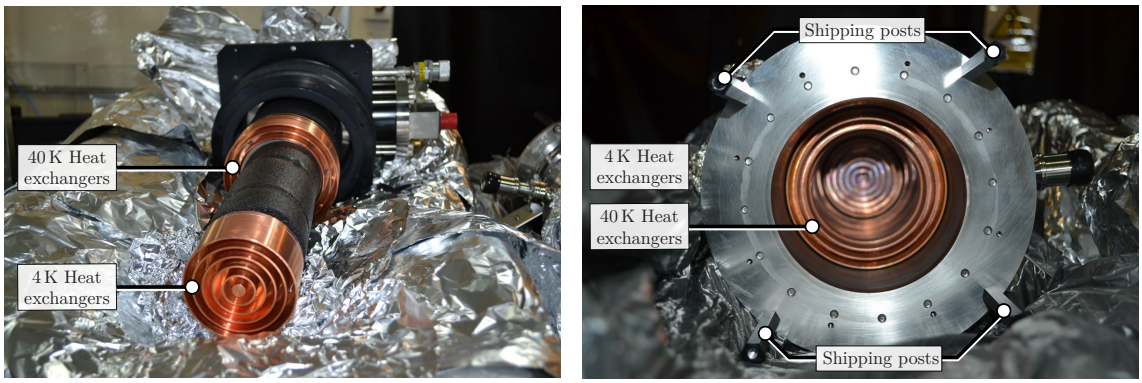

(a) (b)

Figure 4.12: (a) The cryocooler with concentric copper ring heat exchangers attached to the 40 K and 4 K stages. (b) A view of the interior of the low vibration interface, showing the concentric copper ring heat exchangers attached to the interior of the interface.

foil for a better thermal contact and acts a indicator of the temperature of the stage itself. The secondary sensor is attached to the surface of the second stage (figure 4.13). This is attached via a flexible connection that allows the sensor to be mounted anywhere in the sample region for a more local temperature measurement. Both temperature sensors are connected using four-strand wires (Lakeshore QT-32). The wires are wrapped tightly along the length of the interface to ensure a good thermal anchoring (figure 4.13). The heater is mounted within the second stage of the interface (figure 4.13) and is capable of delivering 25 W of power to the stage. This power can be controlled such that the interface maintains a given temperature or it follows a pre determined temperature curve as a function of time when connected to the Cryocon 24C controller unit.

4.5 Vacuum system

The total cryogenic system is formed by creating a vacuum chamber around the ULVI. An image for the assembled system is shown in figure 4.14. The vacuum chamber is similar to the room temperature vacuum system as it includes many of the feedthroughs and devices described in section 3.4. This includes the ion pump, ion gauge, titanium sublimation pump (TSP), 2×50 pin D-sub feedthrough, a 6 pin high voltage feedthrough, and four CF40 quartz silica viewports with AR coating for 369 nm, 399 nm, 638 nmand 935 nm.

The system also includes two 1.33” 1 pin SMA feedthroughs (Allectra 242-SMAD50-C16) and one 2.75” 2 pin SMA feedthrough (Allectra 242-SMAD50-C40-2). This allows for high frequency ($\leq$ 18 GHz) coaxial connections within the system for microwave and rf delivery and measurement. The imaging window consists of custom recessed CF160

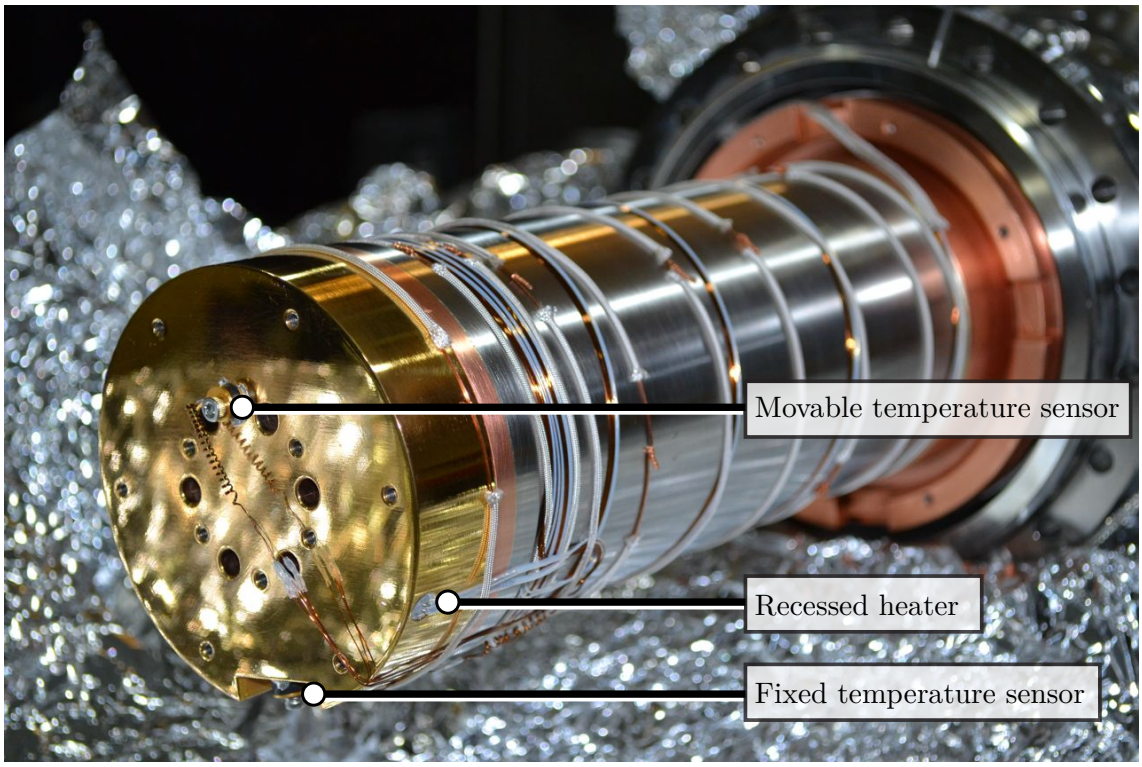

Figure 4.13: An exterior view of the low vibration interface with the gold plated solid copper sample stage. Two temperature sensors are attached, one within a recessed section at the bottom of the stage and the other on the front surface of the stage with a flexible wire connection. A 25 W heater is also integrated into the side of the stage.

quartz silica window described in section 4.5.2. An over-pressure burst disc (Allectra 461-PBD-C40) is also used as a safety precaution. If a cryostat is operated for a long period of time, the effects of cryopumping can lead to a large accumulation of cryopumped material within the system. This accumulation can be accelerated in the presence of small undetectable vacuum leaks and in the case of an emergency when the cooler stops operating, the condensed material will return to a gaseous state. This could result in an over pressure within the system that could damage the system, particularly the windows which are not designed for high over-pressures. The overpressure disc prevents this from occurring by rupturing first to relieve the pressure at 1.7 bar.

4.5.1 Radiation shields

Methods for attaining low temperatures have been discussed in sections 4.3 and 4.4, however, the aim for the vacuum chamber is to maintain that low temperature. One of those most significant thermal loads into the cryogenic system is radiation. All bodies will emit radiation at a rate dependant on its temperature and emissivity which is given by

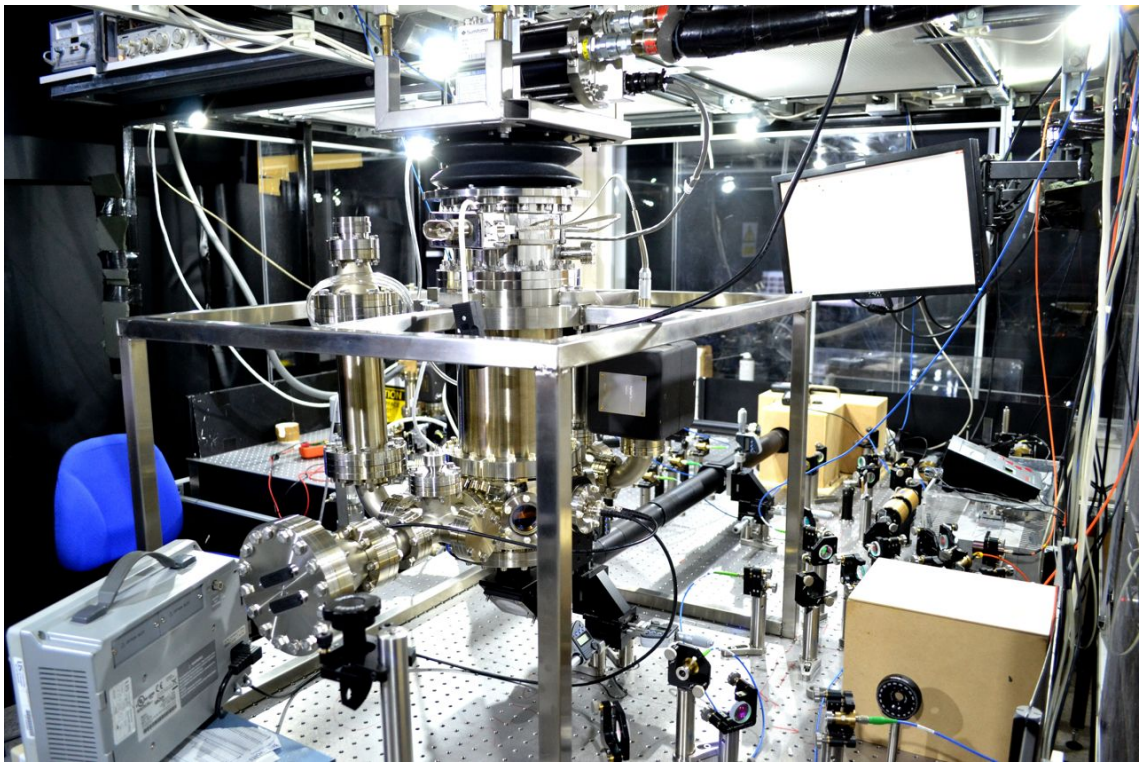

Figure 4.14: The full assembled system showing the cryocooler, interface and vacuum chamber.

$$E = \epsilon\sigma T^4 \tag{4.3}$$

where ϵ is the emissivity, σ is the Stephan-Boltzmann constant and T is the temperature. The emissivity of a body is a property of its surface that determines the fraction of light emitted and absorbed. For an ideal black body object $\epsilon = 1$. To reduce the thermal radiation into the system we can aim to do two things; reduce the emissivity and reduce temperature of our local environment. Both of these requirements can be accomplished by using materials with low emissivity, that are cooled by the interface and shield the experimental region. Table 4.4 shows the emissivity for commonly used materials.

Material	Emissivity
Polished copper	0.02-0.04
Lightly oxidised copper	0.1
Aluminium	0.6
Highly oxidised Aluminium	0.2
Electroplated gold	0.015-0.03
Electroplated nickel	0.015-0.04
Polished stainless steel	0.075

Table 4.4: Emissivity values for commonly used radiation shield materials [2].

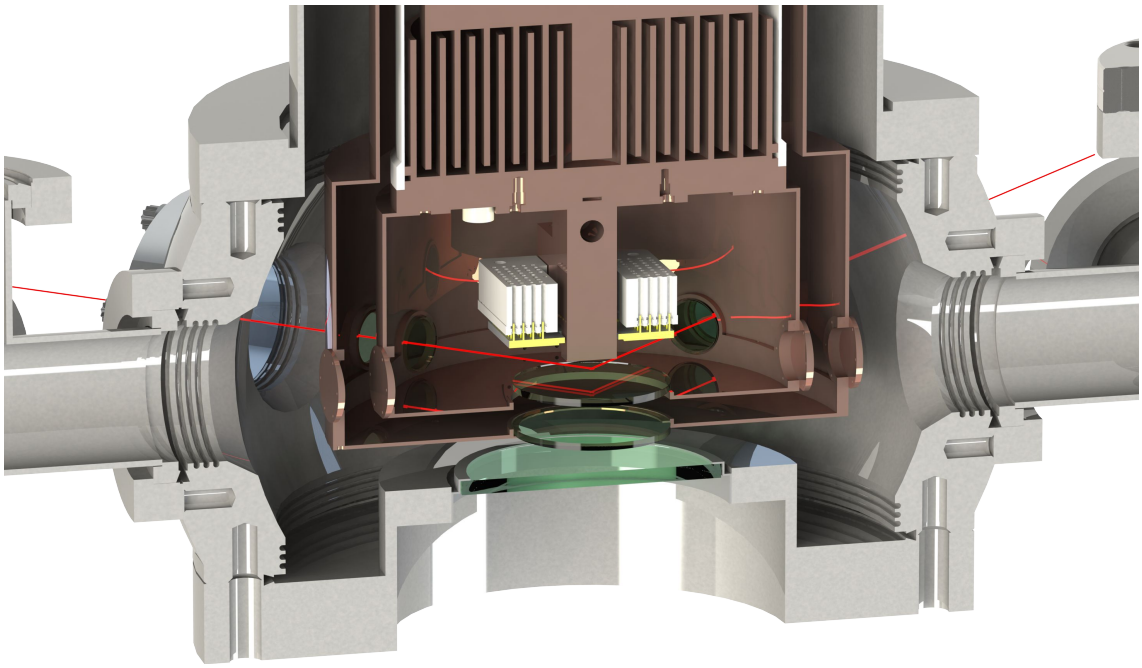

Figure 4.15: Cross section of the cryogenic system showing the position of radiation shields and interface with respect to the vacuum chamber.

Polished copper is a common choice for radiation shields, however, surface oxidisation when the shield is not under vacuum can lead to degradation in quality. The ideal choice would be a gold coated polished copper shield to offer low emissivity without the risk of oxidisation. In this experiment only polished oxygen free high conductivity (OFHC) copper was used due to the high cost of gold/nickel coating for both shields. This has proven a cost effective solution as the condition of the radiation shields has shown minimal degradation after several cycles to room pressure. However, care should be taken to minimize the exposure of the radiation shields to atmospheric pressure to prevent oxidization. An additional benefit of radiation shields is that they provide a significantly larger surface area for cryopumping helping to reduce the background pressure.

In the cryogenic system two radiation shields are used, one attached to the 40 K cold stage and one to the 4 K stage. Figure 4.15 shows a cross section of the vacuum system with the relative positions of the radiation shields. Figure 4.16 shows a picture of the both radiation shields which are polished using 20 μm, 5 μm and 1 μm grit lapping paper successively prior to installation.

4.5.2 Custom viewport

The focal length of the imaging objective used is 40 mm. To be able to position the ion trap within the centre of the spherical octagon for laser access the imaging window must

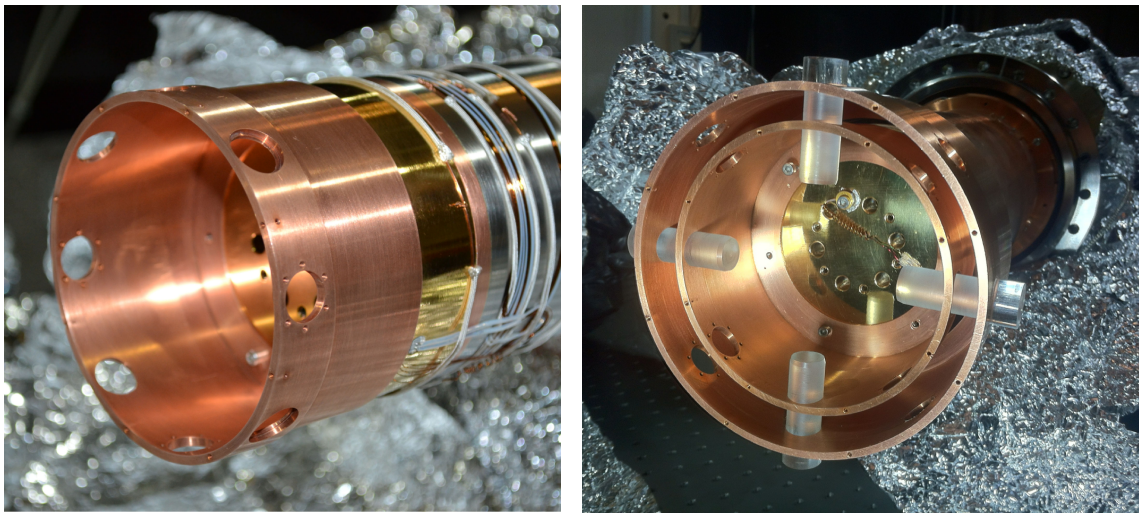

(a) (b)

Figure 4.16: (a) The 4 K radiation shield and (b) 40 K radiation shield with plastic rungs placed through the radiation shield windows for alignment.

be recessed from the CF160 flange of the spherical octagon. Figure 4.17 shows the custom viewport design that reduces the distance from the ion trap surface to the outer surface of the window to $\sim$ 35 mm. The viewport design also allows the objective to image a 12×12 mm surface electrode ion trap unimpeded.

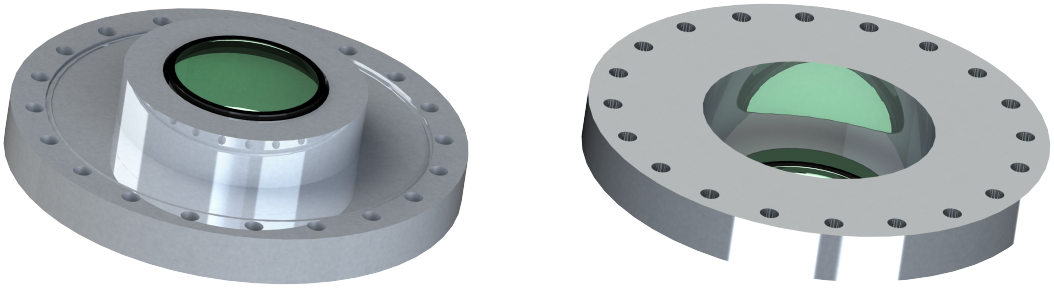

(a) (b)

Figure 4.17: The interior (a) and exterior (b) view of the recessed custom viewport.

4.6 Wiring

Wiring within a cryogenic vacuum system becomes a complex task due to thermal loads introduced into the system. Both electrical connections from external sources via feedthroughs and internal wiring are all important factors. This section briefly outlines the considerations that need to be made when selecting wires, such as geometry, material, installation

procedures and a list of wires used within the system.

4.6.1 Wire geometry and material

The total heat flow $\dot{Q}$ along a wire can be given by [148]

$$\dot{Q} = \frac{A}{L} \int_{T_1}^{T_2} \lambda(T) dT \tag{4.4}$$

where A is the cross sectional area of the wire, L is the length of the wire, λ is the thermal conductivity of the wire and $T_2 - T_1$ is the thermal gradient across the wire. From equation 4.4 it can be seen that the wire geometry can have a direct impact on the thermal dissipation in the vacuum system. Preliminary steps to counteract heat dissipation is adjust the ratio of A/L such that a smaller cross sectional area and longer wires are used. However, by decreasing the ratio, the resistance of the wire will also increase and care should be taken that the electrical conductivity is sufficient for the application.

The second factor that can be altered is the thermal conductivity of the wire λ, which varies across different wire materials. Figure 4.18 shows the thermal conductivity of wires commonly used in cryogenic systems from 300 K to 4 K.

If choosing a low thermal conductivity wire it should be noted that the Wiedmann-Franz law states that the electrical σ and thermal conductivity λ are proportional to each other and dependant on the temperature. This can be expressed as

$$\frac{\lambda}{\sigma} = LT \tag{4.5}$$

where L is the Lorenz number and is given by

$$L = \frac{\pi^2}{3} \left(\frac{k_B}{e} \right)^2 . \tag{4.6}$$

4.6.2 Thermal anchoring

To minimize heat dissipation at the sample, all wires entering the system need to be thermally anchored. This method usually involves the wires being wrapped around a bobbin (copper rod) attached to a cold stage. In the cryogenic system the radiation shields are used instead to wrap the wires around (figure 4.19). The shields provide a large cold surface area to accommodate all the wires entering the system. For multiple stages, the wires should be wrapped around the warmer stage with the higher cooling power first and then subsequently around the colder stage.

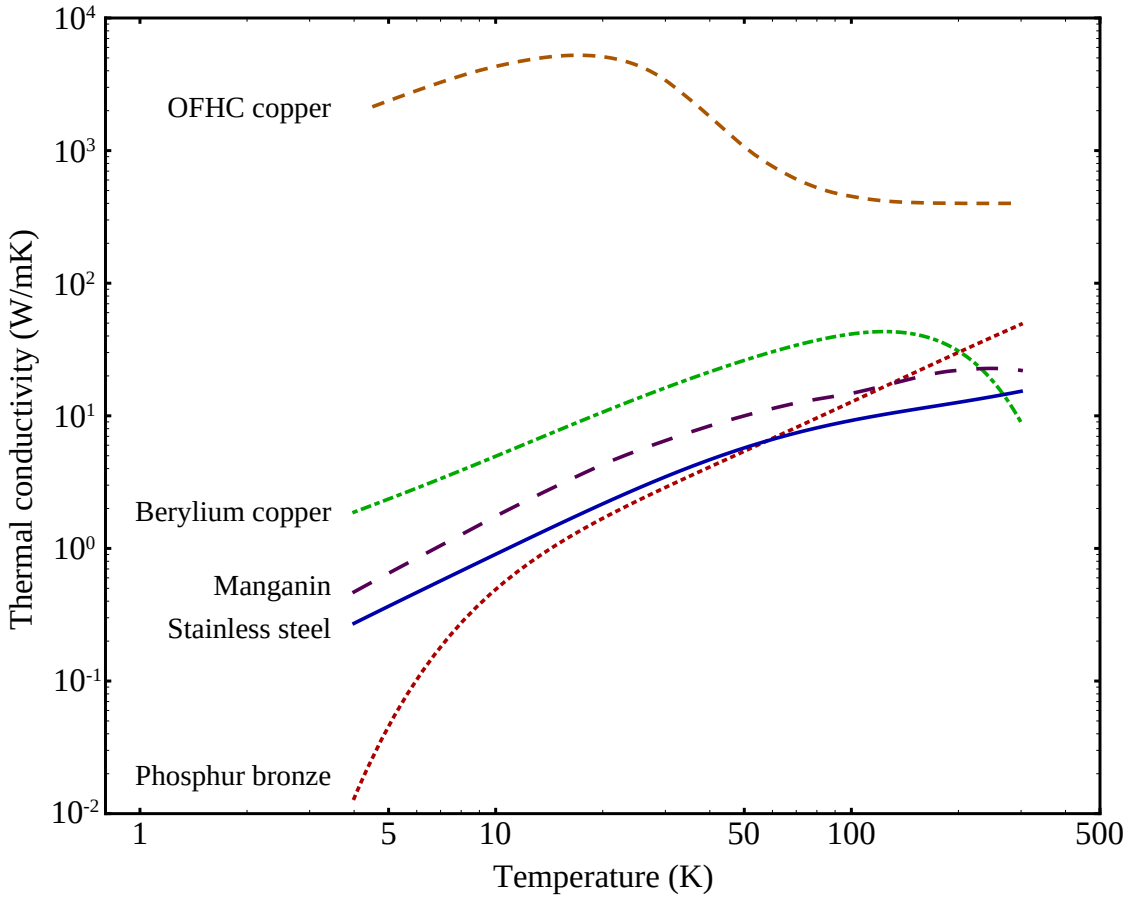

Figure 4.18: The thermal conductivity for common materials used for wires in cryogenic applications between 4-300 K [27].

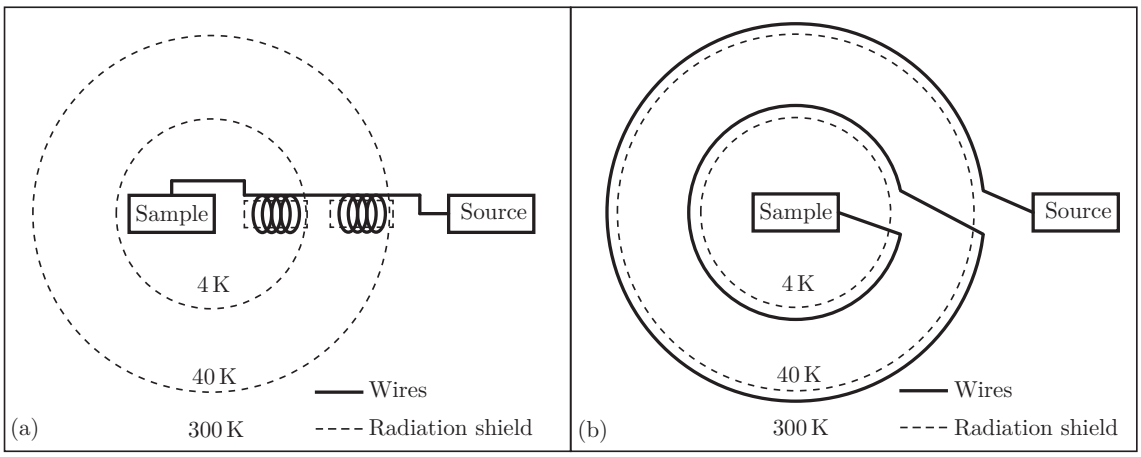

Figure 4.19: Diagrams of thermal anchoring where wires are wrapped around a bobbin (copper rod) attached to each cold stage (a) and with wires wrapped around both radiation shields (b). Scheme (b) is used for the cryogenic system described within this chapter.

4.6.3 Wires used

Below are the wires selected for use within the cryogenic system with the motive for their selection across various applications.

- **Coax cable for rf and MW** - Silver plated copper central conductor and ground shield with PTFE insulator (RS 794-7206). The first key requirement for coaxial cables within the cryogenic system is the absence of an insulating outer wrap. A braided silver plated outer shielding allows for direct thermal anchoring by wrapping wires around radiation shields and flexibility to avoid breaking the cable due to sharp angles within the system. THe PFTE insulator is also a UHV compatible material suitable for cryogenic temperatures temperatures at 4 K and baking at 200°C.

- **dc trap electrode wires** - Polymide insulated single strand Phosphur Bronze (Lakeshore WSL-32-250). With a 100 dc connections, a narrow gauge or wire (32) helps to minimize heat transfer from the 300 K feedthrough to the 40 K radiation shield. From figure 4.18 we can also see that phosphur bronze offers the lowest thermal conductivity for commercially available wires within 1-50 K. A thin polymide insulation, which is UHV compatible material suitable for cryogenic temperatures temperatures at 4 K and baking at 200°C, allows all wires to be wrapped together in a a single group.

- **rf resonator coil wire** - Kapton coated OFHC Copper with NbTi matrix (Goodfellows SC Composite Wire (Nb/Ti+Cu) 10M). The copper clad NbTi matrix offers an ideal solution to wires operating at high frequency and at temperatures of ∼4 K. The NbTi allows the wire to become superconducting at 10 K. The matrix configuration also increases the surface area for the NbTi to counteract the decrease in skin depth for higher frequency signals. The copper cladding provides a highly thermally conductive material to ensure that the NbTi is cooled effective and prevents the fracturing of the thin NbTi strands. A Kapton insulation is also UHV compatible and suitable for cryogenic temperatures temperatures at 4 K and baking at 200°C.

- **Temperature sensors wires** - Phosphor Bronze quad-twist wires (Lakeshore WQT-36-25). As mentioned early, phosphur bronze offers the lowest thermal conductivity for commercially available wires within 1-50 K. A twisted wire configuration also offers further benefits for sensitive sensor measurements. The twisted configuration is a common technique to minimize electromagnetic interference into the wires and also decreases the combined resistance of the four wires in parallel.

4.7 Chip mount

4.7.1 Copper mount

A chip mount was designed to incorporate several requirements, the primary of which being a direct highly thermally conductive link from the ULVI cold stage to the chip. This is done by using an OFHC copper mount to which the trap can be attached. The mount is split into two sections to allow the chip to be easily removed while leaving as much of the mounting structure and wiring in place. Figure 4.20 shows the design for the top block which holds the chip and the bottom block that is attached to the cold stage using six M3 bolts.

To ensure an optimal thermal connection, a cryogenic grease (Apiezon N-type grease) (K. J. Lesker APNB) is applied to the base of the mounting structure. Apiezon N-type grease is a UHV compatible grease designed for cryogenic systems that is capable of withstanding frequent thermal cycling between 4 K and 300 K, and has the ability to fill micropores of adjoining surfaces to improve thermal contact. The grease is relatively viscous at room temperature which can result in trapped bubbles during application that lead to virtual leaks. The trapped gas can be removed by applying firm pressure between joints and heating the grease above its melting point of 42-52°C. The grease is also applied in between the top and bottom copper blocks. As an additional thermal connection, one end of two tin plated copper braids (RS Components 358-012) are bolted through the top copper block with the other end bolted directly to the cold stage. This provides a directly solid connection which has been demonstrated to reduce the base temperature by ~ 1 K.

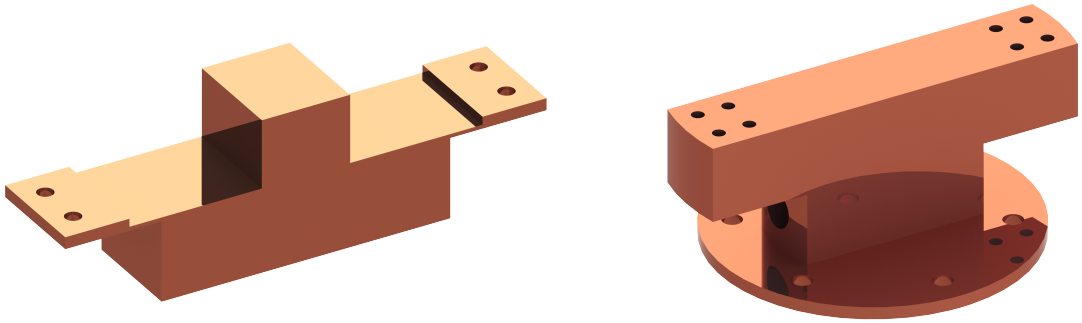

(a) (b)

Figure 4.20: Top copper mounting block (a) that holds the chip and the bottom copper mounting block (b) which is attached to the cold stage. The assembly of these mounting blocks with its relation to the ion trap can be seen in figure 4.32.

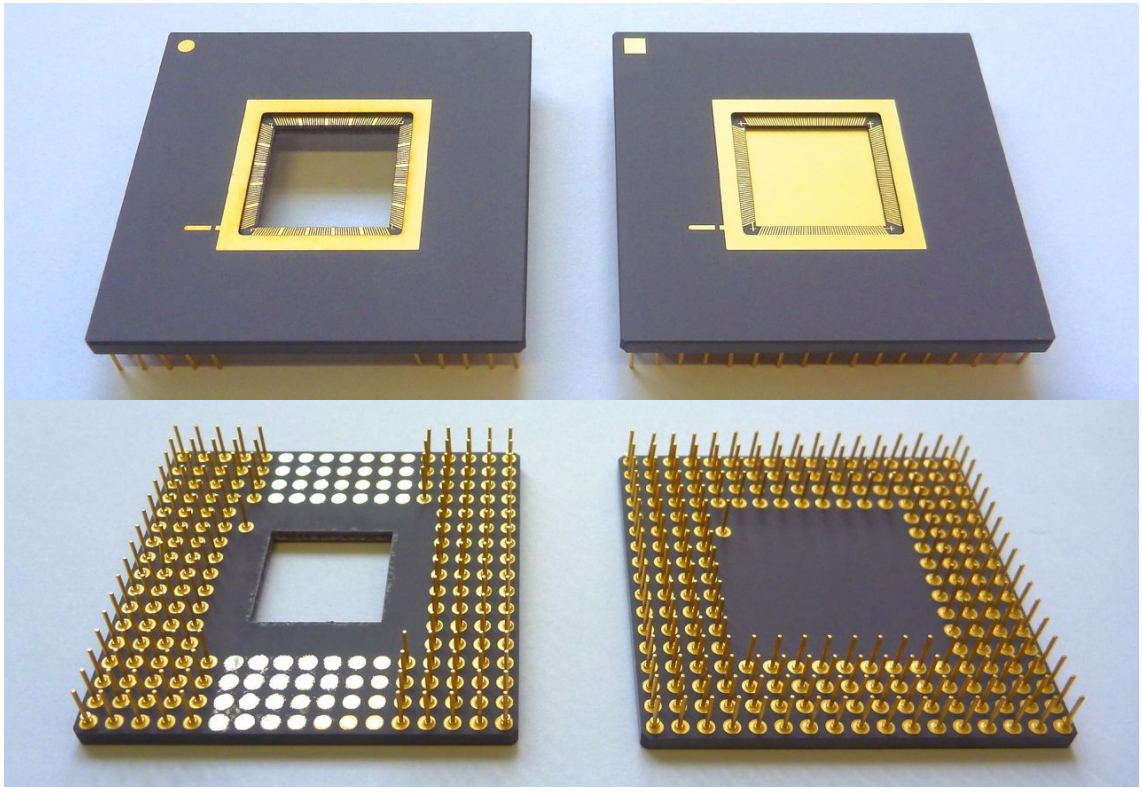

Figure 4.21: A top and bottom view of a modified and unmodified CPGA 208 pin chip carrier (Global Chip Materials PGA10047002).

4.7.2 Chip carrier

To provide wired connections to the ion trap, a CPGA 208 pin chip carrier (Global Chip Materials PGA10047002) is used (figure 4.21). To integrate the chip carrier with the copper mounting structure the central gold pad was removed to allow the copper structure to protrude through the centre, effectively replacing the gold pad with the copper mount. The central gold pad is removed in a two stage process. The gold plating is first removed using a diamond tipped drill and the remaining AlN is laser cut. To allow the main body of the chip carrier to sit on the arms of the top copper mount a central column of 7 pins are removed. The remaining pins were shortened by 2 mm to allow the chip carrier to be mounted into the receptacles by hand with minimum force. The chip carrier was attached to the top copper mounting piece using Stycast epoxy, a cryogenic compatible two part epoxy that is thermally conductive and electrically insulating (Elliot Scientific 2850-FT epoxy with Catalyst 9).

4.7.3 Chip mounting

To mount the ion trap chip on the top copper mount, Stycast or silver epoxy can be used. Care should be taken when mounting the chip as differences in thermal expansion

Material	Liner thermal expansion coefficient (10^{-6} m /mK)
OFHC Copper	17
Silicon	3
Quartz	0.77 - 1.40
Sapphire	5.3
Alumina	5.4
Stycast Epoxy[1]	35.0
Kapton	20
Nickel	13
Niobium	7
Steel	13 - 17
Ytterbium	26.3

Table 4.5: Radiation shield materials. (1)Cured using catalyst 9.

coefficients between the copper mount and chip substrate can cause undue stress to the point of fracturing the chip. Figure 4.22 shows a fracture running across the lower right quadrant of the chip due to thermal stress over just one cooling cycle. However, it should be noted that this trap used a relatively thin 200 μm quartz substrate. Other surface traps with a 500 μm quartz substrates subjected to several cooling cycles were observed to have no damage due to thermal stresses. The thermal expansion coefficients for commonly used materials are given in table 4.5.

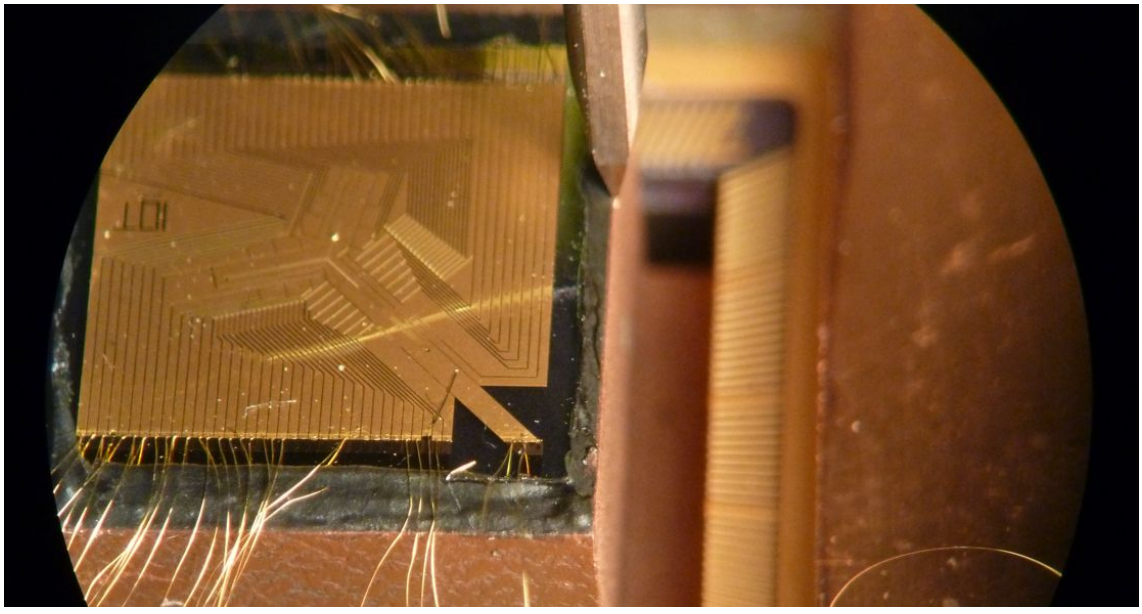

Figure 4.22: Gold on 200 μm quartz surface ion trap with a fracture running across the lower right quadrant due to thermal stress over just one cooling cycle.

The high level of stress resulting in a fracture was due to the entire back of the chip being epoxied to the copper surface. Subsequent traps were only epoxied under one single

corner of the trap. This method allows the chip to be free from excess stress as the copper mount contracts and expands during the cooling down and warming up phase respectively. However, this method also reduces the contact surface area between the chip and copper mount and therefore limits the cooling of the chip. To partially compensate for this, Apiezon N-type grease is applied to the copper mount top surface prior to epoxying the trap to ensure a larger contact surface area. During the wire bonding process the chip and grease is heated to $\sim 115°$C, which removes any trapped bubbles within the grease.

4.7.4 Wirebonding

The wirebonds to the chip were made using a wedge wire bonder (K& S 4523A Digital). For gold ion trap chips a 25 μm thick gold wire (Coining 4828) was used to create the bonds. For niobium chips, a 25 μm thick aluminium wire (Coining 4666) was used since gold wire does not bond to niobium. The bonding processes for both wires are essentially the same except that the Aluminium wire is bonded by purely frictional welding, where two metals are pressed together with a given force and are friction welded with an ultrasonic oscillation at room temperature. Gold wire on the other hand cannot typically be bonded at room temperature. Instead the wire needs to be thermosonically bonded with the temperature of the bonding surface raised to 100-150°C. Table 4.6 lists the key parameters used during the wire bonding process for different wires and surfaces.

Wire	Surfaces	T(K)	1^{st} Bond			2^{nd} Bond		
			Power	Time	Force	Power	Time	Force
Al	Au - Au	30	1.17	2.5	2.1	1.17	5	2.1
	Au - Nb	30	1.17	2.5	2.1	1.17	5	2.1
	Au - Nb	120	1.17	2.5	2.1	1.33	5	2.5
	Nb - Nb	120	0.97	3.5	1.7	1.17	5	2.1
	Cu - Cu	120	1.21	3.4	1.7	1.44	5	2.7
Au	Au -Au	90	4.54	6.0	5.0	3.44	3.4	3.5

Table 4.6: Wire bonding parameters used for bonding between different materials and using different wires.

4.7.5 PEEK mounting brackets

Polyether Ether Ketone (PEEK) is an easily machinable and UHV compatible organic polymer thermoplastic. Two PEEK plates were used to house gold plated pin receptacles allowing the chip carrier to be 'plugged' in easily and securely (figure 4.23). The designs are similar to the PEEK brackets described in section 3.4, however, they have been redesigned

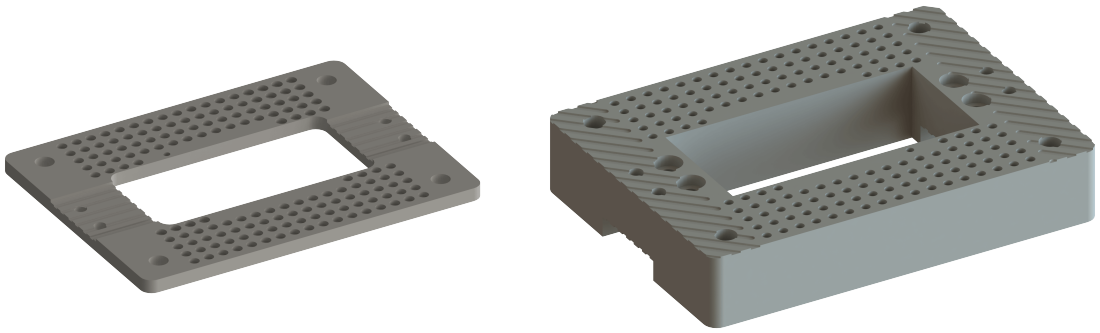

(a) (b)

Figure 4.23: Top (a) and bottom (b) PEEK plates used to hold gold plated pin receptacles.

to incorporate the copper mounting structure. The holes for both plates were designed for a press fit for the receptacles allowing the two plates to be secured together only with the receptacles. Figure 4.24 shows how the system with both PEEK plates and receptacles are connected.

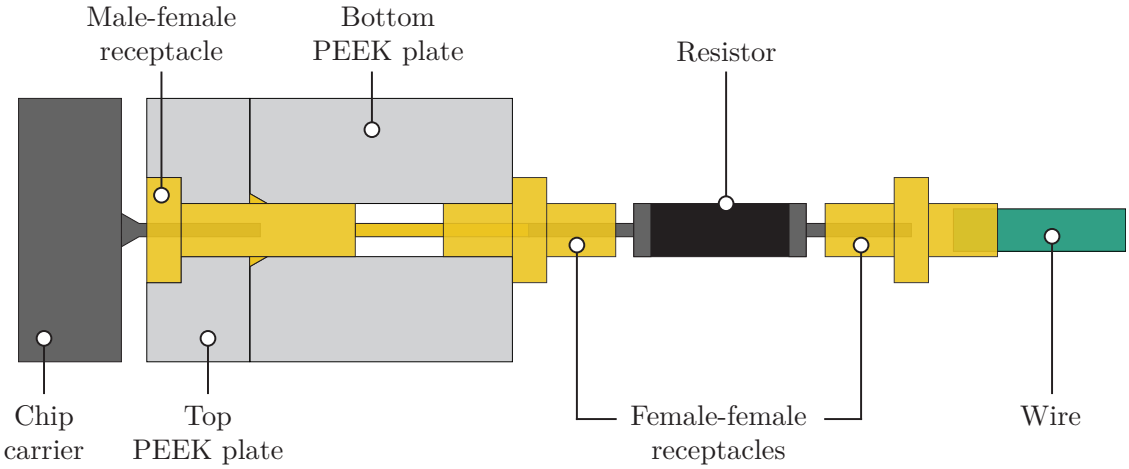

Figure 4.24: The electrical connection from the chip carrier to the dc feedthrough wires.

4.7.6 In-vacuum dc filter

DC signals supplied to the ion trap can be subject to electrical noise, which can result in perturbations in the rf pseudopotential thereby destabilizing the trapping field. The noise can be minimized through several methods. Firstly, the distance from the source to the trap (i.e. cable length) should be minimized as much as possible. This will reduce the area over which the cabling can be subject to external field fluctuations. Another method is to use passive electronic filtering to remove any unwanted noise. Both the room temperature and cryogenic vacuum systems use two low pass filter networks. Section 4.8 describes an external filter and this section described an in-vacuum filter. In-vacuum filtering provides

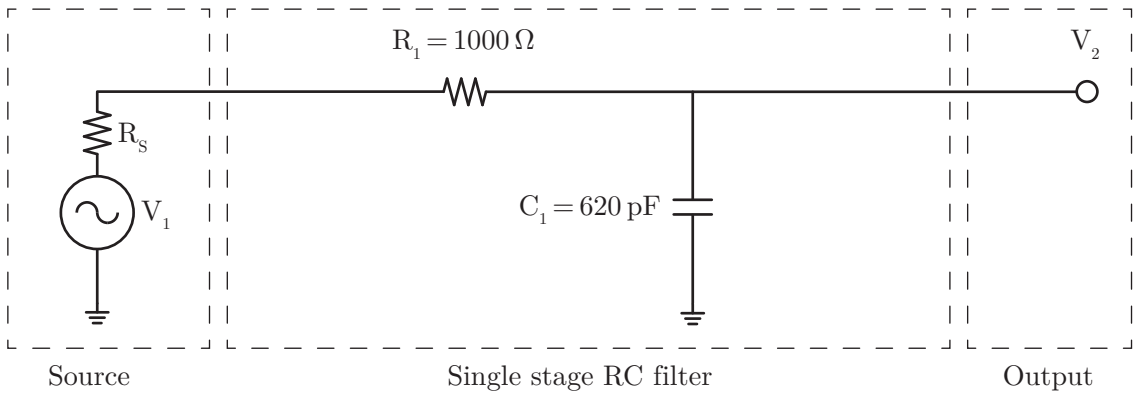

Figure 4.25: Circuit diagram for a single stage RC low pass filter.

the benefit of filtering as close as possible to the trap before the signal is delivered on to the trap itself. The filter network used is an RC low pass filter that attenuates high frequency signals. Figure 4.25 shows circuit diagram for the filter. The filter is composed of a 1 kΩ resistor (Token Electronics Industry MF-1/4W-1K-J-T52) and a 620 pF capacitor (Presidio MVP0505N621KAG1R-6). This produces a cut off frequency of 257 kHz which is given by

$$f_c = \frac{1}{2\pi RC}. \tag{4.7}$$

Resistors

The series resistor is mounted by crimping one female-female receptacle to one end of the resister. This is then inserted into PEEK plates with a press fit. The dc wires from the feedthrough also have a female-female receptacle crimped onto the end of the wire are then plugged into the other side of the resistor. This can be seen in schematically in figure 4.24. Figure 4.26a shows the underside of the mounting setup with the attached resistors. To prevent electrical shorting between resistors (and hence trap electrodes) a Macor spacer block is used (figure 4.26a). Macor, similar to PEEK, is a more easily machinable glass based ceramic. The ceramic comprises of a fine dispersion of crystallites within a glass matrix and is UHV and cryogenic compatible [149]. To determine the stability of resistance as a function of temperature, two 1 kΩ resistors (pictured in figure 4.26a) were measured at room temperature and at 4 K using a multimeter. No variation in resistance was found to a 1 Ω accuracy.

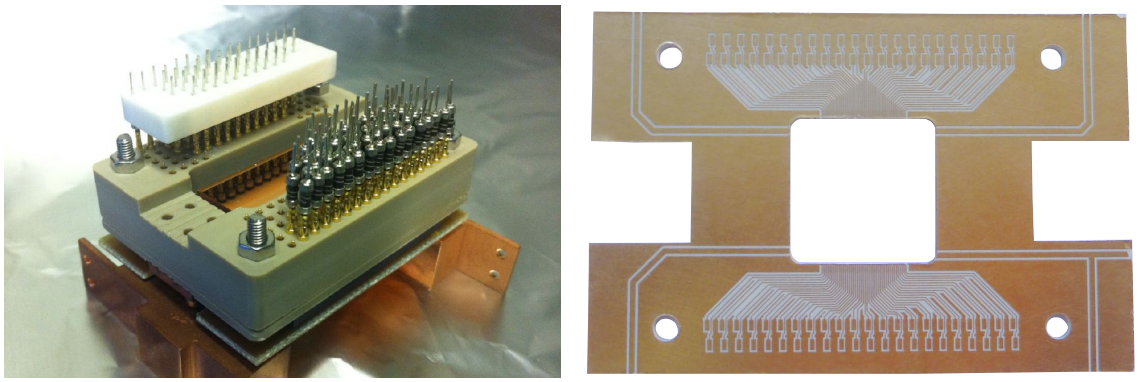

(a) (b)

Figure 4.26: (a) Resistors with crimped gold receptacles inserted into the PEEK block. A Macor spacer is also used to ensure the resistors are separated to prevent electrical shorts. (b) The in-vacuum filter PCB which has been machined to fit the mounting structure.

Capacitors

High Q ceramic NP0 capacitors (Presidio MVP0505N621KAG1R-6) were used. Typically ceramic based capacitors offer low outgassing properties and are suitable for UHV applications. For cryogenic applications not all ceramic capacitors are suitable, such as popular X7R and Y5V dielectric ceramics. X7R and Y5V capacitors exhibit an exponential and linear decrease respectively in their capacitances by two orders as they are cooled from 300 K to 4 K [150]. NP0 capacitors on the other hand show minimum variation in capacitance (<2%) across this temperature range. Like the resistors, two 620 pF capacitors were measured at room temperature and at 4 K and showed a variation less than ±5 pF.

PCB

The capacitors are mounted on top of a 1.6 mm thick Rogers 4350b printed circuit board (PCB) with a soft gold top layer. Rogers 4350b is a UHV compatible glass reinforced ceramic with a low dielectric constant 3.48 ± 0.05 at 10 GHz at 296 K [151]. The PCB (figure 4.26b) includes bond pads for 88 1.40×0.38 mm (0505 type) capacitors. Four paths are also included for rf and microwave connections which can have edge or surface mount SMA or SMP connectors. The PCB is mounted on top of the chip carrier with gold wirebonds connecting the chip carrier to the PCB (figure. 4.27). The final assembled in-vacuum filter setup can be seen in figure 4.28 with edge mounted SMA connectors.

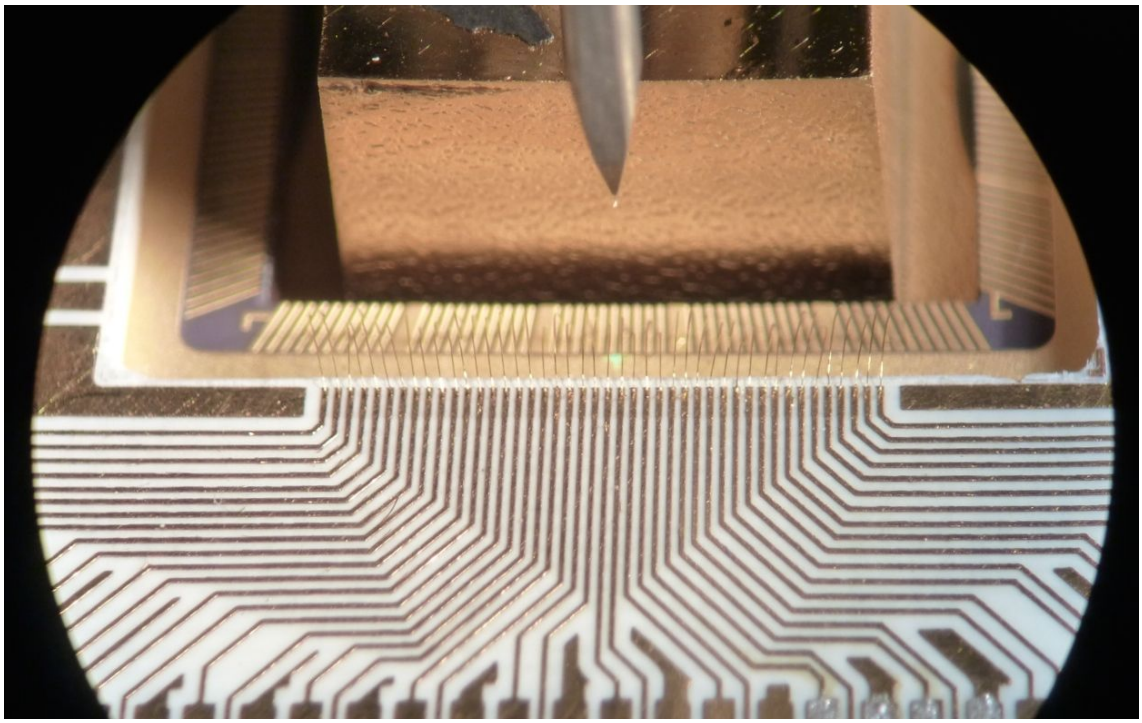

Figure 4.27: Gold wirebonds connecting the filter PCB and the chip carrier.

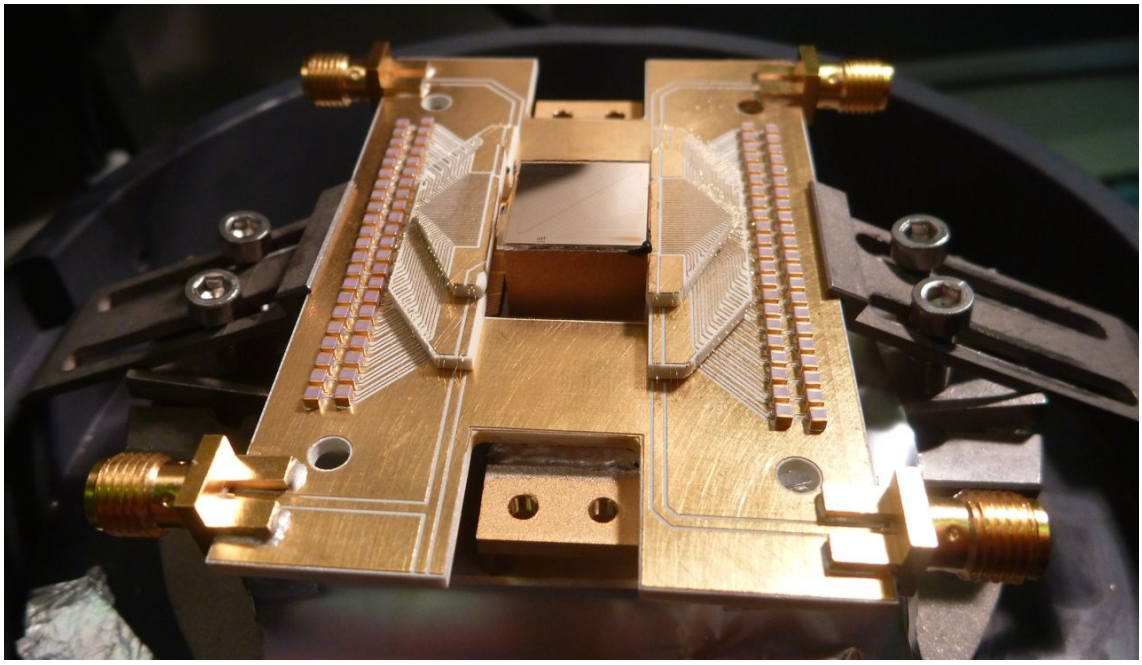

Figure 4.28: The final assembled in-vacuum filter PCB with 88 surface mounted capacitors and four edge mounted SMA connectors.

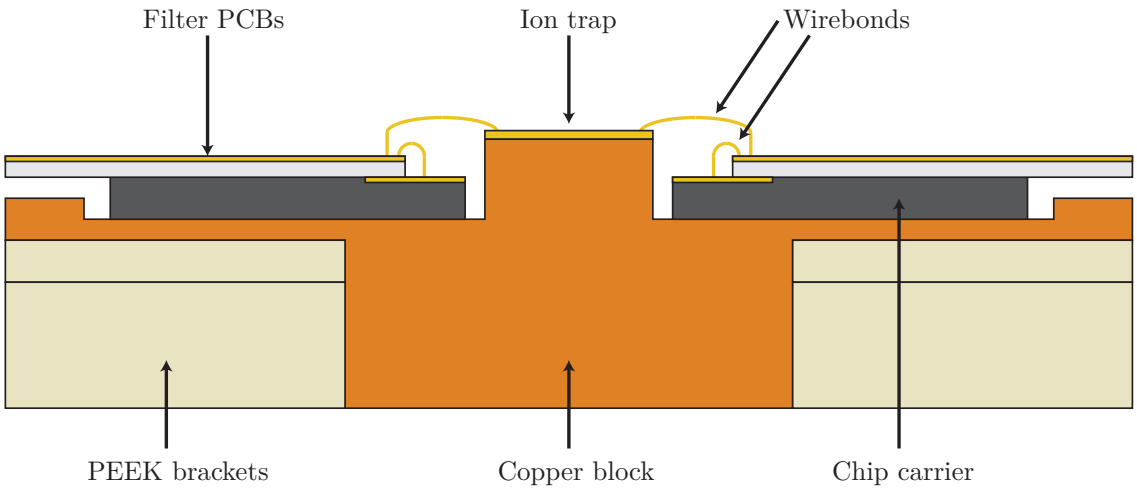

Figure 4.29: Cross section of the mounting structure showing the wirebonds from the chip to chip carrier and from the chip carrier to chip.

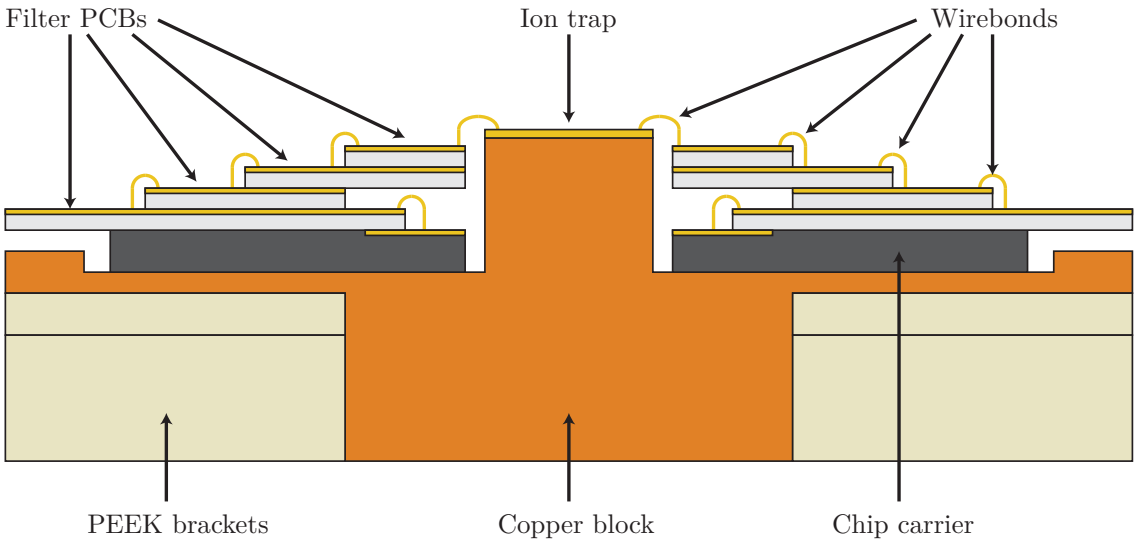

Figure 4.30: Cross section of the mounting structure showing the wirebonds from the chip to chip carrier and from the chip carrier to chip. The design includes multiple PCB levels allowing for the chip height to be raised as seen in figure 4.28. The raised mount allows magnets to be placed next to the ion trap as described in section 4.11.

4.7.7 Mount heater

A second heater (Lakeshore HTR-25), identical to the one mounted within the ULVI, is also used closer to the trap by mounting it directly into the lower copper mounting block (figure 4.31). The heater allows for an additional heat load into the system to accelerate warm up cycles and provide temperature control via the Cryocon controller unit. The localized heating source also allows the trap to be kept at a warmer temperature during cool down, reducing the effects of cryopumping on the chip surface. The heater is connected to the 6 pin HV feed through by wires connected to two gold plated receptacles crimped onto the two heater wires.

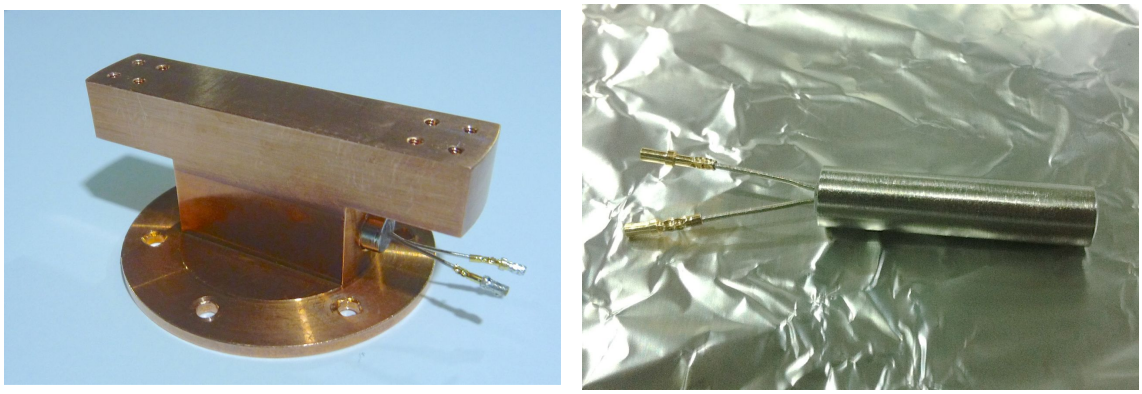

(a) (b)

Figure 4.31: 25 W resistive heater (a) mounted with the lower copper mounting block (b).

4.7.8 Final mount

Figure 4.32 shows an exploded view of the mounting structure. The lower PEEK bracket and the top copper block are both bolted to the to lower copper mount independently and therefore allows the trap (mounted on the top copper block) to be removed independently. Four bolts on the corners of the PEEK bracket also support the PCB mounted on top and are orientated such that additional equipment (e.g. magnets (section 4.11)) can be attached in situ.

4.8 External dc filter

In addition to the in-vacuum RC filter, an external RC filter is used to minimize any high frequency fluctuations from the signal generator and laboratory environment. A significant source of noise in this environment originates from alternating current at 50 Hz from mains electricity. Attaining a low cut off frequency (<50 Hz) can be difficult as the attenuation

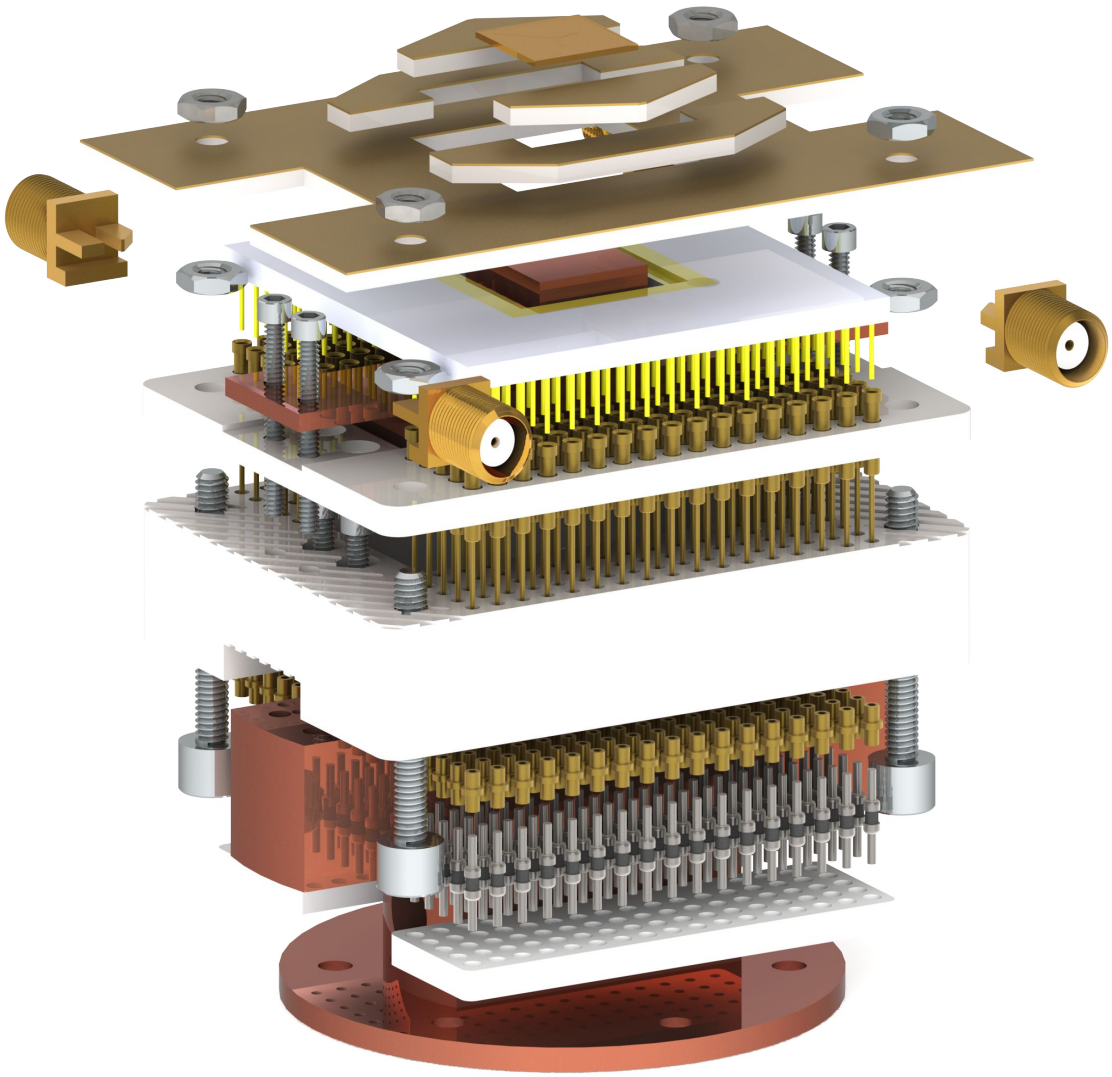

Figure 4.32: Exploded view of chip mounting structure with in-vacuum filtering.

may not drop sufficiently quickly at low frequencies. The voltage division for a single RC stage shown in figure 4.33 can be given as

$$V_1 = \left(\frac{Z_2}{Z_1 + Z_2}\right) V_0 = \left(\frac{\frac{1}{j\omega C_1}}{R_1 + \frac{1}{j\omega C_1}}\right) V_0 = \left(\frac{1}{j\omega R_1 C_1 + 1}\right) V_0. \tag{4.8}$$

Here the voltage drops off as $1/\omega$ which is equivalent to -20 dB/decade. To increase the response in cut off frequency additional RC filters can be used. The effect of multiple RC filters can be described as

$$V_N = \left(\frac{1}{j\omega R_1 C_1 + 1}\right)\left(\frac{1}{j\omega R_2 C_2 + 1}\right) \ldots \left(\frac{1}{j\omega R_N C_N + 1}\right) V_0. \tag{4.9}$$

The voltage now drops off as $(1/\omega)^N$, which is equivalent to $N \times (-20\,\mathrm{dB/decade})$. The

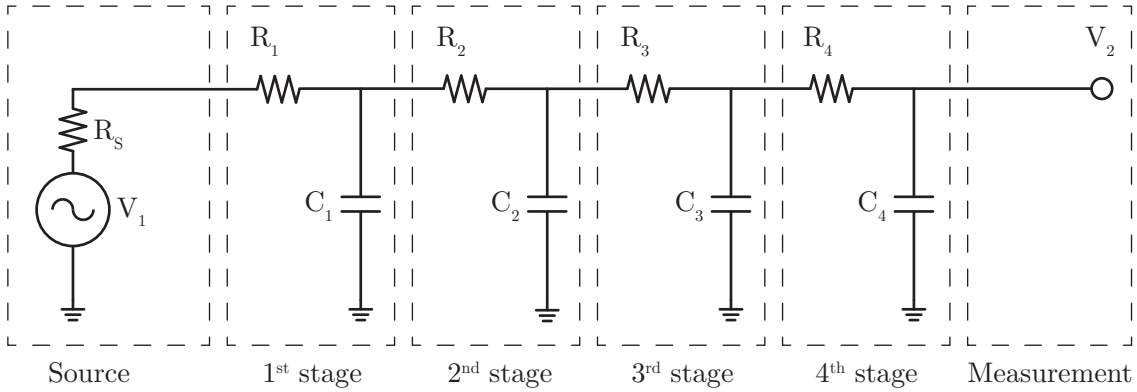

Figure 4.33: Circuit diagram for a four stage RC filter used as an external filter

external filter used is formed of a four stage RC filter which results in an attenuation of ∼80 dB/decade. The filter box is formed of one primary PCB that holds two female output D-sub connectors and ten secondary PCBs that contain ten female input SMA connectors each. Figure 4.34 shows the external dc filter box used which has -3 dB cut off frequency of 32 Hz.

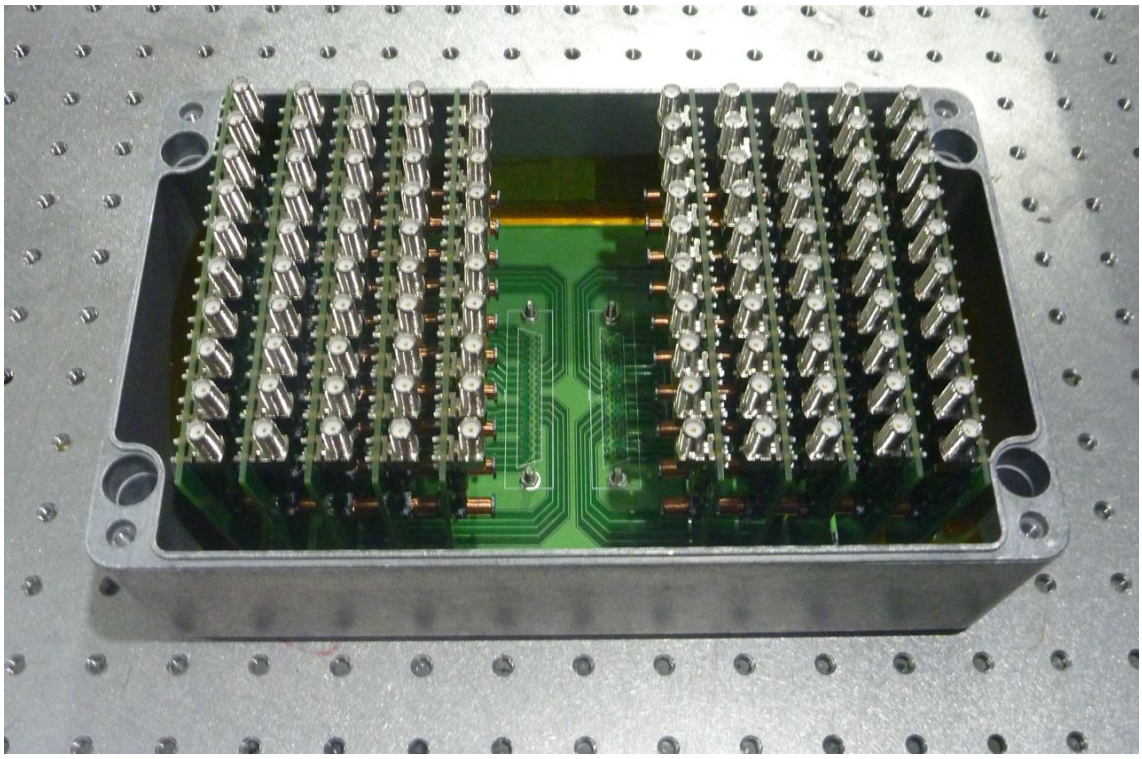

Figure 4.34: External dc filter box with 100 filtering channels.

4.9 Resonator

The use of a helical resonator to a provide a confining pseudopotential with a narrow bandwidth, high voltage and impedance matching is not an ideal solution for an cryogenic

vacuum system. In room temperature systems the wires to the trap from the helical resonator are kept short. The helical resonator is either mounted on or close to the vacuum system and the internal wires travel directly to the trap from the nearest feedthrough with the length of wire being <10 cm. The primary reason for this is that an increase in the length of the wire corresponds to an increase in the total capacitance of the wire which decreases the quality factor of the resonant circuit. The quality factor Q for a helical coil resonator can be given by [105]

$$Q = \frac{X_{L_C}}{R_{ESR}} \tag{4.10}$$

where $X_{L_C} = L_C\omega$, L_C is the helical coils self inductance and ω is the resonant frequency. R_{ESR} is the effective series resistance for a helical coil with a low self capacitance and resistance. For a low resistance ion trap this can be given by [105]

$$R_{ESR} \simeq R_j + R_C + R_S + R_t \left(\frac{C_t}{C_S}\right)^2 \tag{4.11}$$

where R_j is the coil to shield resistance, R_C is the coil resistance, R_S is the shield resistance, R_t is the trap resistance, C_S is the shield capacitance and C_t is the trap capacitance (including the capacitance of the wires).

For cryogenic vacuum systems care must be taken to thermally anchor all incoming cables as described in section 4.6. Failure to do so can result in the base temperature of the system increasing by several Kelvin. However, the capacitance of coax cabling increases at a rate of 50-100 pF per meter. This adds a significant capacitance to the resonant circuit where a typical surface trap has a capacitance of only 5-20 pF (based on trap measurements within the lab). Figure 4.35 shows the effect of adding 1-2 m of additional coax cabling within the system, resulting in an additional 50-100 pFper meter.

One alternative is to place the helical resonator on the inside of the vacuum chamber [138]. This ensures that the entire system is thermally anchored and reduces the length of the cabling from the resonator to the trap. An added benefit of cooling the entire system to 4 K is the decrease in resistance of the copper material used to construct the resonator. Cooling from 300 K to 4 K can increase the Q by a factor of 4 [138]. Despite providing better results, helical resonators are relatively large and occupy a significant volume of the central octagon of the vacuum chamber. Coupling the resonator and the trap also becomes difficult as the coupling changes when the system is cooled down and the resistance of the system drops. Coupling therefore requires the system to be opened,

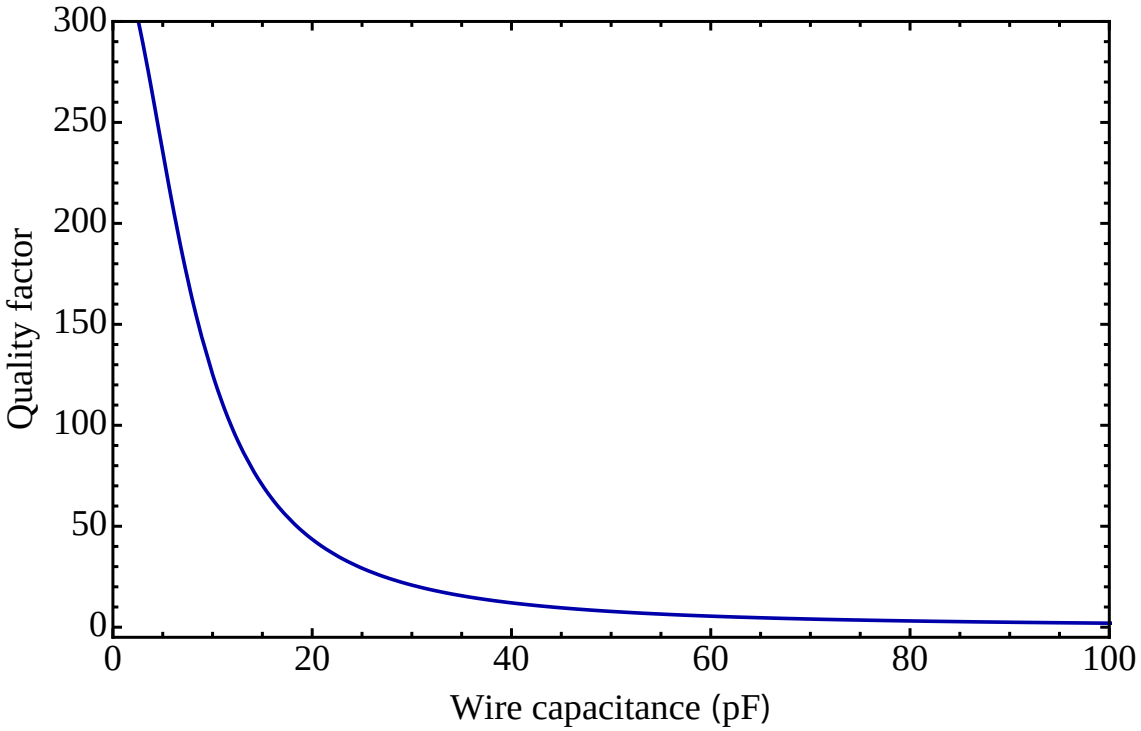

Figure 4.35: The quality factor of a typical helical coil resonant circuit to keep a fixed resonant frequency of 20 MHz with a trap capacitance of 5 pF.

the resonator antennae coil adjusted, the system closed and retested until the coupling is sufficient.

4.9.1 Compact resonator (Design 1)

As an alternative to helical resonators a compact in-vacuum lumped-component RLC resonator was developed to drive the ion trap. This allows a small amount of rf power into the vacuum system which is then impedance matched and amplified close to the trap. The compact resonators small size and minimal power dissipation makes it ideal for cryogenic use. At room temperature, Joule heating limits the quality factor (<10) of lumped component resonators with a trap, however, at lower temperatures this effect is minimized allowing for higher quality resonators. Initial resonator designs were based on designs by Gandolfi *et al.* [28]. Figure 4.36 shows the circuit diagram used for the resonator.

Trap LC circuit

Figure 4.36 shows the circuit diagram for the resonator. The circuit is formed of three separate sections. In the middle of the circuit is an LC resonator formed from the capacitance of the trap, an inductor and an effective resistance due to power dissipation. The

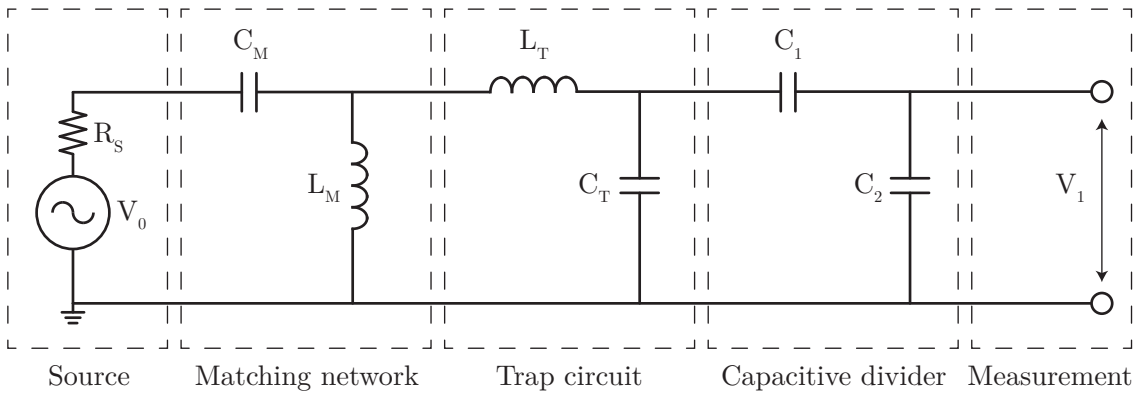

Figure 4.36: Circuit diagram for an in-vacuum PCB based rf resonator using an L-section matching network [28]. The capacitance of the ion trap C_T along with an inductor L_T forms a resonant circuit, which is impedance matched to a voltage source via a matching network formed from another capacitor C_M and inductor L_M

.

resonant frequency of the circuit is given by

$$\omega_0 = \frac{1}{\sqrt{LC}}, \tag{4.12}$$

and the quality factor is given by

$$Q = \frac{\omega_0 C}{R} = 1/\sqrt{LC} \tag{4.13}$$

where the resistance R is purely real at resonance. To fully utilize the cryogenic environment to minimize the resistance of the L and C components, superconducting material can be used. Section 6 describes the fabrication of superconducting ion traps that can be used. For the inductor coil a copper wire with a NbTi internal matrix (Goodfellows SC Composite Wire (Nb/Ti+Cu) 10M) was used. Below 10 K NbTi becomes superconducting (table 4.1) and above 10 K the copper cladding still provides a low resistance line.

Matching network

Before the LC section of the trap, another LC section is included that acts as a impedance matching network in between the source and trap. The L-section matching network helps to minimize any reflections due to an impedance mismatch. Two reactive components are used as they provide a passive coupling network without the need for power consumption or constraints due to cryogenic compatibility. The coupling circuit can be formed of an inductor or capacitor in series with the opposite component in parallel. Providing a dc path to ground for the trap can prevent charge build up which would result in a dc bias on the rf electrode. Therefore, placing the inductor in parallel is the optimum solution.

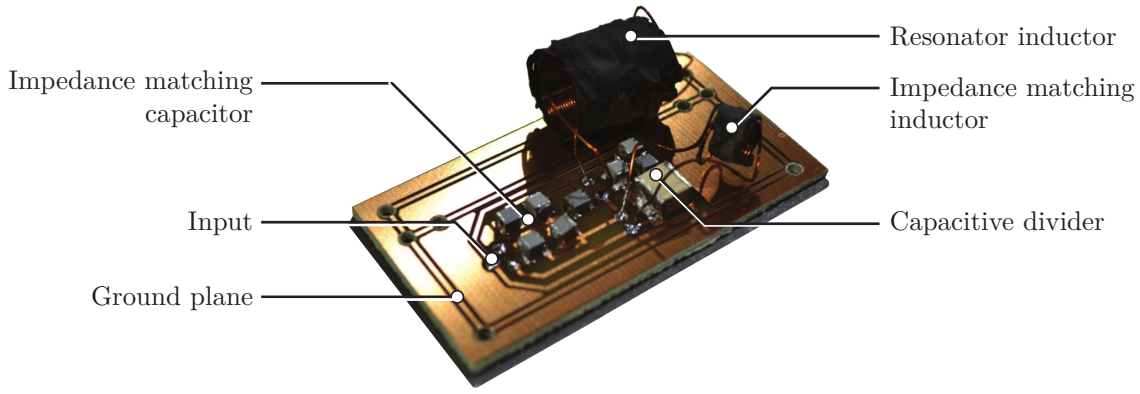

Figure 4.37: First iteration resonator with multiple high-Q NP0 capacitors for each capacitance with a Cu with NbTi matrix wire for inductors.

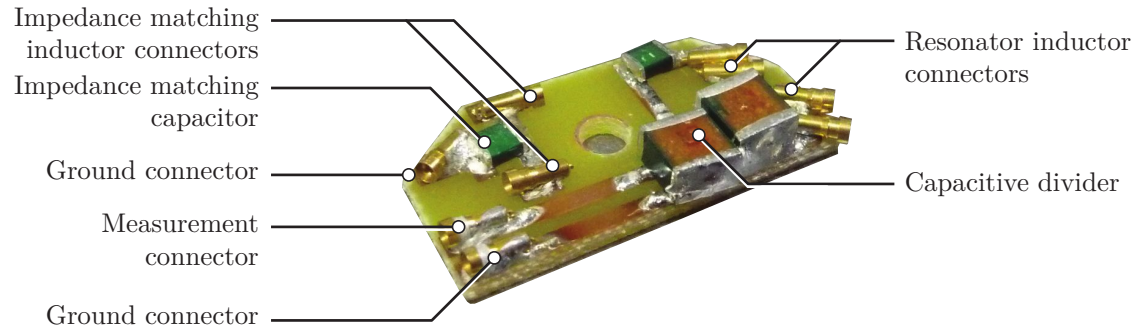

Figure 4.38: Second iteration resonator created with a smaller PCB and smaller high-Q MICA capacitors. The inductor coils remained the same across both iterations.

A capacitor can then be used in series to complete the L-section. A variable capacitor is then used to tune the circuit to match the impedance. This requires opening the vacuum chamber to match the circuit as the matching changes as the system is cooled to 4 K, however, the matching was found only to drift by $\lesssim$5%.

Capacitive divider

The capacitive divider is a voltage divider composed of two capacitors. The purpose of the divider is to increase the input impedance of the measuring equipment in order to not affect the resonator during measurements. The capacitors should be chosen such that $C_1 << C_2$ and $(\omega C_1)^{-1} >> 50\,\Omega$ [28]. Using these requirements the impedance as seen from the resonator is dominated by the impedance of C_1. This makes the effect of the length of the transmission line to the measurement equipment (e.g. oscilloscope, spectrum analyser, etc.) on the resonator negligible. It also allows the measurement equipment to be disconnected without affecting the resonator.

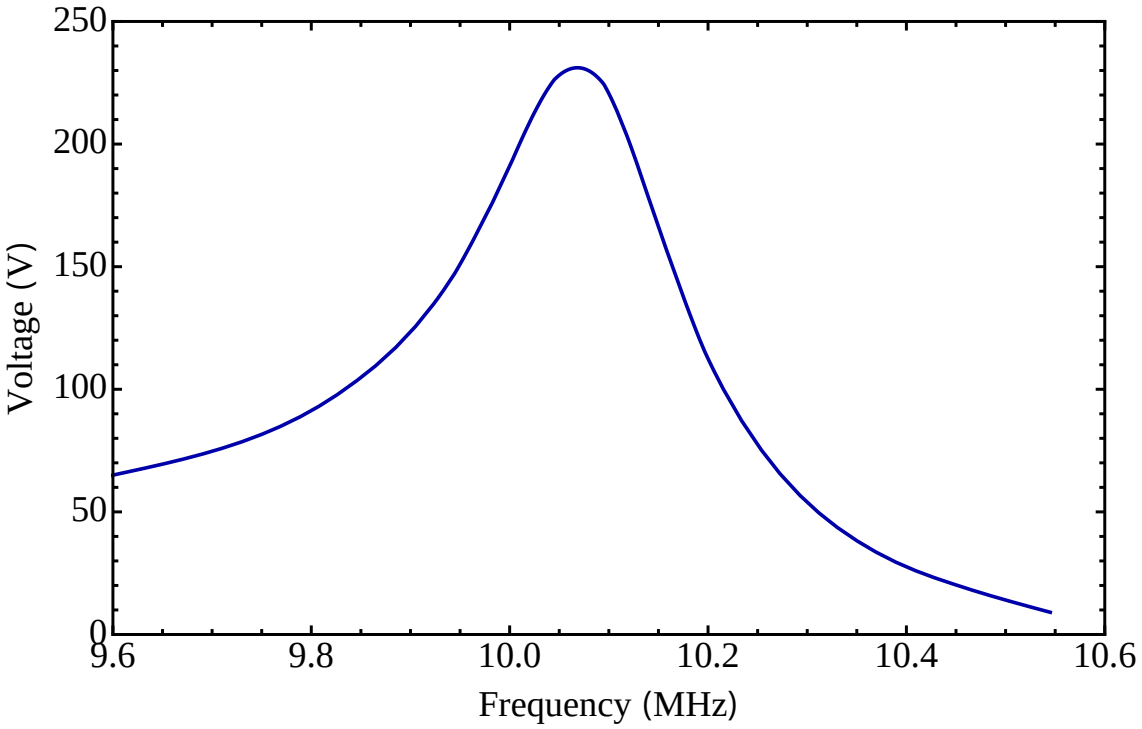

Figure 4.39: In-vacuum resonator with a resonance frequency of 10.10 ± 0.05 MHz. A -3 dB bandwidth of 140 kHz was measured giving a Q of 72. The voltage gain G_V was measured as 23 ± 1. The data was gathered by measuring the voltage through the capacitive divider while driving the circuit across a range of frequencies.

Results

Figures 4.37 and 4.38 shows the resonators used. Initially a large PCB was used with two bolt holes for thermal anchoring directly to the 4 K cold stage. Multiple high-Q NP0 capacitors were used for each capacitance along with a Cu and NbTi wire for inductors (figure 4.37). A second iteration was designed to create a smaller spatial footprint within the system and used a smaller PCB with a single mounting hole and smaller high-Q MICA capacitors (figure 4.38). The inductor coils remained the same across both iterations. Figure 4.39 shows the resonance measured across the capacitive divider. The resonance frequency was measured to be 10.10 ± 0.05 MHz. A -3 dB bandwidth of 140 kHz was measured giving a Q of 72. For an input voltage of 10 V the peak voltage at resonance was measured as $\sim$230 V giving a voltage gain of 23 ± 1 as the circuit behaves like a transformer.

4.9.2 Compact resonator (Design 2)

A second resonator design was developed and introduced a number of changes to improve upon the first designs. The primary change was the replacement of the matching network in

design 1 with an autotransformer. Unlike transformers that are formed from two separate coils, an autotransformer is formed from a single coil with at least three electrical taps. An autotransformer is capable of performing impedance matching as well as providing a step up voltage.

The voltage and current to turns ratio can be determined using the same method as a two-winding transformer and is given by

$$\begin{aligned} V_1 &= \frac{N_1}{N_2} V_2, \\ I_1 &= \frac{N_2}{N_1} I_2, \end{aligned} \tag{4.14}$$

where the subscripts '1' and '2' denote the primary and secondary coils respectively for the voltage V, current I and number of turns N. Assuming that the source is connected to the primary circuit and the load is connected to the secondary circuit, the resistance of the load can be given as $R_L = V_2/I_2$. The effective resistance R' of the load in the primary circuit is given by

$$\begin{aligned} R' = \frac{V_1}{I_1} &= \left(\frac{N_1}{N_2}\right)^2 \frac{V_2}{I_2}, \\ &= \left(\frac{N_1}{N_2}\right)^2 R_L. \end{aligned} \tag{4.15}$$

Therefore the effective load resistance can be made to match the source impedance by selecting the appropriate turns ratio. This method also has the benefit of minimizing the effect of parasitic capacitances of the inductors used with previous designs. Figure 4.41 shows the circuit diagram used for the resonator circuit.

Results

Figures 4.42 and 4.43 show two iterations of the resonant circuit. While the first iteration was smaller, the input and output connectors were simple press fit pin receptacles with no grounded shielding (figure 4.42). The second iteration used surface mount SMP connectors which are smaller in size than SMA connectors and are 'press on' instead of 'screw on' making them significantly easier to use inside the vacuum system (figure 4.43). Figure 4.44 shows the resonance measured across the capacitive divider for the resonator shown in figure 4.43. The resonant frequency was measured at 11.50 ± 0.05 MHz. A -3 dB bandwidth of 200 kHz was measured resulting in a Q of 57. For an input voltage of 10 V the peak

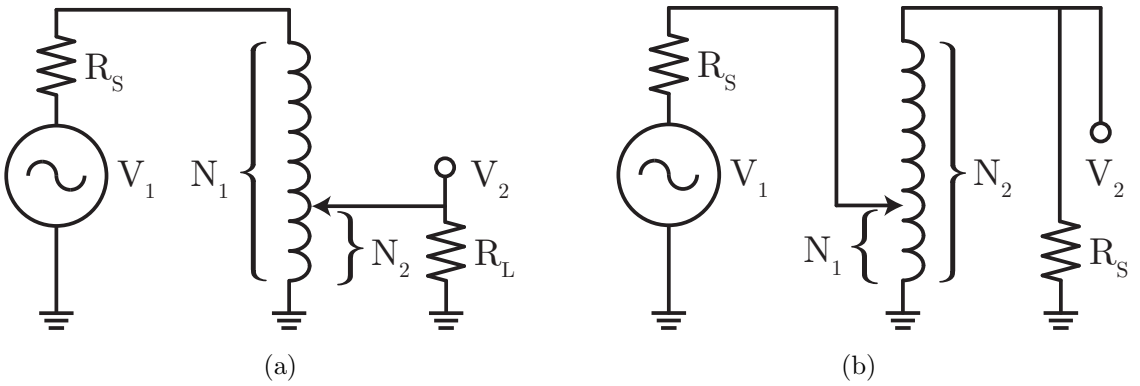

Figure 4.40: Circuit diagrams for a step down autotransformer (a) and a step up autotransformer (b).

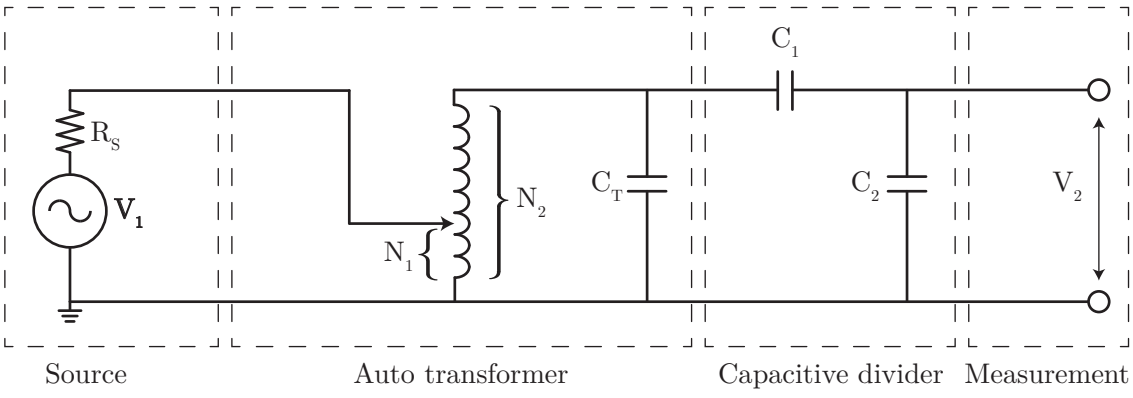

Figure 4.41: Circuit diagram for an in-vacuum rf resonator using an autotransformer.

voltage at resonance was measured as $\sim$250 V giving a voltage gain of 25 ± 1.

Resonator improvements

The performance of the resonator can be improved through a number of methods to reduce the rf voltage bandwidth and filter out unwanted noise [104]. Firstly, the order of the filter can be increased. This is accomplished in a simialr manner to that of the external dc filer described in section 4.8. By increasing the number of individual inductors in series with the capacitance of the trap, we can reduce the bandwidth of the resonance and therefore increase the quality factor of the resonator. However, in practice it is not practical to introduce multiple inductors on to the resonator due to limited space and coupling between the electromagnetic fields from the inductor coils.

An alternative method to improve the performance of the resonator is to utilize superconducting material throughout the whole resonator. This would result in the effective resistance of the resonator dropping and increasing the quality factor. As the inductor coil is already formed from a NbTi matrix within a copper cladding, the remaining part of the resonator is the capacitors and PCB. High quality factor (10^5) ceramic based NP0 capacitors are already used with the resonator design. The ceramic capacitors can be replaced by microstrip stub capacitors, which are formed from specific track geometries on the PCB. Microstrip stubs are formed from a straight transmission line connected only at one end, with the free end either open or short circuited. Neglecting losses in the transmission line, the input impedance of the stub is purely reactive. Depending on the electrical length of the stub it can act as either a capacitor or an inductor. As the wave propagates down the stubs length, the stub switches between being inductive and capacitative every $\lambda/4$. By fabricating the PCB with a superconducting metal such ans NbN of NbTi, both the PCB and capacitor can be superconducting as well. Alternatively if a PCB with no superconducting plating is available, the superconducting wire used for the inductor can be used to replace the PCB track and used along side the high-Q NP0 capacitors.
The rf voltage must have a relatively small bandwidth such that it filters out any unwanted noise which could otherwise lead to heating of the ion .

4.10 Atomic source oven

Traditional room temperature vacuum systems use ohmically heated atomic sources to provide a flux of atoms that can be ionized [103, 152–155]. Ohmic ovens are created by placing an atomic source (usually a wire or foil) in a small diameter ($\sim$ 2 mm) stainless

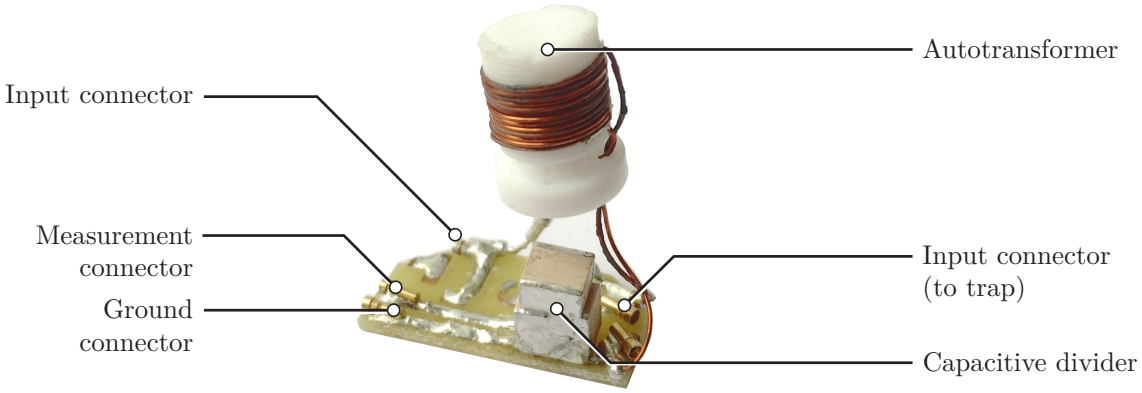

Figure 4.42: First iteration resonator with press fit unshielded wire connectors.

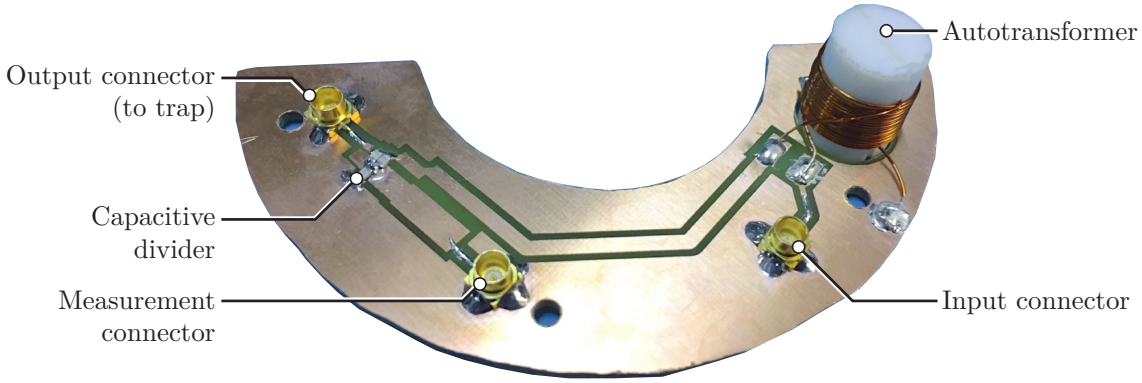

Figure 4.43: Second iteration resonator with surface mounted SMP connectors.

steel tube. The tube is spot welded at one end and grounded at the other end to form a return path. A current is delivered to the steel tube to heat the atomic source. For Yb, the atoms can be evaporated from the surface of the source with an applied current of $\sim 5-15\,\mathrm{A}$, which corresponds to a power dissipation of 10-20 W. For a cryogenic system this presents a significant heat load. The oven would require thermal anchoring within the second stage of the cooler which can only dissipate 1.2 W at 4.2 K. For cryogenic systems an alternative method known as laser ablation can produce an atomic source close to the trap. For this technique a laser is used to ablate material from the surface of a sample placed in close proximity to the ion trap. Using this method an ion trap can be successfully loaded with a single 1.5 mJ pulse directed at the sample [135, 156]. However, as well as being more experimentally difficult to implement, the plume created from the ablation of a target contains a large amount of unwanted material in a wide angle of distribution. This can lead to coating the trap surface as well as additional charge build up with ejected electrons striking the trap. Ablation loading also offers no option for isotope selective loading which can result in a decrease in loading rates. This section describes an alternative novel ceramic based atomic source oven developed which

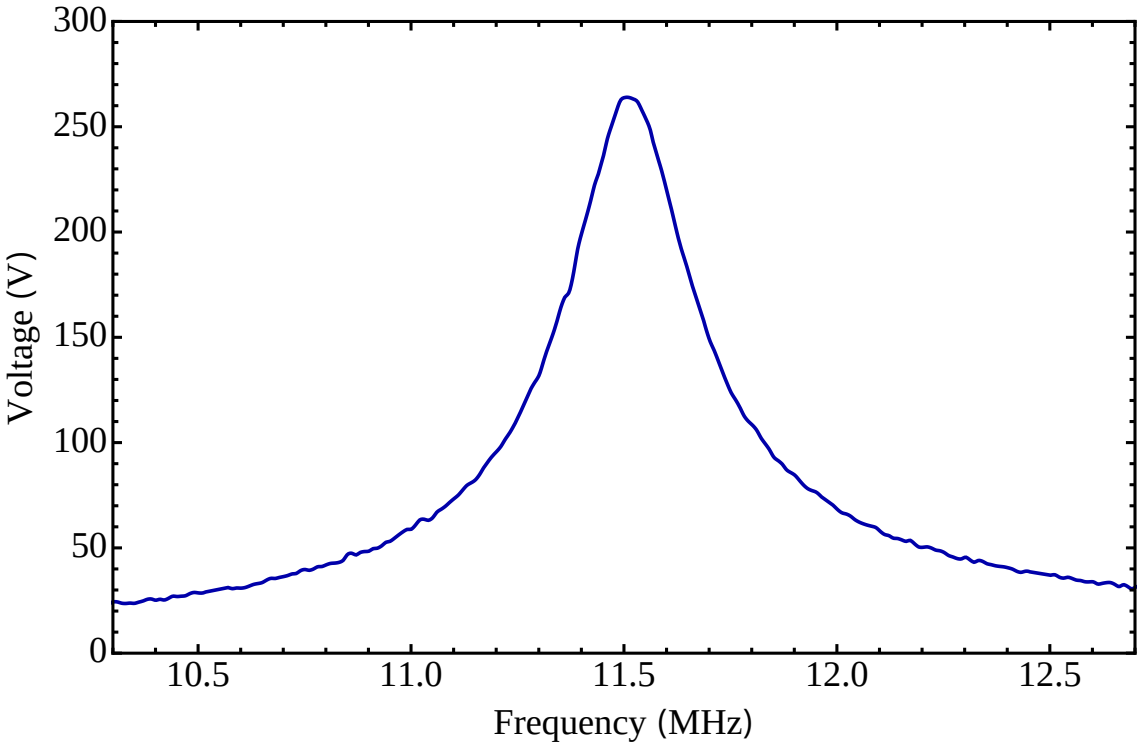

Figure 4.44: In-vacuum resonator with a resonance frequency of 11.50 ± 0.05 MHz. A -3 dB bandwidth of 200 kHz was measured giving a Q of 57. The voltage gain G_V was measured as 25 ± 1.

is ohmically heated but dissipates minimal power at the 4 K stage.

4.10.1 Oven construction

The oven is constructed from three separate components 4.45. The first component is formed from BNP-2 (Ceramic Substrates BNP-2 Rod 5×100 mm), an Aluminium Nitride (AlN) based ceramic that possess a high thermal conductivity (92.6 W/mK). The AlN core is machined with a thread on its outer surface to allow a 0.089 mm diameter tungsten wire (Wires TU0089-010M) to be wrapped around it. The wire is held in place by tying a knot on both ends of the oven and by applying a ceramic based UHV compatible cement (Glassbond Sealing Cement No.33S). The Yb source (Goodfellow GO0196) is a wire with a diameter of 1.2 mm. Gently compressing the wire in a clamp allows it to be firmly inserted within the 1 mm opening in the AlN core, creating a firm contact on the interior walls.

To thermally isolate the tungsten and AlN core, a thermally insulating shield is placed around it. Initial testing used Duratec, a calcium silicate based material with a thermal conductivity of 0.37 W/mK for the insulating material. However, the material was extremely brittle, difficult to machine and porous, which limited the vacuum pressure to 10^{-5} mbar. Macor, a glass ceramic based material as used in section 4.7.6, was used

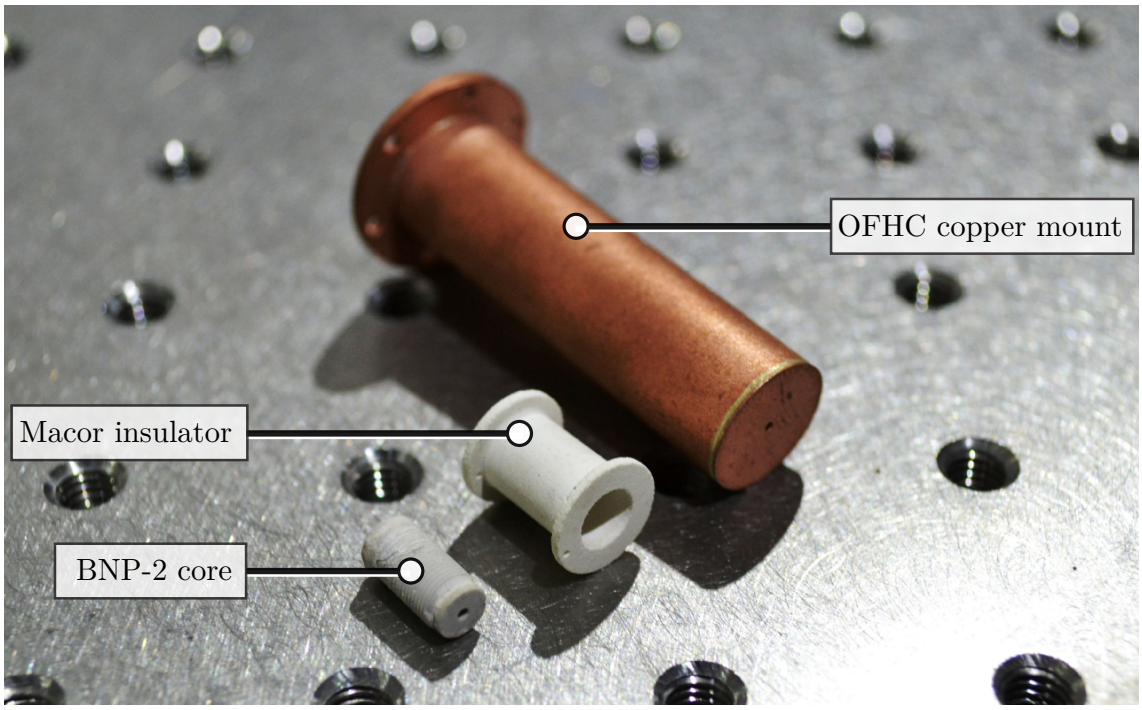

Figure 4.45: The central BNP-2 central core, Macor insulating shield and OFHC copper mount.

instead as it also possessed a low thermal conductivity (1.46 W/mK).

The third component is the OFHC copper mounting structure. The mount is formed from a hollow 44 mm long cylinder with a curved mounting flange allowing it to be mounted directly to the radiation shield. A copper spring is placed before and after inserting the oven into the mount, allowing the oven to be held firmly in place within the mount. The springs can also be adjusted to allow the distance between the oven and the mounts aperture to be varied, effectively providing collimation for the atomic flux beam. The back end of the mount is closed with a PEEK endcap that provides two electrical feedthroughs using two gold female-female receptacles. Figure 4.46 gives a cross sectional view of the oven showing its internal configuration.

4.10.2 Oven operation

The oven was tested by attaching it to a six pin vacuum feedthrough as shown in figure 4.47. The oven was placed inside a closed vacuum system and evacuated to 10^{-7} mbar using a turbo molecular pump. The oven was aimed towards a residual gas analyser (RGA) (ExTorr XT200M) to measure to the output flux. The testing setup can be seen in figure 4.47. Results for a natural ytterbium source showed the emission of ^{171}Yb and ^{174}Yb within 120 s of the application of 0.3 A (figure 4.48). This corresponds to a power dissipation of only 0.1-0.2 W into the surrounding environment.

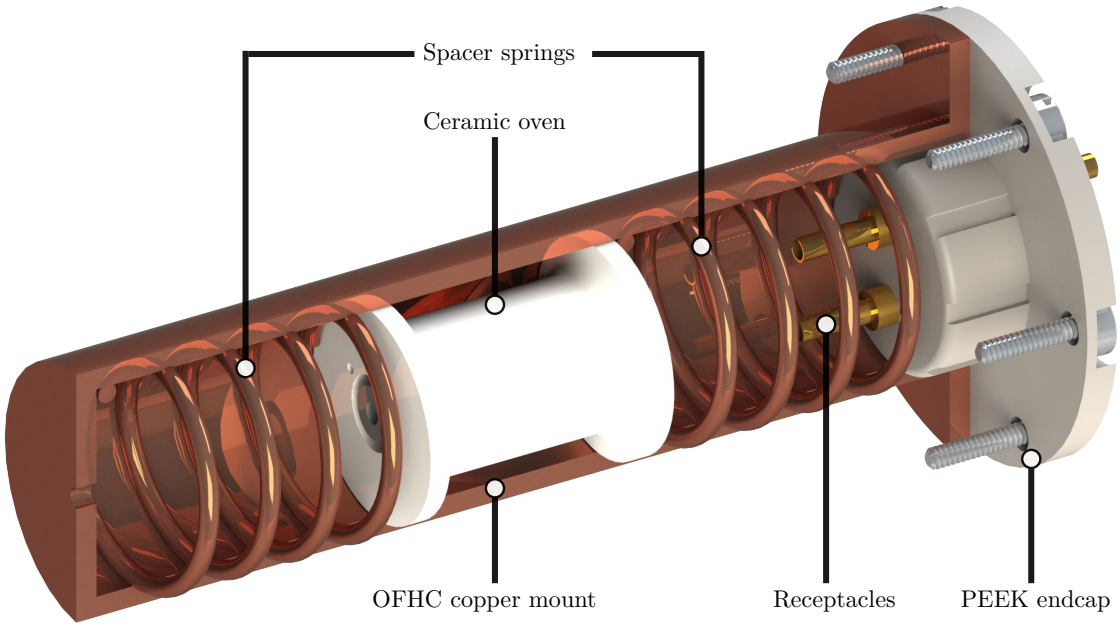

Figure 4.46: A cross sectional view of the ceramic based oven design showing the internal configuration.

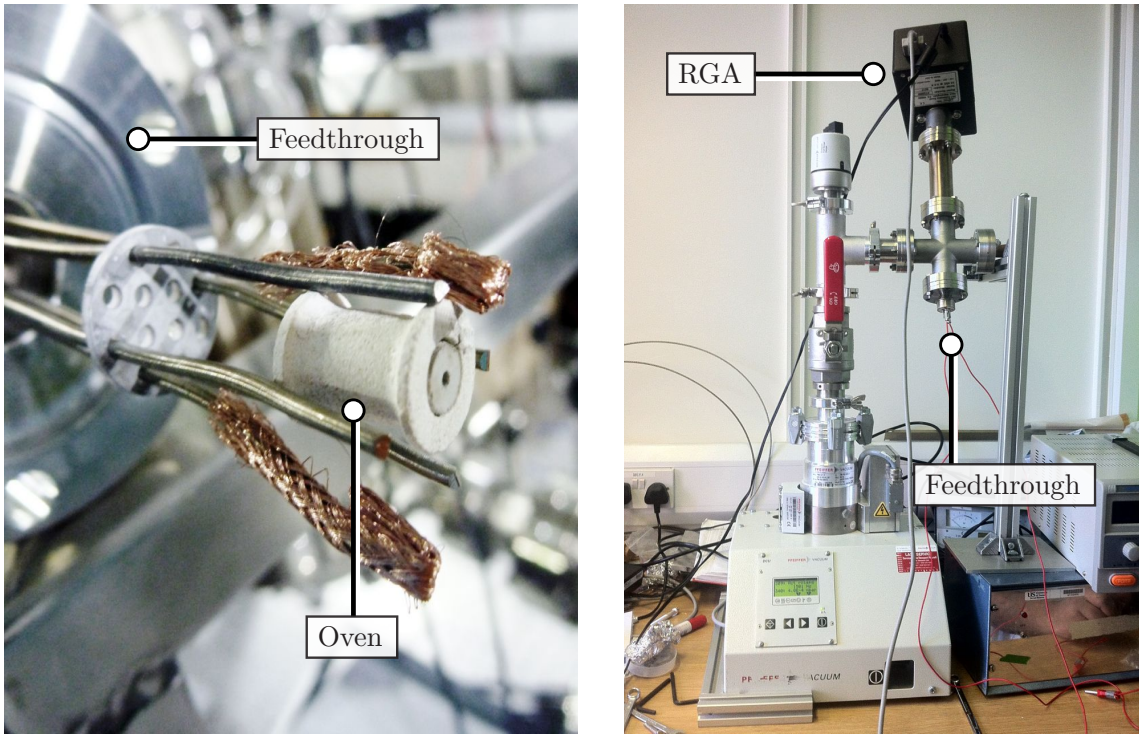

Figure 4.47: Ceramic based oven mounted on a 6 pin feedthrough (left) and the vacuum system, with TMP, oven feedthrough and RGA used for testing (right).

4.11 Magnets

This section describes the motivation behind the generation of a magnetic field gradients at the ions position, the simulation of magnet geometries and the construction of a mechanical

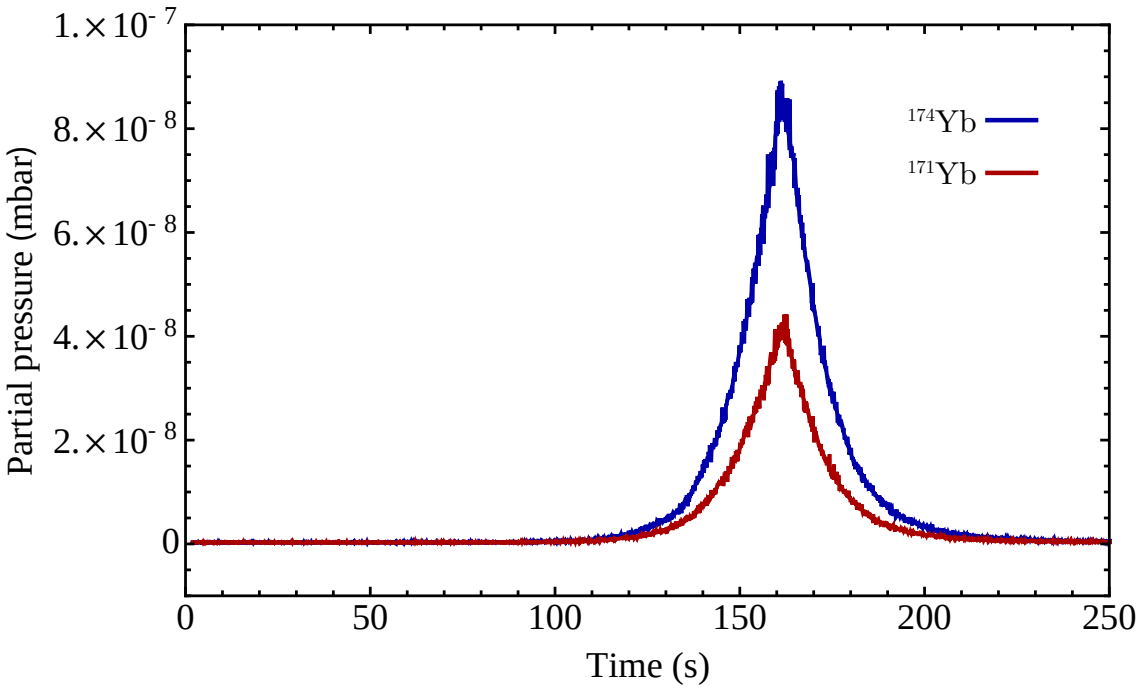

Figure 4.48: Partial pressure plot for the ceramic based oven with 0.3 A applied. The drop in pressure at corresponds to the oven being turned off.

translation stage to mount the magnets.

4.11.1 Magnetic fields for long-wavelength quantum computing

The original proposal for quantum computing using ions [79] required tightly focussed lasers for individual ion addressing and ground state cooling of the ions. While this scheme has been demonstrated [50, 157], it still remains experimentally very difficult to perform. To eliminate the prerequisite of ground state cooling, approaches to multi-qubit gates that do not require ground state cooling, known as 'hot gates', have been proposed [94, 115] and demonstrated with entanglement of up to 14 ions [158].

Despite the success with these techniques it still remains a difficult proposition to scale to a large number of ions for a number of reasons. Firstly, the experimental infrastructure and financial investment need to increase significantly to provide more lasers to address each ion individually. The stability of each laser frequency, phase and intensity can also be a source of decoherence. Even for stable lasers, beam pointing and quality can be a source of decoherence. Spontaneous scattering of photons from the gate laser beams [159] can also result in a limit to maximum gate fidelities achievable.

As an alternative to laser-based gates, a microwave-based gate was proposed by Minert *et al.* [160]. Due to the relatively long wavelengths of microwaves it is insufficient to achieve coupling between the internal state of the ion and the ions motion. However, with the

introduction of a static magnetic field gradient it is possible to achieve a coupling similar to that of lasers. This is due to the two qubit states having a different magnetic moment and hence a different interaction with the magnetic field gradient. The inhomogeneous magnetic field also results in a shift of magnetic field sensitive Zeeman states which allows the ions to be individually addressed in frequency space. Both individual addressing [161] and two ion gates have already been experimentally demonstrated [162].

One of the current limiting factors in this scheme is magnetic field fluctuations. This is due to the their effect on the field sensitive qubit states which can lead to decoherence. To overcome this, techniques using dressing fields to produce effective dressed states that are less susceptible to magnet field noise have also been proposed and demonstrated [163, 164]. Another limiting parameter in achieving high gate fidelities using this scheme is the generation of high magnetic field gradients.

One method of producing a magnetic field gradient is to use a pair of anti-Helmholtz coils either side of the chip. However, due to the space constraints within the vacuum chamber, sufficient field gradients cannot be generated. Placing coils outside of the vacuum system require considerably larger coils with higher currents to produce sufficient gradients which becomes impractical. Another method of providing sufficient magnetic field gradients is to use permanent magnets [165]. Section 4.11.2 describes how the magnetic field gradient can be simulated and section 4.11.4 describes the construction of an adjustable mount for the magnets that can be attached to the mounting structure discussed in section 4.7. It should be noted that a third alternative is the microfabrication of current carrying wires directly within the chip substrate. In theory, this can produce far larger field gradients (1000 T/m) than coils or permanent magnets due to its proximity to the ion and provide a truly scalable future for microwave based quantum logic.

4.11.2 Magnetic field simulation

The choice of magnet material is determined by two important factors; its magnetization and its Curie temperature. The magnetization of a material can be defined by the remanence of that material, which is its ability to retain its magnetization after the application of an external magnetic field. The Curie temperature is the critical temperature above which a material's intrinsic magnetic moments change direction, leading to demagnetization.

Neodymium is the strongest commercially available rare earth magnet, possessing a remanence of $B_r = 1.0 - 1.3T$ [166]. However, the Curie temperature of Neodymium is

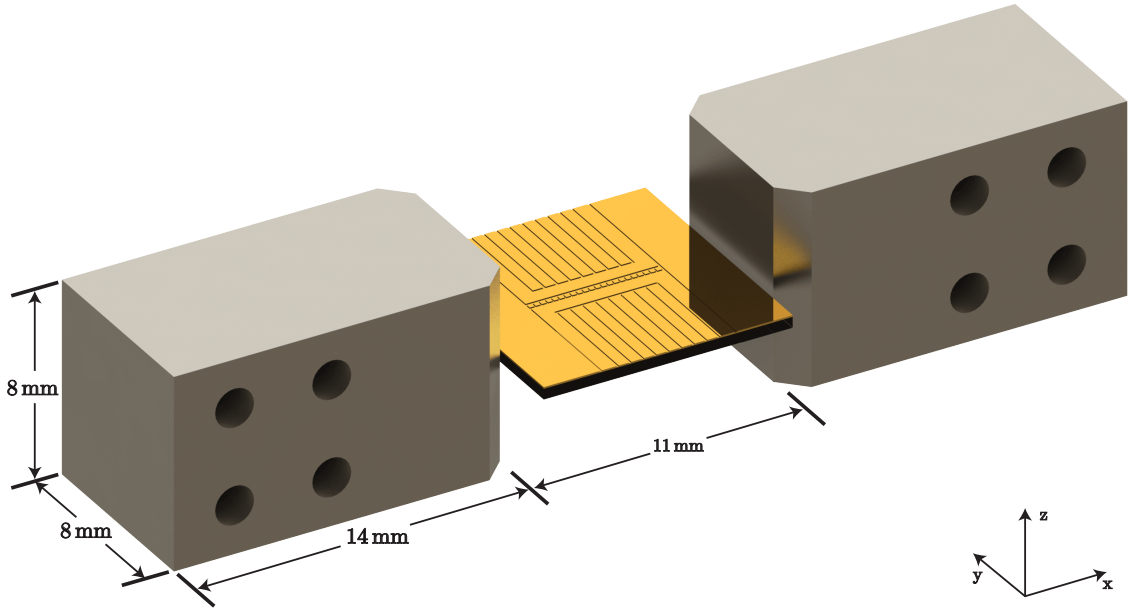

Figure 4.49: Two samarium colbalt magnets surrounding a 10×10 mm ion trap.

320°C [166] which could result is demagnetization during the baking process at 200°C for two weeks. Instead, the material chosen is Samarium Cobalt, which possess the next highest remanence of $B_r = 0.82 - 1.16T$ but with a Curie temperature of 800°C. To ensure the magnets are suitable for UHV a commercially available coating of nickel copper nickel was added to the simulations.

A symmetric pair of magnets about the centre of the trap were designed in SolidWorks and simulated in Computer Simulation Technology (CST) software. The magnets are $8 \times 8 \times 14$ mm and include two 1 mm chamfers as shown in figure 4.49. The simulation placed the like poles of both magnets facing each other. Figure 4.50 shows the magnetic field gradient along the x-axis through from the centre of one magnet to the other.

4.11.3 Magnetic field gradient

We can see from figures 4.50 and 4.51a that at an absolute magnetic field of zero, the field gradient will also be zero. Therefore, to attain a magnetic field gradient at the ion, there will also be a static magnetic field offset. For efficient Doppler cooling the Zeeman sublevels in the $^2S_{1/2}$ ground state hyperfine structure must be close enough in frequency space to be addressed by a single laser to be driven to the $^2P_{1/2}$ state. This limits the maximum magnetic field the ion can experience. For the 369 nm laser the natural linewidth is $\gamma = 19.6$ MHz. The power broadened linewidth can be given as [167]

$$\gamma_P = \gamma\sqrt{1 + s_0} \tag{4.16}$$

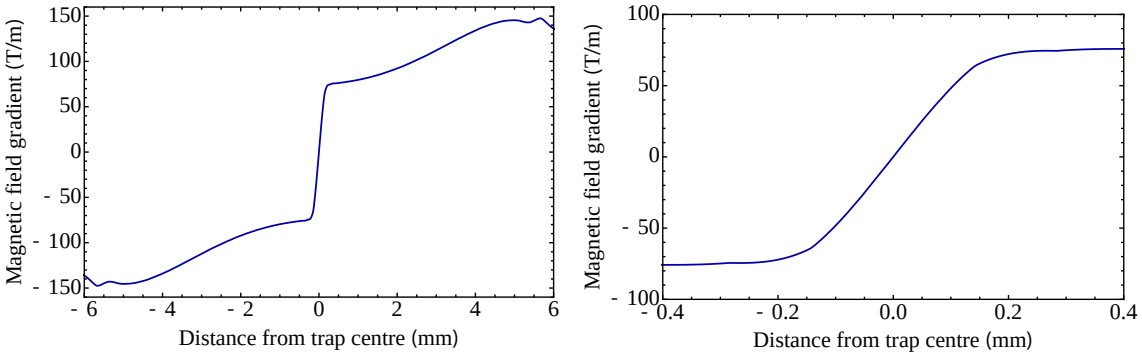

(a) (b)

Figure 4.50: Magnetic field gradient across the 11 mm seperating the magnets (a) and across the central 0.8 mm between the magnets.

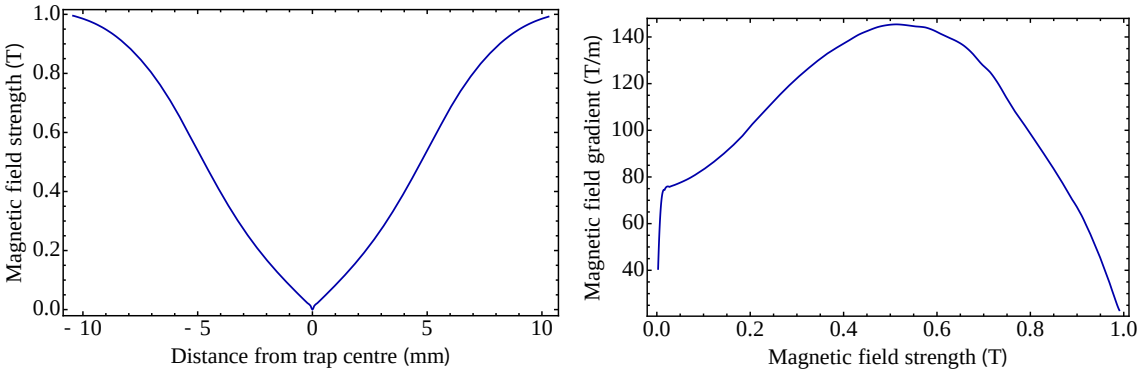

(a) (b)

Figure 4.51: Magnetic field gradient strength across the 11 mm separating the magnets (a) and the magnetic field strength as a function of magnetic field.

where $s_0 = I/I_s$ is the saturation parameter, I is the intensity of the laser and I_s is the saturation intensity which is given as [167]

$$I_s = \frac{\pi hc}{3\lambda^3 \tau} \tag{4.17}$$

where $\tau = 1/\gamma$ is the lifetime of the excited state. To minimize off-resonant scattering during coherent manipulation a low saturation parameter is required ($s_0 < 1$), however, for initial trapping a much higher saturation parameter can be used ($s_0 \approx 100$).

The Zeeman splitting of the hyperfine structure for $J = 1/2$ can be calculated using the Breit-Rabi formula which is given by [168]

$$\epsilon = \frac{E}{\Delta E_{hf}} = -\frac{1}{2I+1} - \frac{g_I \mu_B m_F B}{\Delta E_{hf}} \pm \frac{1}{2}\sqrt{1 + \frac{4m_F}{2I+1}\chi + \chi^2} \tag{4.18}$$

where E is the energy of the state, $\Delta E_{hf} = \hbar\omega_0$ is the energy splitting of the transition,

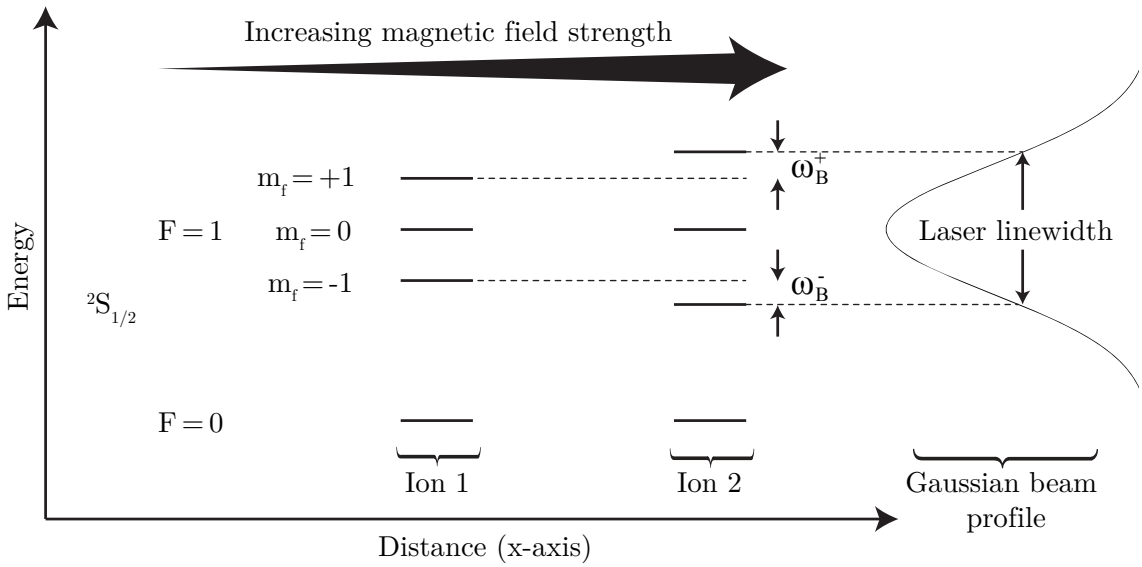

Figure 4.52: Zeeman splitting due to a magnetic field gradient.

$\omega_0/2\pi \simeq 12,642,812.1\,\text{kHz}$, I is the nuclear spin quantum number, g_I is the nuclear g-factor, B is the magnetic field and χ is a dimensionless parameter given by

$$\chi = \frac{(g_J - g_I)\mu_B B}{\Delta E_{hf}} \tag{4.19}$$

where g_J is the Lande g-factor. For ^{171}Yb the $\pm$ term corresponds to $F = I \pm 1/2$. The term is negative for $|F = 0, m_F = 0\rangle$ and positive for $|F = 1, m_F = \pm 1\rangle$. As $g_I << g_J$ by three orders of magnitude, the nuclear g-factor can be ignored. This reduces equation 4.18 to

$$\epsilon \approx -\frac{1}{2I+1} \pm \frac{1}{2}\sqrt{1 + \frac{4m_F}{2I+1}\chi + \chi^2} \tag{4.20}$$

where $\chi = g_J\mu_B B/\hbar\omega_0$. The values for ω_B^+, ω_B^- and ω_B^0, given in figure 4.52, can now be given by [168]

$$\begin{aligned}
\omega_B^+ &= \frac{\omega_0}{2}\left(1 + \chi - \sqrt{1+\chi^2}\right), \\
\omega_B^- &= -\frac{\omega_0}{2}\left(1 - \chi - \sqrt{1+\chi^2}\right), \\
\omega_B^0 &= \omega_0\sqrt{1+\chi^2}.
\end{aligned} \tag{4.21}$$

The linewidth of the laser dictates the maximum splitting $\Delta\omega_B$ for efficient Doppler cooling without adding further laser sidebands. Using equations 4.21 we can write $\Delta\omega_B$ as

$$\begin{aligned}\Delta\omega_B &= \omega_B^+ - \omega_B^- \\ &= \frac{\omega_0}{2}\left(1+\chi-\sqrt{1+\chi^2}\right)+\frac{\omega_0}{2}\left(1-\chi-\sqrt{1+\chi^2}\right) \\ &= \omega_0\left(1-\sqrt{1+\chi^2}\right)\end{aligned} \tag{4.22}$$

Solving equation 4.22 for χ gives

$$\chi = \pm\frac{\sqrt{\Delta\omega}\sqrt{\Delta\omega-2\omega_0}}{\omega_0}, \tag{4.23}$$

therefore

$$B = \pm\hbar\frac{\sqrt{\Delta\omega}\sqrt{\Delta\omega-2\omega_0}}{g_J\mu_B}. \tag{4.24}$$

Therefore the ion can be placed in a maximum B-field of 0.007 T (70 gauss) while maintaining efficient Doppler cooling without additional sidebands. This corresponds to a maximum B-field gradient of $60 \pm 2\,\mathrm{T/m}$ using the magnet configuration designed, where the uncertainty refers to the uncertainty within the simulation.

4.11.4 Mechanical magnet translation stage

There are several sources of errors that can result in the simulated fields being inaccurate. One potential source of errors originates from the fabrication of the two Samarium Cobalt magnets. Fabrication errors for the magnet dimensions given in section 4.11.2 are approximately $\pm 50\,\mu$m. To determine the error on the magnetic field gradient, the magnets were resimulated using CST, firstly with all dimensions greater by $50\,\mu$m, and then with all dimensions smaller by $50\,\mu$m. The error in gradient across all three axes are $\Delta\delta_x B = (+1.2/-0.8)\,\mathrm{T/m}$, $\Delta\delta_y B = (+2.7/-1.5)\,\mathrm{T/m}$ and $\Delta\delta_z B = (+1.1/-0.7)\,\mathrm{T/m}$.

Another source of error originates from the accuracy of mounting the magnets in relation to the chip. This error incorporates several factors such as; the mounting structures fabrication error, the error in attaching the magnet to its exact position and the error in mounting the chip to its exact position. An estimate of $250\,\mu$m is assumed for a combination of these errors. Similarly to the fabrication errors, the offset of $250\,\mu$m was simulated in all three axes. The error in gradient across all axes are $\Delta\delta_x B = (+2.4/-1.6)\,\mathrm{T/m}$, $\Delta\delta_y B = (+4.2/-2.7)\,\mathrm{T/m}$and $\Delta\delta_z B = (+2.2/-1.5)\,\mathrm{T/m}$.

As well as these errors the magnet configuration becomes problematic when using different ion trapping architectures. Architectures such as rings and junctions discussed in

3 may not be suitable for these magnets as the magnetic field nil will not be located at a trapping region. Conversely, utilizing all potential trapping regions within a single trap can also be difficult if only a certain area is useable due to the magnetic field nil. To overcome this issue a mounting structure which can vary the magnets position and angle was developed.

Construction

A magnet mount was designed and developed that could be attached to the chip mounting structure described in section 4.7. The magnet mount consists of three variable linear stages, a rotational stage and a clamping stage to hold the magnets. Each linear XYZ stage can be adjusted by individual fine pitch captivated bolts allowing for a movement of ± 5 mm in all three axes. The rotational component can be adjusted by $\pm 10^{\circ}$ by loosening and fastening a bolt located on the underside of the mounting setup. The mounting structure and bolts are made entirely from non-magnetic Aluminium.

Figure 4.54 shows the actual magnet mounts attached to the chip mount with proxy magnets. Figure 4.53a shows a rendering of the magnet mount attached to the trap mount while figure 4.53b highlights the individual sections of the mount. A future iteration for the mounting structure can directly replace the captivated bolts with piezo actuators. This can allow the magnets to be varied remotely without opening the vacuum system.

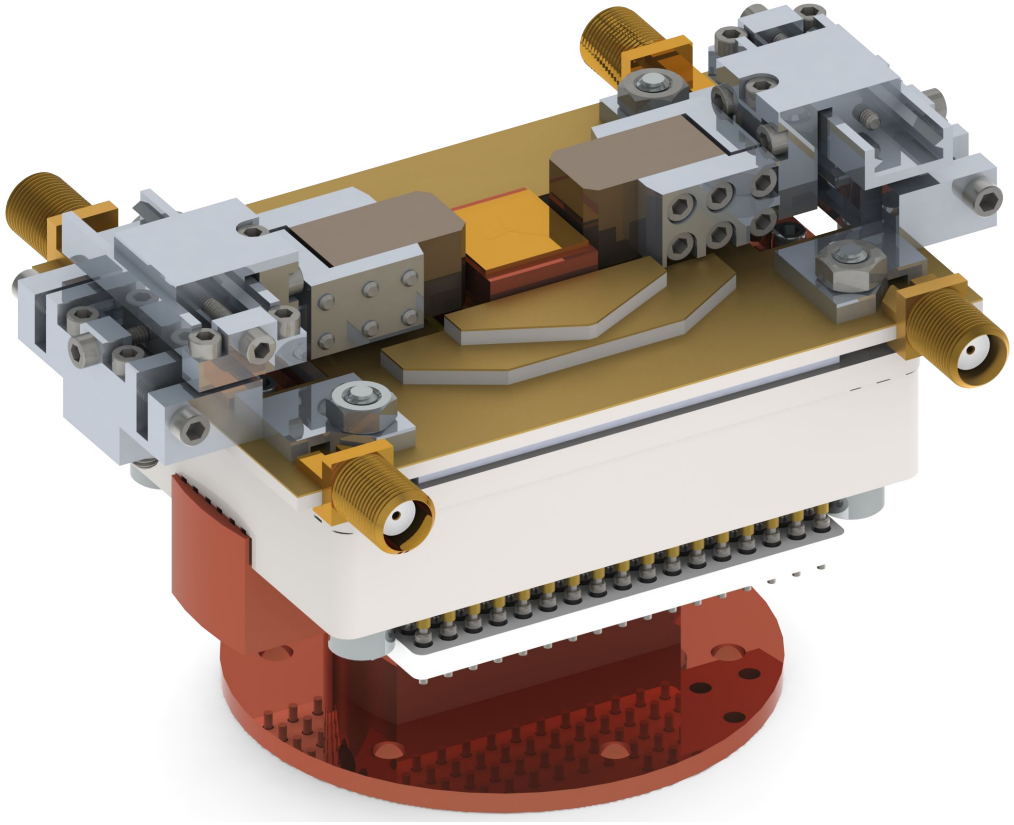

(a)

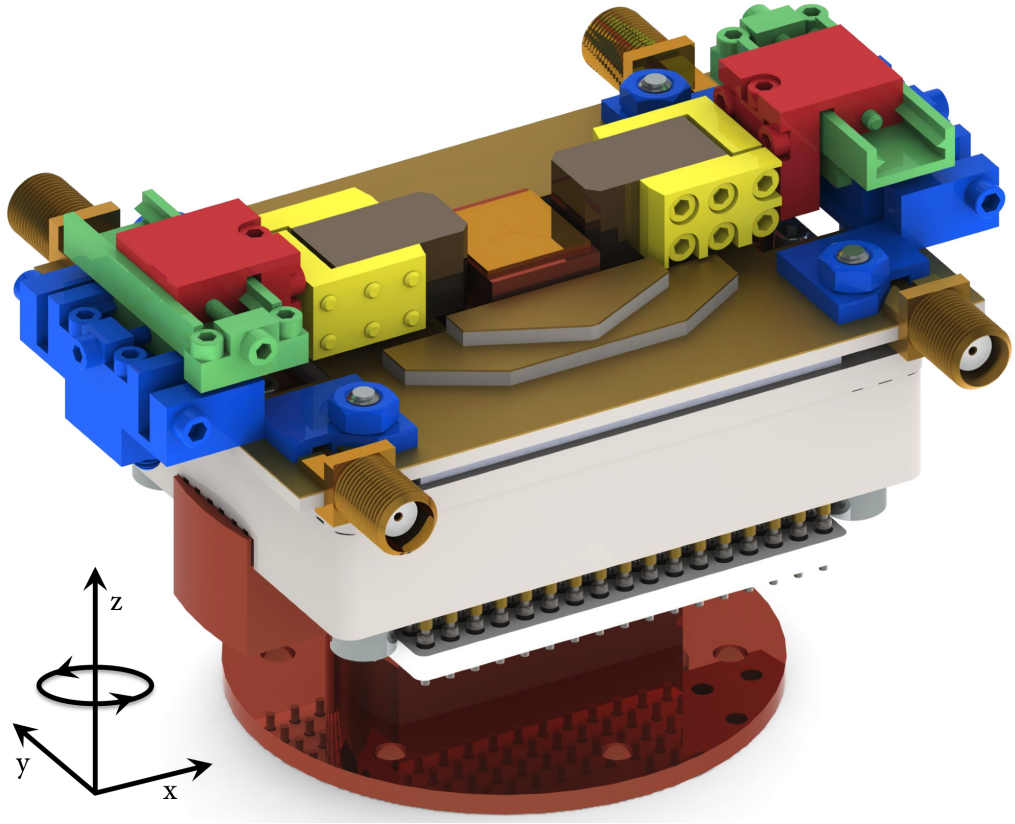

(b)

Figure 4.53: (a) Magnet mount and magnets attached to the chip mount. (b) Highlights the separate translation stage regions including x-axis and rotation (blue), y-axis (green), z-axis (red) and magnet clamp (yellow). Note that the blue stage provides linear movement and rotation in different axes.

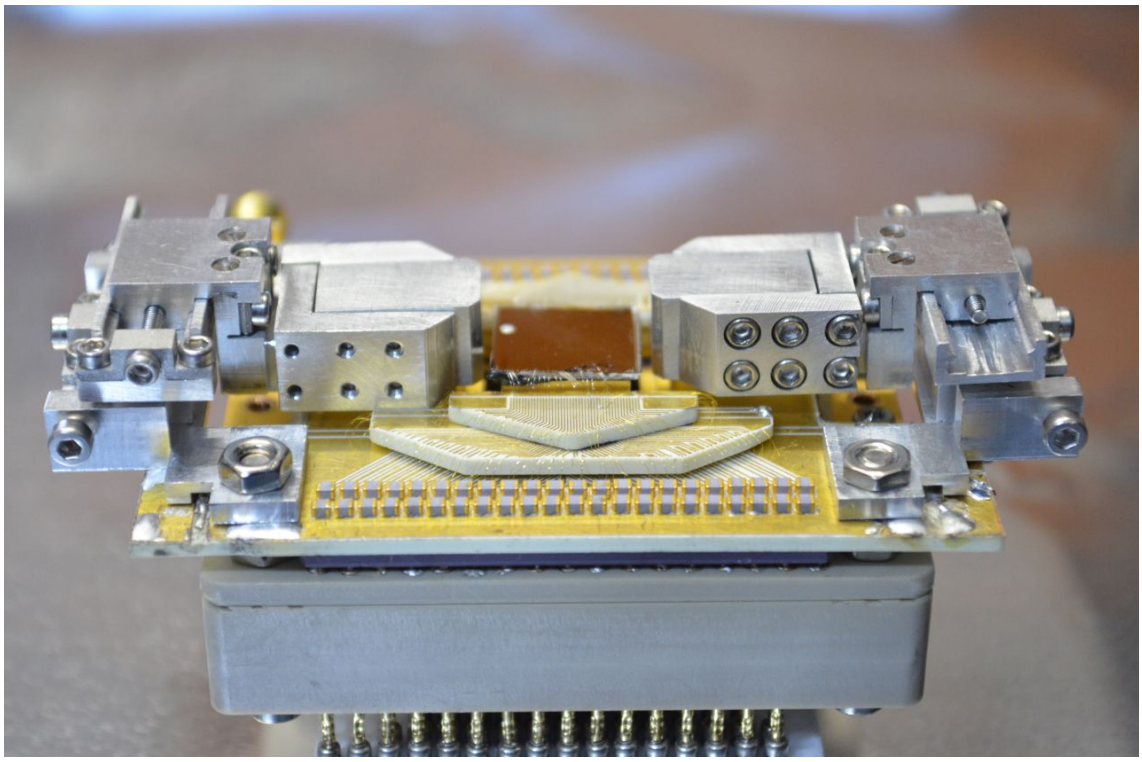

Figure 4.54: Final magnet mounts attached to the chip mount with proxy magnets

4.12 Cryostat operation & cooling results

This section describes the operational procedures for the cryogenic vacuum system. Figure 4.55 shows a surface ion trap mounted within the vacuum chamber along with the ancillary technology discussed in this chapter. Figure 4.56 shows the system with the first (4 K) radiation shield fully closed. Once both radiation shields are fully attached and the chamber is closed, the cool down procedure can begin.

4.12.1 Cool down procedure

The following procedure describes the individual steps and considerations required to cool the experiment to the cryogenic base temperature.

1. The vacuum system should first be evacuated to 10^{-6} mbar using a TMP.

2. Ideally the ion pump should be turned on and allowed to settle at a stable pressure. This pressure may vary depending on the contents of the chamber. Some materials that are not UHV compatible at room temperature (e.g. PbSn solder) can lead to the pressure not dropping below $10^{-6} - 10^{-7}$ mbar. In some cases the load may be too great for the ion pump, in which case it is still safe to proceed given that the system is below 10^{-6} mbar.

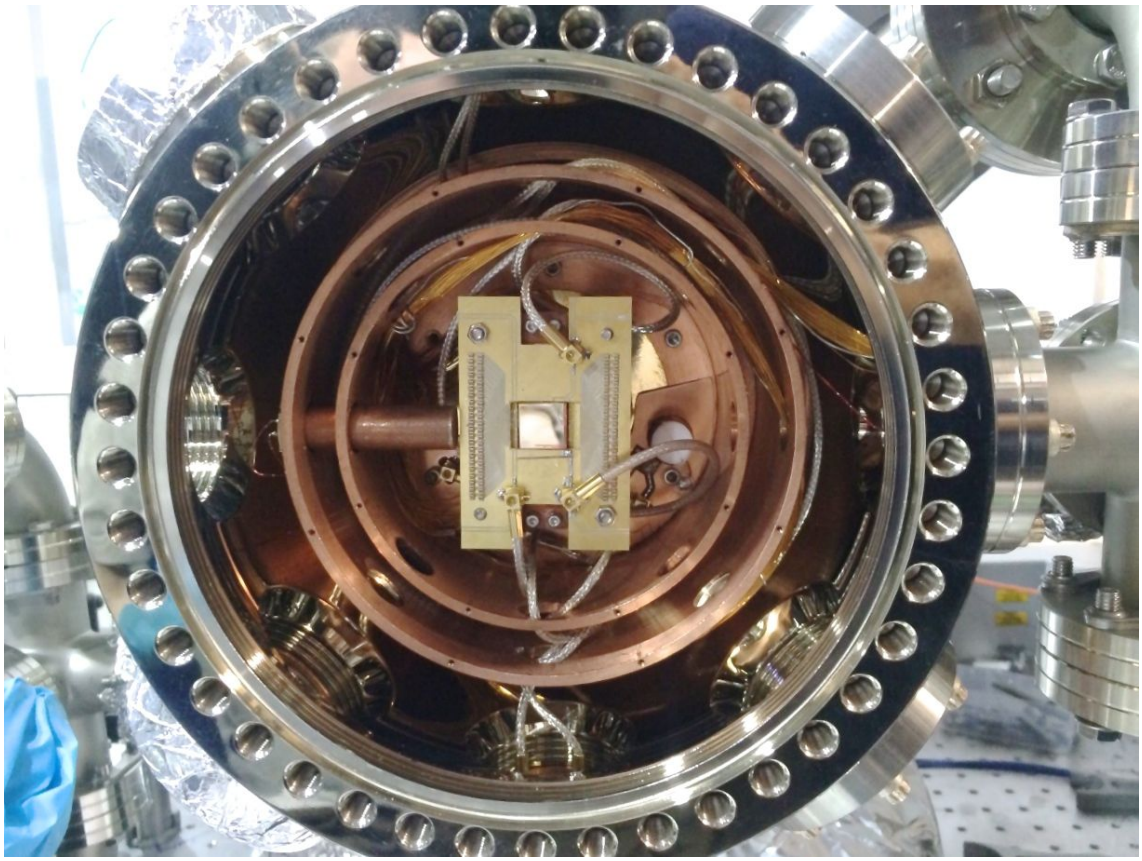

Figure 4.55: The central chamber within the cryogenic vacuum system.

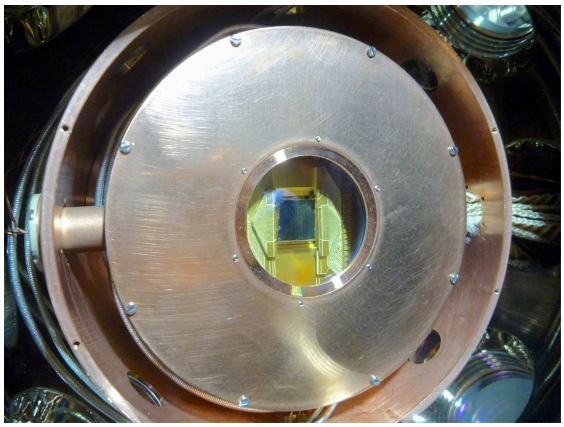

(a)

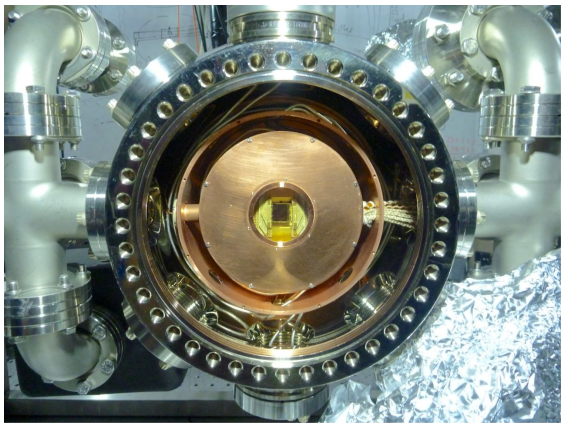

(b)

Figure 4.56: The central chamber of the cryogenic vacuum system with the 4 K radiation shield completely closed.

3. The interior of the low vibration interface should be flushed with CP grade helium. This can be performed by opening the valve on the helium supply cylinder to 1 psi. Allow the bellows to inflate and then gently dislodge the cap on the overpressure valve to deflate the bellows. Repeat the process 20 times to ensure the interface is primarily filled with helium and then maintain the pressure at 0.5 psi.

4. The ring heater attached to the interface skirt should be turned on. This prevents the risk of condensation forming on the vacuum skirt during operation.

5. A final check should be made that the supply and return pipes from the compressor are connected to the correct ports on the cryocooler head.

6. The water cooling supply to the compressor should be turned on by opening the mains release valve to the compressor.

7. The compressor can now by turned on (assuming its already connected to a 3 phase power supply) at the main control panel interface of the compressor.

8. If the ion pump was not turned on before the cooler was started, it should be reactivated once the system drops below 273 K. If the pump fails to start, the process should be repeated after the system cools down a further 10-20 K. Once the ion pump can maintain a stable pressure at 10^{-7} mbar, the right angle valve on the vacuum chamber can be closed to disconnect the TMP.

9. Figure 4.57 shows that the cooling cycle will take approximately 160 minutes to reach its final base temperature.

10. During cool down a critical step is to maintain the helium buffer gas pressure at 0.5 psi within the interface. During the majority of the process the variation in pressure is negligible, however, during the last 50 K there is a significant decrease in pressure. This can lead to the bellows deflating and even being drawn inwards into contact with the interface. This sudden change in pressure is due to the rapid condensation of helium gas across this final temperature range. It is therefore important to gradually adjust the pressure to compensate for this change in pressure.

If the heat load within the system is low enough to achieve a base temperature of 4.2 K, the helium buffer gas will begin to condense into liquid. Figure 4.58 shows that after $\sim$ 30 minutes at 4.2 K, a sufficient amount of liquid helium has formed to bridge the gap

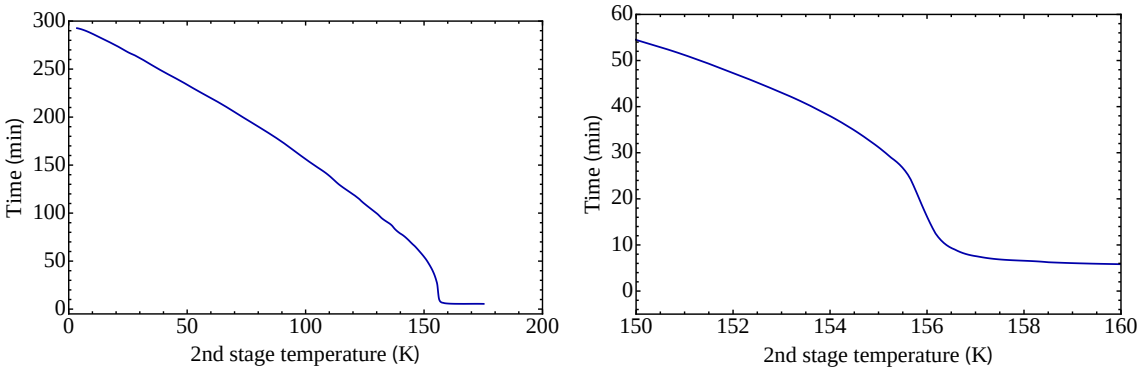

(a) (b)

Figure 4.57: Both (a) and (b) show the temperature of the sample stage after the cooler has been turned on.

between the cryocooler and interface heat exchangers. The liquid helium provides a more efficient method of heat transfer than the buffer gas and the temperature begins to drop further. When the cooler is eventually turned off after ~ 60 minutes below 4.2 K, the liquid bridge is removed and the cold stage maintains a temperature of 4.2 K for a further 30 minutes (unlike figure 4.57). This effect is due to the remaining liquid helium cooling the cold stage independently while slowly evaporating. This offers the possibility of turning off the cryocooler to remove any magnetic and spatial fluctuations while still maintaining a constant temperature at 4.2 K for a short period of time.

4.12.2 Warm up procedure

The warm up procedure is simpler than the cool down procedure, however, certain precautions should be taken to avoid damage to equipment.

1. The cooler can be turned off at the main control panel interface on the compressor.

2. The water cooling supply to the compressor should be turned off by closing the mains release valve to the compressor.

3. The condensed buffer gas helium within the interface will begin to rapidly evaporate and expand. The over pressure valve will safely eject the helium and the valve itself can be gently dislodged by hand to accelerate this process if required.

4. Some cryosorbed material will also begin to rapidly expand during the initial warming up phase (4-20 K). This can lead to a rapid pressure spike (10^{-10} mbar to 10^{-6} mbar) within the first $\sim$5 minutes of the cooler being turned off. As a safety

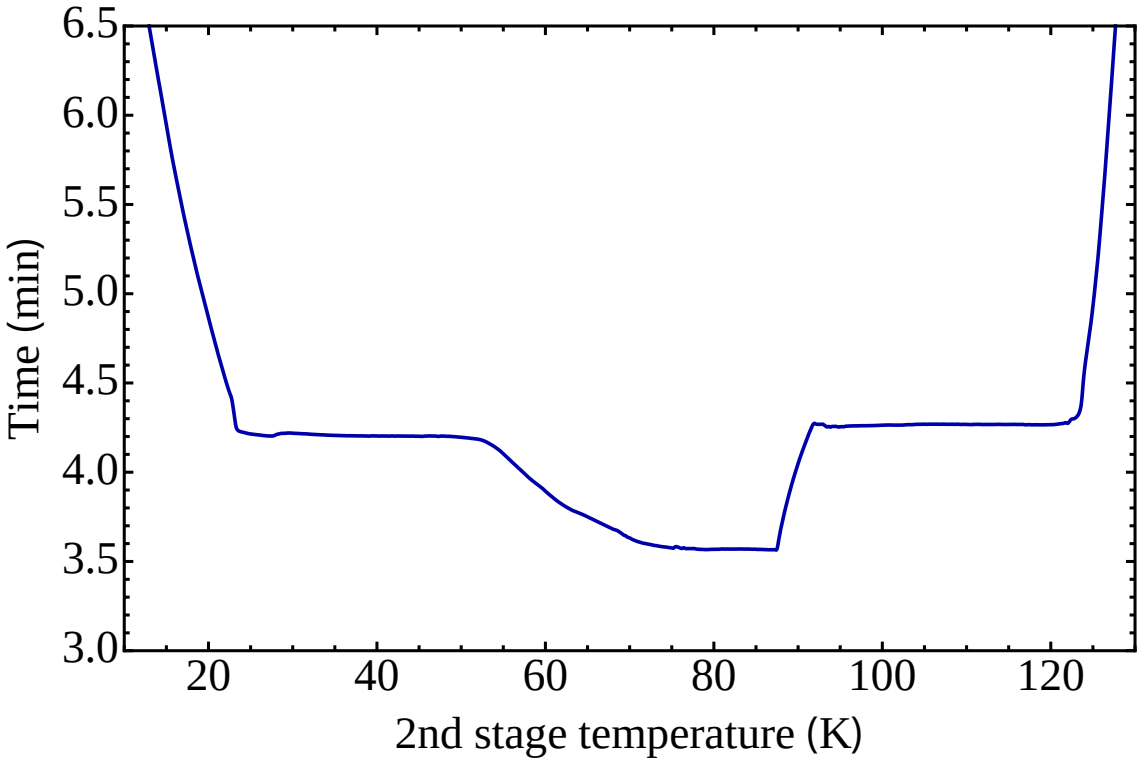

Figure 4.58: At a base temperature of 4.2 K liquid helium will begin to condense and after 30 min it will bridge the gap between the cooler and interface heat exchangers. Turning the cooler off results in the liquid evaporating but maintaining 4.2 K for a period of time.

precaution it is recommended that the pressure is carefully observed so that the ion pump and ion gauge can both be prematurely turned off to prevent damage.

5. Once the pressure drops to 10^{-6} mbar the right angle valve can be reopened to the TMP.

6. Once the temperature has passed 273 K, the ring heater attached to the interface skirt can be switched off.

7. The natural warm up cycle will take $\sim$ 30 hours to reach room temperature. The warm up time can be accelerated by using the two 25 W heaters within the system. It is important to wait until the system achieves a stable room temperature reading before opening the system. Opening the system even 10°C below room temperature can lead to condensation forming within the vacuum chamber.

Application of cryopumping for UHV

During the cool down of the system, the effects of cryopumping can be observed immediately. As the temperature reduces the background pressure will also fall and begin to

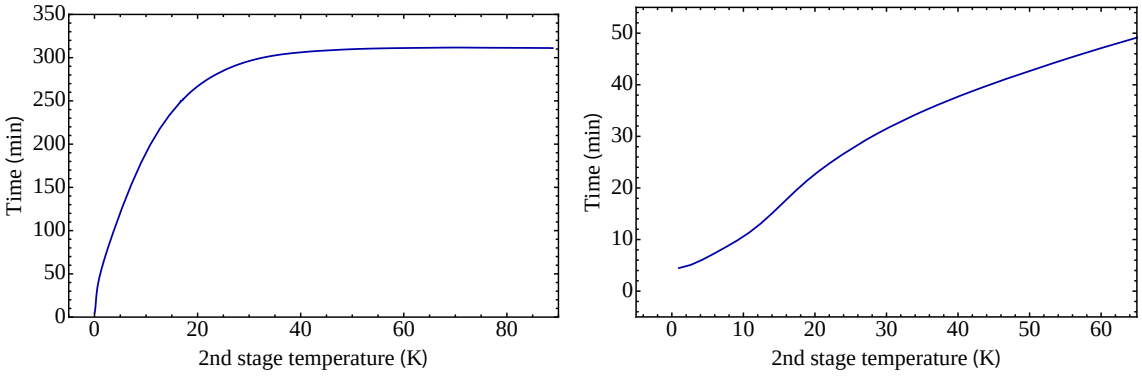

(a) (b)

Figure 4.59: Both (a) and (b) show the temperature of the sample stage after the cooler has been turned off.

plateau shortly after reaching the base temperatures (figure 4.60). The pressure of the system will eventually stop decreasing once an equilibrium vapour pressure is reached. At this state the number of gas molecules moving to a solid phase (condensing) becomes equal to the number of energetic particles returning to a gaseous phase (vaporising). Figure 4.60 shows the pressure drop four orders of magnitude from 10^{-6} mbar to 10^{-10} mbar with a drop in temperature from 300 K to 5 K. It should be noted that this pressure measurement comes from outside of both radiation shields and will therefore be higher than inside the 4 K radiation shield.

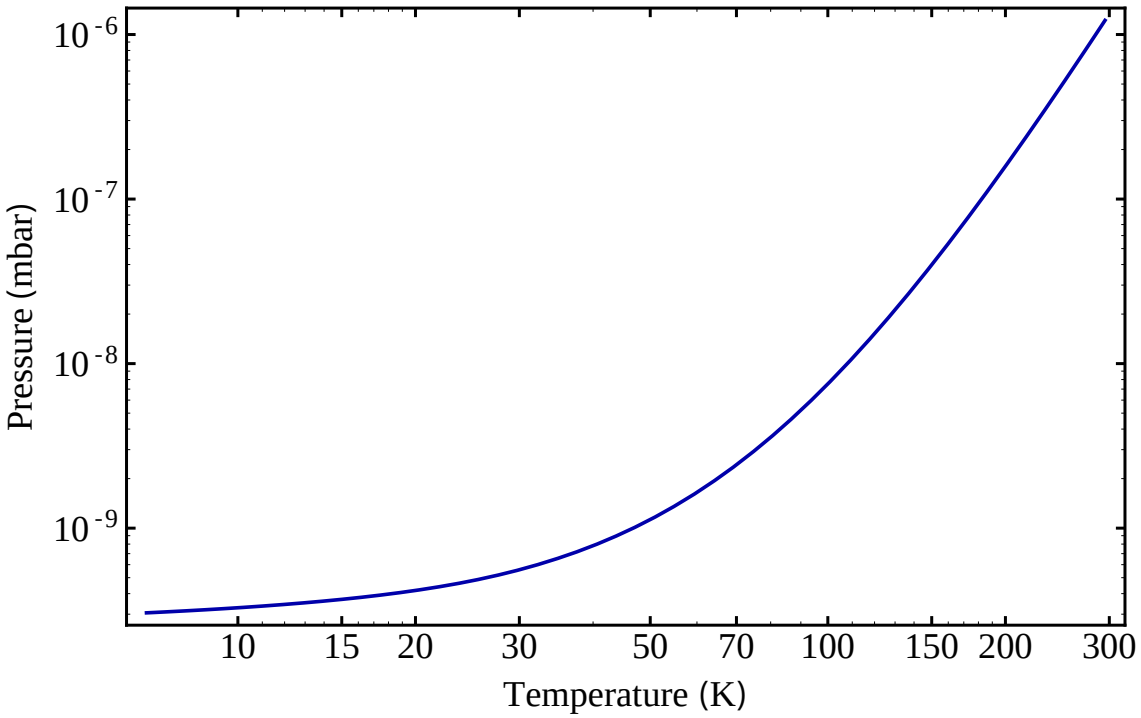

Figure 4.60: The effects of cryopumping decrease the pressure of the system from 10^{-6} mbar to 10^{-10} mbar with a drop in temperature from 300 K to 5 K.

Chapter 5

Surface electrode ion traps

Surface ion traps, also known as asymmetric ion traps, possess architectures where all electrodes lie within a single plane (section 2). This offers the possibility to create more complex and versatile ion trap designs, as well as the opportunity to microfabricate structures on the micron scale (section 6) to produce a truly scalable quantum computer. This chapter presents two novel surface ion trap designs and discusses features specifically incorporated for technology development towards quantum hybrid system with superconducting qubits.

The first design presented is an ion trap capable of shuttling ions vertically between two separate ion heights (section 5.1), with an integrated high quality factor (Q) microwave resonator (section 5.2). The second design presented is flat multipole ion trap with multiple uniform linear trapping regions (section 5.3). The motivation for each trap design and electrode optimization process using numerical methods described in section 2.2 is given. The final mask design fabricated at the Southampton Nanofabrication Centre is given in appendix A.

5.1 Vertical shuttling ion trap

5.1.1 Motivation

A stronger coupling between an ion and a microwave resonator can be produced by confining the ion closer to the resonator. The larger magnetic field strength formed from the resonator results in a stronger interaction with the ion's nuclear magnetic moment. Experimentally this can be difficult to achieve, with a primary reason being the need to use lasers to perform Doppler cooling on the trapped ions. Laser manipulation of trapped ions typically requires the ion not to be too close to a surface of the trap in order to

minimize any laser scatter from the surface to achieve high detection fidelities. However, the use of lasers with a strong ion-resonator coupling can be reconciled if the ion can be shuttled from a relatively high ion height to a location close to the waveguide resonator. This allows the ion to be laser cooled and trapped at a high ion height, shuttled to a low ion height for interaction with the resonator, and then shuttled back to a high ion height for readout and cooling.

5.1.2 Trap design

The key features required for the design of the trap are vertical ion shuttling capabilities and an integrated high quality factor microwave resonator. We can begin by first considering how the ion height can be varied across a trap. For asymmetric quadrupole ion traps, the rf nil produced by a pondermotive dop is a function of the rf and ground electrode geometries. The rf nil, and therefore the ion height (h), can be given as [169]

$$h = \frac{\sqrt{abc(a+b+c)}}{(b+c)} \tag{5.1}$$

where a is the separation between rf electrodes, and b and c are the widths of each rf electrode. For a general case, larger electrode widths generate a higher ion height and smaller widths give rise to a rf nil closer to the trap surface. However, the key geometry in determining the ion height is the separation of electrodes as it is inherently the dominant factor in equation 5.1. Nizamani *et al.* have shown for a given rf electrode separation, there exists an optimum rf electrode width to maximise the trap depth (Ξ), where Ξ is given by [169]

$$\Xi = \frac{e^3 V_{rf}^2}{\pi^2 m \Omega_{rf}^2 h^2} \kappa \tag{5.2}$$

where e is the charge of an electron, V_{rf} is the peak to peak rf voltage, m is the mass of the ion, Ω_{rf} is the frequency of the rf voltage and κ is a geometric factor given by

$$\kappa = \frac{\sqrt{abc\,(a+b+c)}}{(a+b+c)} \times \left(2\left(a+b+c+2\sqrt{a\,(a+b+c)}\right)\right)^2. \tag{5.3}$$

When both rf electrodes have equal width ($b = c$), the optimum ratio is given by $\zeta = b/a = 3.68$. Therefore, by following equations 5.1 - 5.3, an optimal rf electrode geometry (a, b, c) can be analytically calculated for a given ion height (figure 5.1).

Another design consideration that must be taken into account is the principal axes of the trapped ion. For complete laser cooling of the ion in all three axes, the laser wave

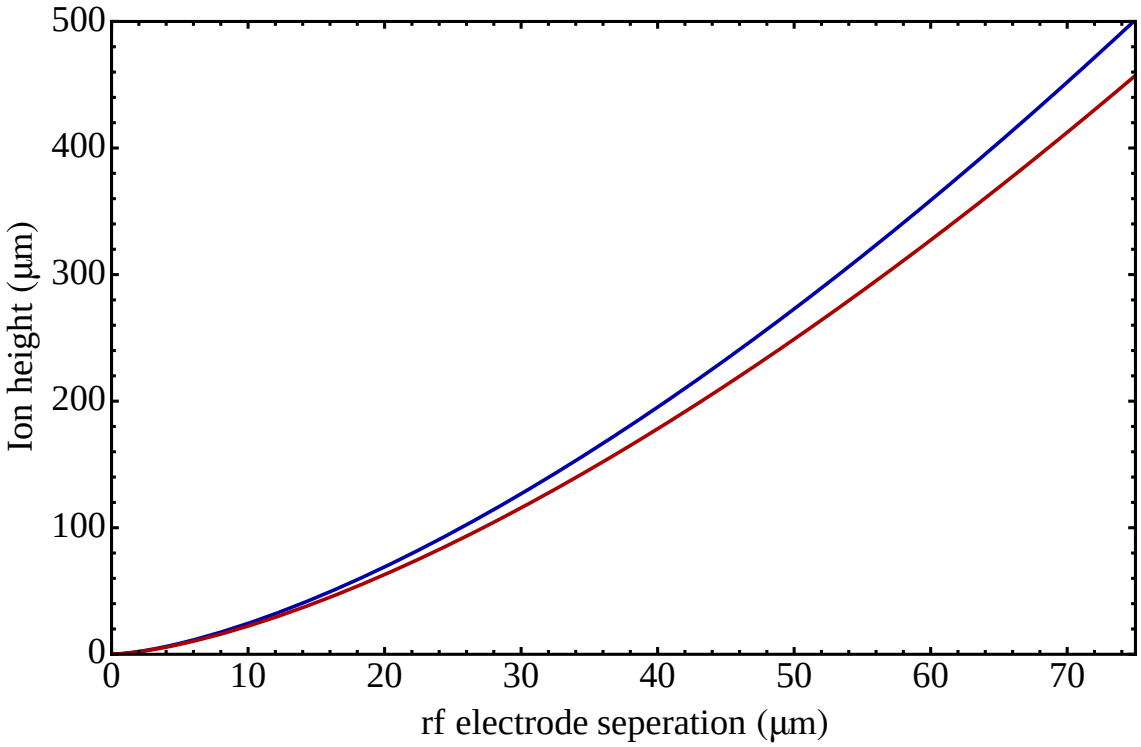

Figure 5.1: Ion height as a function of rf electrode separation for equal rf electrode widths ($b = c$) with $\zeta = b/a = 3.68$ (blue) and for unequal widths ($b \neq c$) with $\zeta = b/a = 4.90$ (red).

vector k must have a component along all three principal axes (section 2.3.1). This can be achieved by making the rf electrodes with differing widths such that $b \neq c$. For $c = b/2$, the optimum ratio of rf electrode separation is given by $\zeta = b/a = 4.90$ [169]. Figure 5.2 shows the effect of asymmetric rf electrodes on the rotation of the principal axes.

For a linear ion trap, a varying ion height can be created by forming a tapering electrode structure (figure 5.3), where $c = b/2$ and $\zeta = b/a = 4.90$ for all points. As the ion is shuttled along the axial direction, the ion height will also change. This allows for the ion height to be varied across the ion trap. However, a continuously tapering electrode structure would not be desirable for several reasons. For Doppler cooling with a fixed beam position, only a small region could be addressed. Similarly, for resonator interaction, ions at different heights would possess different interaction strengths with the resonator. A constant variation in ion height along the axial direction of the trap would also result in a continuous rf potential barrier. This barrier is the increase in the potential of the rf minimum due to the varying electrode geometry, which can result in uncompensatable micromotion for the ion.

The tapering structure for the vertical shuttling region therefore provides minimal benefit, except for varying the height of the ion. Ideally, the region used for vertical shuttling

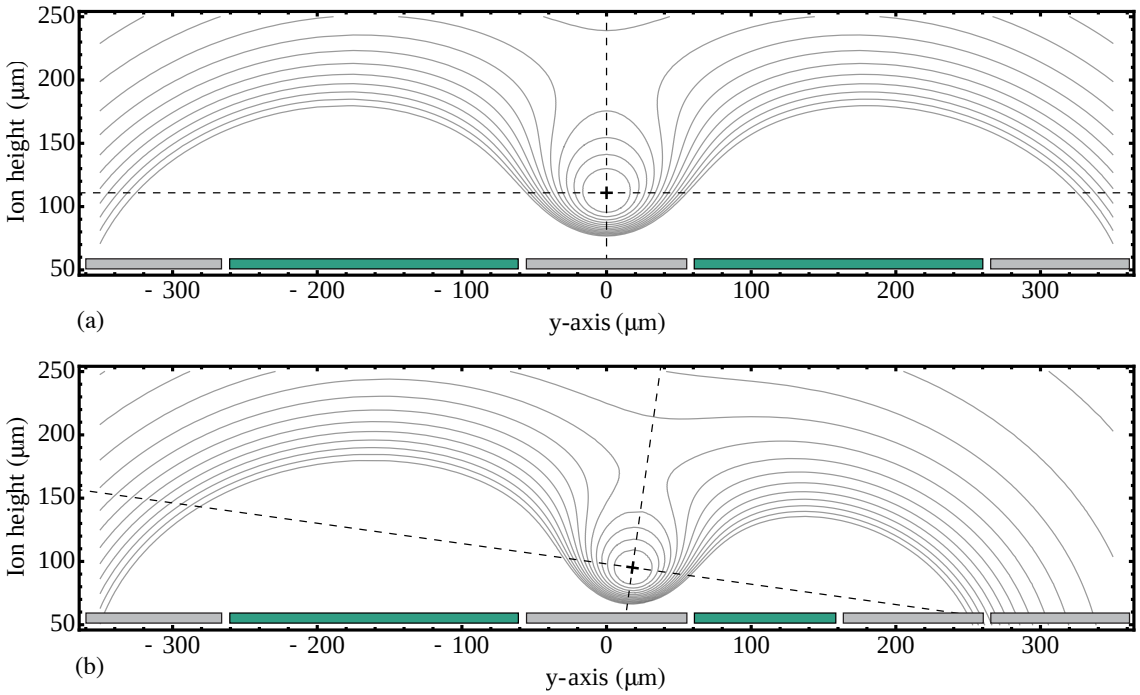

Figure 5.2: (a) An unrotated principle axes where the rf electrode widths are equal ($c = b$), and (b) a rotated principle axes where the rf electrode widths are unequal ($c = b/2$) [29].

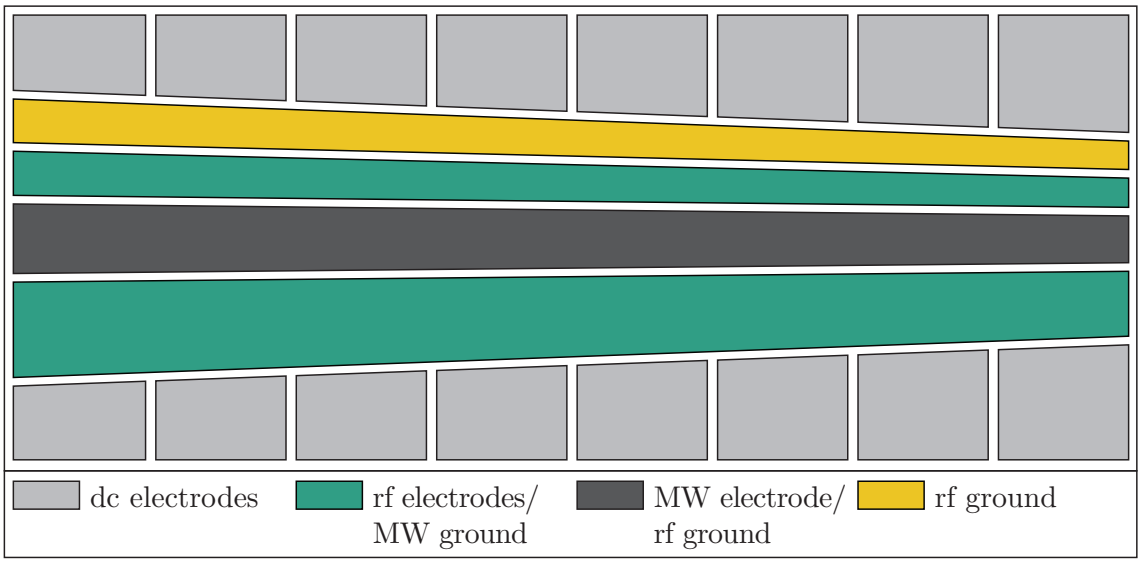

Figure 5.3: Ion trap geometry with continuously tapering linear electrodes for vertical shuttling, where the rf and MW electrodes are far off resonance with each other and can serve as the others ground.

should be kept to a minimum to allow for trap geometries which contain several distinct linear electrode structure regions on a single chip. These regions can then be connected via vertical shuttling regions. To maximize the regions with constant ion height, only a single vertical shuttling region was chosen.

From equation 5.2 we can see that varying the ion height will also vary the trap depth. Therefore, to maintain a sufficient trap depth at different ion heights, a sufficient V_{rf} and Ω_{rf} must also be applied. However, variation of V_{rf} and Ω_{rf} will also affect stability parameters for the periodic motion of the ion, a and q, given in equation 2.8. Therefore, for simplicity, a fixed V_{rf} and Ω_{rf} that would be suitable for all ion heights was chosen for simulations. The maximum achievable variation in ion heights will therefore be limited by the constraints of stable a and q parameters. It should be noted that a fixed V_{rf} and Ω_{rf} are not necessarily required. Shuttling protocols can be calculated to shuttle the ion between arbitrary ion heights while varying V_{rf} to maintain stable trapping parameters. However, in section 5.1.3 it will be shown that sufficient variations in ion height can be achieved for a constant V_{rf} and Ω_{rf}.

5.1.3 Trap simulation

To determine the parameters of a given ion trap, such as its trap depth, secular frequency and ion height; accurate simulations of the electric potentials from each electrode need to be produced. This was performed as described in section 2.2 by first performing preliminary analytical calculations using a gapless plane approximation and then using a boundary element method for numerical simulations. An ion height of 30 μm was chosen for the low ion height region. This was made as a compromise between a sufficiently low ion height and increasing heating rates, scaling as $1/d^{-4}$ as described in section 4.1.2. Microfabrication techniques, as described in chapter 6, also become limited as the rf electrode separation drops below $\sim$20 μm (required for ion heights below $\sim$30 μm) and approach microfabrication errors of $\sim$2 μm.

For an ion height at 30 μm, initial analytical calculations determined the separation for the two rf electrodes to be 22.0 μm with widths of 54 μm, and 109 μm. More accurate numerical simulations reveal the ion height produced to be lower than anticipated and a separation of 24.5 μm and rf electrode widths of 60 μm and 120 μm are required to produce an ion height of 30 μm (figure 5.4). At this ion height a V_{rf} of 50 V at $\Omega_{rf}/2\pi = 10$ MHz can be applied to produce a trap depth of 0.1 eV, which is sufficient to confine an ion originating from an ohmically heated oven. This gives secular frequencies of $\omega_{y,z}/2\pi \approx 4.9$ MHz in

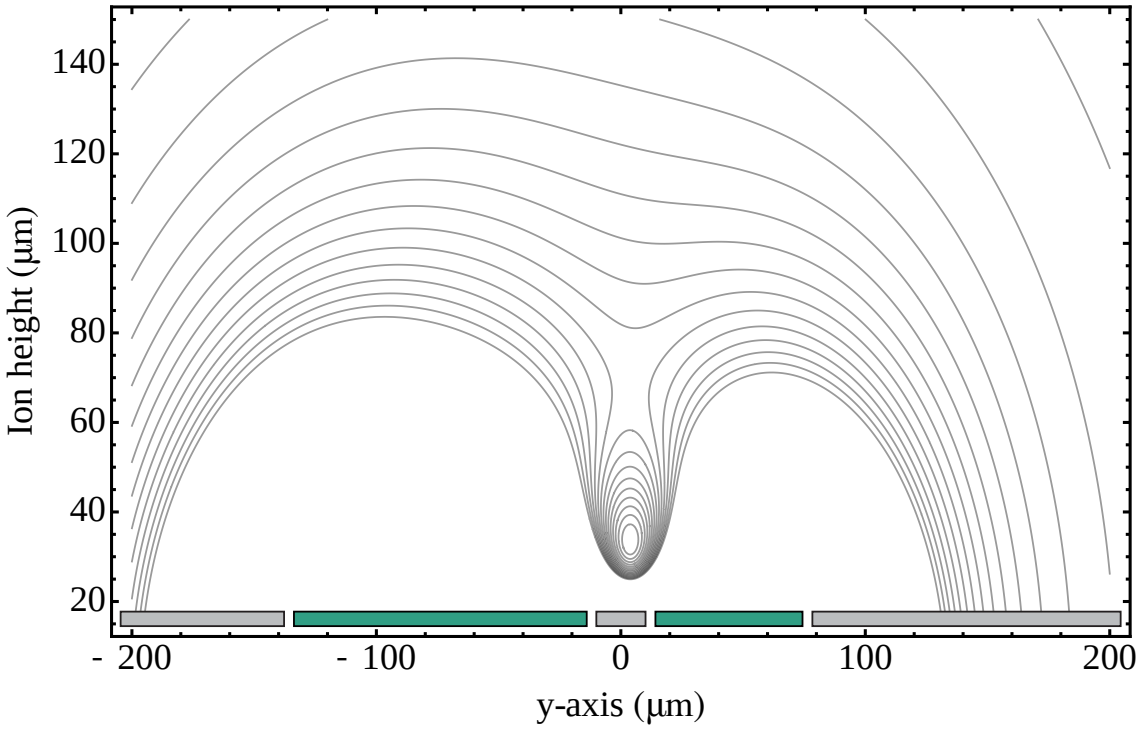

Figure 5.4: Pseudopotential for the low ion height region with an ion height of 30.0 μm. The potential is calculated numerically with an rf electrode separation of 24.5 μm and rf electrode widths of 60 μm and 120 μm.

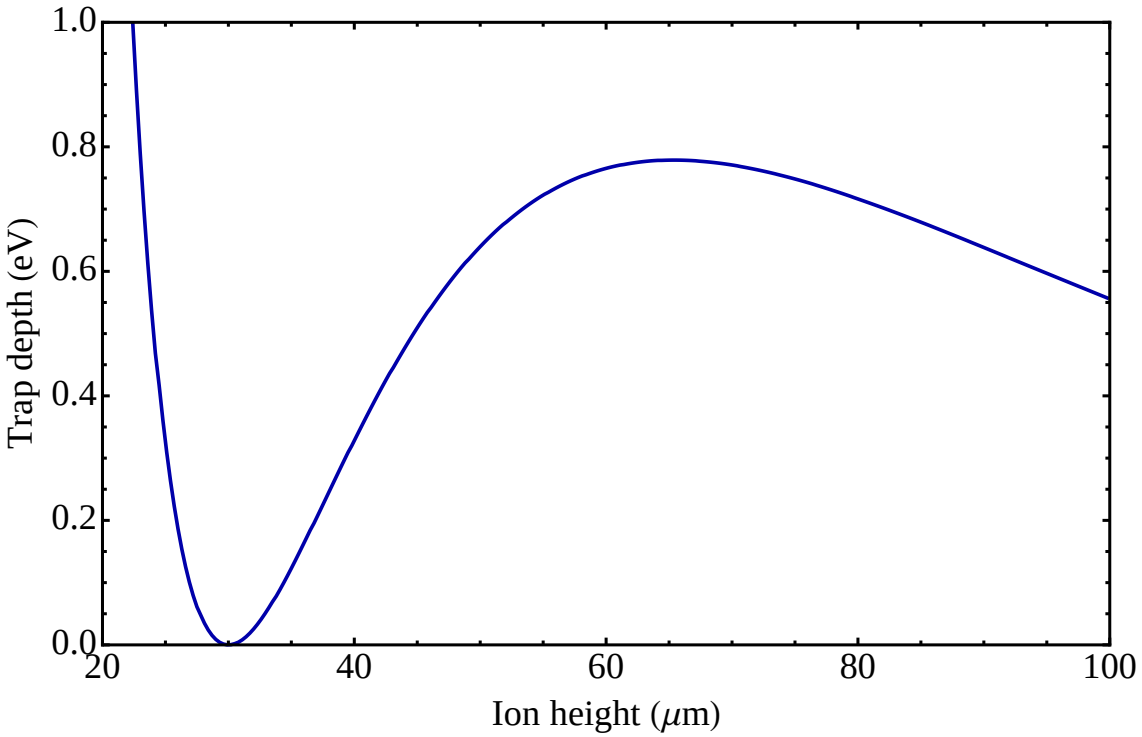

Figure 5.5: Variation in trap depth at the low ion height region for $\Omega_{rf}/2\pi = 10\,\text{MHz}$ and $V_{rf} = 150\,\text{V}$. The linear data segments are taken in the z-axis at an offset of approximately 4 μm in the y-axis. A trap depth of $\sim 0.80\,\text{eV}$ is produced for 150 V.

the radial directions, $\omega_x/2\pi \approx 0.27\,\text{kHz}$ in the axial direction and a stability parameter of $q = 0.22$.

To create a sufficient trap depth at a higher ion height, a higher V_{rf} is required. This will also lead to a higher stability parameter q and therefore it will places a limit on the maximum V_{rf} that can be applied while still maintaining stable parameters. An upper limit of $q \approx 0.7$ was used to determine the maximum V_{rf} that could be applied, as this is well inside the stability region shown in figure 2.5 in chapter 2.1.

As q scales as h^{-2}, where h is the ion height, q will be greatest at the low ion height region. For the low ion height electrode geometries given, this allows for a maximum V_{rf} of 150 V for $\Omega_{rf}/2\pi = 10\,\text{MHz}$. This produces a trap depth of 0.8 eV (figure 5.5). Through the same iterative combination of analytical and numerical simulations, the high ion height region of the trap was then calculated. This was done by assuming that the given parameters need to produce a minimum trap depth of 0.1 eV. For $V_{rf} = 150\,\text{V}$ and $\Omega_{rf}/2\pi = 10\,\text{MHz}$, an ion height of 85 μm which maintains a 0.1 eV trap depth can be achieved (figure 5.6). This requires an rf electrode separation of 64.5 μm and electrode widths of 170 μm and 340 μm. This gives trapping parameters of $\omega_{y,z}/2\pi \approx 2.1\,\text{MHz}$, $\omega_x/2\pi \approx 2.48\,\text{kHz}$ and $q = 0.10$.

Shuttling between the two regions can then be performed by connecting the regions via a tapering electrode structure. For linear regions, this can be done with minimal motional heating of the ion [12, 170]. For the vertical shuttling region, the variation in electrode geometry and pseudopotential along the axial direction results in a non-zero potential minimum across the region resulting in an rf barrier. Careful consideration must therefore be taken when designing this region as in some cases the barrier potential could become high enough for the ion to lose sufficient trap depth and be lost from the system. It has also been shown that motional heating of the ion is related to the slope of the pseudopotential [58, 171] . The rf barrier must therefore be minimized across this region allowing for minimal motional heating from one ion height to the other.

Through an iterative process of vertical shuttling region designs that varied the length and shape of the region, an rf barrier of $\sim$3 meV was achieved for a shuttling region of 1 mm in length (figure 5.8). It was found that a sinusoidal transition region (figure 5.9) produced the minimum rf barrier by allowing for a gradual variation in trap electrodes. A length of 1 mm was chosen as it was a relatively small region with respect to the chip size (12 mm $\times$ 12 mm) and was capable of producing a barrier height $\sim$3 orders of magnitude lower than our trap depth of 0.1-0.8 eV. A plot of the pseudopotential of the vertical

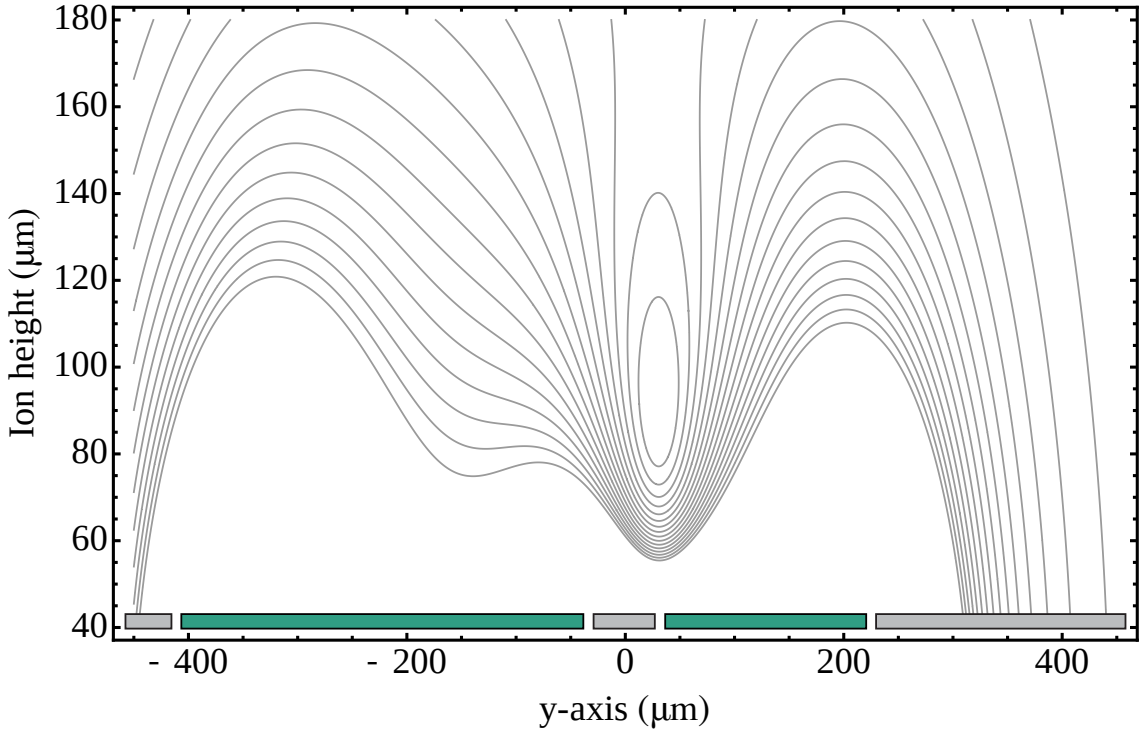

Figure 5.6: Pseudopotential for the high ion height region with an ion height of 85.5 μm. The potential is calculated numerically with the rf electrode separation of 64.5 μm and rf electrode widths of 170 μm and 340 μm.

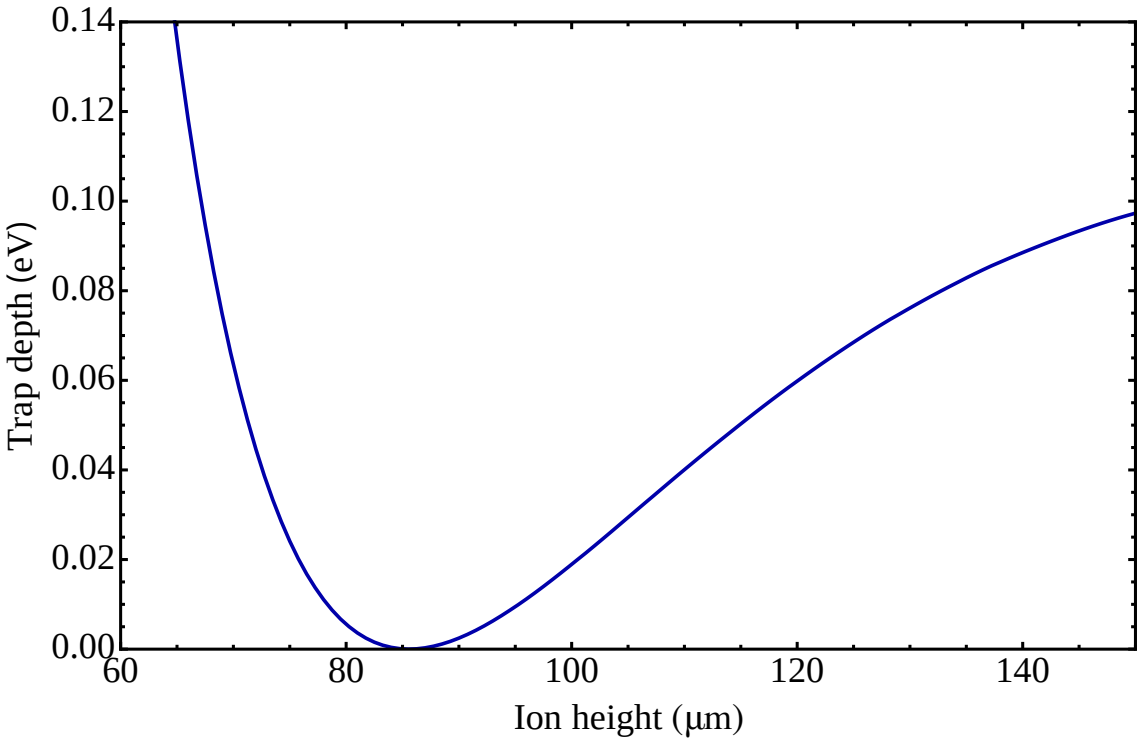

Figure 5.7: Trap depth at the high ion height region for $V_{rf} = 150\,\mathrm{V}$ and $\Omega_{rf}/2\pi = 10\,\mathrm{MHz}$. The linear data segment is taken in the z-axis at an offset of approximately 18 μm in the y-axis. A trap depth of $\sim 0.10\,\mathrm{eV}$ is produced using the given parameters.

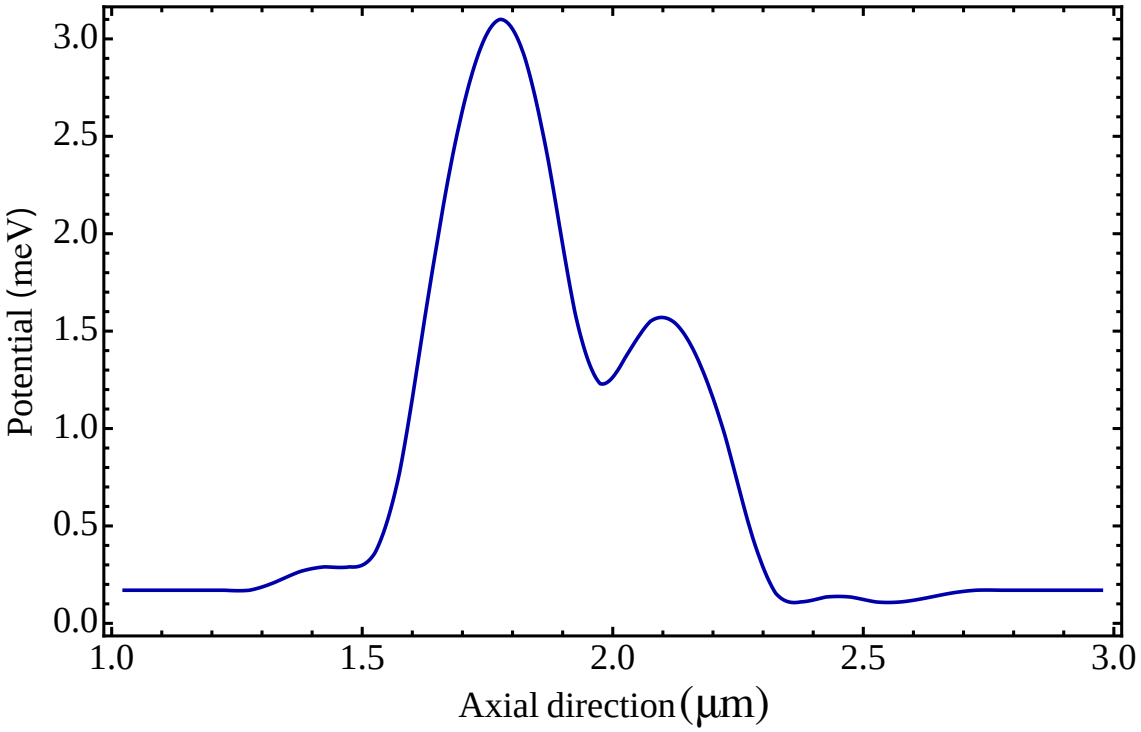

Figure 5.8: rf potential barrier along the axial direction of the vertical shuttling region. A double peak is observed at 3.0 meV and 1.5 meV which corresponds to the rate of change of the change in ion height.

shuttling region in the axial direction can be seen in figure 5.10. From this we can see more clearly the two distinct constant height regions and the connecting vertical shuttling region.

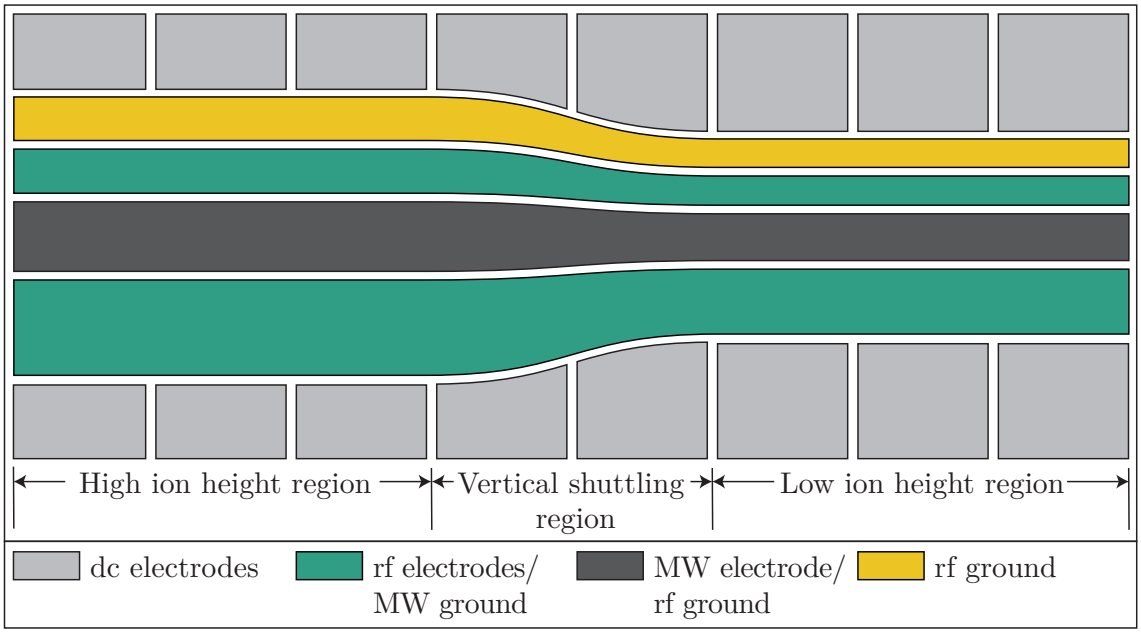

Figure 5.9: Trap geometry for a linear ion trap with a vertical shuttling region.

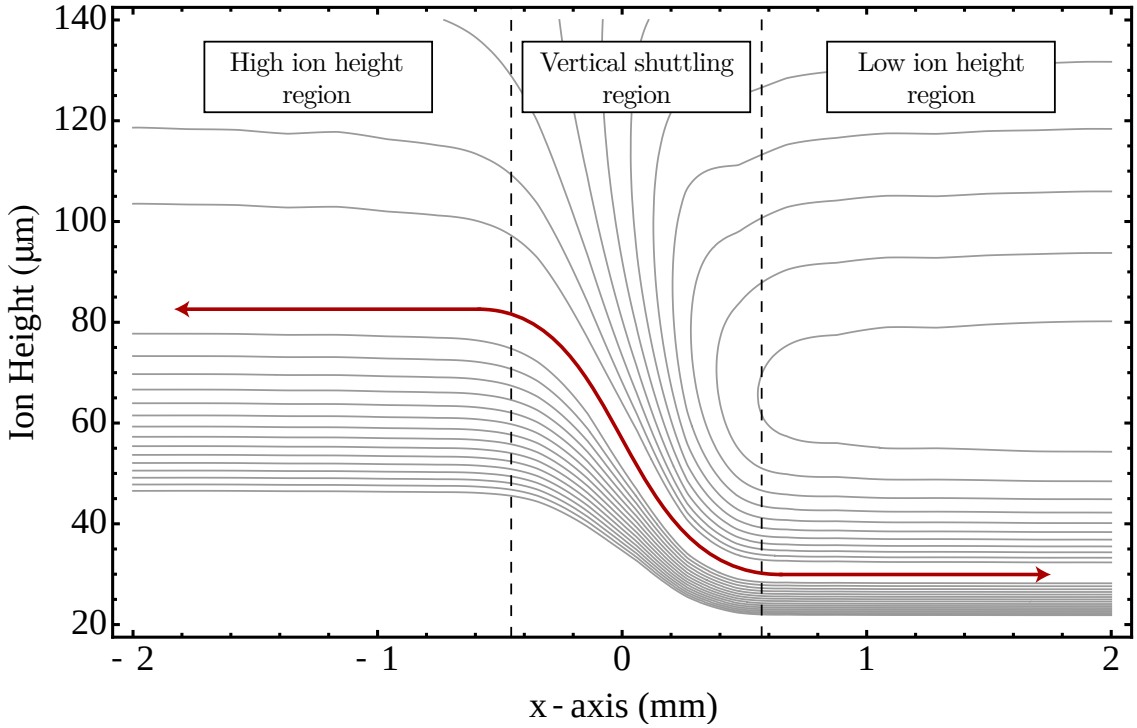

Figure 5.10: Pseudopotential of the vertical shuttling region along the axial direction for $V_{rf} = 150\,\mathrm{V}$ and $\Omega_{rf}/2\pi = 10\,\mathrm{MHz}$. The plot shows the variation in potential minimum from the high ion height region to the low ion height region.

The final design for the vertical shuttling ion trap chip described is shown in figure 5.11. The chip has been designed to be $12 \times 12\,\mathrm{mm}$ to meet mounting requirements in the cryogenic system described in section 4.7. The chip contains 40 dc control electrodes to provide axial confinement and shuttling capabilities. All bonding sites from electrodes to chip carrier bond pads are located on two opposite sides of the trap. This provides two sides of the chip that are free from wirebonds, which the allows for uninterrupted laser access along one axis.

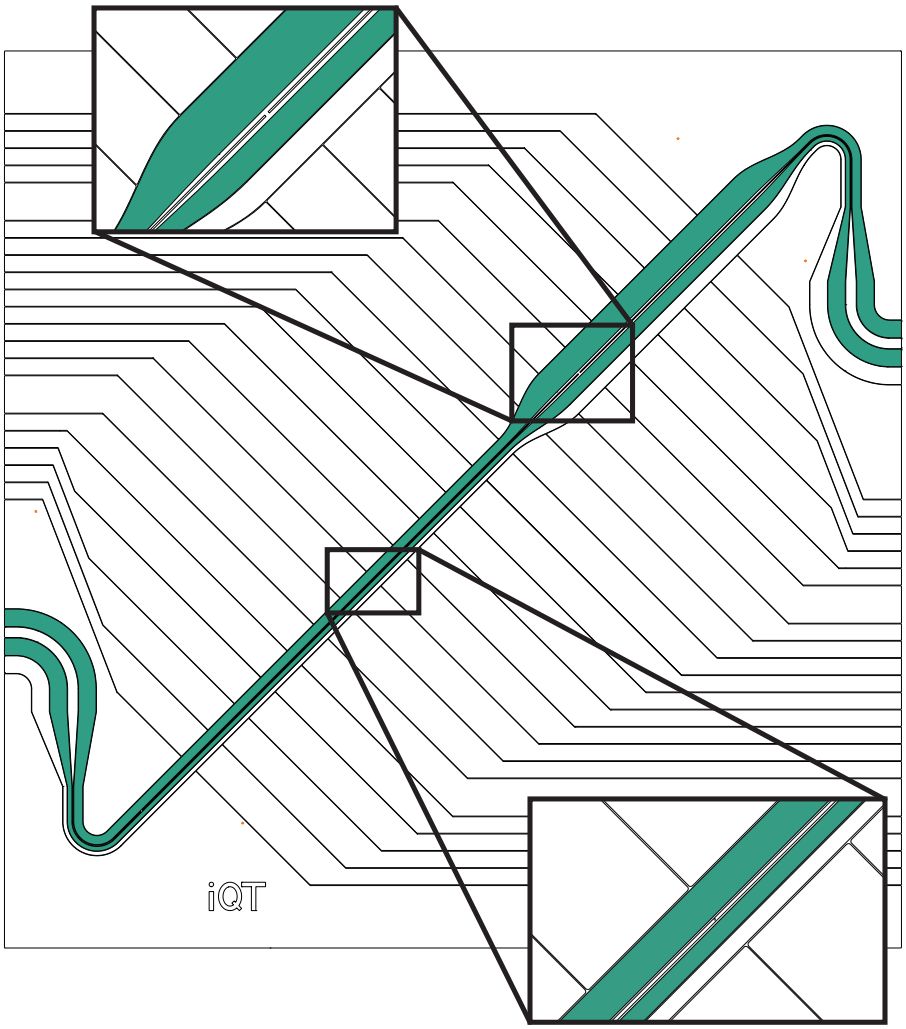

Figure 5.11: Complete design for the vertical shuttling trap with integrated high quality factor microwave resonator. The rf electrodes are shaded in green. The trap posses 40 dc control electrodes for ion shuttling.

5.2 Microwave resonator

In this section the integration of a high-Q superconducting resonator on a surface ion trap is explored. Firstly, the resonator type (section 5.2.1) and materials are discussed (section 5.2.3). Using commercially available finite element simulation software packages such as Microwave Studio (MWS) from Computer Simulation Technology (CST), the key parameters of the resonator were then estimated. The parameters considered were Q factor, resonator length, resonant frequency, line impedance, skin depth and scattering parameters (sections 5.2.4 - 5.2.7).

5.2.1 Planar transmission lines

Planar type transmission lines are a common form of transmission line that can be fabricated accurately and at a low cost. These structures are specialized in transmitting electromagnetic waves at frequencies between 300 kHz and 300 GHz. The transmission lines are formed from one or more layers of metallization on a dielectric substrate, with a signal and ground on separate conductors. This section describes three types of transmission lines, striplines, microstrips and coplanar waveguides (CPW) (figure 5.12), which possess different geometries and characteristics suitable for different application.

Stripline designs feature three layers of metallization, with a top and bottom ground layer and a central conducting strip. Striplines are ideally suitable for multilayer structures as they can be routed in between layers. The ground planes help to confine the central lines electromagnetic field, which provides a stronger field at a given distance compared with microstrip and coplanar structures. However, this feature also makes it unsuitable for interaction with an ion.

Microstrip designs are a popular choice for a planar transmission line due to their simplicity. Microstrips are formed with a ground plane on one surface of a substrate and a conductive line on the other. The structure is the printed circuit or microfabricated equivalent of a wire above a ground plane, which provides an ease of fabrication and integration within solid-state devices.

CPW resonator consists of a central conductor strip separated by a gap on either side from semi-infinite ground planes. As with microstrips the structure can also include a ground plane on the opposite side of the substrate. CPW resonators are used within the telecommunication industry due to their low dispersion, offering the potential to construct wide band circuits and components which do not require cryogenic cooling. CPWs which utilize superconducting conductors were initially used for the measurement of absolute

penetration depth, defined as the distance to which the magnetic field penetrates a superconducting material and becomes equal to $1/e$ of the magnetic field at the surface. At present they are widely used for interrogation and manipulation of the state of qubits and for Circuit Quantum Electrodynamics (CQED) experiments [172, 173]. They have been used to communicate information between two phase qubits [174]. For integration within an ion trap architecture, the rf electrodes and central ground electrode required for ion trapping provides a natural CPW structure. Therefore, a CPW design was chosen for the resonator.

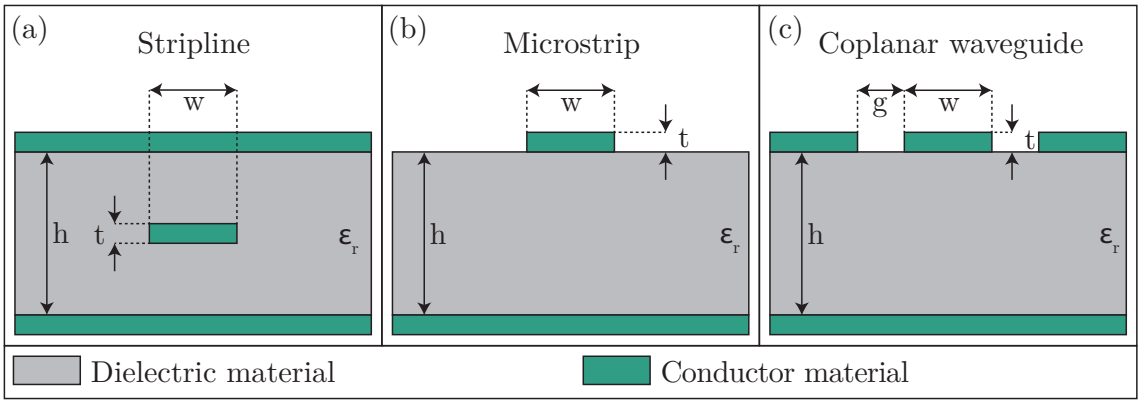

Figure 5.12: (a) Microstrip, (b) stripline and (c) coplanar waveguide transmission lines.

5.2.2 Coplanar waveguide resonator properties

A CPW resonator can be described as a distributed device with voltages and currents varying in magnitude and phase over its length. Using a lumped element model of the resonator (figure 5.13) the basic resonator properties can be analytically calculated [30, 175]. Near the resonant frequency, the properties of a transmission line resonator can be approximated by those of a lumped element parallel LCR oscillator. The capacitance C describes the electric energy stored between the conducting strip and the ground planes. The inductance L describes the magnetic energy stored, which is dependent on the length and width of the conducting strip and the total separation between the two ground planes $w/(w + 2g)$. Finally, R represents the resistance of the conductor.

The input and output circuitry can be modelled by load resistors R_L and the coupling gaps are modelled as coupling capacitors C_k. For further analysis, the series connection between C_k and R_L can be replaced by a Norton equivalent circuit. Norton theorem states that any collection of voltage sources V, current sources I and resistors R with two terminals is electrically equivalent to a parallel combination of an ideal current source I^* and a single impedance R^* [175, 176]. The Norton equivalent circuit consists of C^* and

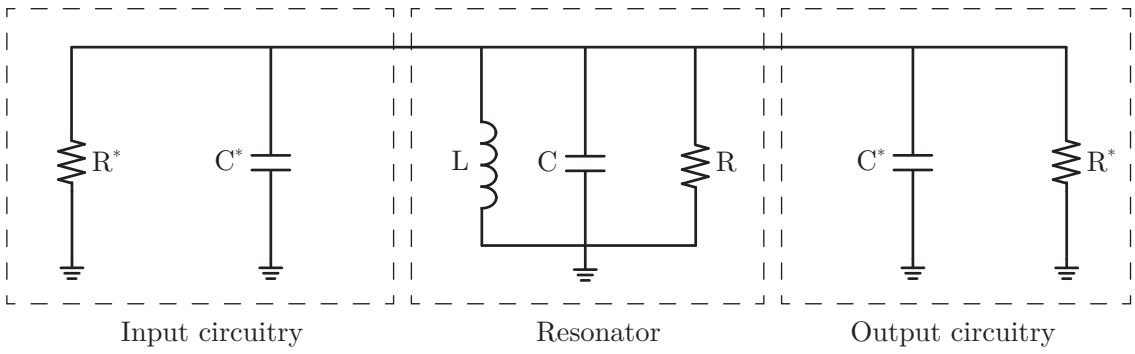

Figure 5.13: Norton equivalent circuit of a symmetrical coupled resonator [30]. The outer areas represent input and output circuitry, and the central area represents the resonator, where the length of the resonator is chosen depending on the wavelength of the frequency desired.

R^* where

$$R^* = R_L \left(\frac{1 + k^2}{k^2} \right), \tag{5.4}$$

$$C^* = C_k \left(\frac{1}{1 + k^2} \right), \tag{5.5}$$

where $k = \omega_n C_k R_L$ and ω_n is the angular frequency of the n^{th} mode.

5.2.3 Substrate and electrodes

To perform accurate simulations, a choice of substrate and electrode material must be selected. The choice of substrate material was based on investigation on the loss, which is intrinsic to the resonator. The intrinsic loss of a resonator accounts for the resistive loss, radiation loss and dielectric loss. Well below the critical temperature of the superconductor resistive losses are negligible. Radiation loss arises due to the dimension of the resonator being the same order of magnitude as the wavelength of the applied signal. The resonator therefore behaves as an antenna, radiating some of its energy into the environment. Such losses are usually small for CPW structures [30, 177] and can be ignored. Dielectric loss are the most damaging loss channel and are due to defects in the dielectric, which absorbs energy and limits the quality factor of the resonator. Initially proposed by Phillips and Anderson [178], these defects can be referred to as two level systems. The two level systems are groups of atoms tunnelling between two sites, where sites have electric dipole moments that can couple to the resonators electromagnetic field. The use of a substrate with low loss tangent can therefore reduce this loss. Al_2O_3 sapphire is a commercially available substrate that was chosen as it posses a low microwave loss tangent (10^{-4}). Sapphire also

possess a dielectric high dielectric constant of 11.5. This is an important factor as the resonant frequency of the resonator, f_0, can be given as [179]

$$f_0 = \frac{c}{\sqrt{\epsilon_{eff}}} \frac{1}{\lambda} \tag{5.6}$$

where c is the speed of light, ϵ_{eff} is the effective dielectric constant and λ is the wavelength of the microwaves in vacuum, which is $\sim$2.38 cm for 12.6 GHz in air ($\epsilon_{eff} \simeq 1$). A high dielectric constant allows for a smaller wavelength for a given frequency, which is smaller than the size of the ion trap (12×12 mm). The thermal conductivity of sapphire (25.2 W/mK) is also high in comparison with common substrate materials such as quartz (1.46 W/mK). This aids cooling the superconducting material attached to the substrate.

Choice of superconducting electrode material is based on the critical temperature (T_c) and critical magnetic field (B_c). Similar to T_c, the B_c is the critical magnetic field for a superconducting material, at which the electrical resistivity of the material drops to zero from a finite value. Hence for $T < T_c$ and $B < B_c$ there is a phase transition of the material from normal state to a superconducting state. As well as type II superconductors being mechanically harder than Type I superconductors, they also exhibit much higher critical T_c and B_c and are therefore preferable for a 4 K environment. The type II superconductor niobium nitride (NbN) was chosen for the resonator design. The choice was based on a high T_c of 16 K and ease of fabrication as described in section 6.4.

5.2.4 Quality factor and coupling optimization

The quality factor of a resonator can be described by one of two methods. Firstly, it can be given by

$$Q = \frac{f}{\Delta f} \tag{5.7}$$

where f is the resonant frequency and Δf is the half power bandwidth. Secondly, the Q factor can be described as the ratio of the energy stored in an oscillating resonator to the energy dissipated per cycle by damping processes. This can be given by

$$Q = \omega \times \frac{Energy\ Stored}{Power\ Loss} \tag{5.8}$$

$$= \omega \times \frac{W_M + W_E}{P_{loss}}, \tag{5.9}$$

where ω is the angular frequency, W_M is the average magnetic energy stored by the inductor, W_E is the average electric energy stored by the capacitor and P_{loss} is the power dissipated by the capacitor. W_M, W_E and P_{loss} can be given by

$$W_M = \frac{1}{4}LI^2, \tag{5.10}$$

$$W_E = \frac{1}{4}CV^2, \tag{5.11}$$

$$P_{loss} = \frac{1}{2}\frac{V^2}{R}. \tag{5.12}$$

For a CPW resonator, the effective quality factor (known as a loaded the loaded Q factor), Q_L, can be divided into a parallel combination intrinsic (or internal), Q_I, and the extrinsic (or external), Q_E, quality factors. Q_L can be given by

$$\frac{1}{Q_L} = \frac{1}{Q_E} + \frac{1}{Q_I}, \tag{5.13}$$

where

$$Q_E = \frac{\omega_n R^* C}{2}, \tag{5.14}$$

$$Q_I = \omega_n RC. \tag{5.15}$$

Where R^* is given in equation 5.4. Q_I describes the resistive, dielectric and radiation losses as described in section 5.2.3. Below the critical temperature of the superconductor, resistive losses are negligible. Q_E describes the losses associated with the coupling to the external microwave sources. As Q_E is related to the external coupling of the resonator, the strength of capacitive coupling g_c can be given by

$$g_c = \frac{Q_I}{Q_E}. \tag{5.16}$$

The coupling strength also depends on how the microwave signal in coupled to the resonator. Figure 5.14 shows a three methods of coupling a resonator, using a coupling gap, coupling strip or inter-digital capacitor. While coupling strips and inter-digital capacitors have been shown to provide higher coupling strengths, a coupling gap was chosen for the design as higher quality factors have been demonstrated [30].

If the capacitive coupling gap is small, the resonator is said to be over coupled ($g_c > 1$). In this regime $Q_E << Q_I$ and Q_L is governed by Q_E. On the other hand, if the capacitive coupling gap is large, the resonator is said to be under coupled ($g_c < 1$). In this regime

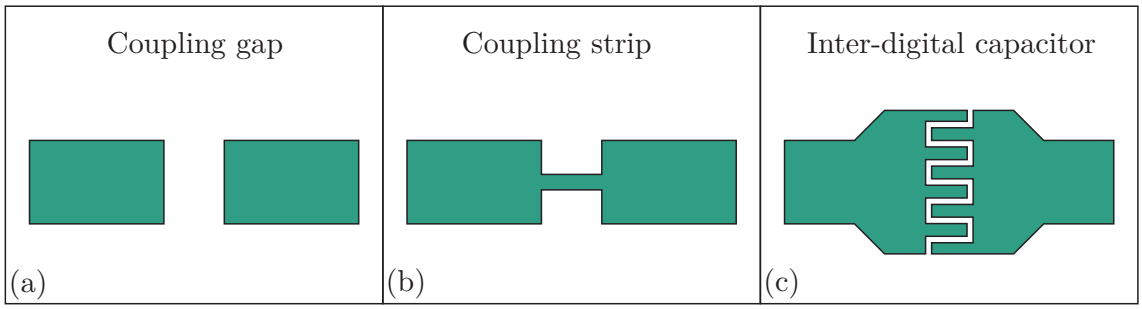

Figure 5.14: Coupling gap (a), coupling section (b) and inter-digital capacitor (c) [30].

$Q_E >> Q_I$ and Q_L is saturated at Q_I. The resonator is said to be critically coupled when $g_c = 1$. This is considered as an ideal situation, since below this limit Q_L starts to drop and beyond this limit the insertion loss becomes significantly high. The dependence of Q_L as a function of capacitive coupling gap is shown in Fig. 5.15.

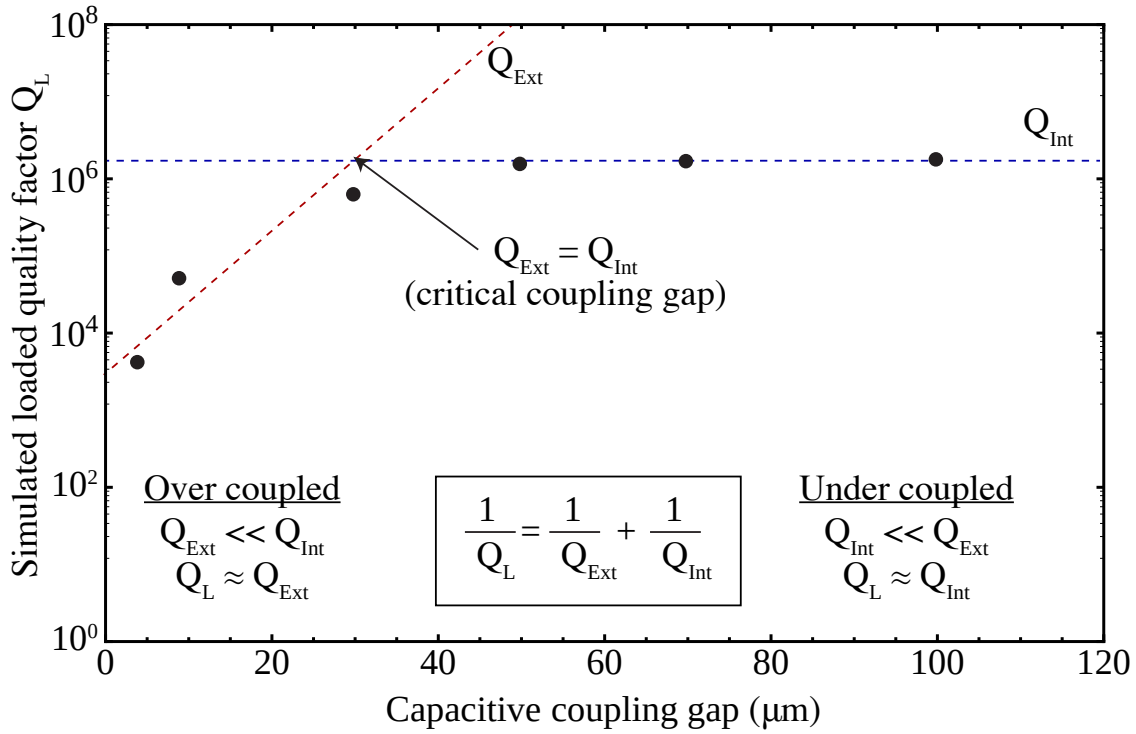

Figure 5.15: Dependence of the loaded quality factor Q_L on the capacitive coupling gap with data points acquired using CST.

5.2.5 Resonant frequency

The geometry of the resonator was modelled in CST and simulated using different solvers. The eigenmode solver was employed for an accurate determination of resonant modes, current and voltage standing wave distribution, and Q factor. The frequency domain solver was employed for an accurate determination of the fundamental resonant frequency

and line impedance.

The estimation of the resonant frequency and Q factor was performed by calculating the scattering parameters for the resonator. The scattering parameters can be described by treating the resonator as a two port system (figure 5.16), with each port having an input (a) and output (b).

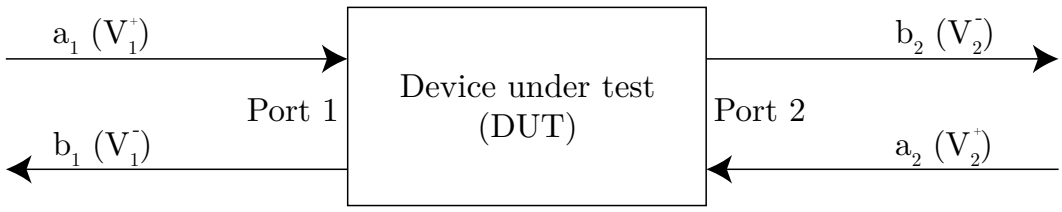

Figure 5.16: A model of a two port network.

The input and output voltages are related with the scattering matrix which is defined as

$$\begin{bmatrix} V_1^- \\ V_2^- \end{bmatrix} = \begin{bmatrix} S_{11} & S_{12} \\ S_{21} & S_{22} \end{bmatrix} \begin{bmatrix} V_1^+ \\ V_2^+ \end{bmatrix}, \tag{5.17}$$

and the scattering parameters are defined as

$$S_{ij} = \frac{V_i^-}{V_j^+} \text{ for } V_k^+ = 0 \ (k \neq j). \tag{5.18}$$

where S_{11} is the input port voltage reflection coefficients, S_{12} is the reverse voltage gain, S_{21} is the forward voltage gain and S_{22} the output port voltage reflection coefficient. Since the capacitive coupling gaps at both ends of the resonator are the same, the resonator is said to be symmetric and for such a resonator $S_{11} = S_{22}$ and $S_{12} = S_{21}$. On resonance the transmission coefficients (forward and reverse voltage gain) show a Lorentzian line shape when plotted as a function of frequency.

5.2.6 Characteristic line impedance

To prevent unwanted reflection within the resonator, the impedance is matched closely to 50 Ω. The characteristic impedance of the transmission line, Z_0, can be given by [180]

$$Z_0 \approx \begin{cases} \dfrac{60}{\sqrt{\varepsilon_{\text{eff}}}} ln\left(\dfrac{8h}{w} + \dfrac{w}{4h}\right) & w/h \leq 1 \\ \dfrac{120\pi}{\sqrt{\varepsilon_{\text{eff}}}\left[\frac{w}{h} + 1.393 + 0.667 ln\left(\frac{w}{h} + 1.444\right)\right]} & w/h \geq 1. \end{cases} \tag{5.19}$$

where w is the width of the resonator, h is the height of the resonator and ε_{eff} is the

effective dielectric constant, which depends on the geometry and dielectric material, and is given by [180]

$$\varepsilon_{\text{eff}} = \frac{\varepsilon_r + 1}{2} + \frac{\varepsilon_r - 1}{2} \frac{1}{\sqrt{1 + 12\frac{h}{w}}}, \tag{5.20}$$

where ε_r is the relative dielectric constant.

5.2.7 Skin depth and proximity effect

At microwave frequencies the skin effect and proximity effect produce a complex distribution of currents in the conductor, as well as induced currents in other nearby conductors which cannot be calculated analytically. Skin effect describes the effect of an alternating electric current becoming distributed in a conductor such that the current density is greatest near the surface of the conductor and decreases with depth in the conductor. The electric current flows primarily between the surface of the conductor and a given level known as the skin depth. This skin depth becomes smaller for higher frequencies. Conductors carrying alternating current within close proximity to each other will cause the distribution of current within each conductor to be constrained to smaller regions. The resulting current crowding is termed the proximity effect. This crowding gives an increase in the effective resistance of the circuit, which increases with frequency. To improve upon the accuracy of resonator design, the resonator must therefore be numerically simulated to take into account the skin and proximity effect.

5.2.8 Simulation results

The resonator geometry was optimized by iteratively varying its length (l) and width (w) while observing the S_{21} and to maximize the Q factor. The height was set at 1 μm due to fabrication constraints. The simulations were performed by placing the resonator within the rf electrode structure of the vertical shuttling ion trap designed in section 5.1.3. As the length of a full wave resonator at 12.6 GHz (16.5 mm) was too large for the trap design, a half-wave resonator ($l = \lambda/2$) was simulated. The resonator will also resonate at the higher harmonics, however, the quality factor goes down approximately as $1/n$, where n is the mode number. The optimum geometry for a half-wave resonator at 12.6 GHz, was found to be $w = 11.5\,\mu$m and $l = 8250\,\mu$m for $h = 1\,\mu$m. For this geometry, a bandwidth at 3 dB below the 12.6 GHz peak was measured to be $\sim$100 Hz, giving a Q factor of $\sim 10^8$ (figure 5.17).

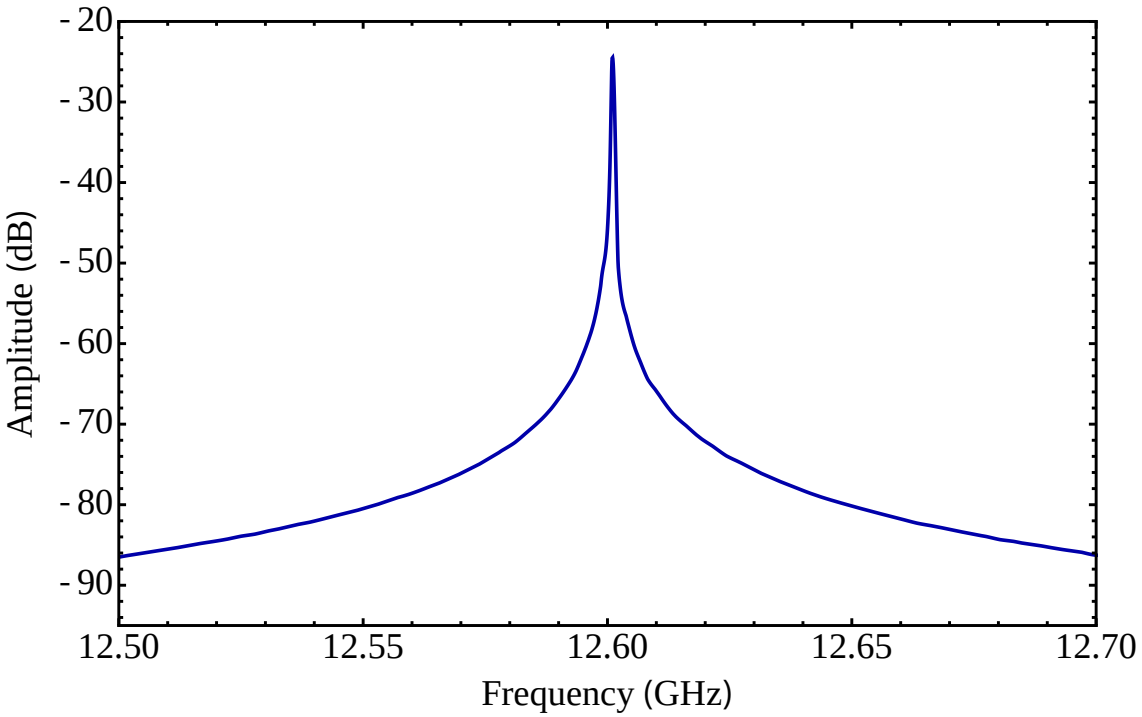

Figure 5.17: Simulation result using CST for the S_{21} parameter assuming electrodes are in the superconducting regime. The bandwidth of $\sim 0.1\,\text{kHz}$is measured yielding a Q factor of $\sim 10^8$ at 12.6 GHz.

Errors

It should be noted that errors in fabrication and can result in a deviation resonators resonant frequency. Typical microfabricated errors for the resonator structure were estimated at approximately $\pm 0.5\,\mu$m. A variation of $\pm 0.5\,\mu$m in the width of the resonator changes the resonant frequency by $\pm 28\,$MHz and a variation of $\pm 0.5\,\mu$m in the length of the resonator changes the resonant frequency by $\pm 3\,$MHz. Figure 5.18 shows a diagram of the resonator width and length variation.

A disadvantage of a CPW structure can be the unintentional excitation of the highly unwanted parasitic slot line modes, also known as odd modes, in addition to the fundamental mode (even mode) [181, 182]. The odd modes are predominantly present in resonator circuits with asymmetric geometries. Such modes are lossy modes and can significantly suppress the Q factor. They can be characterized by counter propagating E and H field lines. Simulation results of input and output modes reveal that we have only even mode and any odd modes do not coexist.

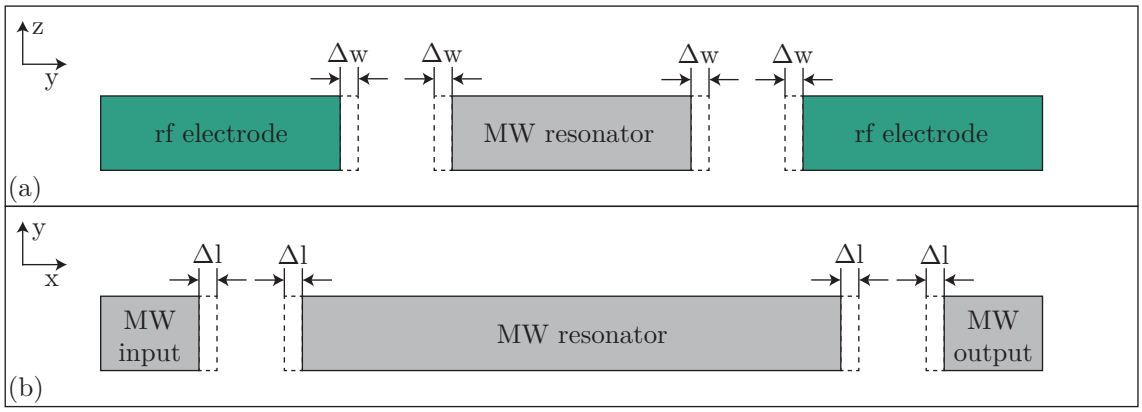

Figure 5.18: Variation of resonator dimensions in radial (a) and axial (b) cross sections, corresponding to the typical accuracy in microfabrication. Typical variations of $\pm 0.5\,\mu$m for the width and length of the resonator correspond to resonant frequency deviations of ± 28 MHz and ± 3 MHz respectively.

5.2.9 Resistance measurements

The first tests performed on the NbN on sapphire chips was to determine whether or not they became superconducting when cooled using the cryogenic system described in section 4.12.2. To do so, a test chip was adhered to a temporary copper L-piece testing mount (figure. 5.19) using a two-part silver epoxy (*EPO-TEK H21D*). The measurement was made across a section of ground plane spans the whole length. As the resistance of the chip at room temperature is low to begin with, a more sensitive 4 point measurement was used to measure the resistance. This is shown in figure 5.19 where the 4 wires on the right of the chip are connected via Al wire bonds to the chip. The two outer connections apply a constant current, while the inner two connections measure the voltage across the desired area. The constant current allows a precise and stable voltage measurement to be made allowing for an accurate calculation of the resistance. Figure 5.20 shows the trap successfully entering the superconducting regime. This can be seen as the voltage measured across the trap goes to zero as the temperature drops below 6 K.

Further tests were performed using an identical chip from the same fabrication run in a dilution fridge by Matus Réhak at the Department of Experimental Physics, Comenius University. The results of the test are shown in figure 5.21. For this sample, a critical temperature is observed at a much higher temperature of 12 K. One potential reason for the discrepancy is variations in the crystal structure and carrier density [183], which can be verified using x-ray diffraction to characterize the morphology [184]. However, as the difference between the transition regions is significant, and the chips were fabricated in the same fabrication run, this is unlikely to be the cause. The most probable source of the discrepancy is due to a systematic error in the measurement of the temperature in

our cryogenic system. The temperature of the system is measured using a diode sensor attached directly on the cold finger, whereas the chip is attached to the end of a copper mount, suggesting a temperature offset between the two locations.

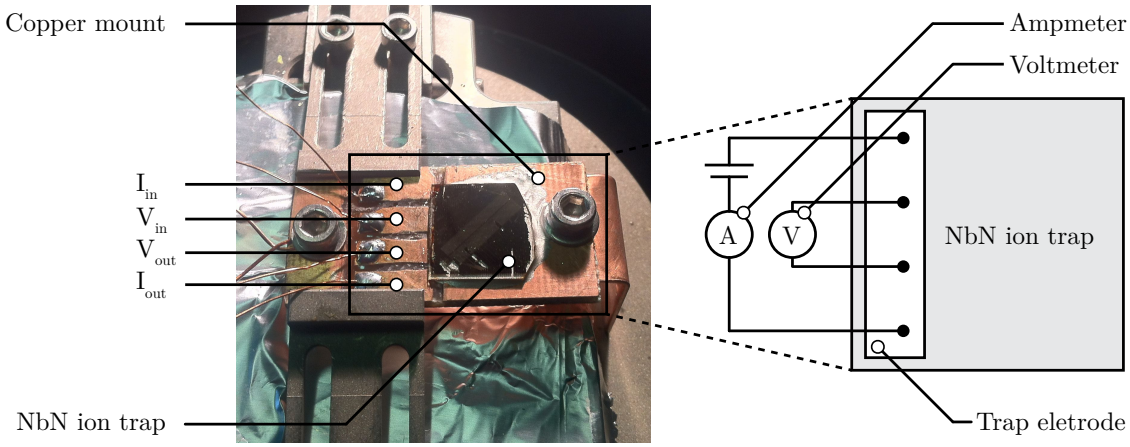

Figure 5.19: Experimental setup used for performing a 4 point measurement of the resistance of a surface ion trap. The trap used possessed a NbN surface electrodes. The connections were made on opposite ends of a ground plane at approximately 8 mm separation.

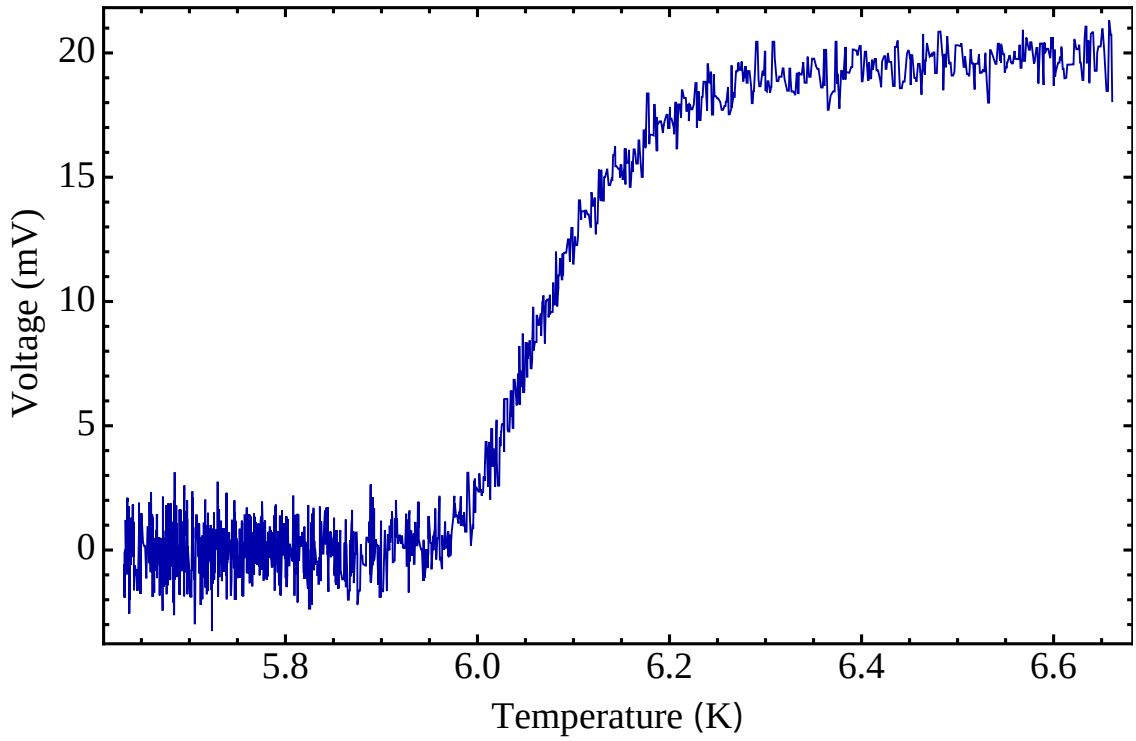

Figure 5.20: Four point measurement of the NbN trap resistance in the cryogenic system described in section 4.12.2, showing a T_C of ~ 6.1 K.

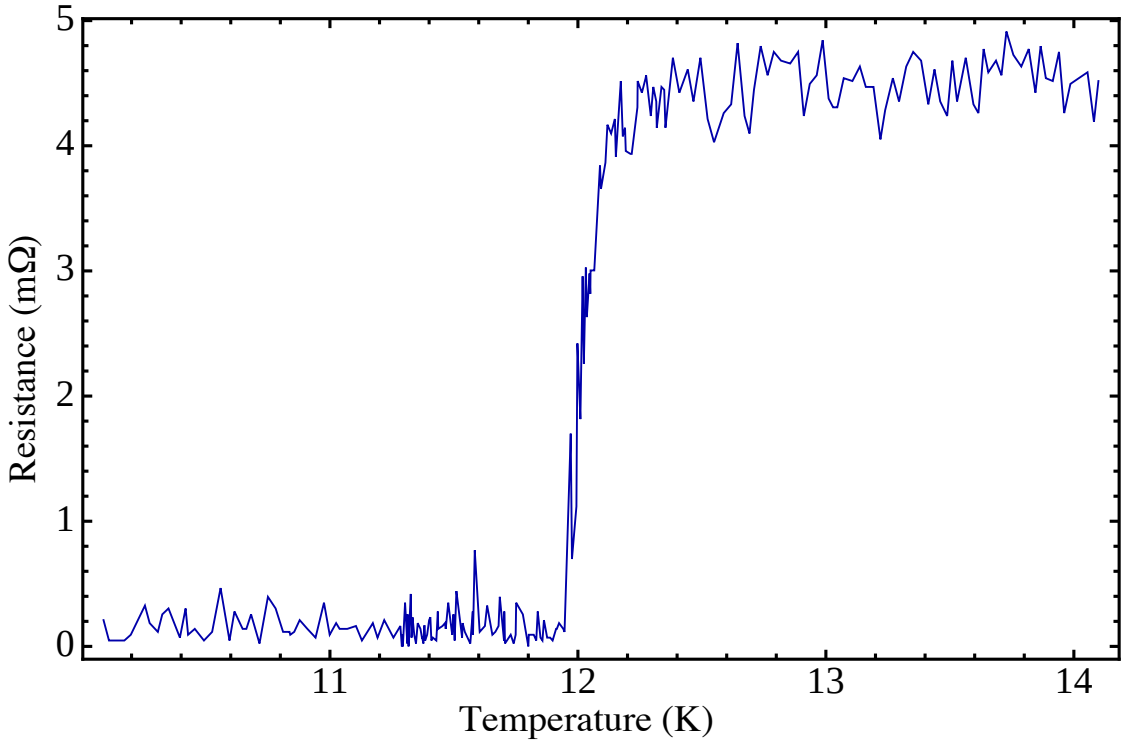

Figure 5.21: Four point measurement of the NbN trap resistance in a dilution fridge at Comenius University, showing a T_C of $\sim 12\,K$.

Improvements to trap temperature measurements

The temperature offset between the cold finger and the ion trap is an undesirable consequence of having the temperature sensor at an arbitrary distance away from the trap itself. While we were able to determine the minimum offset by comparing an identical trap in a system with a temperature sensor mounted closer to the trap, the process of doing so is not practical and does not take into account any differences between the traps. One future improvement for the temperature measurement inside the cryogenic system is to mount an additional diode temperature sensor nearer to the trap. The sensor can be attached to the copper mount to give a more accurate temperature measurement closer to the trap. This can also help to determine the thermal gradient between the mount and the cold finger.

It should also be noted that despite improving the accuracy of the temperature measurement, the temperature of the trap itself may still be offset from the position of the temperature sensor. To measure the temperature at the chip directly, a simple technique using the same diode sensor (Lakeshore DT-670B-CO) has been demonstrated [67, 185]. The bare diode sensor without the mounting housing can be directly epoxied to the trap surface using the same two-part silver epoxy (*EPO-TEK H21D*) as used for the trap. To adhere the diode to the trap a number of experimental factors must be considered. Firstly,

the diode requires a 2×3 mm area on the edge of the trap where the sensor can be epoxied. For most surface electrode ion traps, this is a relatively large area which would need to be allocated during the design phase of the trap. The sensor also has a height of 1 mm, which is higher than most ion-electrode distances. The trap design must therefore take into account the limited optical access around the diode sensor. Finally, the position of the sensor will also be restricted by the path of the laser beam across the trap surface.

An alternative method to measure the temperature on the trap directly is to use a thermocouple wire. Several thermocouple cables such as type E (chromel - constantan), type K (chromel- alumel) and type T (copper - constantan) can be used to measure temperatures down to 3 K. Such wires can have diameters <0.2 mm, providing a small profile on the trap surface. While the thermocouple offers a smaller footprint on the trap, the voltage response from the thermocouple is significantly lower than the diode sensor at lower temperatures. Between 4 K and 10 K the voltage response from the thermocouple is approximately $\sim 10^4$ smaller than that of the diode sensor. We can see from figure 5.20 that the readout error in the diodes response signal is greater than what we would expect from the thermocouple. Hence, for temperatures below <10 K, where we are interested in looking at superconducting transition regions, a thermocouple would not be suitable. However, for non-superconducting ion traps, thermocouples offers a simpler and cheaper method for determining the temperature at remote locations.

5.2.10 Resonator measurements

The resonator measurements presented here were performed by measuring the S_{11} parameter (equation 5.18). A microwave signal was supplied by a dedicated microwave source (*HP 8673C Synthesized Signal Generator*) and fed directly to the resonator via an SMA vacuum feedthrough. The output signal travels via an SMA vacuum feedthrough directly to a spectrum analyser (*Rohde & Schwarz ZNB 20*). The resonators resonant frequency and Q is measured by observing the output power from the resonator at the expected resonant frequency. A drop in output power indicates the resonator is resonating with the input power being radiated at the resonator as it begins to act as an antenna.

The measurement itself is performed by controlling the microwave source and spectrum analyser remotely using a Python script. A start and stop frequency is given as well as a frequency step. For the highest precision measurements the frequency steps were set to 10 kHz. For each step, the spectrum analyser readjusts its centre frequency so that it is equal to the applied frequency from the microwave source and keeps a bandwidth constant.

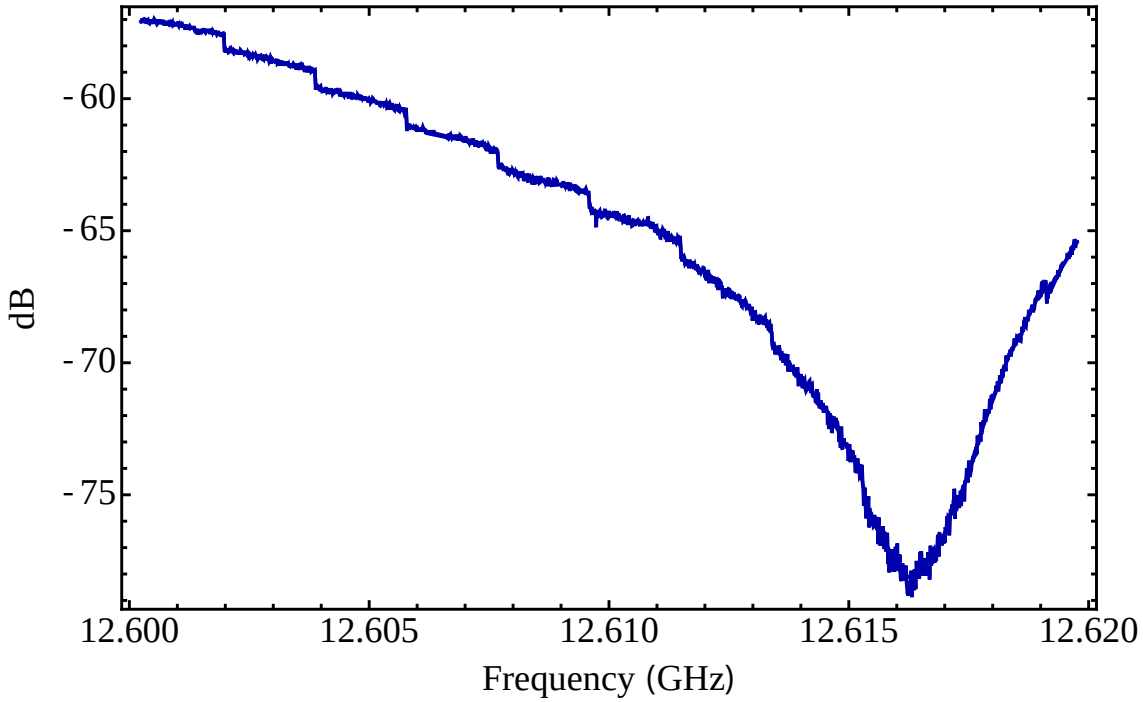

Figure 5.22: Q measurement for a microfabricated NbN coplanar waveguide resonator at 6 K. S_{11} scattering parameter is plotted as a power in dB relative to 10 dBm. A 3 dB bandwidth of 1968 Hz was measured corresponding to a Q of 6411 ± 20.

An automated function for locating the peak amplitude on the spectrum analyser is then used to read out an amplitude value to the computer. Keeping a smaller bandwidth window of $\sim$ 60 kHz is key as a bandwidth spanning the entire frequency range being scanned can include anomalous noise or amplitude variations that could be detected by the automated function.

For the NbN on sapphire resonator a Q factor of 6411 ± 20 was measured at 12.616 ± 0.001 GHz. Fabrication of the same trap design was also performed with gold on quartz as described in chapter 6. For the gold trap a Q factor of 15744 ± 20 was measured at 12.815 ± 0.001 GHz. The higher quality factor for the gold trap compared with the NbN trap can be attributed to a superior fabrication process described in chapter 6. It should be noted that the step functions observed in figure 5.22 and 5.23 is a feature of the signal generator and not the ion trap. The sharp variations in amplitude is a result of the signal generator being out of calibration. Multiple internal oscillators are used to vary the output frequency for different frequency regions. The transition region between two local oscillators can drift such that the frequency change across such regions is not constant, resulting in observable steps when switching between oscillators.

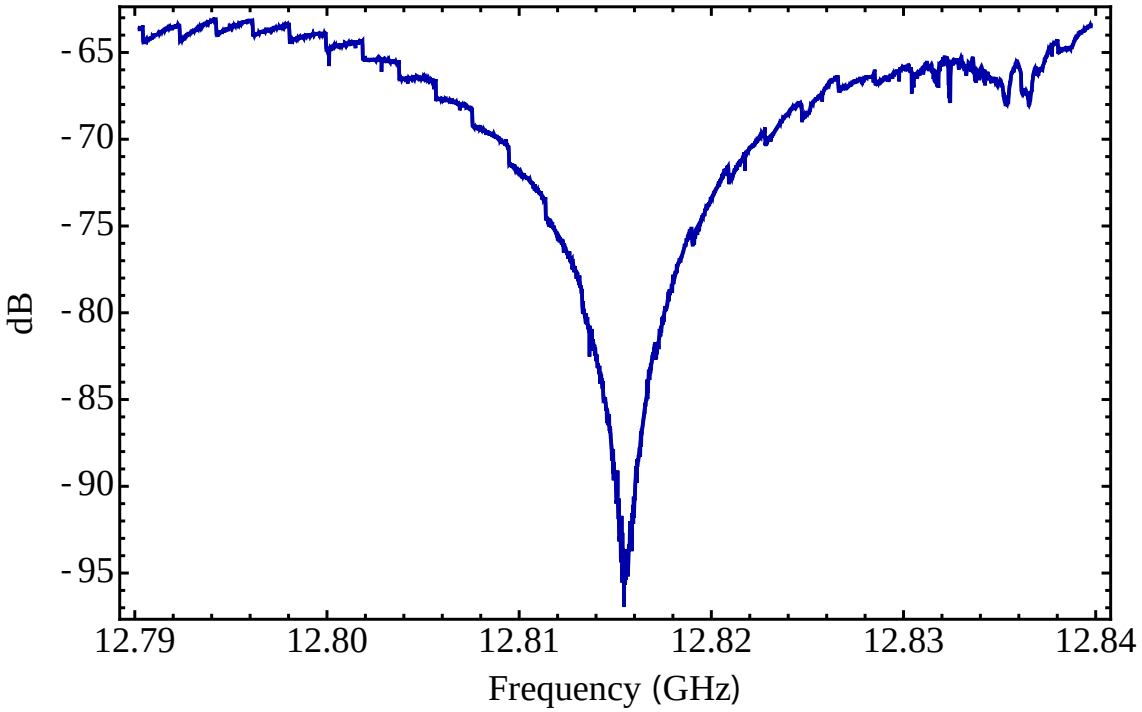

Figure 5.23: Q measurement for a microfabricated gold coplanar waveguide resonator at 6 K. S_{11} scattering parameter is plotted as a power in dB relative to 10 dBm. A 3 dB bandwidth of 814 Hz was measured corresponding to a Q of 15744 ± 20.

5.3 Flat multipole ion trap

5.3.1 Motivation

The coupling strength g between the ion and an on chip resonator can be enhanced if multiple ions are used. The effective coupling strength $g^{'}$ scales as $g^{'} = g \times \sqrt{N}$ [186], where N is the number of ions. In order to realize a trap that can hold many ions with negligible micromotion, a multipole ion trap geometry was developed in parallel to the vertical shuttling traps described in section 5.1. The multipole geometry was designed such that multiple linear trapping region were created, allowing for multiple large ion crystals to be confined next to each other. Analytical methods in a gapless plane approximation and a more accurate numerical BEM simulations incorporating all three dimensional features were used again to determine the geometries of the rf electrodes.

5.3.2 Trap design

The dynamics of a quadrupole surface Paul trap will always produce a singular point above the surface of the ion trap where the potential is zero (or some minimal non-zero value). To be able to create a pseudopotential that produces multiple points of minimum potential, or a finite region with a minimum potential, additional rf electrodes are required. Figure

5.24 shows an example of this multipole geometry with the addition of a third rf electrode to a linear surface electrode geometry. The result of this multipole structure creates a second rf nil, resulting in 2 rf nils above and in between the three rf electrodes. This can be expanded upon with an indefinite amount of rf electrodes to generate more rf trapping nils. Figure 5.25 shows one such example with the addition of a fourth rf electrode that produces a third rf nil.

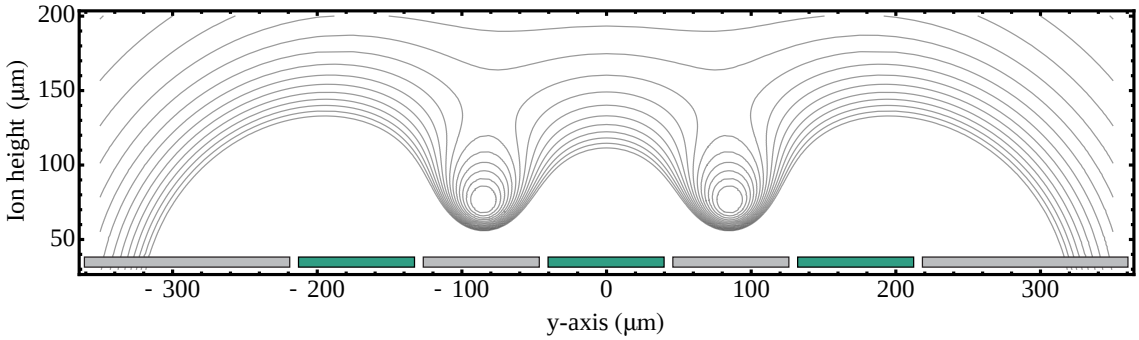

Figure 5.24: Pseudopotential for an asymmetric ion trap with 3 linear rf electrodes and 2 corresponding identical rf nils at $\sim 70\,\mu$m.

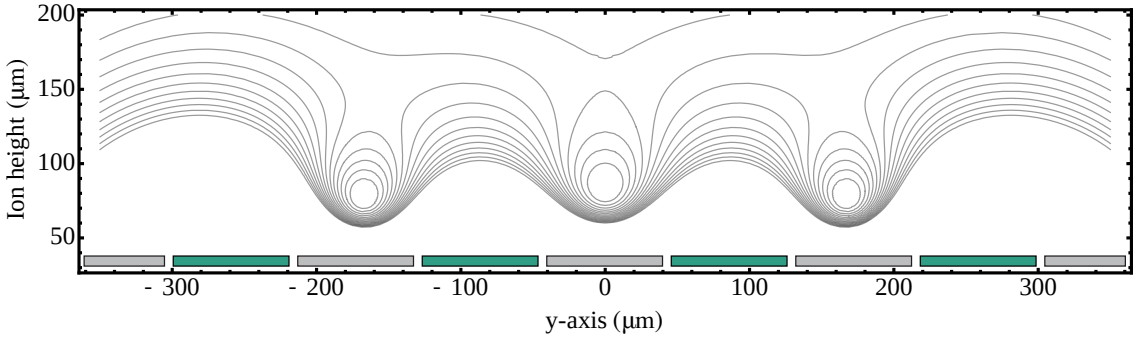

Figure 5.25: Pseudopotential for an asymmetric ion trap with 4 linear rf electrodes and 3 corresponding rf nils at $\sim 70\,\mu$m.

Initial work performed was towards developing this principle and exploring the possibility of creating a truly flat pseudopotential geometry. To do this the 3 rf electrode structure was used. The geometry of the rf electrodes, their separation and central ground lines were varied to generate a flat potential well. Figure 5.26 shows how the manipulation of the physical parameters of the electrodes can push the two rf nils closer together. After several iterations an approximately flat potential was be created. However, it can be seen that the resultant flat pseudopotential results in the loss of a confining potential in the z-axis. With the addition of end cap electrodes, the total trapping potential will only support confinement in 2 axes, and therefore will not be capable of trapping ions. With the inability to create a trap architecture that provides a single flat potential, the ideal choice

is to create a multipole trap with several individual rf nils. If these individual trapping sites can share similar trapping parameters such as trap depth, ion height and secular frequency then this would be analogous to a single flat potential.

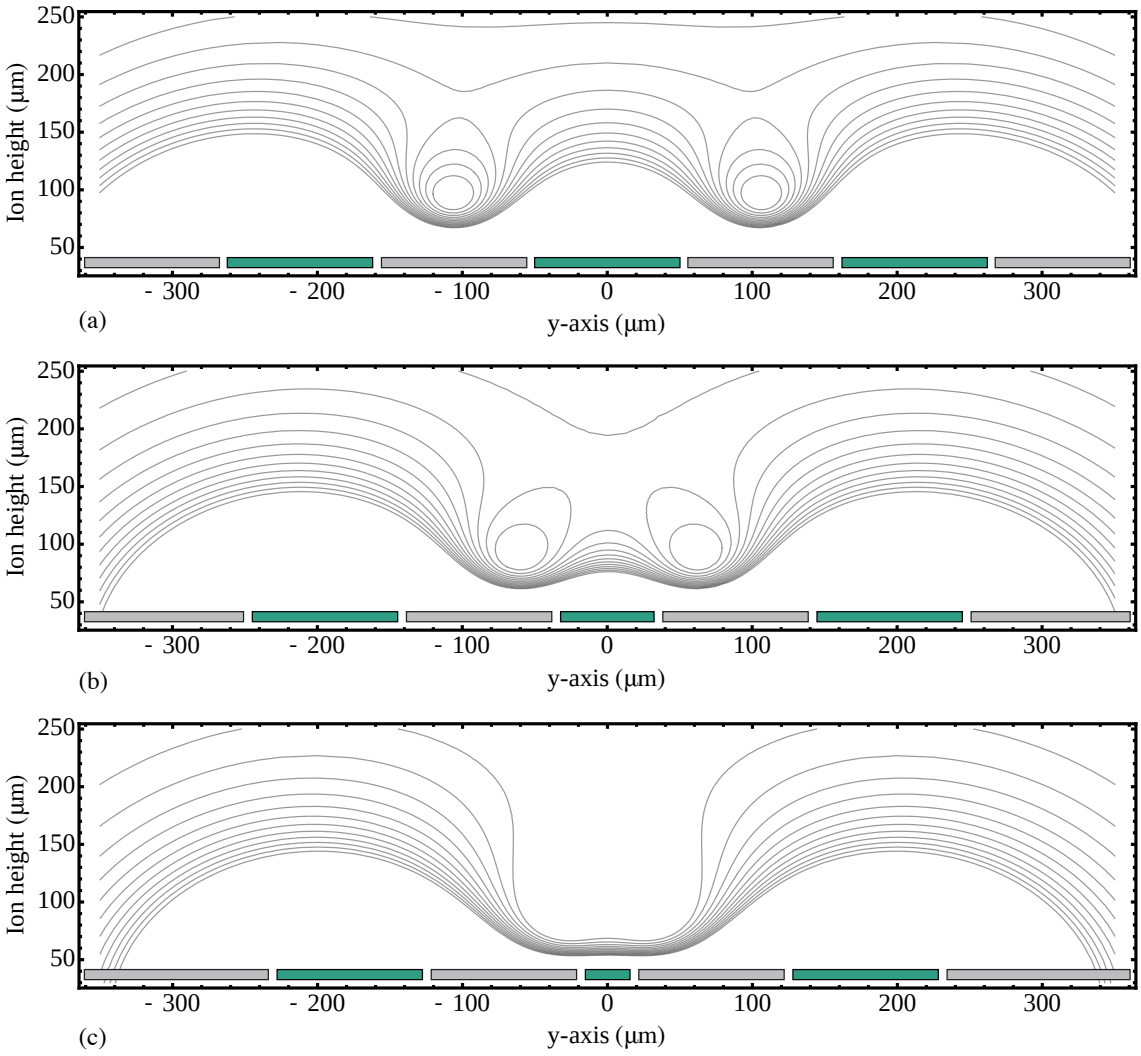

Figure 5.26: The radial pseudopotential plots for (a), (b) and (c) show the gradual merging of two distinct rf nils into a single flat potential by the manipulation of trap electrodes.

Initial design considerations focussed on work performed by Siverns et al [187] towards the optimization of ion trap arrays for quantum simulations. In the example given in figure 5.27 for a 5 by 5 square array, the parameters such as trap depth, ion height and secular frequency are made homogenous across all trapping sites. This is done by minimizing a homogeneity factor, H, given by [187]

$$H = \frac{1}{N}\Sigma_{n=1}^{N}|1 - \frac{K_{sim_n}}{K_{sim_{centre}}}|. \tag{5.21}$$

where N is the number of trapping sites along one axis and K_{sim} is given by [187]

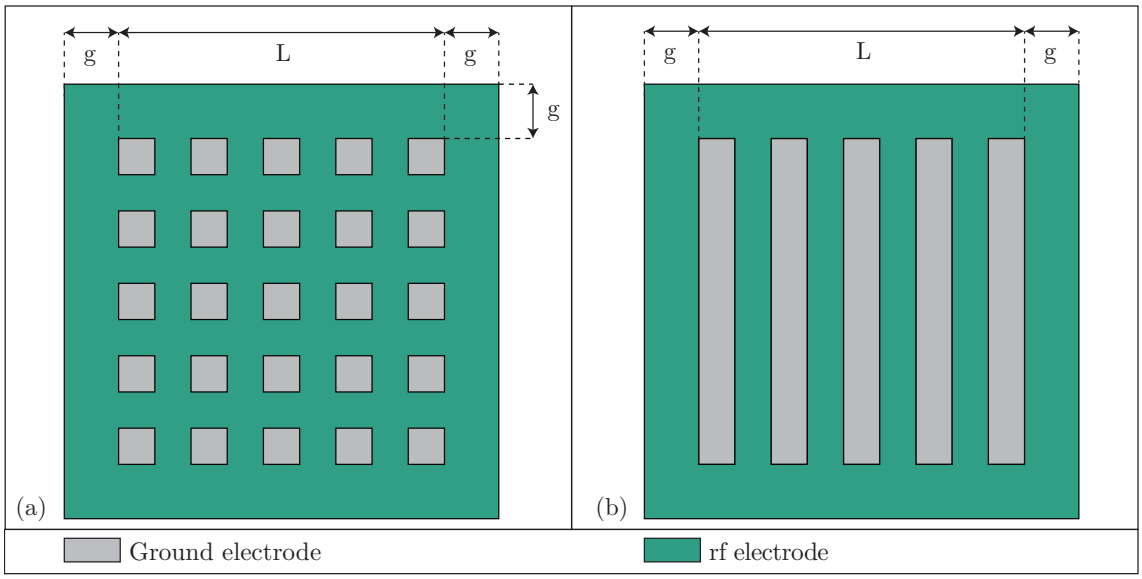

Figure 5.27: (a) Schematic diagram of a 5 by 5 square ion trap array. (b) Adapted array geometry that replaces columns of individual sites with a single linear grounding region.

$$K_{sim} = \frac{2\hbar F^2}{S_E(\omega)\epsilon_0 m\omega^3 A^3 h} \tag{5.22}$$

where m is the mass of the ion, ω is the secular frequency of the trap, $S_E(\omega)$ is the electric field noise density, A is the ion-ion spacing, F is the state dependant force applied to the ions, h is the ion height and ϵ_0 is the permittivity of free space. The subscripts of '*centre*' and 'n' in equation 5.21 correspond to the central trapping region and an outer n^{th} trapping region respectively. As K_{sim} is a function of ion height, trap depth and secular frequency, the homogeneity for all parameters can be optimized by optimizing K_{sim} alone. The optimization is performed by varying the gap between the outer trapping site and the outer edge of the rf electrode (figure 5.27).

5.3.3 Trap simulation

Using the design guidelines for a square array [187], a linear electrode structure was created in AutoCAD. The square ground sites were replaced with linear electrode of the same width, and the rf plane was replaced with individual linear rf electrodes. The width and separation of central rf electrodes were chosen to be 90 μm and 35 μm respectively, which produced an ion height of $\sim 60\,\mu$m. The outer rf electrodes were then varied produce the most homogenous distribution of trap site parameters. Figure 5.28 shows the variation in the homogeneity factor, H, as a function out rf electrode width.

Figure 5.29 shows the result of an optimized electrode structure, with an optimal outer rf electrode with of $\sim$135 μm. For a trap operating at $V_{rf} = 150\,\mathrm{V}$ and $\Omega_{rf}/2\pi = 10\,\mathrm{MHz}$ a

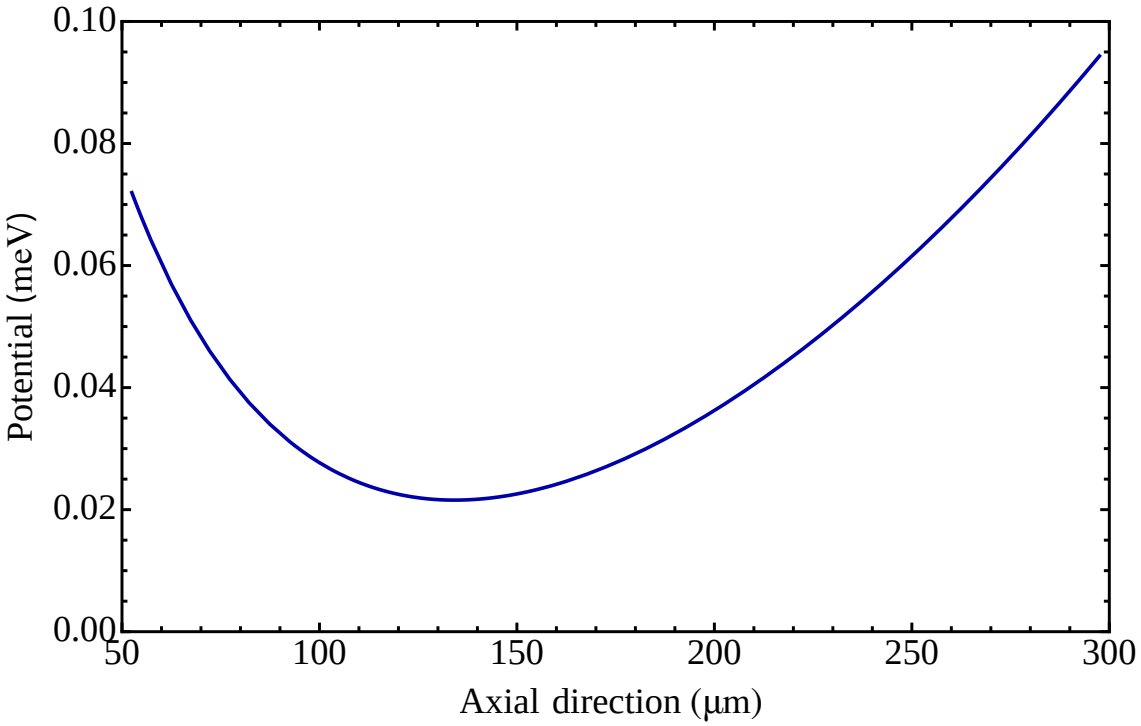

Figure 5.28: Variation in homogeneity of trapping sites as a function of outer rf electrode width. A minimum inhomogeneity can be found with an outer rf electrode width of approximately $\sim 135\,\mu$m.

trap depth of 0.10 eV, 0.11 eV and 0.17 eV could be achieved for the central site, the two middle sites (adjacent to the central site) and the outer site respectively. The ion heights at the central, middle and outer sites were also measured to be 60.3 μm, 60.2 μm and 59.0 μm respectively, which can be seen in figure 5.30. Finally, radial secular frequencies for the central middle and outer sites were calculated as $\omega_y/2\pi \approx 2.65$ MHz, $\omega_z/2\pi \approx 2.76$ MHz and $\omega_x/2\pi \approx 3.90$ kHz respectively.

The central three sites can be seen to produce relatively homogenous parameters with minimal variation. However, the parameters for the outer sites deviate noticeably from the central three sites for this given electrode structure. This edge effect is a result of the pseudopotential at the outer trapping site being significantly more dependent upon the outer rf electrode. If a trap is required to have a closer homogeneity, such as that shared by the central sites, then a trap geometry can be created with two additional rf nils beyond requirement. This will allow the outer rf nils suffering from edge effects to be neglected with focus solely on the central sites. Alternatively, further simulations could be performed with the added variation of the central rf lines to investigate increased homogeneity across all sites.

As principal axis rotation could not be provided via asymmetric rf electrodes due to the requirement of uniform rf electrodes, an alternative rotation method was chosen. In

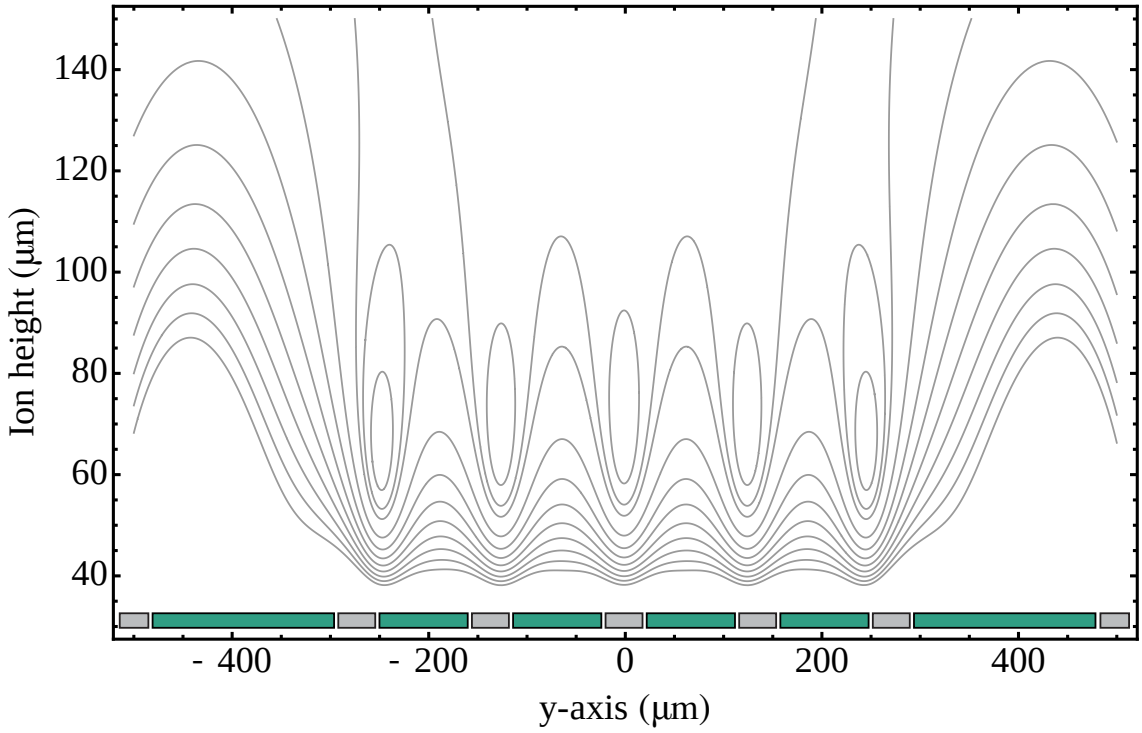

Figure 5.29: Pseudopotential for an optimized asymmetric multipole ion trap with 6 linear rf electrodes and 5 corresponding rf nils. The trapping regions are symmetric along the axial direction at $y = 0$. The yellow markers show the exact position of the rf nils.

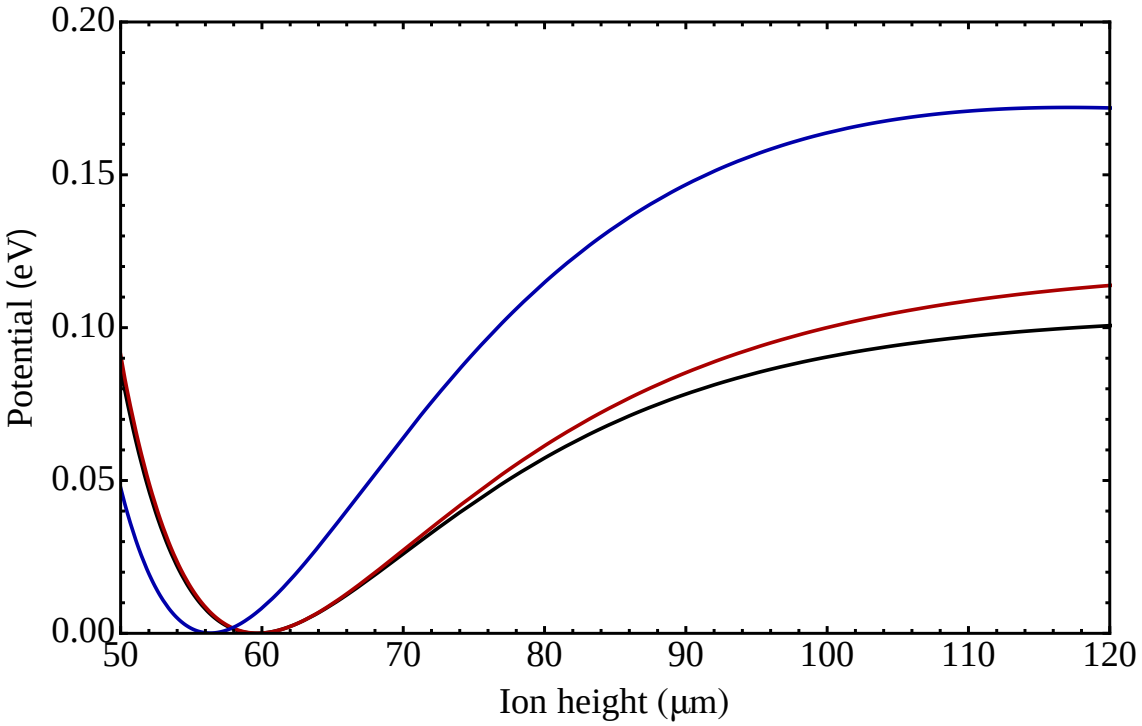

Figure 5.30: Trap depth for the central trapping point (black), middle trapping points (adjacent to the central nil) (red) and outer trapping points (blue) at $V_{rf} = 150\,\mathrm{V}$ and $\Omega_{rf}/2\pi = 10\,\mathrm{MHz}$.

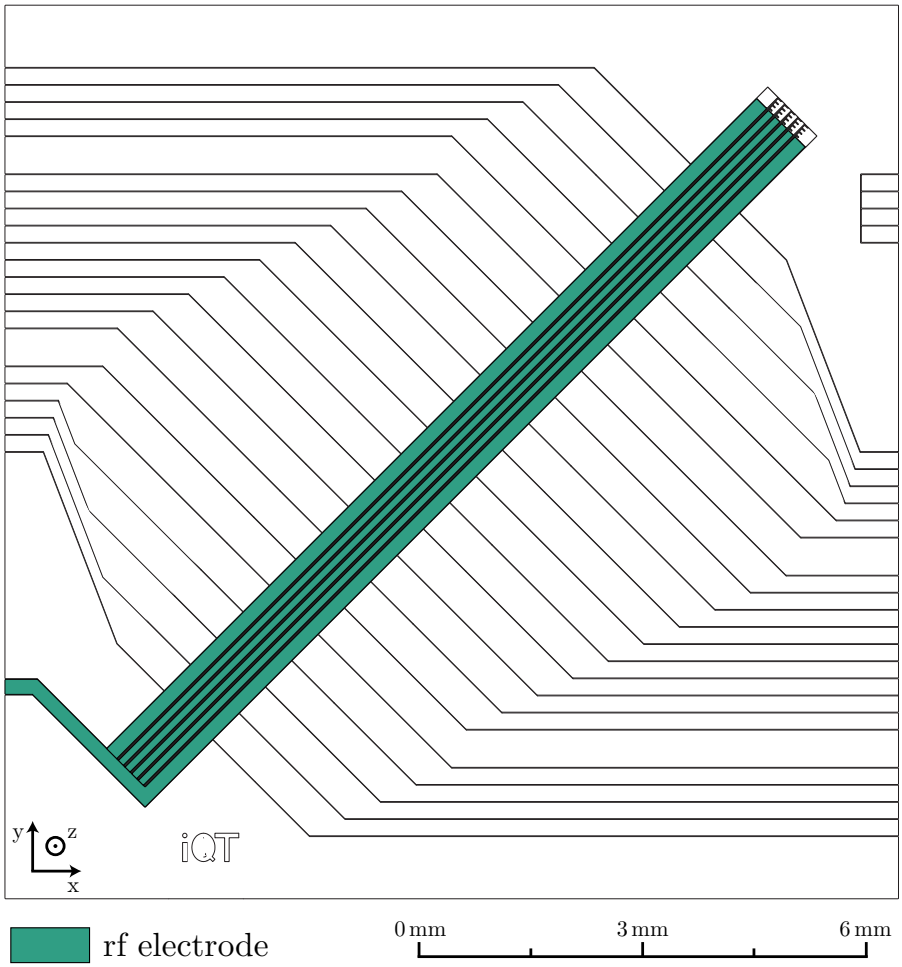

Figure 5.31: Complete design for the flat multipole trap. The rf electrodes are shaded in green. The trap possess 40 dc control electrodes for ion shuttling and 6 rf electrode lines to produce 5 linear trapping regions.

between each rf electrode the ground electrodes are replaced with four control electrodes which can be used to apply principal axis rotation. Each electrode has a 4 μm width and are separated by a 3 μm gap.

The final design for the flat multipole ion trap chip described is given in figure 5.31. Similarly to the vertical shuttling trap, the flat multipole chip has been designed to be 12$\times$ 12 mm to meet cryogenic mounting requirements described in section 4.7. The chip also contains 40 control electrodes to provide axial containment and shuttling capabilities. While each linear trapping region can trap $\sim$ 2000 ions, the separation between each of the linear regions is too large to allow for strong coupling across regions.

Chapter 6

Microfabrication

A key challenge towards a universal ion quantum computing is the development of a scalable trap architecture. While macroscopic ion traps have demonstrated several features and requirements for a quantum computer [50, 53, 157, 158], the underlying architecture is inherently less scalable to complex systems with large numbers of ions. An alternative to macroscopic traps, which possess mechanically machined features on the centimetre scale, is microelectromechanical systems (MEMS), which possess features on the micron scale. The microfabrication technologies used for creating MEMS devices offer precise fabrication processes, allowing ion traps to be scaled down in size with features orders of magnitude smaller than macroscopic traps. The increase in fabrication resolution also brings several other advantages, such as superior ion control, and the inclusion of microwave [20,188] and magnetic field generating structures [189] close to the ion. Complex electrode architectures enable the creation of confining potentials in novel geometries with small ion-ion distances, allowing for quantum simulations not possible with macroscopic traps, and multi-ion operations using advanced shuttling protocols [84]. Coherent manipulation techniques can also be scaled to large numbers of ions, paving the way for large scale quantum computing. This chapter describes the techniques used to create microfabricated ion traps, which are photolithography (sections 6.1), deposition (section 6.2) and etching (section 6.3); as well as the fabrication processes used to create NbN and gold based ion traps (section 6.4-6.5).

6.1 Photolithography

The photolithography process involves the application of optical radiation to pattern a photosensitive material which has been applied to a substrate. To begin the process, the substrate is first cleaned using solvents and then baked in a convection oven or on a hot

plate to dehydrate the surface. A photosensitive chemical, known as a photoresist, is then applied to the centre of the substrate. To ensure a uniformly thick coating of the resist, the substrate is spun at 1000-6000 rpm for 30-60 s, providing a layer a few microns thick. The thickness of the photoresist can be controlled by varying the quantity of photoresist applied and the rotation speed of the sample.

An unwanted consequence of the spin coating process is the thickness of the photoresist being greater towards the edges of the substrate. This effect, known as edge bead, is a result of the surface tension and the viscosity of the photoresist. The variation in thickness can be problematic as it could lead to a degradation in fabrication quality for several reasons. Firstly, thicker areas may not be fully removed during later stages resulting in difficulties for subsequent deposition and etching processes. Secondly, the mask which holds the design to be patterned may not sit tightly on the surface of the resist, leading to errors in exposure. One solution to remove edge bead is to use a photoresist dissolving solvent, such as acetone, to remove the excess.

Once the photoresist has been applied, it is soft baked on a hot plate to dry the layer. A patterned chrome mask is then aligned and pressed on top of the dried photoresist using a mask alignment tool to an accuracy of 2 μm. The pattern on the mask is then applied to the photoresist by exposing the photoresist through the mask using a UV light source. Shorter wavelengths can produce more accurate results due to a reduction in diffraction, therefore typically wavelengths below 400 nm are used. For exposures described in sections 6.4 and 6.5 an I-line optical bandpass filter corresponding to the Hg vapour lamp I-line emission at 365.4 nm was used. After exposure the design can be developed by placing the wafer in an alkaline based developer solution. The chemical developer removes either the exposed or unexposed areas depending on the polarity of the photoresist applied. For a negative photoresist the exposed areas become soluble in the developer. Similarly, unexposed regions using a positive photoresist become soluble in the developer. Figure 6.1 shows the photolithography process steps for both positive and negative photoresists.

6.2 Deposition

Deposition is another fundamental process in MEMs technology. As the name suggests, the process allows the deposition of various materials to produce complex structures with thicknesses $>100\,\mu$m. There are several types of deposition processes depending on the materials being deposited and the structures being formed. This section outlines common deposition processes used for fabricating ion traps.

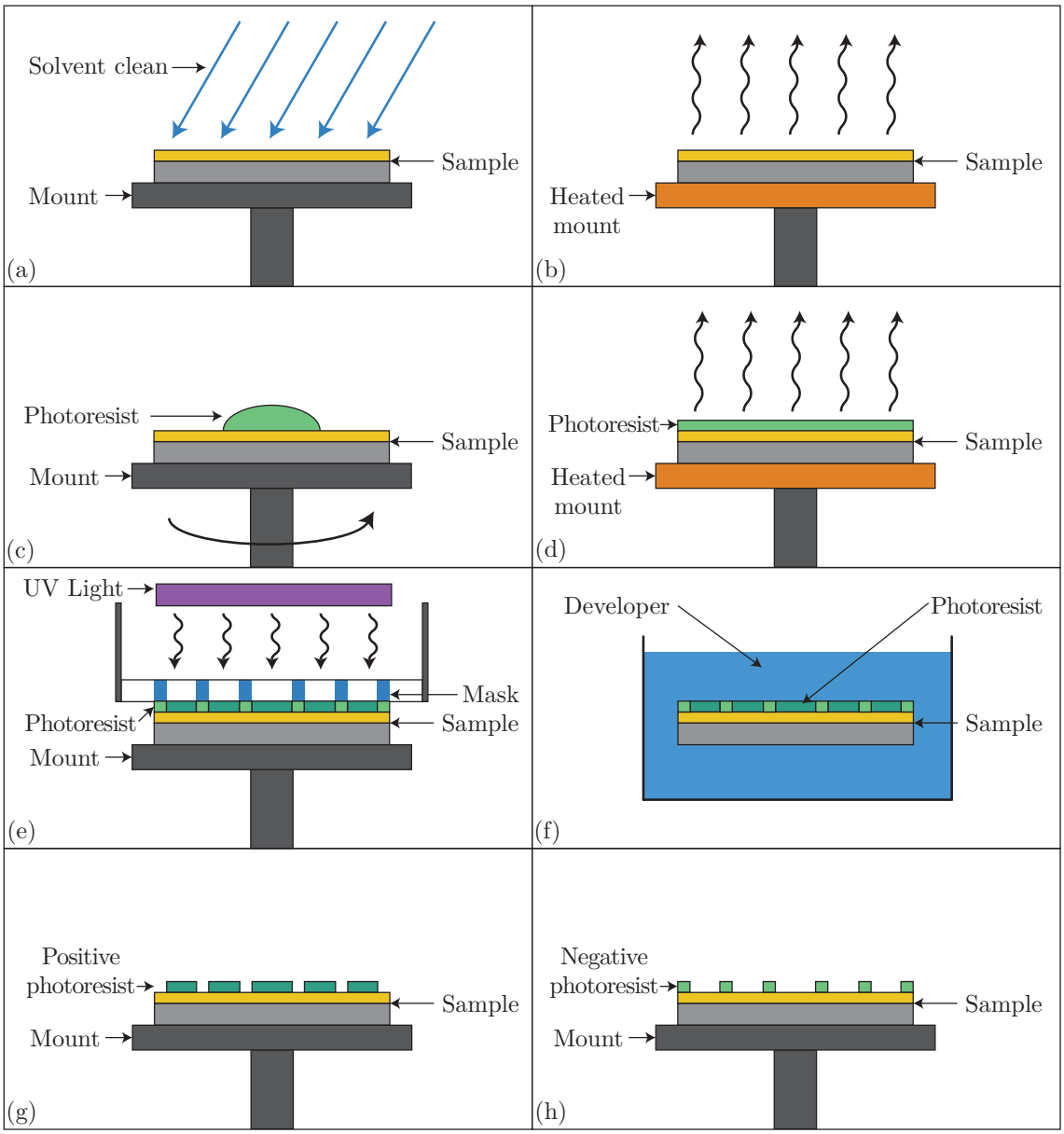

Figure 6.1: Process steps for photolithography showing (a) solvent cleaning, (b) dehydration, (c) photoresist application, (d) soft bake, (e) exposure, (f) development, and the results for (g) positive and (h) negative photoresist.

6.2.1 Sputtering

The sputtering technique uses a solid target formed from the metal or dielectric material to be deposited. The target is placed in a vacuum chamber and is subjected to high energy accelerated plasma ion beam. This results in the target material being ejected from the surface. To deposit the ejected material, the sample is placed within the vacuum chamber and opposite to the target (figure 6.2). A shutter is used in between the target and sample to allow the precise control of exposure times. The thickness of the deposition can be measured by observing the oscillation frequency of a quartz crystal placed next

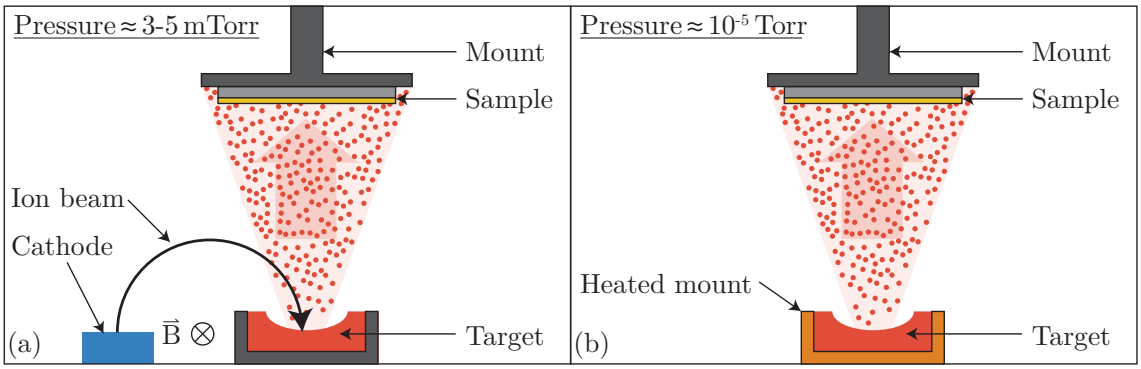

Figure 6.2: (a) Sputter deposition process and (b) thermal evaporation.

to the sample. The resonant frequency of the crystal will vary as a function of the deposited material upon its surface. A significant benefit of the sputtering process over other deposition techniques is the ability to deposit metals with a high melting temperature. However, due to the profile of the sputtered flux it is difficult to deposit material precisely within a confined region of the sample as most of the sample area will be coated. The deposition rate from the sputtering technique also varies as a function of time. As the ion beam strikes the target and removes material, it creates a channel on the target surface. The changing profile of the target surface at the point where the beam strikes results in a decrease of the sputter deposition rate.

6.2.2 Thermal evaporation

Thermal evaporation is a deposition technique used to form thin metal layers ($\sim$0.5 μm). The process begins by placing the source material in vacuum (10^{-7} mbar) and ohmically heating it until it begins to evaporate. Similar to the sputtering process, the sample is placed opposite the source material, with a shutter in between and a quartz crystal used to measure the deposition thickness. The evaporated material is deposited as it condenses upon striking the surface of the sample. An alternative method to ohmic heating is the use of a high energy electron beam to heat the source. This allows localized heating, preventing contamination from other heated sources. Typical evaporation rates during this process are 0.2-0.4 nm/s. Similar to the sputter deposition technique, thermal evaporation is also limited to the coating the entire sample area simultaneously. However, a benefit of thermal evaporation over sputtering is a constant deposition from a thermally heated target material.

6.2.3 Electroplating

Electroplation is a common deposition technique that can produce relatively thick metal layers $> 100\,\mu$m. The technique is an electrochemical process and requires a negatively charged sample (cathode) and a positively charged source (anode) placed within an electrolyte solution (plating bath). To electroplate an ion trap a conductive seed layer is required, which can be electrically connected to the positive end of a voltage supply. Passing a current through the solution creates a circuit between the source material (anode) and the sample (cathode) (figure 6.3). As an example, for gold plating the negatively charged cathode attracts gold ions within the solution, which form gold atoms on the cathode. The plating bath is then replenished with gold ions from the positively charged anode and the process repeats.

6.2.4 Plasma-enhanced chemical vapour deposition (PECVD)

The PECVD process is used for the deposition of thick dielectric layers, which can provide an insulation layer in between conductors. The deposition is performed by a reaction of gases that results in deposition on a sample. The process begins by placing the substrate within a specialized vacuum chamber, known as a reactor, and heating the sample to $\sim$300°C. The deposition material is fed to the vacuum chamber in a gaseous state via a 'shower head' and an rf voltage ionizes the gas to form a plasma. A static voltage offset on the sample plate draws the plasma to the substrate creating a higher density of the plasma nearer the substrate. At the sample surface the ionized gas reacts to form a dielectric layer at a rate of $\sim$300 nm/min. The effective deposition rate is a combination of the deposition from the plasma and the sputtering from the samples surface. An alternative to PECVD is a low pressure CVD (LPCVD) technique. This process can improve the accuracy of the deposition by minimizing defects, however, it requires higher temperatures ($\sim$ 800°C) and has a slower deposition rate of $\sim$ 50 nm/min.

6.3 Etching

Etching is the final key step in the microfabrication process. Etching allows for deposited material to be removed or 'etched' away. As with deposition, the materials and geometries to be etched determine the etching process to be used. This section describes common etching techniques used for the microfabrication of ion traps which can be divided into 'wet' and 'dry' etches.

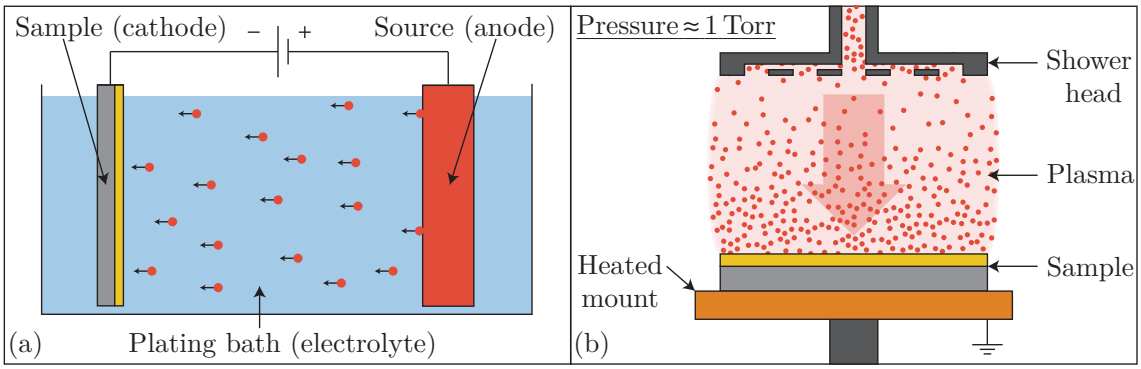

Figure 6.3: (a) Electroplating deposition and (b) plasma enhanced chemical vapour deposition (PECVD) deposition processes.

6.3.1 Wet etches

Wet etches operate by dissolving a targeted material and can be divided into isotropic and anisotropic etches. Isotropic wet etches dissolve the substrate equally in all directions. This can also provide lateral etching under the photoresist resulting in a circularly etched profile. The rate of etching can be increased and decreased by raising and lowering the temperature of the etchant respectively. For SiO_2 a useful etchant is hydrofluoric (HF) acid as it can be used to dissolve the substrate but does not dissolve silicon or gold. Undercut profiles can also be created by using a sacrificial layer. The purpose of a sacrificial layer is to allow additional layers to be deposited on top before being removed later. Sacrificial layers can be also be etched by using a highly concentrated HF acid vapour that selectively etches the layer. Alternatively, anisotropic etches can be used to gives uniform etching in different directions. For crystalline silicon, a potassium hydroxide (KOH) etchant displays an etch rate 400 times faster along the $\langle 100 \rangle$ plane compared with the $\langle 111 \rangle$ plane. Figure 6.4 shows the etching profiles for isotropic and anisotropic wet etches, anisotropic dry etches and undercut etches.

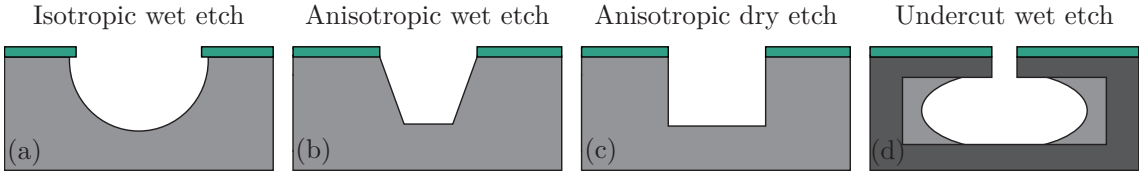

Figure 6.4: The etching profiles for (a) isotropic wet etches, (b) anisotropic wet etches, (c) anisotropic dry etches and (d) undercut wet etches.

6.3.2 Reactive ion etching (RIE)

RIE is a dry etching technique which unlike wet etching techniques does not require the substrate to be immersed in a solution. The RIE technique begins by placing the sample to be etched in vacuum. Selected gases are introduced into the chamber and are ionized using an rf field, similar to a PECVD process. The ions are then accelerated to the sample using a negative dc offset voltage to attract the ions. The ions striking the surface have sufficient kinetic energy to remove atoms from the surface of the sample in an anisotropic etching process. The process gases can also be varied such that the ions reacting with the surface form a gas to produce an isotropic etch. For SiO_2 a C_4H_8 plasma can be used to perform RIE.

Another RIE technique is deep RIE (DRIE) which is capable of etching deep channels with aspect ratios up to 50:1. DRIE is performed by alternating between two process gases during the etching process every few seconds. Firstly, one of the gases is used to create a protective polymer on the surface of the sample. The other gas is then introduced which etches anisotropically downwards via ion bombardment only at the bottom of trenches. As it does so, the polymer coating on the sidewalls prevents any lateral etching. This process can be repeated to etch downwards creating vertical sidewalls. Due to these features the RIE technique is the preferred over wet etches for anisotropic etching. Figure 6.5 shows the a diagram of the RIE procedure.

6.3.3 Inductively coupled plasma (ICP) etch

An ICP etch uses a denser and more highly energetic plasma compared with RIE to etch a sample. The process is performed by using a conducting coil connected to an rf source to generate an alternating magnetic field (figure 6.5). The inductive coupling creates a dense plasma which is then accelerated towards the sample using an additional rf field. The combination of the two rf fields provides ICP etching with superior control of the etching process and faster etch rates compared with RIE and wet etches. While ICP etching provides superior performance compared with RIE, the ICP equipment and process can be significantly more expensive to maintain and operate. For thin layers such as photoresist layers and layers with large non-critical feature sizes, an RIE process can provide a more cost efficient solution.

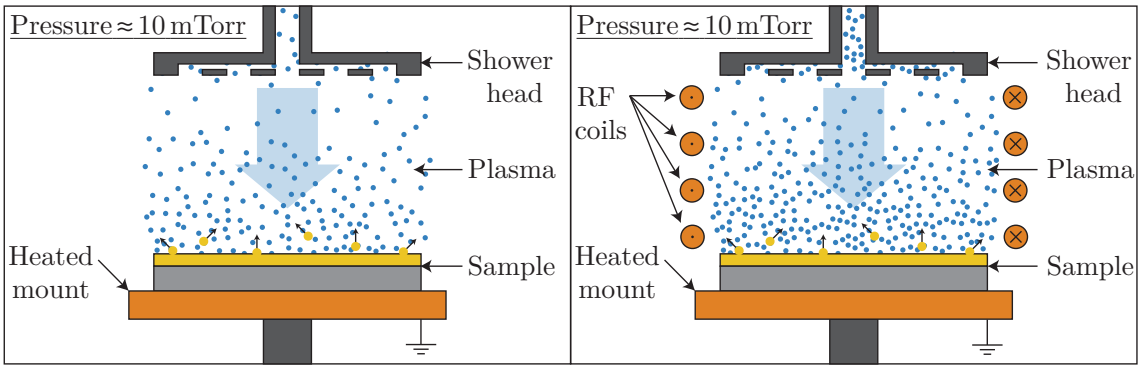

Figure 6.5: (a) Reactive ion etching and (b) inductively coupled plasma etching processes.

6.4 Niobium nitride ion trap fabrication

For the development of a super conducting high-Q microwave cavity, described in section 5.2, there are several considerations to the fabrication procedure that need to be taken into account. The following goals were considered while designing the NbN ion traps with integrated MW cavity:

- The effect of exposed dielectric on the trapped ion must be small for low ion electrode spacing.
- The MW cavity must be grounded without affecting the performance of the trap and cavity.
- The wafer must be formed from a low dielectric loss substrate.

Exposed dielectrics are an intrinsic problem for surface electrode ion traps as charge build up on dielectric surfaces can lead to the destabilization of the trapping potential. When the ion height is very low, $< 50\,\mu$m, the ion can become extremely susceptible. Exposed dielectrics can be reduced by increasing the ratio of electrode thickness and inter-electrode spacing. While the inter-electrode spacing is limited by the desired ion electrode spacing, the upper bound on the electrode thickness is determined by the choice of material and its fabrication process. Being a transition metal, the hardness of niobium (Nb) and all its nitrides with high T_c, such as niobium nitride (NbN) or niobium titanium nitride ($Nb_{1-x}Ti_xN$), is extremely high (6-7 on the Mohs scale of hardness [190]). In comparison, gold and aluminium are ∼2-3 times softer (2.5-3 on the Mohs scale). This makes the fabrication of a thick layer of niobium or its nitrides difficult. Thick layers of such materials have shown to develop internal stress resulting in cracks [191] and sometimes detachment off the substrate [192]. Moreover, since the growth rate of such materials is very low, typically 2-3 nm/min, growing a thick layer can take weeks of clean room time.

An alternative approach to reduce exposed dielectrics is to introduce a thin conductive ground plane above the substrate. This provides the added advantage of having a conductive ground plane that the half wave microwave cavity can be grounded to using a vertical interconnect access (via). The use of a grounding via also prevents the requirement of having additional space to place the microwave grounding electrodes on the surface of the ion trap.

For the ground and electrode layers the feasibility of microfabricating NbN was explored. The critical temperature of NbN (∼16 K) is higher compared to that of Nb (∼9 K) which is extremely beneficial when placed in a cryogenic system that operates at 4 K with minimal heat load. The deposition process of NbN is very similar to that of Nb, except for the use of a few standard cubic centimetres (∼5-20 cm^3) of ultra-high pure N_2 gas at a low partial pressure (typically 50 mTorr). The nitrogen gas is employed as a reactive gas in addition to the ultra-high pure argon used for Nb sputtering. The deposition process of $Nb_{1-x}Ti_xN$ is more complex as the experimental conditions such as temperature and gas pressure affect the stoichiometry, which in turn affects the critical temperature. NbN was therefore chosen as the material for the electrode and ground plane. The process design sequence can be divided broadly into the following three steps.

- Deposition of a conductive ground plane.
- Deposition of an insulating layer and generation of dielectric pillars.
- Deposition of a top electrodes layer.

Figure 6.6 shows the fabrication steps used to create the NbN surface ion trap. The fabrication process for both NbN and gold (section 6.5) ion traps was performed by Bjoern Lekitsch and carried out at the Southampton Nanofabrication Centre.

6.4.1 Wafer preparation

The wafer used for the NbN traps was a single crystal Al_2O_3 sapphire wafer (PI KEM ALC100D05C2) with a 4" diameter and a 500 μm thickness. Both surfaces of the wafer are polished to a surface roughness of <0.5 nm. Each trap design requires 13 × 13 mm of space resulting in space for 21 trap designs on each wafer.

For the deposition of a ground plane, the surface of the substrate was first cleaned with acetone, methanol and isopropanol, followed by baking to dehydrate the surface. The wafer was cleaned further by using a fuming nitric acid (FNA) at a concentration of >90%. The FNA is a strong oxidizer and can effectively remove organic material on the

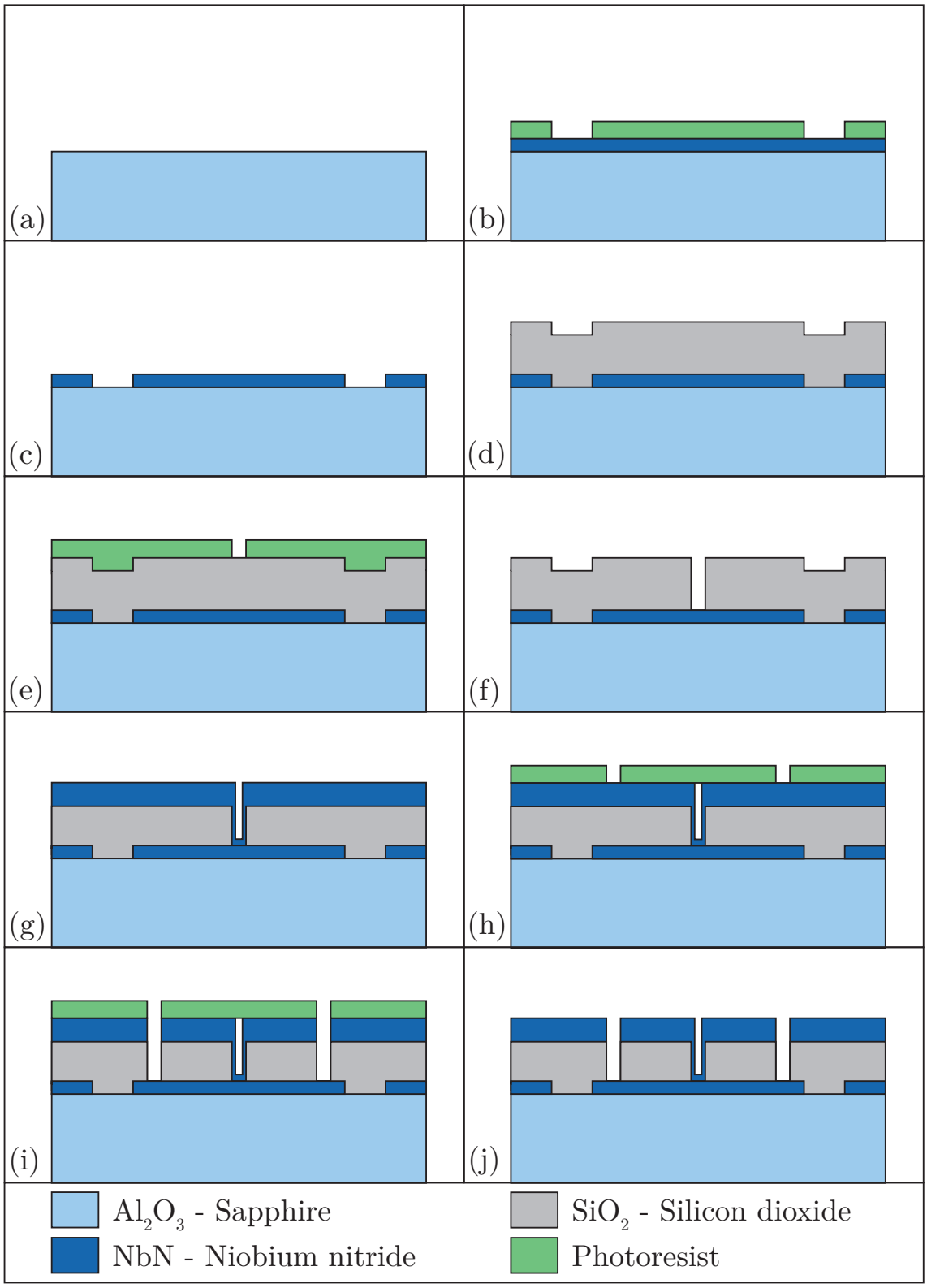

Figure 6.6: Fabrication process steps used to create NbN surface ion traps.

surface of the wafer. As well as ensuring a clean surface to fabricate upon, a clean surface also prevents the contamination of instruments used during the fabrication procedure. The FNA clean is performed by placing the wafer in an FNA tank for ∼10 min. Any FNA residue is then cleaned using deionized (DI) water and the process is repeated for a total of three times. Finally, the wafer is blown dry using an ultra pure nitrogen gas and the substrate is cleaned using an oxygen plasma. The oxygen plasma clean is known as a 'plasma ash' as it turns surface contaminants into ash which is then removed by the vacuum pump.

6.4.2 Conducting ground layer

The conducting NbN ground layer is deposited using a two stage sputter deposition process to produce a 500 nm thick layer. During the first stage, Nb is sputtered using an argon gas on a Nb target. The sample is rotated during this stage to ensure a uniform deposition. In the second stage, the sample is rotated towards a nitrogen plasma. The deposited Nb undergoes a nitrogenation process with the nitrogen plasma to form NbN on the surface of the sample. A negative photoresist (Shipley S1813) is then applied to the substrate. The sample is spun at 5000 rpm for ∼7 s, leaving a 1 μm thick photoresist layer. The photoresist is then soft baked at 115°C for 1 min. The exposed sample is then placed in a developer (MICROPOSIT MF-319) for 35 s. The NbN is etched using a ICP dry etch with sulphur hexafluoride (SF_6) and argon (Ar) process gases. The plasma is generated using an rf power of 1500 W at ∼2 MHz and accelerated using a 75 W rf field at 13.56 MHz. Figure 6.7 shows two sapphire wafers that have been coated with 500 nm thick NbN ground layer.

6.4.3 Insulating layer

A 3 μm thick insulating layer of SiO_2 was deposited using PECVD to separate the conductive ground layer and the top electrode layer. The process gases used was a combination of silane (SiH_4) and nitrous oxide (N_2O), diluted with nitrogen (N_2). The plasma is generated using 20 W of rf power at 13.56 MHz and the sample is heated to 350°C. The deposition rate for this process occurs at ∼65 nm/min.

After the deposition, a negative photoresist (AZ 2020) is spin coated on top of the SiO_2. The photoresist is spun for ∼35 s at ∼4000 rpm and baked dry at 100°C for 2 min. The sample is then exposed and placed in a developer (AZ 726 MIF). The SiO_2 is dry etched using an RIE process which exposes the underlying ground plane. The process uses octafluorocyclobutane (C_4F_8) and oxygen (O_2) as the process gases. The plasma is

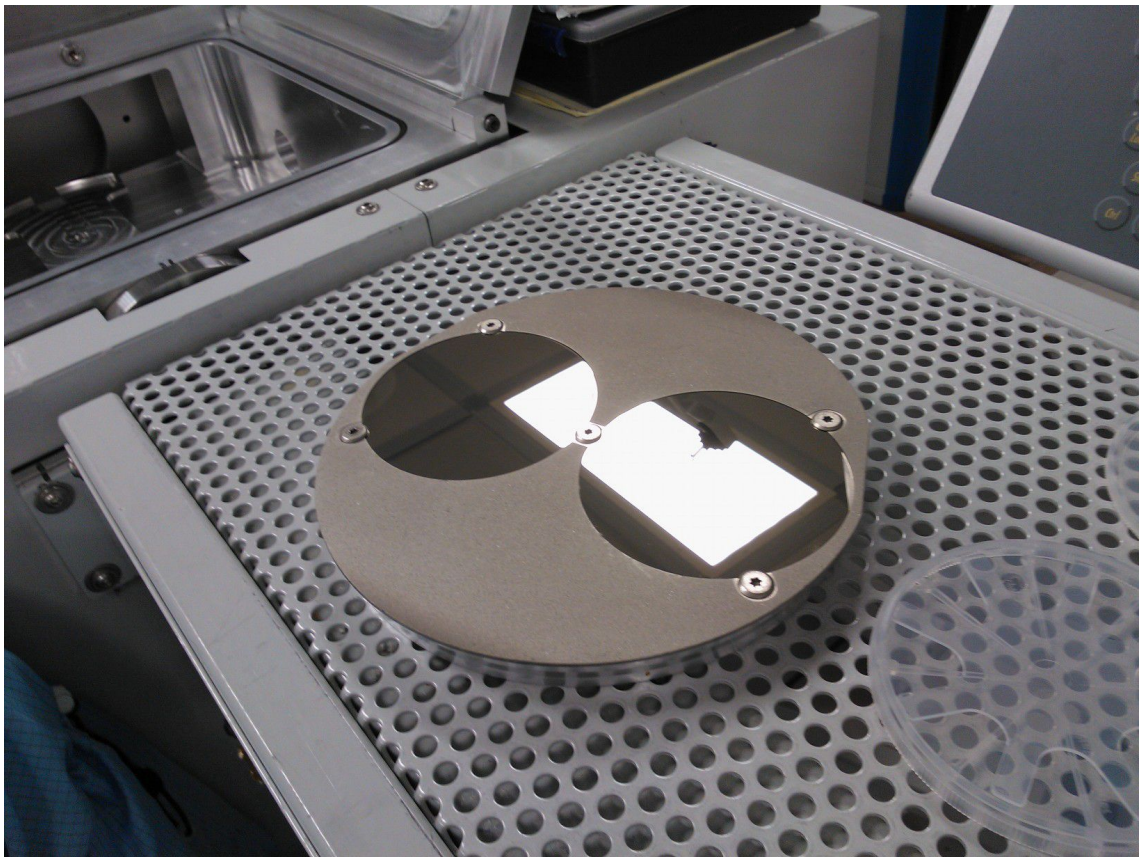

Figure 6.7: Two sapphire wafers coated with a 500 nm thick NbN ground layer.

generated using 1500 W at ∼2 MHz and accelerated using 100 W at 13.56 MHz producing an etch rate of ∼300 nm/min. The lift-off of the photoresist is then performed using hot N-Methylpyrrolidone (NMP) and an oxygen plasma.

6.4.4 Electrode layer and vias

The top electrode layer is formed from a 1 μm thick NbN layer and is deposited using the same process described for the ground layer 6.4.2. Similarly, the same photolithography and etching processes are used to etch the top NbN electrode layer as described in section 6.4.2. The SiO_2 is etched using the dry etch process as described in section 6.4.3.

6.4.5 Fabrication results

Figures 6.8 and 6.9 show scanning electron microscope (SEM) images of the vertical shuttling with microwave cavity ion trap (section 5.1) and flat multipole ion trap (section 5.3) respectively. Figure 6.10 shows a close up images of the microwave cavity's capacitive coupling gap and central via. An estimation using the SEM shows a fabrication error of ±20 nm in feature sizes.

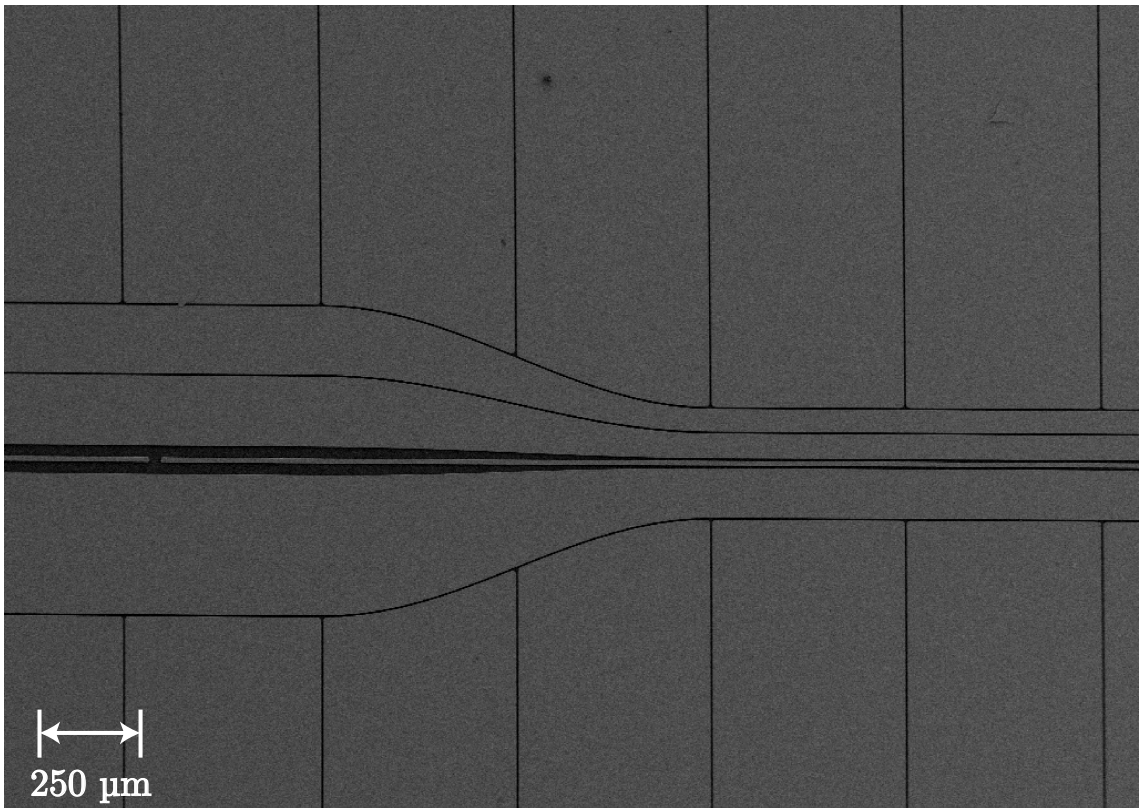

Figure 6.8: SEM image of a vertical shuttling ion trap with an integrated high-Q microwave cavity fabricated using NbN on a sapphire substrate.

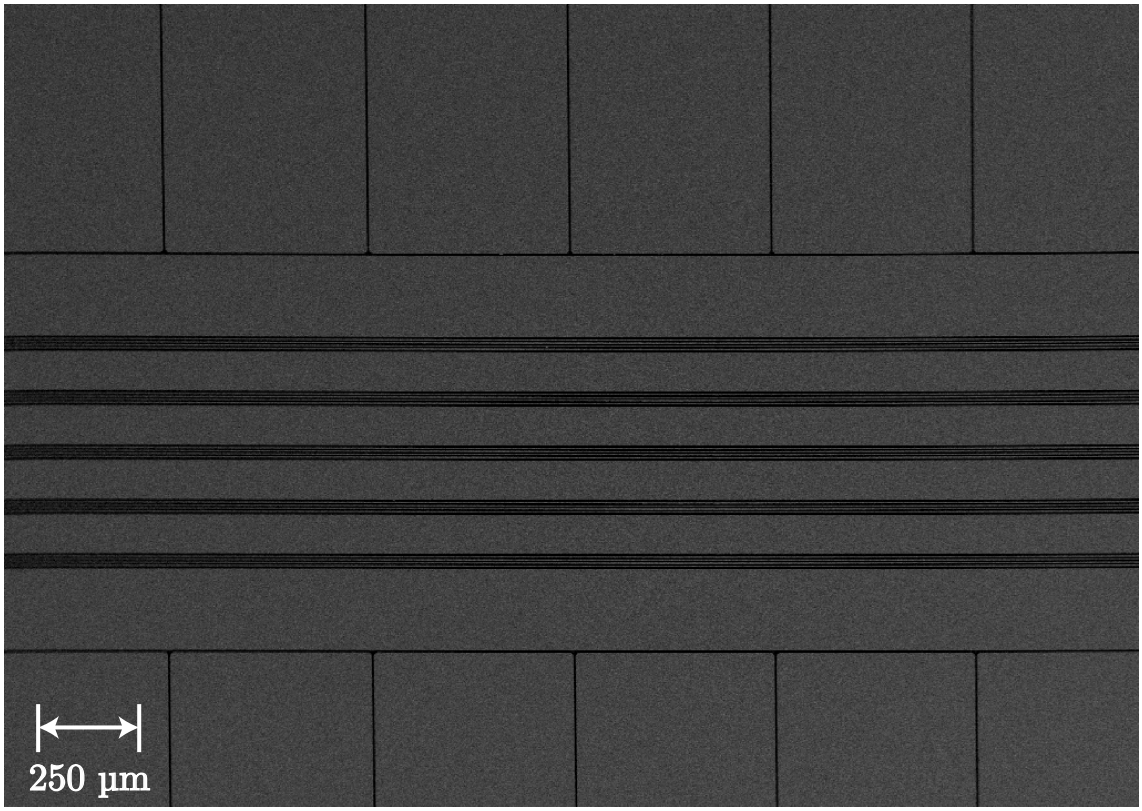

Figure 6.9: SEM image of a flat multipole ion trap fabricated using NbN on a sapphire substrate.

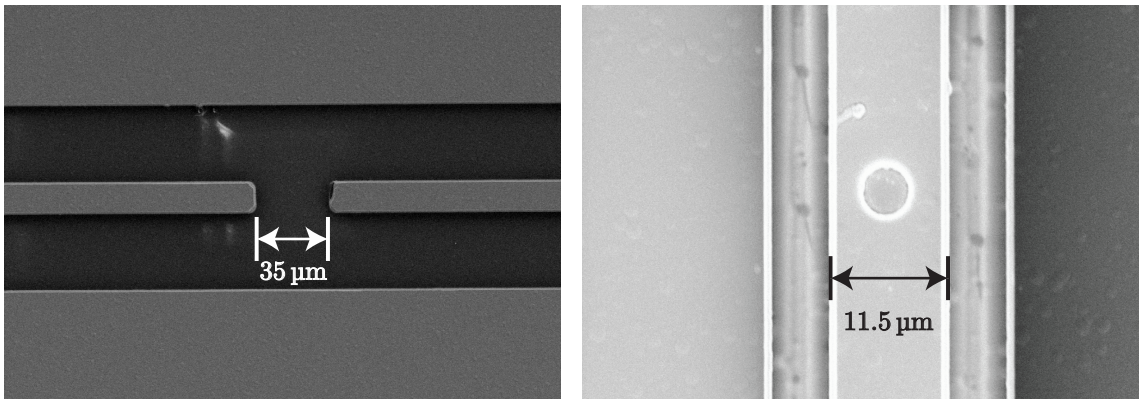

(a) (b)

Figure 6.10: SEM image of the capacitive coupling gap (a) and central via (b) on the vertical shuttling ion trap with an integrated high-Q microwave cavity.

6.4.6 Niobium nitride trap yield

The NbN traps were fabricated on two 4" wafers with 21 individual trap designs patterned on each wafer. The most significant issue with the fabrication of the NbN traps were the stresses observed in the NbN layers. Stresses in the layers resulted in areas appearing compressed or stretch resulting in the lift off of the layer. Figure 6.11a shows the effect of stress on the trap surface resulting in the fracturing of electrodes. Figure 6.12 shows the result of a stressed ground plane resulting in a 'lumped' electrode layer with a surface roughness $> 10^2$ greater than regions without a ground plane below. As a result of the stresses, one complete wafer could had to be discarded. Multiple significant fractures in NbN layers ran across the surface of the entire wafer making the ion traps unfit for use. The second wafer, while still suffering from visible stressing, possessed a number of traps which appeared to have all electrodes intact and fit for use. The exact cause of the stressing could not be determine without further testing. However, the most probable cause is the combination of an unoptimized niobium-nitrogen ratio and the rapid cooling of the layer after being deposited on a relatively hot (>500°C) SiO_2 layer.As well as the optimization of the niobium-nitrogen mixture, a post fabrication annealing process could help to reduce the stresses. This would involve heating the trap, holding it at a temperature close to where the crystalline phase change occurs and then cooling the trap at a slower rate. The annealing process allows the metal to gently soften and relax from its stressed state. Table 6.1 shows the trap yield and quality for all traps from the successful wafer.

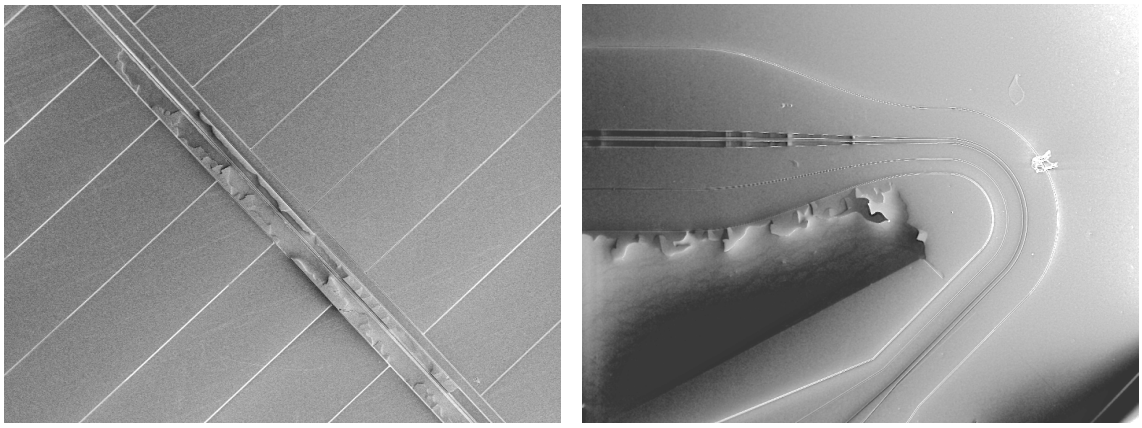

(a) (b)

Figure 6.11: SEM images of NbN ion traps showing the stresses in the NbN layers resulting in the lift off of layers, such as (a) the long rf electrodes and (b) the ground plane.

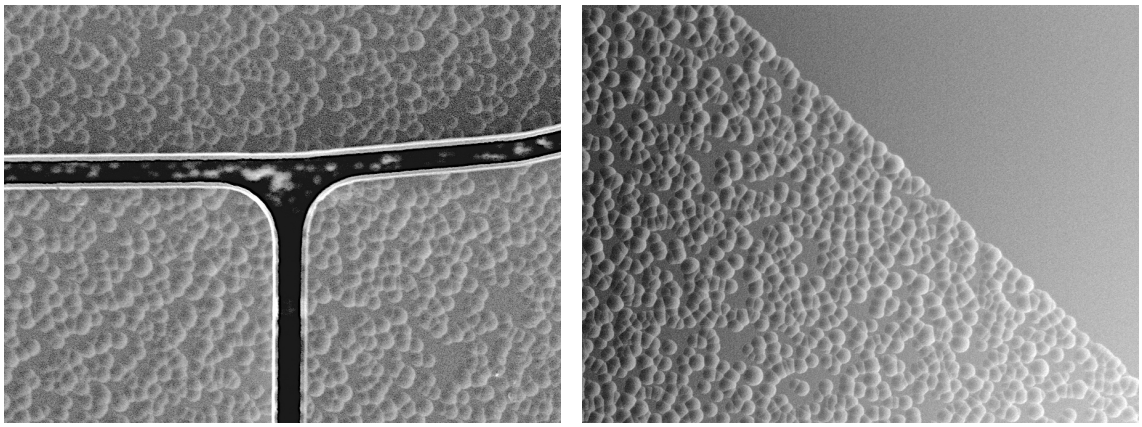

(a) (b)

Figure 6.12: SEM images of the top NbN layer (a) in between electrodes and (b) at the boundary of the ground plane. The lumped surface profile is a result of a stressed ground plane, which can be seen through to the top electrode layer.

Trap type	**Trap quality**			**Total**
	Fully functional[1]	Semi-functional[2]	Broken[3]	
Vertical shuttling trap with MW resonator	5	3	5	13
Flat multipole trap	1	0	1	2
X-Junction trap	0	0	3	3
Ring trap	0	0	3	3
Total	6	3	12	21

Table 6.1: Trap yield and quality for all gold ion traps from two wafers after the post fabrication cleaning procedure. [1] Traps with all electrodes intact with no damage. [2] Traps with broken or missing dc electrodes but still operational. [3] Major damage and cannot be used for ion trapping.

6.5 Gold ion trap fabrication

The same mask design used to fabricated the NbN on sapphire ion traps was also used to fabricate gold on quartz ion traps. Figure 6.13 shows the fabrication steps used to create the gold surface ion traps.

6.5.1 Wafer preparation

The wafer used for the gold ion traps was an optical grade fused quartz wafer (Micro-Chemicals GmbH JGS2) with a 4" diameter and a 500 μm thickness. Both surfaces of the wafer are polished to a surface roughness of <1.0 nm. As with the NbN wafer, each trap design requires 13×13 mm of space and therefore 21 trap designs can be placed on the wafer. Prior to deposition the wafer was cleaned using FNA and an oxygen plasma as described in section 6.4.1.

6.5.2 Conducting ground layer

The first deposition process is a chromium/aluminium/chromium (Cr/Al/Cr) (50/450/50 nm) layer. A thin chromium layer (50 nm) is deposited to increase the adhesion between the wafer and aluminium layer, and the aluminium layer and dielectric layer. The deposition of the chromium layers was performed by electron beam evaporation at a deposition rate of 1 Å/s and in vacuum at 5×10^{-6} mbar. The 500 nm thick aluminium layer is also deposited using electron beam evaporation at a deposition rate of 2.5 Å/s. A negative photoresist (Shipley S1813) is then applied and follows the same application, exposure and development techniques described in section 6.4.2.

6.5.3 Insulating layer

The insulating layer used is a 3 μm thick SiO_2 layer. The deposition of the layer is performed using PECVD and etched using RIE as described in section 6.4.3.

6.5.4 Electrode layer and vias

The final electrode layer is formed from a deposition of Cr/Al/Cr/Au (50 nm/1000 nm/ 100 nm/200 nm). The Al layer servers as the primary conductive electrode layer as thick gold layers of $1 - 2\,\mu$m can be difficult to deposit. The top gold layers serves multiple purposes; it prevents oxidation on the surface of the trap and reduces the resistivity of the electrode from $2.88 \times 10^{-8}\,\Omega m$ for Al to $2.42 \times 10^{-8}\,\Omega m$ for gold. This is most

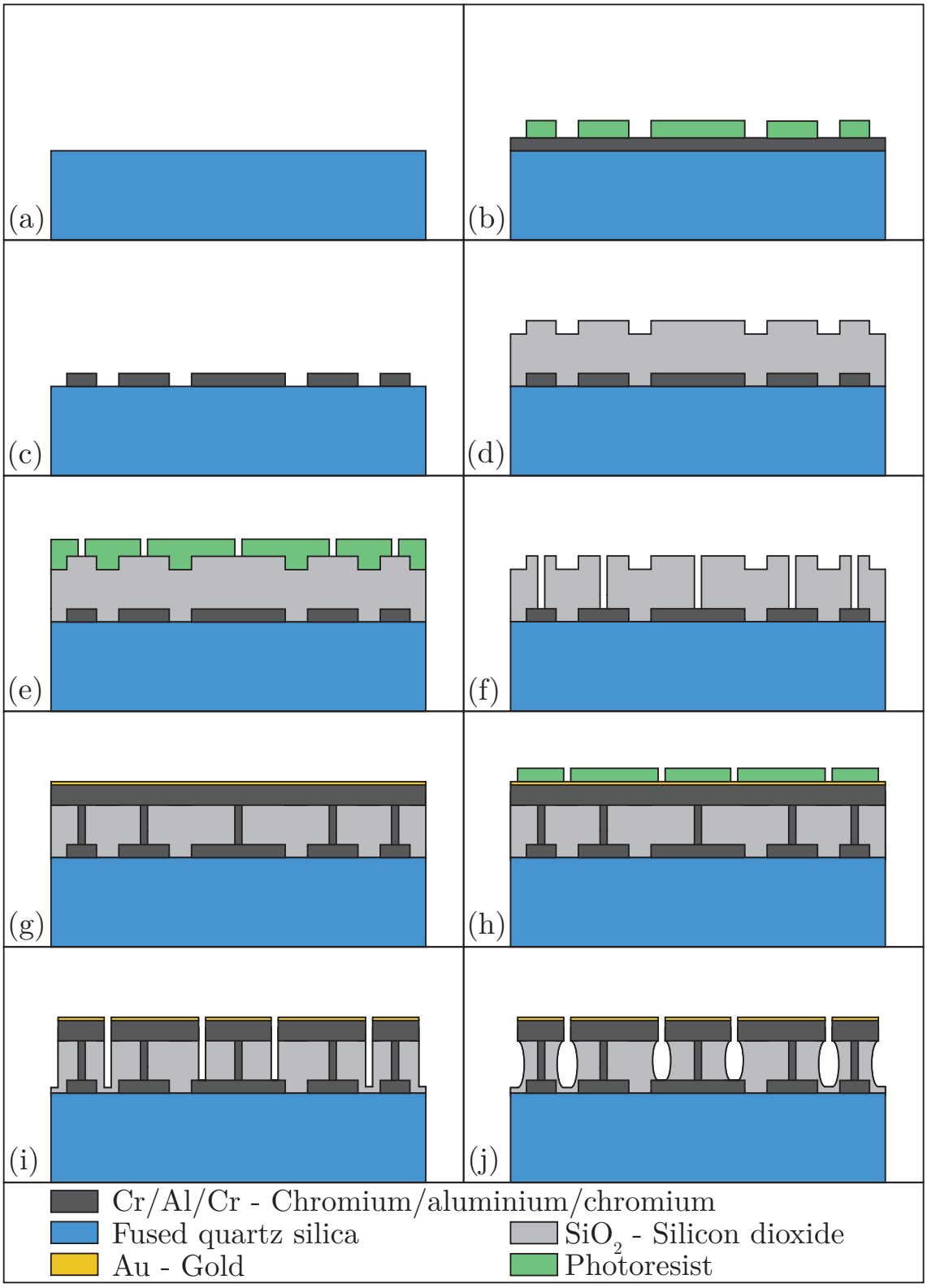

Figure 6.13: Fabrication process steps used to create gold surface ion traps.

significant for alternating voltages applied to the trap, with typical rf drive frequencies of $1 - 100\,\mathrm{MHz}$ corresponding to skin depths between $8 - 80\,\mu\mathrm{m}$ for gold. The soft gold layer also provides an ideal surface for wirebonding processes, which typically make use of gold bonding wire. The Cr layer in between the dielectric layer and Al layer acts as an adhesion layer to help form a stronger interface. The Cr layer between the Al and Au layers serves primarily as a diffusion barrier. This prevents the diffusion of gold into the Al layer, which can be accelerated at higher temperatures during the fabrication procedure and during the vacuum system baking process.

The chromium and aluminium layers are deposited using the same method of electron beam evaporation as described for the conducting ground layer in section 6.5.2. The top gold electrode layer is also deposited using an electron beam evaporation process at a deposition rate of $1\,\text{Å}/\mathrm{min}$. The process is performed in the same run as the aluminium layer without opening the vacuum chamber. A photoresist layer (AZ 9260) is spin coated on top of the gold layer at 3000 rpm for $\sim$60 s, producing a $6\,\mu\mathrm{m}$ thick layer. The resist is soft baked at 110°C for 180 s. The final mask layer is exposed and the wafer is placed in the developer (AZ 400K 4:1 diluted water) for 5 min.

The entire Cr/Al/Cr/Au layer is removed via multiple dry etches. Firstly, the gold layer is removed using an ICP etch with chlorine (Cl_2) and argon (Ar) process gases. An rf power of 1000 W at $\sim$2 MHz is used to create the plasma and 75 W at 13.56 MHz is used to accelerate it to the gold surface, producing an etch rate of $\sim$100 nm/min. The aluminium is removed using an ICP etch with chlorine (Cl_2) and hydrogen bromide (HBr) process gases. An rf power of 800 W at $\sim$2 MHz is used to create the plasma and 49 W at 13.56 MHz is used for acceleration. The SiO_2 is removed using the same ICP etch described in section 6.4.3. The resist is removed using FNA and a final HF acid wet etch is applied to produce an undercut.

6.5.5 Gold trap cleaning procedure

After fabrication, the gold ion traps were inspected using SEM imaging and found to have electrical shorts between electrodes (figure 6.14). To clean the surface and remove excess photoresist and gold material bridging between electrodes, the following procedure was performed.

1. A clean beaker is prepared with an acetone and isopropanol rinse, and filled with 50 ml of photoresist stripper (Technistrip P1316).

2. The beaker is heated using a hot plate to 80°C with the temperature measured

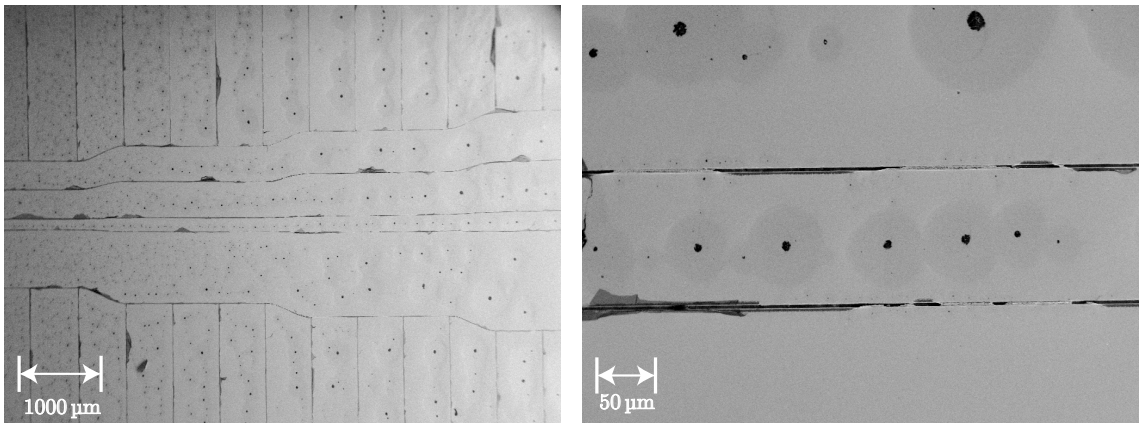

(a) (b)

Figure 6.14: SEM images of a gold ion trap after fabrication and prior to cleaning.

using a thermometer placed within the beaker. A wirebonder (Kulicke & Soffa 4523A) was used as hot plate with the plate temperature set at 110°C to maintain the solution at 80°C. Aluminium foil was used to cover the top of the beaker and prevent evaporation into the surrounding environment.

3. To prepare the trap for treatment, the trap can be placed faced down on clean room tissue and then gripped on the sides using a flat tipped pair of tweezers. A rubber band was used on the arms of the tweezers to prevent the trap from being released.

4. Once the stripper reaches 80°C the chip can be fully submerged. It is important to ensure that the trap does not make contact with the beaker to prevent surface damage. To suspend the chip another pair of tweezers was used to hold the tweezers gripping the chip (figure 6.15). The chip should be left submerged for 10 min.

5. After 10 min the beaker should be removed from the hot plate and placed in a sonic bath. The tweezers holding the chip should be suspended by hand whilst the beaker is in the sonic bath. The sonic bath should be operated for 10 s while holding the tweezers by hand.

6. The chip should then be immediately rinsed with acetone and isopropanol. The chip can be placed face up on a clean room tissue and blow dried using and inert gas such as helium, nitrogen or argon. Care should be taken that the chip does not move during the drying process by applying gentle pressure with the tweezers.

7. The trap can now be treated in a one part gold etch (Iodine 12% Solution) and five parts de-ionised water solution. The trap can be suspended in the solution using the tweezers for 30 s.

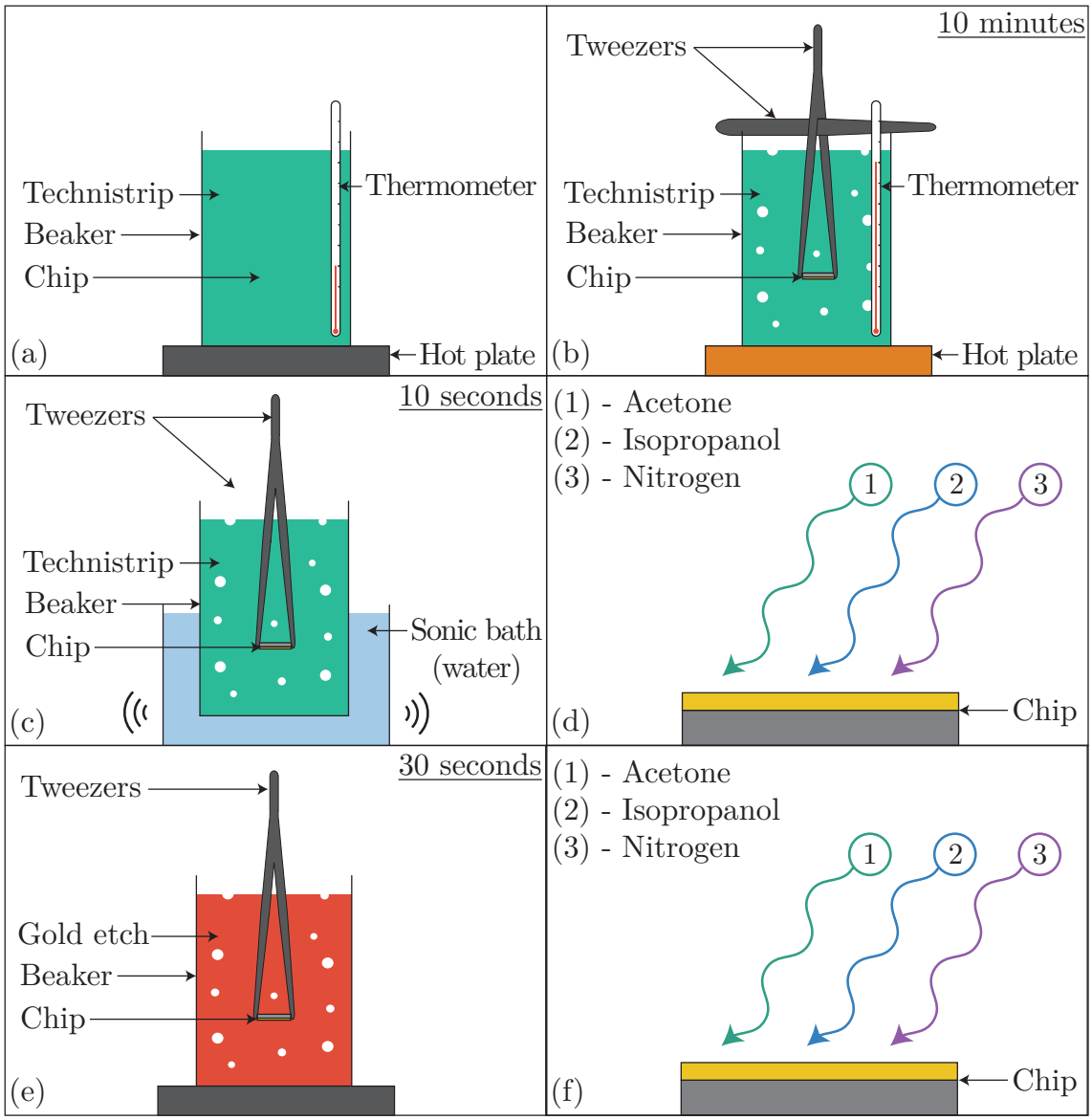

Figure 6.15: Post fabrication cleaning procedure for gold ion traps showing (a) the preparation of Technistrip, (b) treatment in heated Technistrip solution, (c) ultrasonic wash, (d) solvent and gas clean, (e) treatment in gold etch and (f) a final solvent and gas clean.

8. After the gold etch treatment the chip should be immediately rinsed in de-ionised water.

9. Step 6 should be repeated by cleaning the trap with acetone and isopropanol and drying with an inert gas.

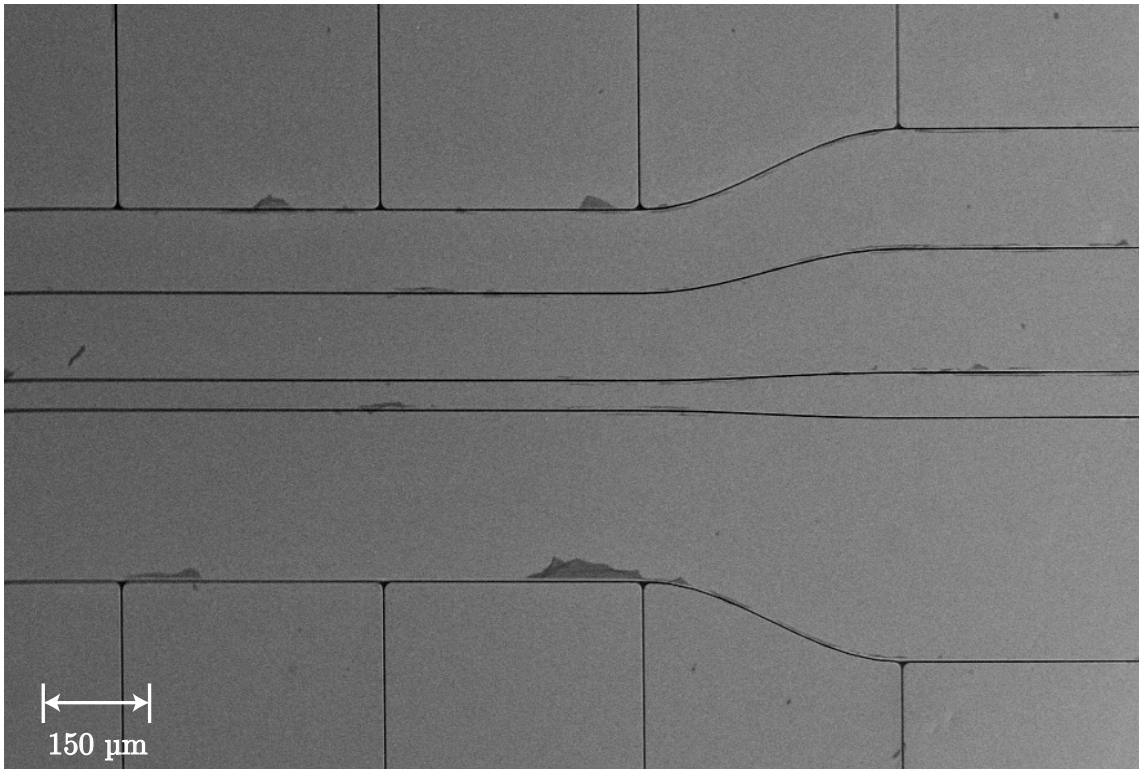

Figure 6.16: SEM image of a vertical shuttling ion trap fabricated using gold on a fused silica substrate after under going a post fabrication cleaning procedure.

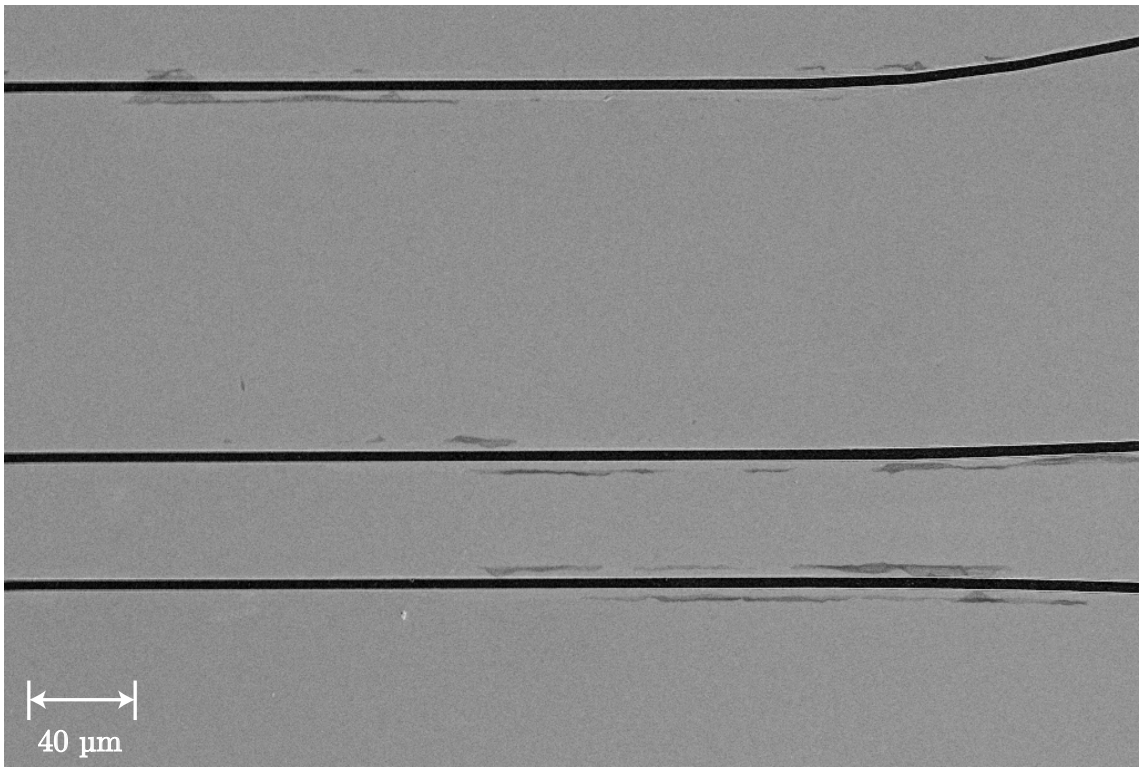

Figure 6.17: SEM image of the electrode gaps on an ion trap fabricated using gold on a fused silica substrate after under going a post fabrication cleaning procedure.

6.5.6 Fabrication results

Figures 6.16 and 6.17 show SEM images of the final microfabricated gold on quartz ion traps after a cleaning procedure. Both figures show a vertical shuttling ion trap with figure 6.17 showing a close up image of the electrode gaps, highlighting the removal of shorting material after the cleaning procedure.

6.5.7 Gold trap yield

The gold traps were fabricated on a single 4" wafer. Using the same mask design, 21 individual trap designs were patterned for the wafer. The most significant issue with the fabrication of the gold traps was the shorting of electrodes on the top gold electrode layer as described in section 6.5.5. As the cleaning procedure was successful, the wafer was suitable for use with varying degrees of fabrication quality across each trap. Table 6.2 shows the trap yield and quality for all traps from both wafers.

Trap type	**Trap quality**			**Total**
	Fully functional[1]	Semi-functional[2]	Broken[3]	
Vertical shuttling trap with MW resonator	10	1	2	13
Flat multipole trap	2	0	0	2
X-Junction trap	3	0	0	3
Ring trap	3	0	0	3
Total	18	1	2	21

Table 6.2: Trap yield and quality for all gold ion traps from two wafers after the post fabrication cleaning procedure. [1] Traps with all electrodes intact with no damage. [2] Traps with broken or missing dc electrodes but still operational. [3] Major damage and cannot be used for ion trapping.

Chapter 7

Integrating ion trapping and superconducting systems

7.1 Introduction

The advance of quantum technologies over recent decades has led to the realisation of qubits in various physical systems, such as ions [47], molecules [41], neutral atoms [42], superconducting qubits [43], quantum dots [44], nitrogen vacancy centres [45] and photons [46]. Some systems posses natural advantages over others in the form of longer qubit coherence times or faster logic gates. This has led to the promising approach of developing a scalable quantum computer, not only by improving the properties of an individual qubit type, but by exploiting the strengths of different systems to perform different tasks in a combined quantum hybrid system [69].

Two key tasks required for quantum computation is the processing and storage of information. In a quantum hybrid system, a dedicated system can be used to perform quantum computation processes, such as quantum logic gates, and a separate system can be used to store the information. An ideal quantum storage system can be formed from a physical system with coherence times much longer than gate operation times, such as atoms, ions or spins. Likewise, quantum processors can be formed from systems that are capable of performing gate operations at the shortest time scales, such as superconducting qubits.

A major challenge in realizing a hybrid system is the ability to transfer information between the different qubit types. In the case of atoms, ions or spins directly coupling to superconducting circuits via their electromagnetic fields, the coupling is relatively weak due to the systems being far off resonance with each other. Alternatively, different qubit types can be coupled indirectly via an intermediate ‘bridge’, which interacts strongly with

both qubit types and allows the transfer of information. This bridge can take the form of superconducting LC and coplanar waveguide (CPW) resonators [69] that serves as a quantum data bus, which can transfer information from a quantum processor to a quantum memory system. For different qubit systems, there exists several proposals and demonstrations of their interaction with superconducting circuits towards their implementation in hybrid systems. Here, we begin by briefly outlining the different approaches to couple trapped ions to superconducting qubits, highlighting the benefits and difficulties in implementing them into a hybrid system.

7.1.1 Superconducting qubits

While superconducting qubits have short coherence times of $\sim \mu$s, they still have significant potential because of their strong electromagnetic interactions and fast gate operation times of 10's ns [142]. Superconducting charge and phase qubits couple to the electric field of superconducting resonators [193], while the flux qubit couples to the resonators magnetic field [194]. The coupling between a superconducting qubit and a single electromagnetic mode in a resonator circuit is the largest across all qubit systems. For the case of a charge qubit coupled to a single electron field mode, the coupling strength g can be given as [193]

$$g = \frac{\beta e}{\hbar}\sqrt{\frac{\hbar\omega_r}{cL}}, \tag{7.1}$$

where L is the length of the transmission line resonator, c is the capacitance per unit length of the transmission line resonator, ω_r is the resonant frequency of the resonator and $\beta \equiv C_g/C_\Sigma$, where C_g is the capacitance of the superconducting island and $C_\Sigma = C_J + C_g$, where C_J is the capacitance of the Josephson junction. For an experimentally realistic system, $\beta \sim 0.1$, $\omega_r \sim 10\,\text{GHz}$, $L \sim 1\,\text{cm}$ and $c \sim 50\,\text{pFm}^{-1}$, resulting in a coupling strength of $g/2\pi = 50\,\text{MHz}$ [193].

7.1.2 Trapped ions

Trapped and laser cooled ions have been extensively used to demonstrate many aspects required for quantum computing [49, 158, 195–200] and is currently a leading technology with which a large-scale quantum computer can be constructed. Ions trapped in an ultra-high vacuum (UHV) weakly interact with their environment and are easily manipulated using electromagnetic fields. While two-qubit gate operations can take $\sim$100 μs to perform [158,201], trapped ions make ideal systems for storing quantum information with coherence times as long as tens of seconds [57].

Magnetic dipole coupling

Developing upon the work by Verdú *et al.* [202], who demonstrates strong magnetic coupling of an ultracold atomic ensemble to a superconducting CPW, we can also calculate the expected coupling between a CPW and the hyperfine ground state of an ion. The coupling between a single $^{171}\mathrm{Yb}^{+}$ ion and a single microwave photon field of a CPW is given as [202]

$$g = \frac{1}{\sqrt{2}} \left\langle 1 \left| \mu_B \left(g_s \vec{S} - \frac{\mu_N}{\mu_B} g_I \vec{I} \right) \right| 0 \right\rangle \vec{B}_{trans}\left(\vec{r}\right), \tag{7.2}$$

where the term in the bra-ket represents the M1 transition matrix elements between the two hyperfine levels in the ground state of a $^{171}\mathrm{Yb}^{+}$ ion, μ_B is the Bohr magneton, μ_N is the nuclear magneton, $g_s \sim 2$ is the electron g-factor, g_I is the nuclear g-factor (where $g_I \ll g_s$) and $\vec{B}_{trans}\left(\vec{r}\right)$ is the transverse magnetic field at an ion height r.

As the magnetic field strength decreases with ion height as $B \propto d^{-2}$, one potential solution to increase the coupling is to ensure the lowest experimentally limited ion height. However, a major limiting factor for surface electrode ion traps is the minimum ion height (d) required above the CPW. This constraint is due to optical access for ionization and Doppler cooling lasers, as well as ion heating, which scales as $d^{-3.5\pm0.1}$ [5]. Following these constraints we can limit the minimum ion height to 30 μm [47].

The transverse magnetic field of a cavity can be calculated by performing a numerical simulation using a boundary element method. The cavity can be simulated such that the total energy within a defined volume around the cavity is equal to the energy of a single photon at 12.6 GHz. For an ion height of $\sim$30 μm, an rf electrode separation of $\sim$20 μm is required. Within the centre of this separation, a superconducting microwave cavity with a width of 10 μm, a gap of 5 μm on either side and a height of 5 μm was simulated. The field strength at the ions position was determined to be $\sim$1 μG. Using Eq. 7.2, this results in a coupling strength between the ion and CPW of $\sim$1 Hz. This is significantly lower than the cavity decay rate of $\kappa = \omega_{CPW}/Q \sim 126$ kHz for a CPW with a quality factor of $\sim 10^5$ and with a resonant frequency of 12.6 GHz corresponding to the hyperfine ground state of $^{171}\mathrm{Yb}^{+}$.

The final technique to further enhance the coupling is to consider an ensemble of ions, where the coupling constant now scales as $g_{ensemble} = \sqrt{N}g$ for N number of two-level systems [186]. However, even for large ensembles of 10^6 ions, the effective coupling strength is still limited to $\sim$1 kHz. Despite this improvement, the coupling strength is still significantly lower than the cavity decay rate. While the cavity decay rate can be decreased

by increasing the quality factor of the CPW, currently technology is limited to Q values of 5×10^5 [203]. For coupling via the magnetic dipole in this scheme the decay rate of the resonator mode is dominant, which prevents the efficient and coherent information exchange between the systems.

Electric dipole coupling

We could potentially increase the coupling between an ion and a superconducting circuit with the use of Rydberg ions, by considering coupling via the electric dipole moment. Rydberg ions are ions whose outermost electrons have been excited into a high energy state with a large principle quantum number n. The highly excited Rydberg state results in a large electric dipole moment, which could be coupled to microwave resonators on the order of MHz as discussed for atoms [204].

Despite the possibility of generating stronger coupling, Rydberg ions also suffer from a number of drawbacks. One primary challenge is the complex laser schemes required to reach the Rydberg states in ions. Either a single vacuum ultraviolet (VUV) laser or a multiple UV laser sources are required. VUV laser light is strongly absorbed by air and thus requires the setup to be in vacuum. A recent demonstration of a single trapped $^{40}Ca^{+}$ ion utilized a laser at 122 nm to reach a Rydberg state with $n = 64$. Additionally, the energy of a photon at 122 nm, given by $E = \hbar\omega \sim$10.2 eV, is much greater than the work function of commonly used surface materials for trap electrodes, such as gold (5.1 eV). This leads to the added difficulty of electrodes charging and perturbing the trapping potential.

Motional dipole coupling

An alternate indirect coupling method has also been proposed by Kielpinkski *et al.* [68], where the ions electric dipole, induced by ion motion, couples to the electric field of a superconducting LC circuit. This method addresses the off resonant systems by modulating the superconducting LC circuit oscillating in the GHz regime, ω_{LC}, with a signal at the ions motional frequency, $\omega_i \sim 1 - 10$ MHz. The ion is then confined between two capacitor plates linked to the LC circuit. The coupling between the ion and the circuit then becomes resonant when $\omega_i \approx \omega_{LC} \pm \nu$, where ν is the modulation frequency of the capacitance. Spin-motion protocols based on laser [205], microwave [47] or radio frequency fields [165] allow for the generation of spin-motion entangled states, allowing the information in the motional state to be swapped to the long lived spin state.

The classical dipole interaction energy of the ion placed within the axial electric field of

the capacitor, E_z, can be given as [68]

$$U = ezE_z = \frac{e\zeta}{h}zV = \frac{e\zeta}{hC}zQ, \tag{7.3}$$

where e is the charge of an electron, z is the harmonic oscillator length of the trapped ion, ζ is the dimensionless geometry factor determined by the structure of the electrodes, h is the ion height, V is the voltage between the capacitor plates, $C = C_0\left[1 + \eta\sin\left(\nu t\right)\right]$ is the total capacitance of the circuit, C_0 is the total static capacitance and Q is the total charge of the circuit. Assuming a modulating capacitance to modulate the circuit frequency, Eq. (7.3) can be given as [68]

$$U\left(Q, z, t\right) = \frac{e\zeta}{hC_0}\left[1 - \eta\sin\left(\nu t\right)\right]zQ, \tag{7.4}$$

where the modulation depth of the capacitor is kept as $\eta \ll 1$. By quantizing the LC and ion motion, keeping the modulated capacitance motion classical and assuming the rotating wave approximation, the Hamiltonian of the LC-ion system is given as [68]

$$H_{int} = \frac{2i\hbar g_0\eta}{3}e^{-i\Delta t}ab^\dagger + \text{H.c.}, \tag{7.5}$$

where $\Delta = \nu - (\omega_{LC} - \omega_i)$, a is the annihilation operator of the microwave photon mode, $b^\dagger$ is the creation operator of the ion motional mode and g_0 is the coupling constant given as

$$g_0 = \frac{e\zeta z_0 q_0}{hC_0\hbar}, \tag{7.6}$$

where q_0 is the zero-point charge fluctuation on the resonator. Kielpinski [68] describes the case for a $^9\text{Be}^+$ ion with a secular frequency of $\omega_i = 2\pi \times 1\,\text{MHz}$ in an ion trap with geometry factor of $\zeta = 0.25$. The harmonic oscillator length of the ground-state mode can therefore be given as

$$z_0 = \sqrt{\hbar/2m\omega_i} = 24\,\text{nm}, \tag{7.7}$$

where m is the mass of the ion. A static capacitance of $C_0 = 46\,\text{fF}$ and an inductance of $L_0 = 400\,\text{nH}$ are chosen to produce a resonant frequency of $1\,\text{GHz}$, with a characteristic impedance of $Z = 2.7\,\text{k}\Omega$. This results in a zero-point charge fluctuation of

$$q_0 = \sqrt{\hbar/\left(2Z\right)} = 1.4 \times 10^{-19}\,\text{C}. \tag{7.8}$$

Using Eq. (7.6), a coupling constant of $g_0/2\pi = 200\,\text{kHz}$ is achieved using the parameters given above. Assuming a capacitance modulation depth of $\eta = 0.3$ (whose motivation is described in section 7.2.1), this gives an effective coupling strength of $g/2\pi = 60\,\text{kHz}$, where $g = g_0\eta$. This coupling is much larger than the decoherence rate of $10^3\,\text{s}^{-1}$ [68].

While this method may be capable of producing a strong coupling between the ion and the resonator, it remains an experimentally challenging task to incorporate all necessary features onto a single microfabricated ion trap. In section 7.2 we discuss how this can be accomplished and present the design, simulation and microfabrication methods for an ion trap incorporating all features to realize this scheme.

The development of an experimental infrastructure capable of operating both systems also provides significant challenges. While some requirements for both systems are similar, such as low noise and the use of vacuum systems, the operation of superconducting qubits requires the number of quasiparticles in the superconductor to be negligible. Thus, the temperature of the system has to be kept under 50 mK for aluminium technology, where the Josephson junction is formed from an aluminium oxide layer in between two layers of aluminium. External magnetic fields must also be kept lower than the critical magnetic field of the superconductor.

The only technology that can currently cool macroscopic objects to temperatures lower than 100 mK is a dilution refrigerator. The requirements for ion trapping, such as lasers beams, electrical connections, atomic source ovens and ion imaging, must therefore be made compatible with the dilution refrigerator environment. The cooling power of commercially available dilution refrigerators (on its mixing chamber) is no more than 400 μW at 100 mK [206]. The power dissipation of all devices mounted on mixing chamber plate must therefore be lower than this value while retaining sufficient radiation shielding and thermal insulation. In section 7.3 we describe the experimental challenges involved in incorporating and operating an ion trapping experiment in a dilution fridge, and propose solutions that can be immediately implemented using current technology.

7.2 Ion trap and LC circuit

To create the hybrid device proposed by Kielpinski *et al.* [68], the complete structure can be first divided into its individual components, where each component performs a specific function. The first feature which can be considered is the ion trapping architecture. For surface electrode ion traps, this is formed from two parallel electrodes which generate a pseudopotential from an applied rf voltage. Additional electrodes with dc voltages are also

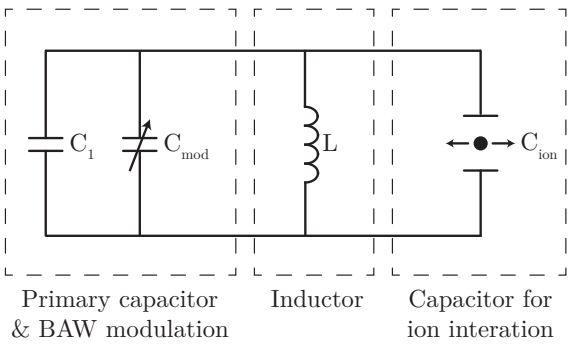

Figure 7.1: Circuit diagram for a superconducting LC circuit with a resonant frequency of ∼1 GHz. A modulated capacitance provides a frequency modulation of ∼1 MHz using a BAW resonator. A secondary capacitor is used to directly couple the motion of the ion with the electric field of the capacitor.

used to provide axial confinement, shuttling capabilities and micromotion compensation [207].

The superconducting LC circuit is formed from four individual components; an inductor, a primary capacitor, a secondary capacitor for ion interaction, and a bulk acoustic wave resonator (BAW). Fig. 7.1 shows the circuit diagram used to model the system, where the BAW is used to modulate the capacitance of the primary capacitor at the ions secular frequency. The BAW itself is formed from a piezoelectric material sandwiched between two conducting layers. Applying a voltage to the conducting plates, generates an acoustic wave which travels through the bulk of the material. Depending on the geometry and material of the piezoelectric layer, the resonant frequency of the device can be determined.

BAWs originally gained popularity as filters [208] and are now also commonly used as sensors [209] and oscillators [210]. They can be designed and microfabricated into two distinct topologies, as film bulk acoustic resonators (FBAR) or solidly mounted resonators (SMR). FBAR topologies are fabricated such that the BAW is surrounded by an air gap. This is accomplished either by fabricating the BAW upon a sacrificial layer or by backside etching directly through the wafer (see Fig. 7.2). SMRs substitute the air gap with alternating layers of different acoustic velocities. Each layer posses a thickness equal to a quarter wavelength with the stack of layers forming a Bragg acoustic reflector.

7.2.1 Design and simulation

Materials

The first requirement of the simulation process is to determine the materials required for each part of the device. For the piezoelectric material there are several options that can be used in a microfabrication process. Aluminium Nitride (AlN), Gallium Nitride (GaN), Zinc Oxide (ZnO) and Lead zirconate titanate (PZT) have all been demonstrated for BAW resonators. While AlN and PZT are the most commonly used materials, offering well established fabrication procedures, PZT was ultimately chosen for simulation due

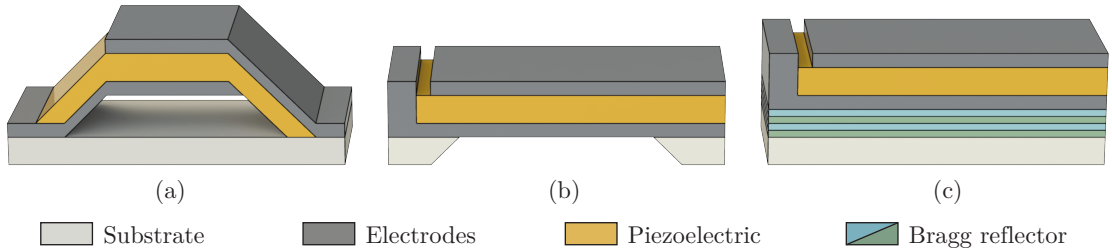

Figure 7.2: (a) An arched film bulk acoustic resonator (FBAR) structure fabricated by depositing the BAW device on top of a sacrificial layer which is later removed to leave an air gap. (b) A flat FBAR structure fabricated by backside etching through the wafer. (c) A solidly mounted resonator (SMR) structure with an alternating layer Bragg reflector stack.

to its lower acoustic velocity ($4600\,\mathrm{ms}^{-1}$) compared with AlN ($11{,}000\,\mathrm{ms}^{-1}$). The lower acoustic velocity results in shorter travelling wavelengths through the material for a given frequency of operation, allowing for smaller feature sizes.

For the ion trapping electrodes and the *LC* circuit, a superconducting material must be chosen. Typically for superconducting qubits the resonator material is formed from Niobium (Nb), a type-II superconductor which has a critical temperature of 9.3 K. Nb has also been demonstrated as an electrode material for surface electrode ion traps [67] and therefore presents itself as an ideal candidate. For insulating layers used in between conducting layers, silicon dioxide (SiO_2) and silicon nitride (Si_3N_4) were chosen due their demonstration in both BAW [211, 212] and ion trap structures [213].

Finally, sapphire (Al_2O_3) was chosen as the wafer material as it posses a low microwave loss tangent (10^{-4}). Sapphire also possess a high dielectric constant of 11.5, which results in shorter wavelengths for a given frequency within the *LC* circuit, allowing for the further reduction in size of the circuit. The thermal conductivity of sapphire (25.2 W/mK) is also high in comparison with common substrate materials such as quartz (1.46 W/mK), which aids in cooling the superconducting material deposited on the wafer.

The ion trap

The design and microfabrication of surface electrode ion traps (including those with superconducting electrodes) has been well described and demonstrated [18, 65, 214–216]. An ion height of 25 μm is chosen by Kielpinski *et al.* [68] as a minimum based on current achievements for ion trapping on surface electrodes ion traps [18, 47]. To create the trapping potential, two rf electrodes with widths of b and c and a separation a are required. For efficient Doppler cooling of the ion in all three axes, the laser wave vector k must have a component along all three principal axes of the ions motion. This can be achieved by

making the rf electrodes with differing widths such that $b \neq c$. For $c = b/2$, the optimum ratio of rf electrode separation is given by $\zeta = b/a = 4.90$ [207]. Using the dimensions of a, b and c, the ion height can be given as

$$h = \frac{\sqrt{abc\,(a+b+c)}}{b+c}. \tag{7.9}$$

For an ion height of $25\,\mu$m, a, b and c can be given as $18\,\mu$m, $90\,\mu$m and $45\,\mu$m respectively, which satisfies Eq. (7.9), $\zeta = 4.90$ and $c = b/2$. Static dc potential electrodes can also be placed in between and on the outside of the rf electrodes. Optimum dc electrode widths can be determined as a function of rf electrode separation a. Following [207], which provides optimal electrode dimensions for ion transport and separation, we choose centre segmented electrode widths of $w_{centre} \approx a = 18\,\mu$m and outer electrode widths of $w_{outer} \approx 3.66a \approx 66\,\mu$m. This can be beneficial if we wish to trap the ion at a specific position and then shuttle the ion to the interaction region. This ability is a key feature for proposed large scale ion trap quantum computers, which possess trapping, detection and interaction zones [59].

The bulk acoustic wave resonator

From the three BAW resonator designs presented in figure 7.2, an arched FBAR structure was chosen for simulation as it provides two key benefits. Firstly, the removal of a single $2-5\,\mu$m layer using a wet etching process offers the simplest fabrication process. This helps to minimize fabrication errors when compared with backside etching through $\sim 500\,\mu$m of wafer material for a flat FBAR, or the repeated deposition of multiple Bragg reflector layers for an SMR. Secondly, FBAR structures require materials only for electrode and piezoelectric layers, unlike SMRs which require an additional two materials for the reflector stack.

For many BAW applications, thin films of PZT in the order of a few hundred nanometres can be sufficient. However, for actuation purposes it is preferably to have thicker layers to obtain structural stability during flexing. For this reason, a $3\,\mu$m thick PZT layer was included in simulations as this is the maximum thickness achievable from a current sputter deposition processes [217]. A $1\,\mu$m thick Nb layer was added to the top and bottom of the PZT to form the electrode structures (see Fig. 7.3). Due to the thickness of the PZT and Nb layers, stresses due to resonator flexing was found to be negligible during simulation. The amplitude of the PZT oscillation also falls below critical limits for single-crystal microresonators [218], with amplitudes up to $5\,\mu$m being demonstrated for

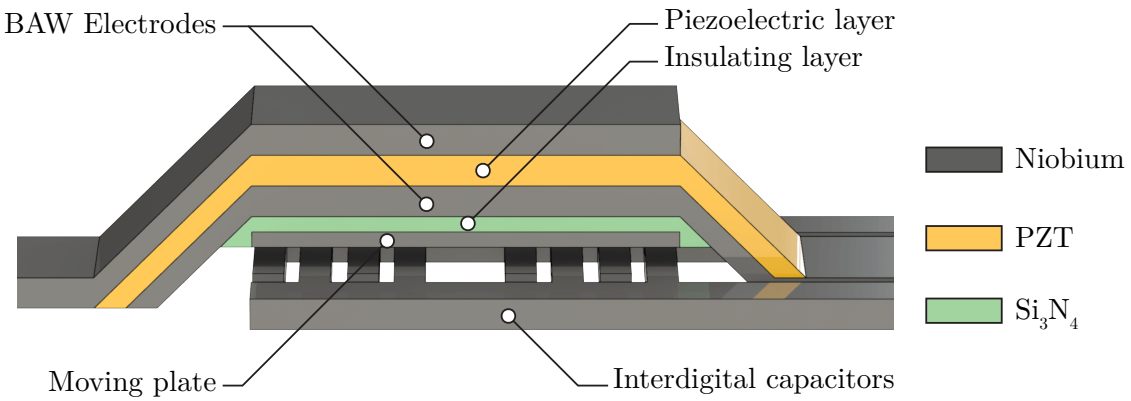

Figure 7.3: An arched film bulk acoustic resonator (FBAR) with a PZT piezoelectric layer and Nb electrode layers. An additional Si_3N_4 and Nb layer are placed on the underside of the resonator, with the Nb layer serving a moving plate that modulates the capacitance of the primary capacitor.

1-3 μm thick and 700 μm long PZT cantilevers [219].

An additional Si_3N_4 and Nb layer was placed on the underside of the resonator to serve as an electrically insulating and conducting layer respectively. The conductive layer serves as a electrically conducting plate near the primary capacitor, which moves with the BAW resonator. In section 7.2.1, the primary capacitor in the form of an interdigital capacitor is chosen. The capacitance forms mainly from the surface area along the edges of each digit of the capacitor. This is due to the electric field being confined primarily in the regions between each digit. By introducing an electrically conductive plate above the fingers of the interdigital capacitor, we can change its capacitance. This is achieved by confining the electric field above the top surface of the interdigital capacitor and increasing its relative contribution to the total capacitance. By attaching the conductive plate to the BAW, we can effectively modulate the capacitance of the primary capacitor.

The introduction of a modulating plate above a capacitor with a fixed capacitance also has a number of benefits, when compared to solely modulating the position of one side of the capacitor. In a two plate capacitor, where the position of a single plate is modulated and the other plate is fixed, the driving signal is coupled strongly to the total capacitance in the circuit. Any noise introduced by the driving signal would also be coupled strongly to the circuit. An effective three plate capacitor design is chosen as the two fixed plates form the bulk of the total capacitance and the third plate forms the modulation. Therefore, any noise on the driving signal is decoupled from the total capacitance and we obtain a larger signal to noise ratio. The insulating layer must be used as the moving plate attached to the BAW forms part of the LC circuit and should be decoupled from any potential sources of noise, such as the driving signal on the BAW.

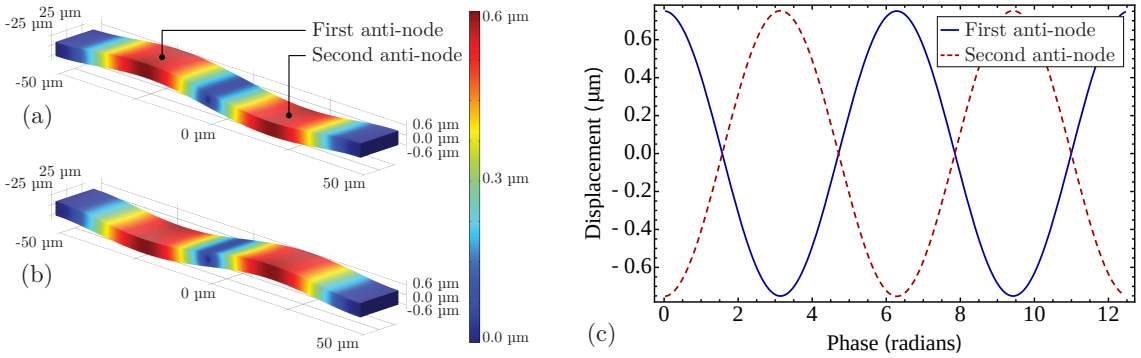

Figure 7.4: A $200 \times 50 \times 3\,\mu$m BAW device resonating at a 1 MHz second harmonic flexure mode, where (a) and (b) show the resonator at a phase of 0 and π respectively during its oscillation. The flexure on (a) and (b) is accentuated by a factor of 5. (c) Displacement at the 1st (solid) and 2nd (dashed) antinodes of the BAW resonator.

During the design process it is important to separate the frequency of the available modes in the BAW such that the driving energy only couples to the single mode we require. It should be ensured that the harmonics of the other principal modes such as longitudinal, thickness shear and face shear are not also driven. This can be accomplished by keeping the dimensions of thickness, width and length non-divisible with each other. This ensures that the resonator only resonates at one mode within the driving frequency range.

While driving the resonator with a sinusoidal signal produces a sinusoidal resonator motion, the variation in capacitance due to the moving plate is not sinusoidal. This is due to the capacitance of the primary capacitor varying as $C \propto 1/d$, where d is the distance between the moving plate and the capacitor. The distance can be given as $d = A\sin(\omega t) + \alpha$, where the term $A\sin(\omega t)$ denotes the modulating distance with amplitude A and frequency ω, and α describes the fixed separation distance when no modulation is present.

This can be partially compensated for by replacing the single primary capacitor with two capacitors connected in parallel and modulated with a π phase difference. This leads to a capacitance given by

$$C \propto \frac{1}{A\sin(\omega t) + \alpha} + \frac{1}{A\cos(\omega t) + \alpha}. \tag{7.10}$$

The same resonator can be used to modulate both capacitors by driving the resonator on its second harmonic, creating two displacement antinodes. Each capacitor can therefore be coupled separately to the motion at each antinode. Figures 7.4a and 7.4b show the second harmonic flexure mode of the resonator, with the curvature of flexure accentuated

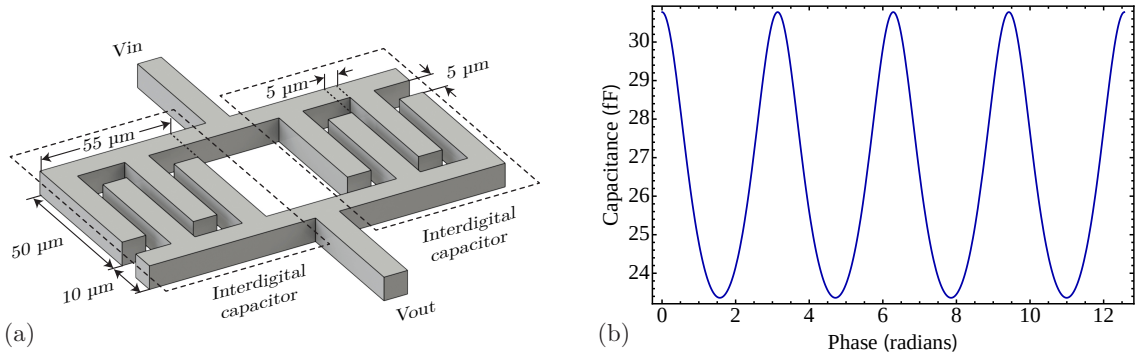

Figure 7.5: (a) Diagram of two four-fingered interdigital capacitors. Each finger has dimensions of $5 \times 84 \times 1\,\mu$m with finger spacings of $5\,\mu$m. (b) Total capacitance of two interdigital capacitors in parallel modulated π out of phase with each other.

by a factor of 5. Figure 7.4c shows the displacement of the resonator at each antinode with figure 7.5b showing the total capacitance for both capacitors modulated in parallel. The final dimensions for the piezoelectric layer are $200 \times 50 \times 3\,\mu$m, which produces a second harmonic resonant frequency of $\sim$1 MHz.

The primary capacitor

For the circuit design described by Kielpinski [68], a total capacitance of 46 fF (coupled with an inductance of 440 nH) is present to produce a resonant frequency of $\sim$1 GHz. From Eq. (7.6) we see that for lower values of capacitance the coupling also increases. However, the value of 46 fF presented was limited primarily due to parasitic capacitances originating from the coiled inductor. In section 7.2.1 we describe the use of an alternate inductor design with parasitic capacitances $<$5 fF, which allows us to reduce the total capacitance of the circuit. However, as proof of principle, we maintain a total capacitance of 46 fF here and present the benefits of a decreased capacitance in section 7.2.1 after all the components of the LC circuit have been described.

Another parameter that requires definition is the modulation of the capacitor using the BAW, which produces the frequency modulation for the circuit. The frequency modulation takes the form of $\cos[\omega_t + f(t)]$, where $f(t)$ is the modulation function. If we assume that the modulation is a sine function of a single frequency, we can express the time evolution of the circuit as

$$y(t) = A_c \cos\left[2\pi f_c t + \frac{f_\Delta}{f_m}\cos(2\pi f_m t)\right], \tag{7.11}$$

where A_c is the carrier amplitude, f_c is the carrier frequency, f_m is the modulation frequency, and f_Δ is the carrier frequency variation under modulation. The fraction f_Δ/f_m

is also known as the modulation index or modulation depth. For a carrier modulated by a sinusoidal signal, the resulting frequency spectrum can be derived using Bessel functions of the first kind, as a function of the sideband number and the modulation depth. Ideally, we wish to keep sideband number to one, confining the energy within carrier and first sideband. Therefore, a modulation depth of $\sim$0.3 is selected as it provides the maximum energy within the first sideband while keeping the majority of power ($\gtrsim 99\%$) within the carrier and first sideband. While the energy within the first sideband can be increased for higher modulation depths, the energy with the carrier decreases such that the combined carrier and first sideband energy is significantly lower.

To modulate the capacitor effectively, the capacitor should also be placed directly beneath the BAW. Any part of the capacitor outside the BAW only contributes to the total capacitance and not to the modulated capacitance. Therefore, it is beneficial to keep the surface area of the capacitor equal to or smaller than the BAW device. A compact solution for microfabricated devices is an interdigital capacitor that uses edge coupling between tracks to produce a capacitance.

Taking the requirements for total capacitance, modulation depth and spatial area, the digits of the capacitor can be optimized to meet all requirements. The simplest geometry, while maintaining feature sizes $>5\,\mu$m for ease of fabrication, is a four finger geometry. Two four-fingered capacitors in parallel are capable of producing a capacitance of 46 fF, a modulation depth of 0.3 (using a BAW with a separation of $2\,\mu$m and oscillating with a $0.6\,\mu$m amplitude) and with a complete geometry smaller than the BAW structure. The dimensions of the capacitor are given in Fig. 7.5a.

Capacitor for ion interaction

When designing the coupling capacitor, we wish to maximise the visible surface area to the ion in order to increase the surface charge affected by the ions motion. As the plate is superconducting, the charge flow will be confined to the surface. By maximising the plate's surface area towards to ion, we also maximise the total number of surface charge carriers and induced surface current density.

For the structure of the plates we can begin by assuming a rectangular geometry to maximise the surface area within the rf electrodes (see Fig. 7.6a). This gives parameters of length, width and separation, which can be optimized. The coupling capacitance formed to ground must also be considered as this increases with the surface area and therefore limits the maximum size of the plates.

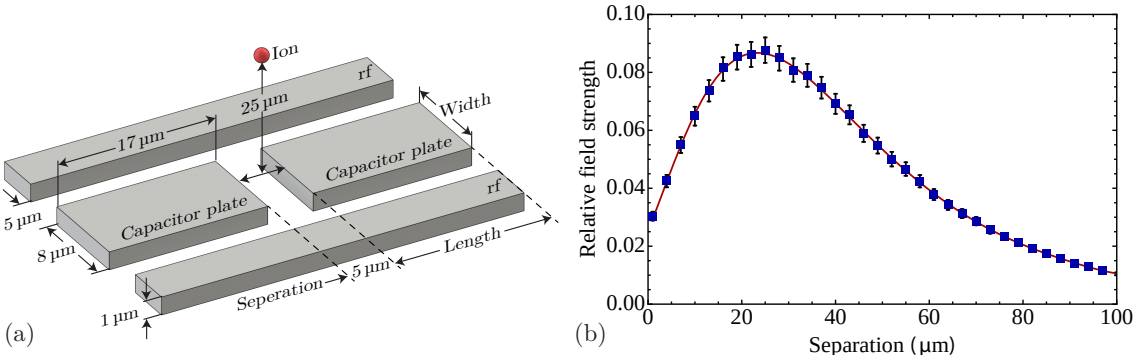

Figure 7.6: (a) Diagram of two capacitor plates used for ion interaction on the surface of the ion trap. Each plate has dimensions of $8 \times 30 \times 1\,\mu$m with a $5\,\mu$m separation in between both plates. (b) Variation in relative field strength for a fixed charge at an ion height of $25\,\mu$m as a function of separation between the centre of two capacitor plates. Note that with the design given in figure 7.9, the ion would see no exposed dielectrics.

For an ion height of $25\,\mu$m, an optimum separation of $\sim 24\,\mu$m between the centre of each plate was found, where the relative field strength for a given surface charge is maximum at the ions position (see Fig. 7.6b). The field strength at the ions position also increases linearly with the length of the plate. A length of $17\,\mu$m was therefore chosen for each plate, which allows for a $24\,\mu$m separation between the centre of each plate while leaving a $5\,\mu$m gap in between both plates for ease of fabrication. Finally, the plate widths, which are limited by the rf electrodes separation of $18\,\mu$m, can be optimized. The maximum width can be determined by selecting an upper limit for the coupling between the plate and the rf electrodes. Here, an upper limit of a 10% increase in the total circuit capacitance was chosen, resulting in a plate width of $8\,\mu$m and a plate-electrode separation of $5\,\mu$m. Figure 7.6 shows the final geometry and dimensions of the capacitor plates.

The inductor

The inductor proposed by Kielpinski [68] is a microfabricated superconducting coil with a 1 mm diameter and a length of $650\,\mu$m. While coiled inductors are a suitable solution in macroscopic circuits, they can be difficult to implement into microfabricated systems, requiring a multilayer fabrication process and multiple vias. Inductor coils can also be susceptible to parasitic and self capacitances, introducing noise to the circuit.

For microfabricated devices there are several alternative geometries which can produce an inductance, such as spiral, meandering and stub inductors. Microstrip stubs provide the simplest solution and are formed from a straight transmission line connected only at one end, with the free end either open or short circuited. Neglecting losses in the transmission line, the input impedance of the stub is purely reactive. Depending on the electrical length

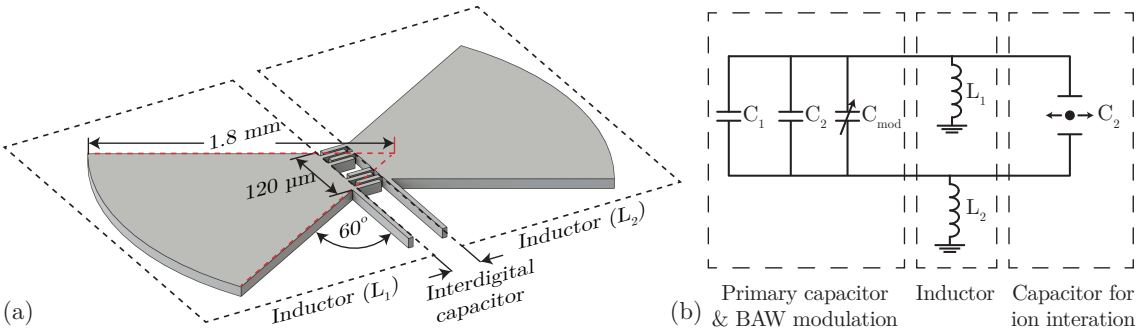

Figure 7.7: (a) Diagram of two dovetail stub inductors on either side of the primary interdigital capacitor. The inductor posses a 120 μm stub width which fans out at 60° to a radius of 1.8 mm. (b) Equivalent circuit diagram for the dovetail inductor geometry and parallel interdigital capacitors.

of the stub it can act as either a capacitor or an inductor. As the wave propagates down the stubs length, the stub switches between being inductive and capacitive every $\lambda/4$.

The geometry chosen for simulations was a radial (or "dovetail") stub design. As radial stubs fan out, this increases the bandwidth of the stub, reducing end effects such as parasitic electric fields. The larger tail perimeter also results in a lower impedance, which scales down any impedance variation due to microfabrication error. For symmetry about the centre of the primary capacitor, one inductor is used on either side of the capacitor (see Fig. 7.7a). The total inductance L_{tot} is given by the sum of the two individual inductors $L_{tot} = L_1 + L_2$ (see Fig. 7.7b). The dovetail inductor geometry is determined at the end of the design process, allowing the resonant frequency of the LC circuit to be finalized once all capacitances have been determined. Each inductor possess a final geometry with a 120 μm stub width, which equals the width of both interdigital capacitors. The stubs fans out at standard 60° to a final radius of 1.8 mm to achieve an inductance of 440 nH.

As mentioned previously, reducing the total static capacitance of the circuit will also increase the coupling strength between the ion and the resonator (see Eq. (7.6)). By using a radial stub design, the parasitic capacitances of the complete system are reduced to <5 fF in simulations. Fig. 7.8 shows the coupling strength for $^{9}Be^{+}$, $^{12}Mg^{+}$, $^{40}Ca^{+}$, $^{87}Sr^{+}$, $^{138}Ba^{+}$ and $^{171}Yb^{+}$ as a function of the total capacitance of the circuit. It can be seen that even for heavy ions, such as $^{171}Yb^{+}$, a coupling strength of $g/2\pi \sim 200$ kHz can be achieved by reducing the total circuit capacitance to ∼5 fF. It should be noted that as we decrease the total capacitance of the resonating system, we will also need to increase the length of the inductor to keep the same resonant frequency. Although increasing the length of the stub increases the capacitance to ground, the increased length causes a larger inductance change per unit length due to the wave propagation in the stub. The net result

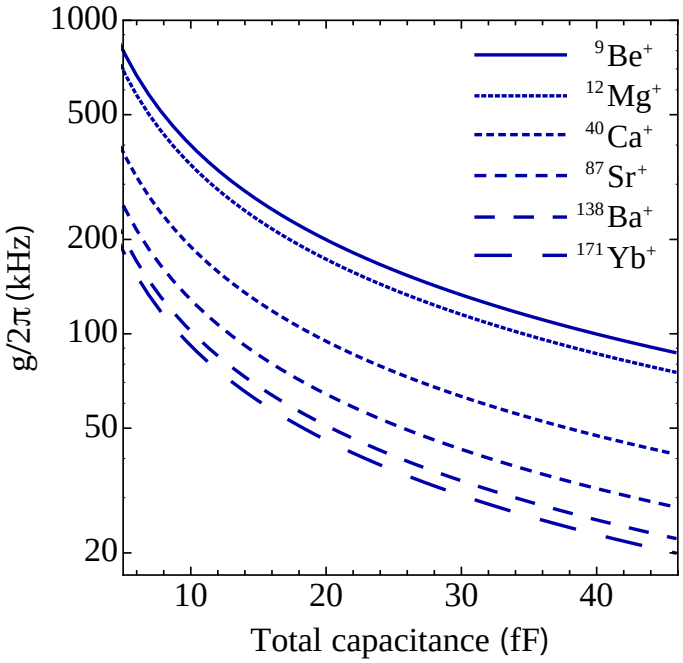

Figure 7.8: Coupling strength as a function of total circuit capacitance for $^{9}Be^{+}$, $^{12}Mg^{+}$, $^{40}Ca^{+}$, $^{87}Sr^{+}$, $^{138}Ba^{+}$ and $^{171}Yb^{+}$. The decrease in total capacitance by minimizing parasitic capacitances throughout the circuit allows for the increase in coupling strength between the ion and the resonator.

is that the capacitance in the stub can be ignored as it appears purely inductive from the input port.

7.2.2 Microfabrication

An overview of the microfabrication process for the ion trap electrodes and BAW device is presented in Fig. 7.9. The process was designed to minimize fabrication difficulties and processing time by limiting the number microfabrication techniques performed. To this end, all deposition techniques described are performed using a sputter deposition process and all dry etching processes are performed by inductively coupled plasma (ICP) etching. The following process steps have been numbered to help distinguish between the different stages of the microfabrication procedure.

The BAW structure

(1) The process begins with the preparation of a $250 - 500\,\mu$m thick Al_2O_3 sapphire wafer, which is polished to a surface roughness of <0.5 nm on both sides. Both surfaces are cleaned with acetone, methanol and isopropanol, followed by baking to dehydrate the surfaces. Further cleaning is performed using a fuming nitric acid (FNA), a strong oxidizer that effectively removes organic material, ensuring a clean surface to fabricate upon.

(2) The first layer deposited is a $1\,\mu$m Niobium (Nb) layer, which forms the interdigital capacitor and inductor of the superconducting LC circuit. Prior to etching the Nb layer and all subsequent layers, a photolithography process is performed. A photosensitive

material (photoresist) is spin coated on top, exposed to UV radiation through a mask and developed to form the desired pattern. The Nb layer can then be etched using a drying etching process.

(3) A 2 μm thick silicon dioxide (SiO_2) layer is then deposited. The layer will be used as a sacrificial layer that will be selectively removed later to form the air gap beneath the BAW device. (4) To ensure a flat surface for the deposition of subsequent layers which form the BAW device, the SiO_2 undergoes chemical mechanical polishing (CMP) to reduce surface roughness to under 10 nm. (5) A second 500 nm thick Nb layer, which will serve as the moving plate that varies the capacitance of the circuit is then deposited, patterned and dry etched.

(6) A 500 nm silicon nitride (Si_3N_4) is then deposited to provides an electrically insulating layer in between the capacitive plate and bottom Nb electrode used for the BAW. The Si_3N_4 and SiO_2 can then be dry etched to form the region underneath the BAW device.

(7) The first BAW electrode layer of 1000/100 nm thick Niobium/Platinum (Pt) is deposited and dry etched. The Pt layer serves as an adhesion layer and diffusion barrier between the Nb and PZT layer. (8) The deposition of PZT can be performed through several methods, such as sol-gel coating [220], sputtering [217], hydrothermal deposition [221], screen printing [222] and aerosol deposition [223]. For a 3 μm layer, rf magnetron sputtering provides an established deposition technique, which can utilize the same deposition tools as used for the other layers. (9) After patterning and dry etching the PZT layer, the second BAW electrode layer of 100/1000 nm thick Pt/Nb is deposited and dry etched.

(10) A buffered hydrofluoric (BHF) acid wet etch is then used to etch the sacrificial SiO_2 layer. This step selectively removes the SiO_2 layer and provides the air gap below the BAW structure without attacking the surrounding Nb and Si_3N_4 layers.

The ion trap electrodes

(11) Once the BAW device has been fabricated, the ion trap electrode structures can then be deposited. The first layer deposited is a 3 μm thick SiO_2 layer used to insulate the ground electrodes of the *LC* circuit from the top electrodes. The requirement of this insulating layer means fabricating the ion trap electrode structures must come after the BAW device, as any prior deposition of SiO_2 would be removed by the previous BHF wet etch. This process is made simpler as the ion trap electrodes and BAW device can be spatially separated on the chip. To prevent depositing subsequent layers over the BAW structure, thick photoresist layers ($\sim$30 μm) can be used to protect covered areas.

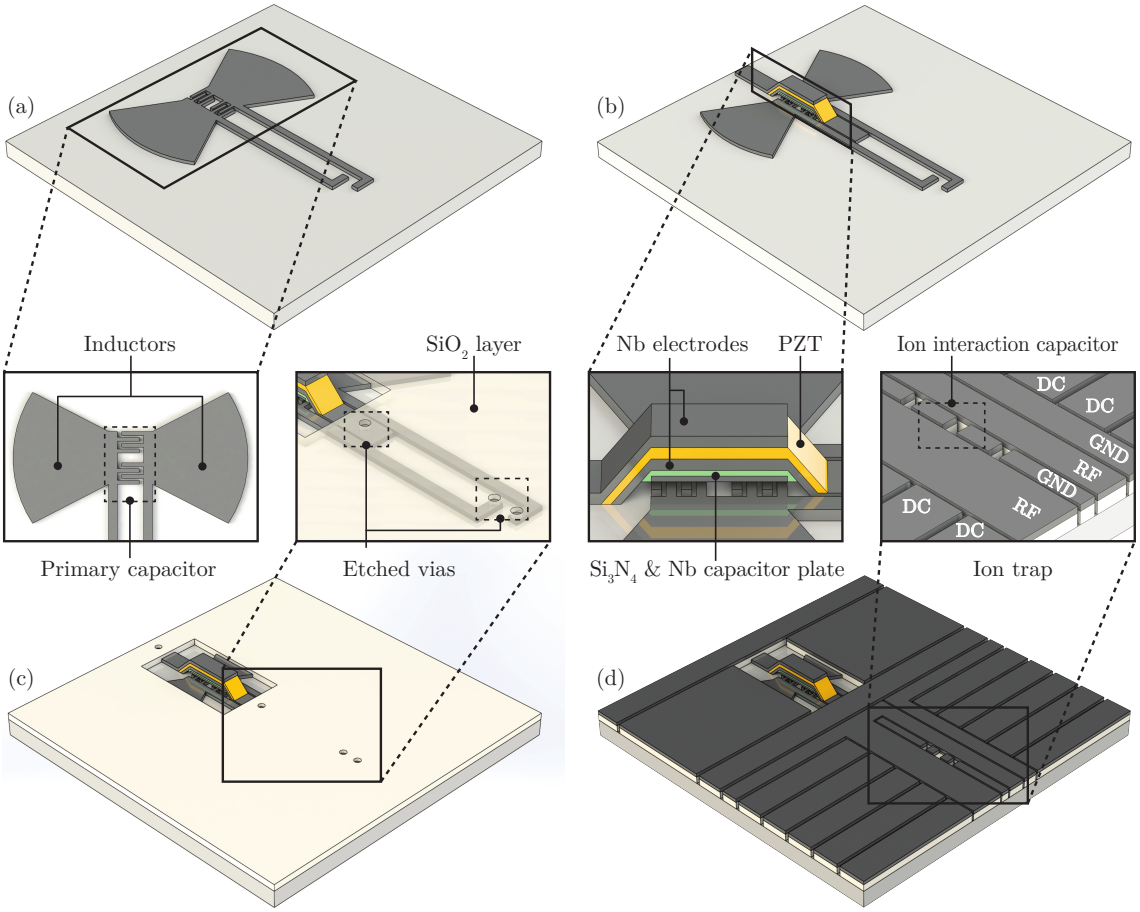

Figure 7.9: Microfabrication process of the BAW device and ion trap structure. (a) Deposition and etching of the first Nb layer forming the *LC* circuit. (b) Formation of the BAW device with the deposition and etching of a SiO_2 sacrificial layer, a Nb layer for the modulating capacitor plate, a Si_3N_4 insulation layer, two Nb BAW electrodes layers and the piezoelectric PZT layer. (c) Deposition of a SiO_2 insulating layer and etching to leave access for vias. (d) Final deposition of Nb with etching through the Nb and SiO_2 to produce the surface electrode structure.

(12) The SiO_2 layer is then dry etched to provide space for vertical interconnects (vias) between the *LC* circuit and the top electrode layer. (13) Finally, a 1 μm thick Nb layer is deposited to form the top electrode layer. The Nb and SiO_2 layer are then dry etched to form the electrode structure.

7.3 Ion trapping in a dilution refrigerator

Ion trapping experiments possess several requirements that need to be adapted to a dilution fridge environment. Firstly, the utilization of a UHV system is necessary to minimize collisions between ions and residual background gases. For this purpose a dilution refrigerator and its cryogenic environment is ideal. When cooled down to mK temperatures it acts as a sorption pump and effectively pumps the cryostat to pressures unobtainable by

room temperature vacuum systems.

The preparation of single ions is traditionally performed by ohmically heating an atomic source material in an oven, followed by photoionization. However, within a dilution refrigerator this would be not possible due to insufficient cooling power at the sub-Kelvin stages. For low temperature ($\sim$4 K) ion trapping systems, alternatives such as laser ablation [66] and photonic crystal fibres have already been demonstrated [224] and show potential for use in dilution fridges.

To generate electromagnetic trapping potentials, rf voltages of $\sim$100 V and dc voltages of $<$10 V are applied to trap electrodes. Superconducting materials must also be used inside the setup to prevent the increase in temperature due to joule heating. A suitable material for trap structures is Nb (as discussed in section 7.2), which has a high critical temperature, critical magnetic field and critical current density. Electrical connections to the trap from outside of the cryostat can be achieved using commercially available NbTi coaxial cables.

Cryostats for ion trapping applications use UHV compatible anti-reflection coated windows for optical access. These windows are coated to filter all wavelengths except those necessary for the experiment. However, dilution refrigerators use six radiation shields to prevent radiation from entering the cryostat to maintain sub-Kelvin temperatures. Therefore, a suitable alternative for the dilution refrigerator is the use of optical fibres and optical feedthroughs compatible with UHV and cryogenic environments. This solution also requires aligning devices such as low temperature piezo elements, which are capable of moving the fibre output within the dilution refrigerator.

Another challenge is the read out of information from the ion through the detection of fluorescence. Typically in ion trap experiments, the fluorescence is collected through an optical viewport using a lens system placed within a few centimetres of the ion trap. Photons collected are detected using either a charge coupled device (CCD) or a photomultiplier tube (PMT). As direct optical access is not desired, an alternative in-vacuum solution for cryogenic environments is a kinetic inductance detector (KID). Traditionally used for astronomical applications, KID technology was developed $\sim$15 years ago, and shows results comparable to conventional CCD detectors [225].

Finally, care must also be taken when dealing with vibrations of the system. If liquid Helium (He) is used for pre-cooling the dilution refrigerator, vibrations will be negligible. However, operation of this kind of "wet" refrigerator is difficult due to the requirement of adding liquid He continuously. Alternatively, a cryocooler can be used, which makes use

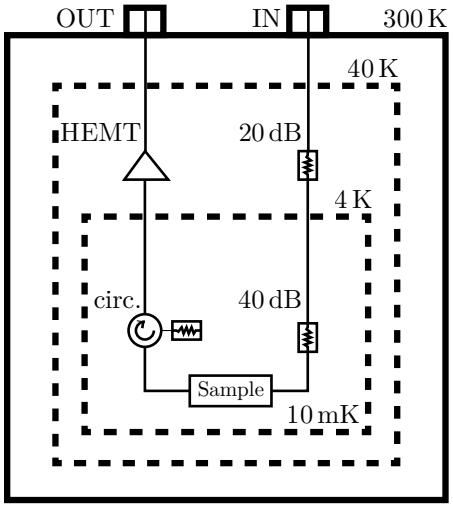

Figure 7.10: Microwave noise suppression setup for dilution refrigerator with base temperature of 10 mK. The input line shows two thermally anchored attenuators summing to 60 dB to attenuate external noise. On the output line a thermally anchored cryocirculator and HEMT (high electron mobility transistor) cryoamplifier are also used to minimize noise [31].

of bellows to mechanically decouple the cryocooler from cryostat [226].

7.3.1 Ultra-high vacuum system

The first challenge in transferring a room temperature ion trapping infrastructure into a dilution fridge is optical access to the experiment. Although optical access to the 100 mK stage in a dilution fridge has been demonstrated [227], optical fibres can be used to reduce heating into the system. As six radiation shields are used within the dilution refrigerator, the use of cryogenic compatible optical fibres and optical feedthroughs becomes inevitable to mitigate losses in laser power incurred at the windows on each shield.

Cryogenic and UHV compatible optical feedthroughs are commercially available with specifications that are technically favourable for the proposed methodology. Such feedthroughs can be baked up to 200°C and cooled down to 3 K, with an attainable vacuum pressure of 1×10^{-10} torr at room temperature. A lower temperature limit of 3 K is sufficient for these feedthroughs as they are attached to the vacuum shroud at room temperature. In addition, internal cabling connected to the feedthrough is first thermally anchored at the 40 K cold stage. The specified transmission ranges between 370 nm and 1200 nm, which is ideal for all wavelengths of the most commonly used atomic systems such as Ba^+, Yb^+, Sr^+ , Ca^+, and Mg^+, with a maximum attenuation of 1.2 dBm^{-1} for the shortest wavelength.

7.3.2 Thermal anchoring

Microwave lines

To avoid increasing the base temperature of the cryostat, the outer environment must be thermally decoupled from the internal environment. Coaxial lines for microwave and rf signals create thermal connections between the outer room temperature part of cryostat

and the internal sub-Kelvin parts of the cryostat. To avoid unnecessary heating of the sample mounted on mixing chamber of the refrigerator, coaxial cables should be thermally anchored to multiple stages of the refrigerator. If the cables are thermally anchored, their temperature will be the same as the stage they are connected to. Therefore, we have a temperature gradient and heat flow through the cable. If the heat flow (the power coming into the cryostat) is higher than cooling power of refrigerator, the mixing chamber will not reach its base temperature.

The power transmitted through the wire can be defined as $P = \lambda \delta T A/L$ [228], where A is the cross-sectional surface area, L is the length, λ is the mean thermal conductivity and δT is the temperature difference across the length. A suitable choice for decreasing heat flow is to use conductors with lower λ. Commonly used materials for such applications are stainless steel or aluminium. For stages with lower temperatures, superconducting wires are also used (e.g. NbTi).

Noise

Thermal noise power can be determined from the Johnson-Nyquist formula $P_{th} = k_B \times T \times \nu_{BW}$ [229, 230], where k_B is the Boltzmann constant, T is the temperature in Kelvin and ν_{BW} is the frequency bandwidth in which the noise is measured. The noise power per hertz on an isolated chip on a 10 mK mixing chamber is 1.38×10^{-25} J/Hz. By connecting the chip to an external measurement system at ∼300 K via coaxial cables, this number increases as the noise power of the outside system is 4.14×10^{-21} J/Hz, which is approximately 3.0×10^4 times greater. To keep the noise at the mixing chamber low, external noise must be attenuated or filtered. For the input line, the ideal option is to use attenuators (in this case at least 60 dB $\rightarrow 1.0 \times 10^5$ times attenuation) that are thermally anchored to the stages of the refrigerator (see Fig. 7.10). Attenuators attenuate both noise and input signal, however, the input signal can be increased by setting the output power on the microwave generator. For the output line, attenuators are not suitable; instead, we should use cryocirculators or HEMT (high electron mobility transistor) cryoamplifiers. As a passive device, cryocirculators can be mounted on any stage of the refrigerator, but preferably on the mixing chamber. Amplifiers on the other hand dissipate energy when operating and require cooling, and must therefore be placed on the stage with a high cooling power (4 K stage cooled by pulse tube in dry refrigerators or by liquid He in wet refrigerators).

DC lines

DC wires must also be thermally anchored to the different stages of the refrigerator. To decrease thermal coupling between the outside of cryostat (300 K) and mixing chamber (10 mK), thermally resistive wires should be used (e.g. constantan, manganin, beryllium-copper or phosphor-bronze). Alternatively, if this is not possible, copper wires with a cross-section as small as possible should be used. For ion trap applications, the effect of joule heating due to high resistance wires is not an issue as there is no current flowing through the DC electrodes.

7.3.3 Atomic sources

Ohmically heated ovens, which are usually located within a few centimetres of an ion trap, are easy to construct, operate and offer a reliable method of delivering a specific atomic species to the trap. However, for cryogenic ion trapping applications these sources are unsuitable as they can dissipate between $10 - 20$ W of power into the environment [231]. It has been shown that power dissipation at the coldest stage can be minimized by locating the atomic oven remotely in a warmer region of a cryostat [185]. The atoms are confined using magneto-optical traps, laser cooled and then pushed towards the ion trap using resonant laser light where they are finally photoionizied and trapped.

An alternate approach that has also been demonstrated is laser ablation, where an ion trap can be successfully loaded with a single 1.5 mJ pulse [66, 156]. This is a considerable benefit for systems operating at $\sim$4 K, however, it is still a significant heat load for dilution fridges that can only extract up to $\sim$400 μW at 100 mK.

Here we focus on the use of photonic crystal fibres which provide the substantial benefit of being a simple and demonstrated technology with the ability to load atoms externally and transport them to the experimental chamber with minimum heat load.

Photonic crystal fibres (PCFs)

Optical fibres with hollow cores have been demonstrated to transport both light and atoms [224, 232]. For atom transport along hollow capillaries, the optical dipole forces of a the laser beam prevent adhesion to the surfaces and also provides the acceleration needed to overcome viscosity [224]. It has been shown that small dielectric particles can be trapped, controlled, and propelled in a laser beam using the forces exerted by light [233]. Fibres have also been shown to maintain UHV even with segments of the fibre exposed to atmospheric pressure and that they are capable of being steered through bends of the

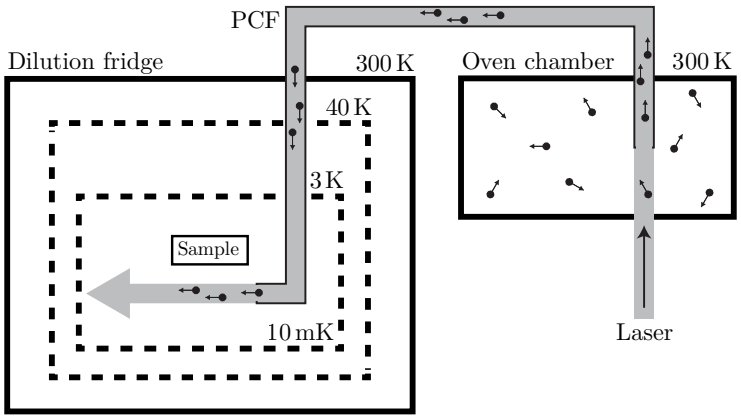

Figure 7.11: Resonant laser light is used to transport atoms from an external oven chamber, filled with an atomic cloud, into the dilution fridge using a photonic crystal fibre (PCF).

flexible fibre [224]. The fibres can therefore be used to transport an atomic source from an isolated system to the ion trap. This system can be located either at a warmer stage within the dilution fridge (4 K or 40 K stage) or outside of the fridge.

As hollow core fibres are based on hollow capillaries to guide light in multiple modes, this can result in losses due to heterogeneous fields causing the destabilization of local fields for atomic transport. PCFs are a developing class of hollow optical fibres capable of transporting atoms using a single low loss spatial mode. PCFs are based on the properties of photonic crystals, which have a periodic optical nanostructure and rely on the photonic band gap principle to confine light allowing the fibre to have a hollow core [234]. Transport of atoms has already been demonstrated using PCFs [235].

7.3.4 Ion imaging

Kinetic inductance detectors (KIDs)

Traditional CCD or active pixel sensors, such as CMOS detectors, do not operate at cryogenic temperatures below 1 K. PMTs can also be used for ion detection [236], even in an array configuration, however, due to their size they are usually used for photon counting or flying-spot scanning. One promising solution is a kinetic inductance detector (KID) (see Fig. 7.12). A KID is a superconducting device that uses the effect of surface kinetic induction [225, 237, 238] to change the resonant frequency, phase and amplitude of a high frequency microwave resonator. This corresponding frequency, phase and amplitude shift can be read out and interpreted as a photon flux density at the detector.

There are several designs for KID detectors [225, 237, 239–241], but the working principle is the same. A resonator structure is fabricated from a superconducting material, typically a $\lambda/4$ waveguide or lumped element design, which is tuned in the microwave frequency range ($10 - 20$ GHz). As photons of sufficient energy strike the superconductor,

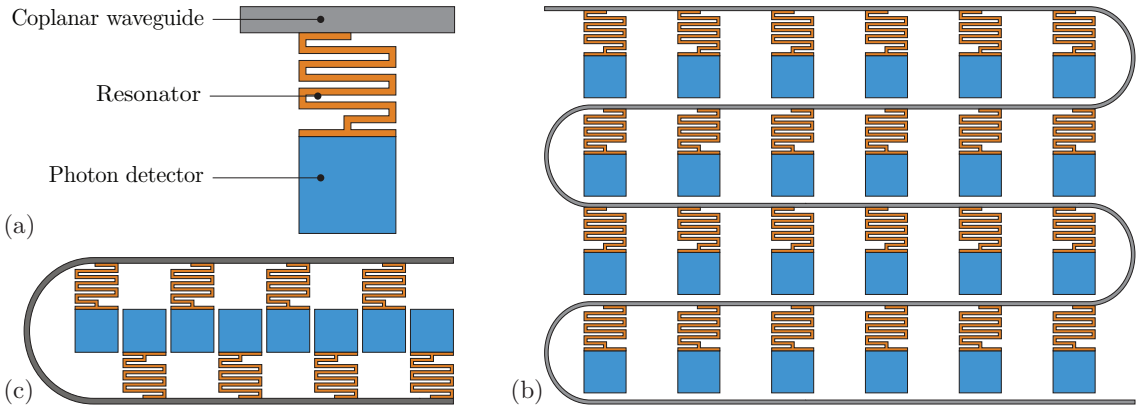

Figure 7.12: (a) Diagram of a $\lambda/4$ KID detector fabricated from a higher band gap superconductor. (b) Typical layout of KIDs in an array sharing a single CPW. (c) A linear high density KID array allowing for image resolutions of less than 10 μm in a single row.

they break up Cooper pairs forming an excess of quasiparticles on the surface of the superconductor [225, 237]. These quasiparticles interact with phonons and cool rapidly forming a population with energies slightly greater than the gap energy and sub-gap phonons in the superconductor. These occupied energy states stop, by the Pauli exclusion principle, Cooper pairs from filling those same states, reducing the density of pairs [238].

This has the effect of increasing the surface inductance of the superconductor and to a lesser extent the effective series resistance (ESR). As the superconductor is part of a resonant circuit, the increase in inductance and resistance lowers the frequency, phase and amplitude of the resonant peak. After a period of time the quasiparticles recombine into Cooper pairs when two interact and the resonator relaxes back into its original mode. The average distance the quasiparticles can travel before recombining is given by $l \approx \sqrt{D\tau_{qp}}$, where τ_{qp} is the quasiparticle lifetime and D is the diffusion constant of the material, which is typically $>8\,\mathrm{cm^2 s^{-1}}$ for aluminium [242]. This recombination time is one of the components that determines the sensitivity of the detector.

To maximise the density of quasiparticles, reduce recombination time and separate the photon detector from the resonator structure, we can employ a quasiparticle trap which separates the quasiparticles and lowers their energy to below the gap energy of the detector superconductor. This can be accomplished by employing two dissimilar superconductors with different gap energies. If the photon strikes a Cooper pair in the higher gap superconductor, then the quasiparticles created will cool rapidly, via phonons, and flow into the lower gap superconductor. These quasiparticles will be unable to return to the high gap superconductor.

Figure 7.12 shows a typical $\lambda/4$ design where the photon detector is connected to the

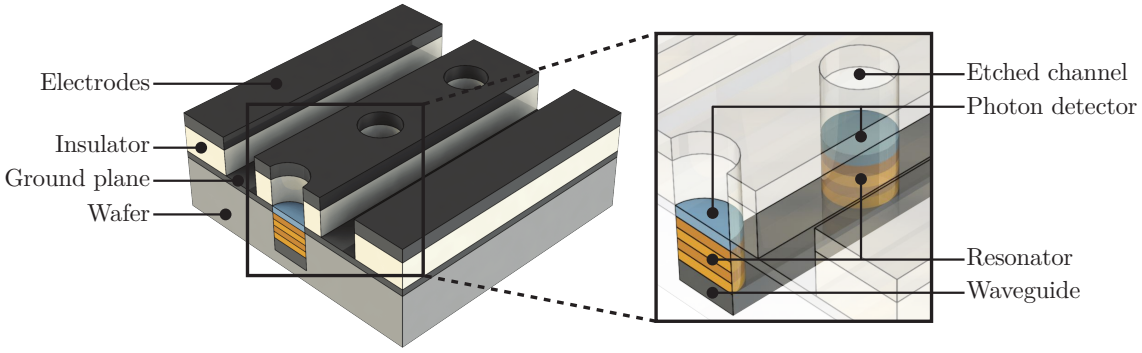

Figure 7.13: Vertical KID structure featuring an into plane resonator. Light passes through etched channels in the electrode and strike the photon detector. The resonator is constructed from multi-plane elements that spiral down to the CPW, which is capacitively coupled to the resonator. The layer materials are Nb for the electrode surfaces, SiO_2 for the insulating layer and a Sapphire substrate.

grounded end of the waveguide. The photon detector is the most sensitive point on a $\lambda/4$ design to quasiparticles and also forms the quasiparticle trap. To form an image, multiple KID cells must be multiplexed together in arrays. Since the resonant frequency of each cell can be tuned to a different frequency, we can address multiple KID detectors using a single wideband microwave waveguide. A 32 pixel [240], 144 pixel [241], 1024 pixel [239] and 2024 pixel [237] KIDs have been fabricated and tested within dilution fridges and adiabatic demagnetization refrigerators at sub 1 K temperatures. Progression has also been demonstrated to larger arrays with theoretical arrays of 100,000 pixels [243] being proposed.

Figure 7.12b shows an example array created using multiple KID elements coupled onto a single coplanar waveguide (CPW) line. This topology is relatively simple to create but suffers from low pixel density as space is required for the CPW line and resonator structure between each photo detector.

Flourescence detection

For ion detection within a dilution fridge, we wish to limit the number of imaging feedthrough cables to reduce the thermal load on the system. The system would also need to have an inter pixel spacing of less than 10 μm so that neighbouring ions can be spatially resolved. These requirements make KID array detectors an ideal choice as designs featuring up to ten thousand pixels have been proposed [244] using only two coaxial feedthrough lines. These arrays have pixel dimensions between $6 - 10\,\mu$m.

While an external KID array and lens system could be designed, the KID network could also be incorporated within the trap structure itself. In such a design the Cooper pair

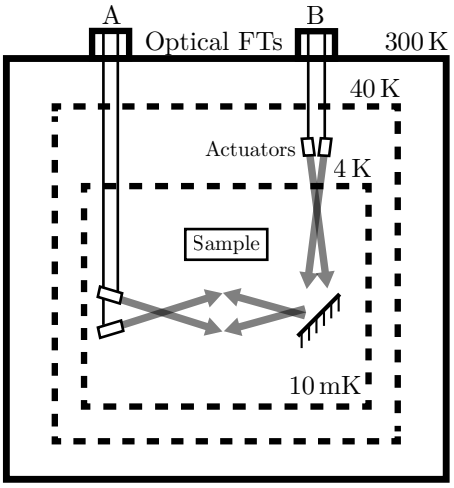

Figure 7.14: Two proposed methods for motion control of optical components within a dilution refrigerator. (A) Direct motion control at the 10 mK stage. This method of control is suitable for both optical and photonic fibres with full independent translational and rotational control, however, it suffers from a reduced range of motion caused by low sub-Kelvin temperatures. (B) Direct motion control at the 4 K stage.

photon detector can be constructed from the ground layer of the surface ion trap (see Fig. 7.13). Each photon detector pad would be separated by a gap of approximately $2 - 3\,\mu$m. Light from the ion would pass through etched channels in the trap structure down to the photon detector.

The quality factor of the resonator must be high such that each KID element can have a well-defined amplitude, frequency and phase component, but low enough that the signal strength is detectable. The signal from the waveguide would then be amplified by a HEMT or HFET (hetrostructure field-effect transistor) before being fed out for measurement. One design criteria of study is the usage of superconducting transistors for amplification purposes as this would allow amplification closer to the trap in the sub-Kelvin temperature range. This would allow for smaller noise floors and increase the potential pixel density for a single waveguide.

7.3.5 Motion control

The need to position devices operating within the dilution fridge brings multiple challenges. The actuator must be capable of withstanding cryogenic temperatures below 1 K, stable under UHV and capable of rotational and translational motion at the micrometre scale. Commercially available ceramic actuators can fulfil these requirements and offer displacements between 6.5 μm and 32 μm with a blocking force of 190 N to 3800 N. These devices have also been stress tested [245] and shown to work even after being placed under ten years of simulated thermal and structural stresses. However, it should be noted that these displacements are only quoted for liquid nitrogen temperatures at 77 K. Studies have also been performed on piezo actuators at sub-Kelvin temperatures, which show that while they continue to operate, they experience reduced expansion and flex motions [246–248].

Utilizing piezoelectric actuators, there are two possible schemes for motion control of the

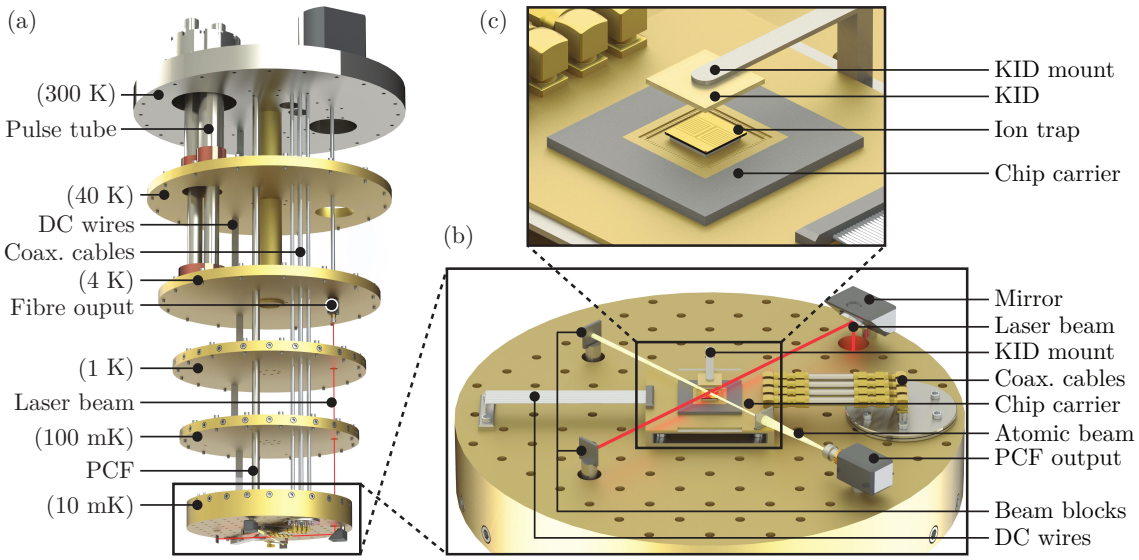

Figure 7.15: Final experimental layout of the ion trapping infrastructure within the dilution fridge environment. (a) The dilution fridge with the multiple temperature stages, cabling and laser access highlighted. (b) Mixing plate showing the ion trap and surrounding ancillary equipment. (c) A magnified view of the ion trap position showing the KID mounted above the ion trap.

fibre outputs. The first design, shown in feedthrough A of figure 7.14, shows the motion controller positioned directly on the coldest stage of the dilution fridge. This provides direct translational and rotational control of the fibre. However, the dissipated heat and vibrational noise is positioned close to the ion trap and at millikelvin temperatures the actuators motion is limited to the micrometre regime [246].

The second design, shown in feedthrough B of figure 7.14, is a hybrid between direct motion control and window access. This allows the positioning of the piezo actuators on a warmer stage, so that their thermal and vibrational noise is kept away from the coldest stage and their motion is maximized. However, in this design a mirror is needed to direct the beam towards the trap, thereby coupling the translational and rotational motion of the fibre together. This design would only work for the optical fibres as the atomic beam from the PCFs cannot be simply reflected.

Figure 7.15 shows the an image of the dilution fridge with cabling and laser access highlighted. It also presents a proposed experimental layout on the mixing plate showing the ion trap, mounting scheme, electrical connections, laser access and delivery of the atomic source.

Chapter 8

Detecting trapped ions with a microwave CPW

This chapter explores the interaction between trapped ions and microfabricated microwave cavities. It begins by describing the dynamics of an empty cavity as well as a cavity filled N two-level systems. The description of the system is based upon that of the optical regime [249], which utilizes optical cavities with mirrors, and is then modified for the microwave regime. Using the cavity designed in chapter 5, the numerical simulation of the magnetic field is presented. The coupling strength between the a single trapped ion and the microwave cavity is then described and presented. A brief description is also given for the different coupling regimes to provide context for the coupling strength achieved using the cavity designed in this thesis. Finally, the emission spectrum of the cavity is explored. Despite the weak coupling achieved, it can be shown that the detection of a single ion using a microfabricated CPW is possible with current experimental technology. This presents the exciting possibility of shifting the detection of an ion from an optical florescence based technique to an integrated on-chip microwave based technique, taking a step towards enhancing the scalability of a quantum computer.

8.1 An empty cavity

To begin exploring the interaction between a cavity and an ion, we can begin by looking at an empty cavity system. The microwave cavity system can be described in the same manner as an analogous optical cavity. Figure 8.1 shows an empty optical cavity and denotes the input, reflected, internal and transmitted fields, as well as the losses at each mirror. In the same way the optical cavity can be described as two reflective surfaces

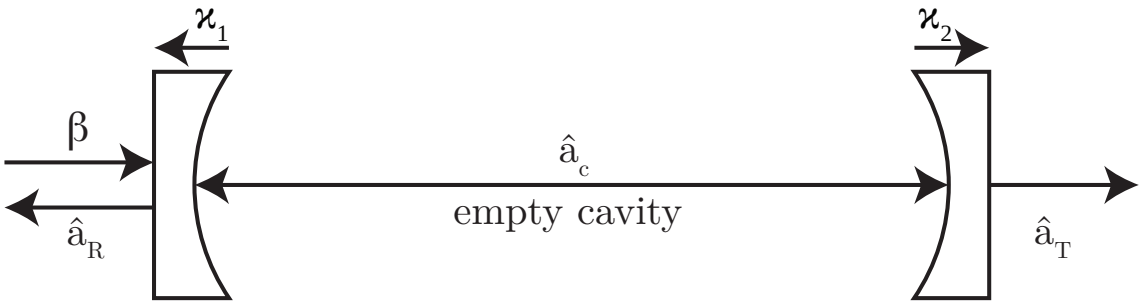

Figure 8.1: Optical cavity filled with no ions.

containing N ions with an internal optical cavity field $\hat{a}_c$, the microwave cavity can be described using the same parameters for a microwave regime. The Hamilitonian describing an empty cavity is given as [249]

$$\hat{H}_{\text{cavity}} = \hbar\Delta_c \hat{a}_c^\dagger \hat{a}_c + i\hbar\sqrt{2\kappa_1}\left(\beta\hat{a}_c^\dagger - \beta^*\hat{a}_c^\dagger\right) \tag{8.1}$$

where $\hat{a}_c^\dagger$ and $\hat{a}_c$ are the creation and annihilation operators of the cavity field, κ_1 is the field decay rate at the input mirror, κ_2 is the field decay rate at the output mirror, β is the input field amplitude such that $|\beta|^2$ is the incident number of photons on the cavity mirror per second and $\Delta_c = \omega_c - \omega$ is the detuning from the cavity resonant frequency, where ω_c is the cavity resonant frequency and ω_L is the cavity drive frequency. In the steady state, the mean field amplitude can be given as [249]

$$\langle \hat{a}_c \rangle = \frac{\sqrt{2\kappa_1}\beta}{\Gamma + i\Delta_c}, \tag{8.2}$$

where $\Gamma = \frac{1}{\tau_{jit}} + \kappa$, τ_{jit} is phase noise originating from fast jitter of one of the mirrors and $\kappa = \kappa_1 + \kappa_2$. In the steady state, the photon number can also be given as [249]

$$\langle \hat{a}_c^\dagger \hat{a}_c \rangle = \left(1 + \frac{1}{\kappa\tau_{jit}}\right) |\langle \hat{a}_c \rangle|^2 . \tag{8.3}$$

The introduction of phase noise ($\tau_{jit} < \infty$) into the system prevents the cavity field from being coherent such that $\langle \hat{a}_c^\dagger \hat{a}_c \rangle \neq |\langle \hat{a}_c \rangle|^2$. For a CPW structure we can assume that $\tau_{jit} \approx \infty$ as it is not subject to a phase noise comparable in amplitude or frequency to that of an optical cavity's mirror jitter. However, at cryogenic temperatures the variation in temperature of tens of mK over ∼hours is common in Gifford McMahon and Pulse Tube systems. This can lead to a variation in length, which is analogous to mirror jitter, however, the time scales involved makes this negligible.

When subjected to phase noise the cavity field $\hat{a}_c$ will possess multiple frequency com-

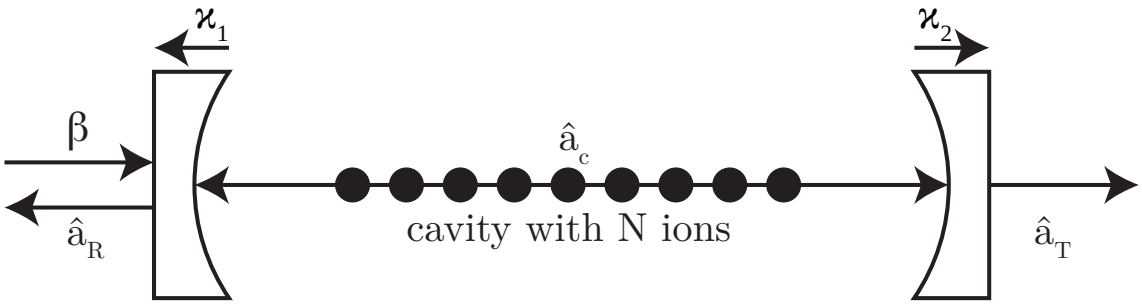

Figure 8.2: Optical cavity filled with N ions.

ponents, which are not equal to the drive frequency. This can be described as the cavity's spectral density $S_{\hat{a}_c}$, which is given as [249]

$$S\hat{a}_c(\omega) = \frac{1}{2\pi}\int_{-\infty}^{\infty}\langle \hat{a}_c^{\dagger}(t)\,\hat{a}_c(t+\tau)\rangle e^{i\Delta t}d\tau. \tag{8.4}$$

For a given drive frequency ω and bandwidth $d\omega$ around ω, the optical energy can be described as $S_{\hat{a}_c}(\omega)\,d\omega$. If we want to look at the total photon number in the cavity we have $\langle \hat{a}_c^{\dagger}\hat{a}_c\rangle = \int_{-\infty}^{\infty} S_{\hat{a}_c}(\omega)\,d\omega$. The spectrum for an empty cavity with noise can then be given as [249]

$$S\hat{a}_c(\omega) = \left[\frac{\Gamma/\pi}{\Gamma^2+(\omega_c-\omega)^2}\frac{1}{\kappa\tau_{jit}} + \delta(\omega-\omega_L)\right]|\langle\hat{a}_c\rangle|^2, \tag{8.5}$$

where $|\langle\hat{a}_c\rangle|^2$ is the steady state cavity field. A full derivation of equation 8.5 can be found in [249].

8.2 A cavity with ions

Now that we have an expression for an empty cavity, we can begin to introduce ions into the cavity system. By introducing N ions into a coherently driven cavity, our Hamiltonian describing the complete system includes that of the cavity $\hat{H}_{cavity}$, the ion $\hat{H}_{ion}$ and of the ion-cavity interaction $\hat{H}_{int}$, and is given by

$$\hat{H} = \hat{H}_{\text{cavity}} + \hat{H}_{\text{ion}} + \hat{H}_{\text{int}}. \tag{8.6}$$

This is essentially the structure for the Jaynes-Cummings model, which describes a two-level atom interacting with a single electromagnetic field mode. Physically, this equates to a single ion interacting with a single photon microwave field. The Hamiltonian for N number of ions within the cavity in the regime of low excitation probability $p_{ext} =$

$\frac{1}{2}\left(\langle\vec{\sigma}_z^{(j)}\rangle + 1\right) \ll 1$, where each atom is modelled by a harmonic oscillator is given by

$$\hat{H}_{\text{ion}} = \hbar\Delta_a \sum_{j=1}^{N} \hat{a}_j^\dagger \hat{a}_j, \tag{8.7}$$

where $\Delta_a = \omega_a - \omega_L$ is the detuning between the atom of the drive frequency ω_L and the atomic resonance frequency ω_a. The Hamiltonian for the ion-cavity interaction is given by

$$\hat{H}_{\text{int}} = \hbar g \sum_{j=1}^{N} \left(\hat{a}_j^\dagger \hat{a}_c + \hat{a}_j \hat{a}_c^\dagger\right), \tag{8.8}$$

where g is the coupling strength between the ion and the cavity. Inserting equations 8.1, 8.7 and 8.8 into equation 8.6 gives [249]

$$\hat{H} = \hbar\Delta_c \hat{a}_c^\dagger \hat{a}_c + i\hbar\sqrt{2\kappa_1}\left(\beta\hat{a}_c^\dagger - \beta^*\hat{a}_c^\dagger\right) + \hbar\Delta_a \sum_{j=1}^{N} \hat{a}_j^\dagger \hat{a}_j + \hbar g \sum_{j=1}^{N} \left(\hat{a}_j^\dagger \hat{a}_c + \hat{a}_j \hat{a}_c^\dagger\right). \tag{8.9}$$

As with the case for an empty cavity, we can then describe the spectral density of the cavity spectrum. For a cavity filled with ions, the spectrum is formed from a coherent part, which oscillates at exactly the drive frequency $\omega = \omega_L$, and a non-coherent broadband Lorentzian part, which is a result of the ion's phase noise. For the microwave regime we expect to see a similar response as the optical regime, with the presence of an incoherent broadband spectrum emerging due to phase noise from the ion coupling to the cavity. We also expect the incoherent spectrum to be much smaller in amplitude compared with what is observed in an optical cavity due to the interaction being via the magnetic dipole as opposed to the electric dipole. The spectrum for a cavity filled with N ions and subject to atomic phase noise is given as [249]

$$S\hat{a}_c(\omega) = \left[\frac{(\kappa+\gamma_\perp)\left(\kappa\gamma_\perp + g^2N\right) + \frac{\kappa\gamma_\perp\Delta_{ac}^2}{\kappa+\gamma_\perp}}{\pi\left|g^2N\left(\kappa + i\left[\omega_c - \omega\right]\right)\left(\gamma_\perp + i\left[\omega_c - \omega\right]\right)\right|^2} \times \frac{h\gamma_\perp^2}{\gamma_\perp^2 + \left(\omega_a - \omega_L\right)^2} + \delta\left(\omega - \omega_L\right)\right] \left|\langle\hat{a}_c\rangle\right|^2 \tag{8.10}$$

where $\Delta_{ac} = \omega_a - \omega_c$ is the detuning between the atomic resonant frequency and the cavity, κ is total losses from the cavity mirrors $(\kappa_1 + \kappa_2)$, $\langle\hat{a}_c\rangle$ in this case is given as [249]

$$\langle\hat{a}_c\rangle = \frac{\sqrt{2\kappa_1}\beta}{\left(\kappa + i\Delta_c\right)\left(1+\nu\right)}, \qquad \nu = \frac{g^2N}{\left(\kappa + i\Delta_c\right)\left(\gamma_\perp + i\Delta_a\right)}. \tag{8.11}$$

and the dephasing mechanism $\gamma_\perp = \frac{1}{\tau} + \frac{\gamma_{||}}{2}$, where τ is the ions dephasing rate and $\gamma_{||}$ is the rate of population decay of the two-level systems.

8.3 Ion-cavity interaction

With an expression for the cavity spectrum of an empty cavity and a cavity with N ions, we can now look in more detail at the ion-cavity interaction, which determines the variation in cavity spectrum. We can begin by determining the coupling strength g between a single ion and the cavity. The ion and cavity interact via microwave photons from the cavity and the magnetic dipole moment of the ion. To determine the coupling strength we must therefore know the magnetic field strength at the ions position. As with the description given in chapter 2 for the determination of the electrical pseudopotential to trap an ion, analytical and numerical simulations can also be performed of the cavity to determine its magnetic field at an arbitrary position. The formulae required for analytical calculations can be found in [250], however, all magnetic field simulations presented within this chapter are performed numerically. This allows us to simulate the exact details of the complete ion trap structure using the full 3-dimensional model.

Throughout the simulations we assume a $^{171}Yb^+$ ion, interacting with a single microwave photon field. We also simulate the cavity described in chapter 5 as it possess the highest demonstrated quality factor for an integrated microwave cavity, as well as an ion height equal to lowest ion height trapped at using a surface electrode ion trap [188].

8.3.1 Numerical simulation of magnetic field

The magnetic field of the cavity designed in chapter 5 was simulated numerically using a boundary element method in COMSOL Multiphysics. As expected, the electromagnetic field of the CPW is strongly confined between the central line and the two rf electrodes as they serve as a ground plane. At the ions position a magnetic field strength of $\sim$10 mG was achieved for an input voltage of 500 V, which was estimated as an upper limit to avoid electrical breakdown.

We must also consider the critical current I_c of the superconducting cavity. The critical current is the current which produces a critical magnetic field B_c at the conductors surface. Generally superconductors expel magnetic fields (Meissner effect), however, at a critical magnetic field for a given temperature T below the critical temperature T_c, the material will make the transition out of the superconducting regime. The critical magnetic field can be given as [251]

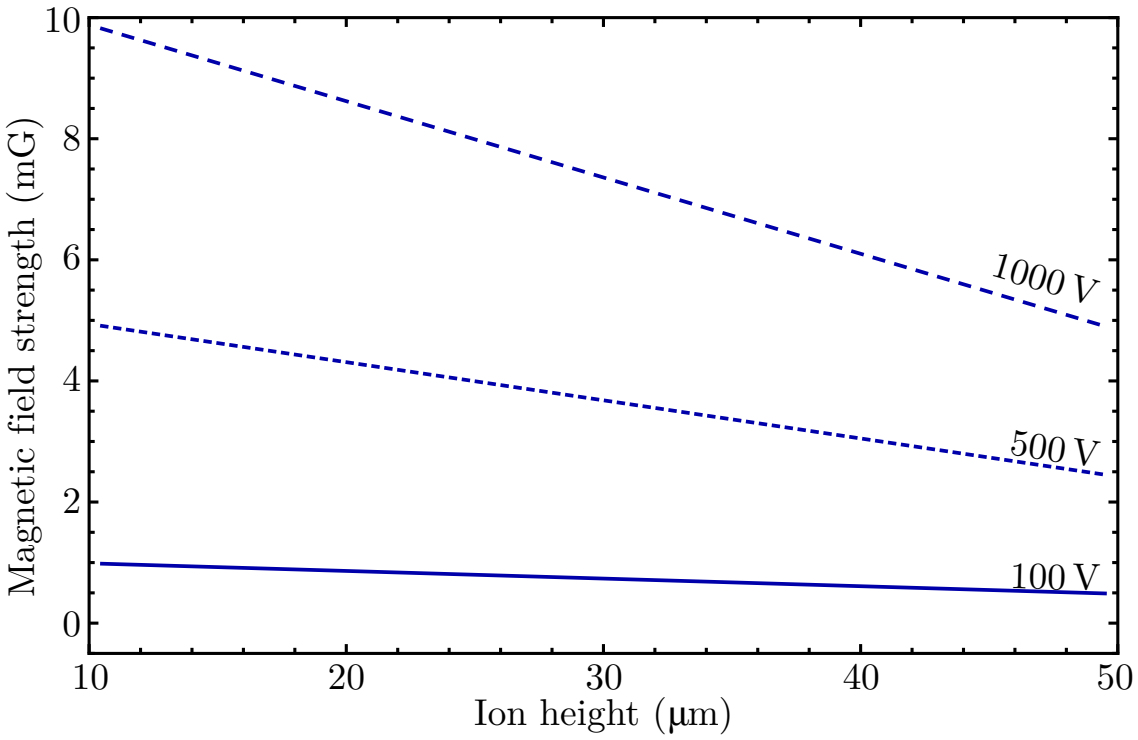

Figure 8.3: Variation in magnetic field strength as a function of ion height for an input voltage of 100 V, 500 V and 1000 V.

$$B_c = B_c(0)\left[1 - \left(\frac{T}{T_c}\right)^2\right], \tag{8.12}$$

where $B_c(0)$ is the critical magnetic field at 0 K. For niobium with a $T_c = 9.3\,\mathrm{K}$, the critical magnetic field is $B_c \sim 12.2\,\mathrm{T}$. For a $50\,\Omega$ impedance matched cavity and a voltage of 500 V, the current can be given as $I = V/Z_0 = 500\,\mathrm{V}\ /50\,\Omega = 10\,\mathrm{A}$. From numerical simulations of the cavity, a current of ∼30 A is required to reach the critical magnetic field strength of $B_c \sim 12.2\,\mathrm{T}$. Therefore, an applied voltage of 500 V results in a current below the critical current limit of the cavity.

Figure 8.3 shows the magnetic field strength as a function of voltage for 100 V, 500 V and 1000 V for a fixed ion height of 30 μm. Typically, rf voltages applied range between 100-500 V and are limited by voltage breakdown [252], however, voltage breakdown in excess of 1 kV have been demonstrated for use on surface electrode ion traps [213, 253]. Figure 8.4 shows the variation in magnetic field strength as a function of ion height for 10 μm, 20 μm, 30 μm, 40 μm and 50 μm for a fixed voltage of 500 V.

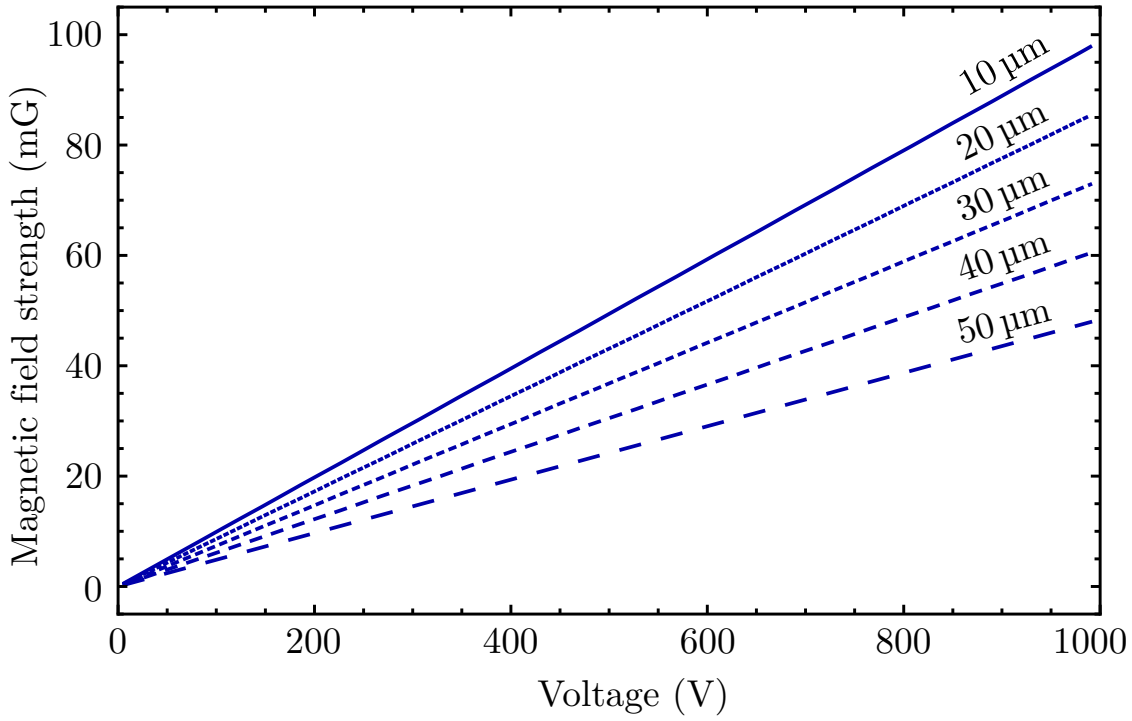

Figure 8.4: Variation in magnetic field strength as a function of input voltage for an ion height of 10 μm, 20 μm, 30 μm, 40 μm and 50 μm.

8.3.2 Ion-cavity coupling strength

When the $\vec{E}$ and $\vec{H}$ fields are perpendicular to each other in the direction of propagation, the mode can be described as a transverse electromagnetic (TEM) mode. This mode occurs when a dielectric material is placed between two excited conductors. One example of a waveguide with a TEM mode is a coaxial cable, where the $\vec{E}$ field lines are in the radial direction and the $\vec{H}$ field lines are perpendicular to the $\vec{E}$ field, such that they are concentric around the cable. Another characteristic of a TEM mode is a constant phase velocity, which means the propagation constant is equal to the wavenumber.

Unlike coaxial cables, inhomogeneous transmission-lines such as microstrip lines and the coplanar waveguides have cross-sections with metallic, dielectric, and free-space regions, which exhibit longitudinal electric field components. These longitudinal field components are necessary to satisfy the boundary conditions at the interfaces between different mediums.

In such a waveguide, the wave propagates with an average velocity, deviating from the TEM velocities corresponding to the material in the various parts of the waveguide cross-section. As the electromagnetic field lines in the CPW line are not contained entirely in the substrate but also propagate outside of the CPW, the propagating mode in the CPW line is not a pure TEM mode and as such is known as a quasi-TEM mode. Although

the wave propagates in two different mediums, an approximate static solution is used and an effective dielectric constant ϵ_{eff} and propagation constant can be calculated. The wave properties can be analysed as if it were propagating through a homogeneous effective medium with ϵ_{eff}, similar to a TEM mode. The transverse field generated by the quasi-TEM mode of the CPW cavity couples the hyperfine sublevels in $^{171}Yb^{+}$ and is given by [202]

$$g = \frac{1}{\sqrt{2}} \left\langle 1 \left| \mu_B \left(g_s \vec{S} - \frac{\mu_N}{\mu_B} g_I \vec{I} \right) \right| 0 \right\rangle \vec{B}_{trans}\left(\vec{r}\right), \tag{8.13}$$

where the term in the bra-ket represents the M1 transition matrix elements between the two hyperfine levels in the ground state of a $^{171}Yb^{+}$ ion, μ_B is the Bohr magneton, μ_N is the nuclear magneton, $g_s \sim 2$ is the electron g-factor, g_I is the nuclear g-factor (where $g_I \ll g_s$) and $\vec{B}_{trans}\left(\vec{r}\right)$ is the transverse magnetic field at an ion height r. The integral of the field amplitude over the mode volume is equal to half the energy in the electromagnetic field and is given as

$$\frac{1}{2\mu} \int dV \left| \vec{B}_{trans} \right|^2 = \frac{1}{2} \hbar \omega_c. \tag{8.14}$$

Figure 8.5 shows the coupling of the cavity to a single photon field as a function of ion height. For an ion height of $30\,\mu$m, corresponding to the cavity designed in chapter 5, a coupling rate of $\sim$1 Hz is achieved.

8.3.3 Coupling regimes

We can now put the coupling strength achieved into context by briefly describing different coupling regimes and the significance of the coupling achieved within these regimes. A strong coupling regime is defined when the coherent interaction of the emitter with the cavity field, described by the coupling constant g, is the dominant interaction. This can be shown as

$$g \gg \kappa, \gamma \tag{8.15}$$

where κ is the cavity decay rate and γ is the decay rate of the two-level system. For a weak coupling regime, the interaction of the emitter is incoherent and dominated by the damping rates κ and γ. The weak regime can therefore be given as

$$g \ll \kappa, \gamma \tag{8.16}$$

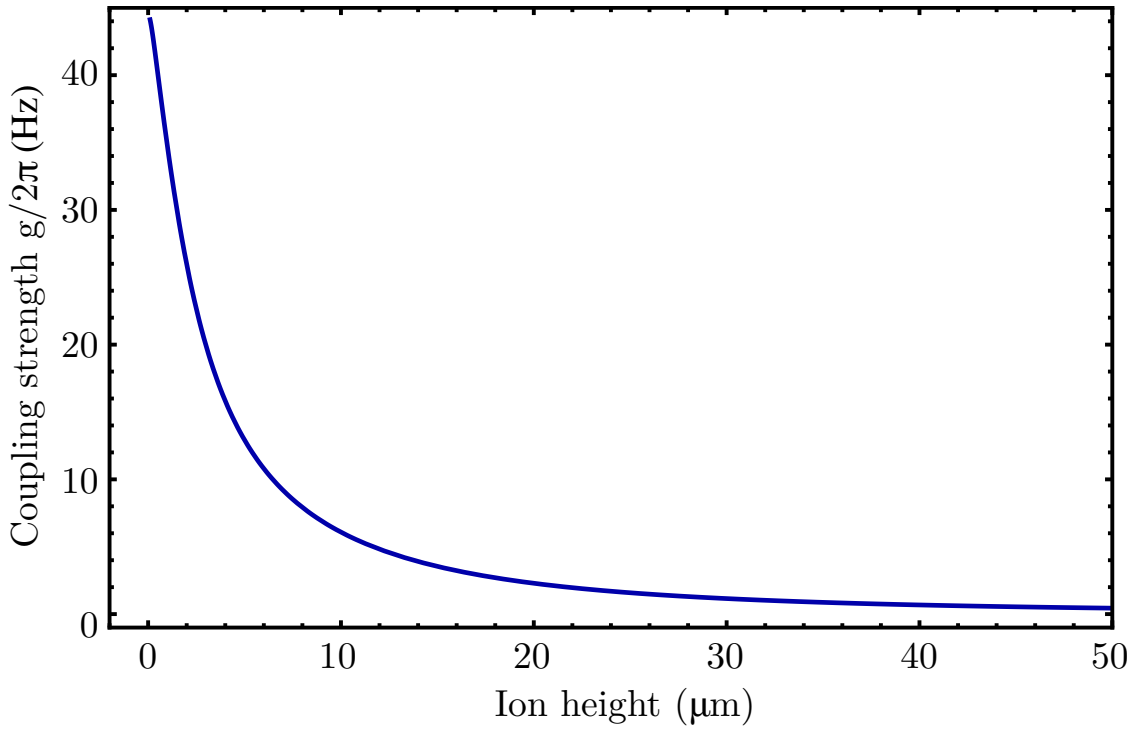

Figure 8.5: Variation in coupling strength as a function of ion height for an input voltage of 500 V.

The lifetime of the hyperfine ground state of $^{171}Yb^{+}$ can be treated as $\tau = \infty$. The decay rate γ is equal to $1/\tau$ and therefore gives $\gamma = 1/\infty = 0$ Hz. In terms of interaction mechanisms for this system, the decay of the two-level system can therefore be ignored. As described in section 8.1, κ describes the losses in the cavity. For an optical cavity this is physically represented by the reflectivity of the mirrors, where the quality factor of the cavity can be described in terms of κ as

$$Q = \frac{\omega_c}{\kappa}, \tag{8.17}$$

where ω_c is the resonant frequency of the cavity. Equation 8.17 is also a useful tool for describing microwave cavities as we can probe the quality factor of the microwave cavity directly and therefore determine κ. Rewriting equation 8.15 and 8.16 using equation 8.17 now gives

$$g \gg \frac{\omega_c}{Q} \qquad \text{and} \qquad g \ll \frac{\omega_c}{Q}, \tag{8.18}$$

for the strong and weak coupling regime respectively. For the cavity described in chapter 5, a quality factor of ∼10 000 was experimentally measured. Assuming an approximate hyperfine ground splitting of 12.6 GHz, we would require a coupling strength of $g \gg$

8 MHz to enter the strong coupling regime.

From figure 8.5 we can see the limiting factor is the position of the ion, which is relatively far for a cavity with field lines concentrated in between the electrodes. While the ion height can be reduced further, we are then affected by increases in ion heating. Assuming a maximum coupling strength of 1 Hz and an ion height of 30 μm, we would therefore require a quality factor of $Q \gg 10^{10}$ to enter the strong coupling regime.

Despite the weak coupling, ion trapping experiments can still utilize cavities for generating rf and microwave fields, which can be used for a number of purposes including driving quantum gates. High-Q cavities still offer the benefit of a low power dissipation on-chip microwave source. It is therefore beneficial to explore other potential uses of high-Q microwave cavities, which operate in the weak coupling regime. One point of interest is the cavity's potential in detecting trapped ions from the weak interaction with the cavity field. In the strong coupling regime we can simply measure the vacuum Rabi splitting down to a 1 Hz resolution using a vector network analyzer. However, assuming a coupling of less than 1 Hz, we can still look at the behaviour of the broadband incoherent part of the cavity spectrum as described in section 8.2 to determine the presence of an ion.

8.4 Cavity emission spectrum

After determining the magnetic field produced by the cavity and the ion-cavity interaction, we can now calculate the cavity emission spectrum using equations 8.5 and 8.10 for an empty and a cavity with N ions respectively. We can begin by looking at how to physically interpret the cavity spectrum into an experimental observable as a cavity *emission* spectrum. The intra-cavity mode operators $\hat{a}_c^\dagger, \hat{a}_c$ are in dimensionless units, where $\hat{a}_c^\dagger \hat{a}_c$ counts the number of photons, which is also dimensionless. The intra-cavity spectrum therefore "counts" the number of photons per frequency interval and has the units $1/s^{-1}$ = seconds. This is can be seen from equation 8.4 as it integrates a dimensionless quantity over time, which yields the unit of time. Equations 8.5 and 8.10 possess factors that multiply out to 1/frequency = time. The delta-functions in frequency also have dimensions of time (such that the integral over frequency yields 1). If all rates are given in s^{-1} the spectrum will then be given in (number of photons)/(1/s) = seconds, where a factor of 2π must be included to account for the angular frequency.

Now that we understand the cavity spectrum, we can look at the output field. For example in the transmitted field, the relevant operator is $\hat{a}_T = \sqrt{\kappa_2} \times \hat{a}_c$, where $\hat{a}_T$ the transmitted field. We must note that the dimensions of $\hat{a}_T$ is $\sqrt{\text{Hz}}$ and that $\hat{a}_T^\dagger \hat{a}_T$ is

frequency. This is because it is no longer the cavity mode content (the number of photons), but the emitted signal, which is a flux of photons, i.e. photons per second. The corresponding power spectrum, κ_1 multiplied by equation 8.4, is therefore dimensionless because it counts the flux per frequency interval (number of photons/s)/(1/s) = dimensionless. To present this value in units commonly used to measure spectral density, we can convert it to W/Hz by turning photon number into energy. This is done by multiplying the cavity emission spectrum with the energy of a single photon $E_\gamma = \hbar\omega_a$. Therefore, to measure the output spectrum we multiply the cavity spectrum with the decay through one cavity end and the energy of each photon to give $\hat{S}(\omega)\,\kappa_i E_\gamma$, where κ_i can be κ_1 or κ_2 for the reflected of transmitted losses respectively.

8.4.1 Experimental measurement limit

Experimentally, we can determine whether we will observe variation in the output emission spectrum for an empty cavity and a cavity with N ions by determining an experimental measurement limit. The measurement limit for detecting the emission spectrum of a microwave cavity is primarily determined by measurement tool, where the most accurate measurement can be performed using a vector network analyser (VNA). High performance VNAs, including the one used with this thesis (Rohde & Schwarz ZNB 20) are specified to measure down to a noise floor of -120 dBm ($\sim 1 \times 10^{-15}$ W, corresponding to $\sim 7.5 \times 10^8$ photons at 12.6 GHz), which is close to the shot noise limit of the measurement electronics. This is the fundamental limit we can measure for any experimental set-up in an ideal noiseless environment. This noise floor also assumes a relatively slow sweep time in 1 kHz steps, with a 200 MHz sweep taking ∼400 ms to perform. It should be noted that in all calculations it is assumed that $\omega_L = \omega_a = \omega_c$ exactly, however, experimentally we will also see deviations in resonant frequency. This will most likely occur for ω_c, which is dependant on the cavity dimensions that are variable due to fabrication errors. External noise originating from stray electric and magnetic fields will also lead to an increase the noise floor. Johnson noise will also be present and scale with the temperature of the system. The use of coaxial cable will also result in the attenuation of the output signal along the length of the cable.

8.4.2 Phase noise

In the case of an empty optical cavity, the phase noise originates from electrical jitter with ($\tau_{jit} < \infty$) resulting in a corresponding jitter in the cavity mirrors. As mentioned

previously, the analogous jitter in a microwave cavity occurs due to temperature variations on the order of mK on the time scale of ∼hours, which can be approximated to $\tau_{jit} = \infty$.

For the cavity with N ions we must also assign values for the dephasing mechanisms due to the ion $\gamma_\perp = \frac{1}{\tau} + \frac{\gamma_{||}}{2}$, where $1/\tau$ is the ions dephasing rate and $\gamma_{||}$ is the rate of population decay of the two-level systems. For a trapped Yb^+ ion, τ can be given as the coherence time where $\tau \sim 1\,\mathrm{s}$. The population decay rate for a two level atom can be given as $\gamma_{||} = 1/\tau''$, where τ'' is the lifetime of the hyperfine ground state. For $^{171}Yb^+$ $\tau'' = \infty$, therefore, $\gamma_{||} = 1/\infty = 0\,\mathrm{Hz}$. The final dephasing mechanism for the ion can then be given as

$$\gamma_\perp = \frac{1}{\tau} + \frac{\gamma_{||}}{2} = \frac{1}{1\,\mathrm{s}} + \frac{0\,\mathrm{s}^{-1}}{2} = 1\,\mathrm{Hz}. \tag{8.19}$$

8.5 Simulation results

The final simulation results using the preluding calculations can now determine whether the broadband signal, due to the ion's phase noise, produces a cavity signal that is higher than the detection limit.

Figure 8.6 presents the spectral power density $S\hat{a}_c(\omega)E_\gamma\kappa_2$ as a function of frequency detuned from 12.6 GHz for an empty cavity and a cavity with 1 ion driven with an input voltage of 500 V, which shows a clearly distinguishable incoherent broadband emission from the coherent field of the empty cavity. A resolution bandwidth of $\pi\kappa_p = 10^{-2}$ with a Lorentzian filter is applied to the data, where κ_p is the half-width half-maximum. We can see that for larger detunings from resonance we are better able to distinguish the variation in the cavity signal for and empty cavity and a cavity with one ion. However, further from resonance the cavity signal also decreases below the lower measurement limit.

Figure 8.7 shows the cavity response at a 2 kHz detuning from 12.6 GHz for an empty cavity and a cavity with 1 ion driven with a input power of 1 mW as a function of frequency. Here, we notice that as Q increases we get a general increase in the off resonant spectral power density from the increased field strength from a higher Q with the same input power. However, beyond a certain point the reduced cavity bandwidth reduces the off resonant transmission more than the field strength increases, which causes a drop in the measurable spectral power. The experimentally demonstrated quality factor of the cavity presented in chapter 5 is $Q \sim 10\,000$. From this we can see that the signal from the cavity is greater than the the fundamental noise limit of -120 dBm for a limited range in Q. We can also increase the spectral power density a few orders of magnitude further by increasing the

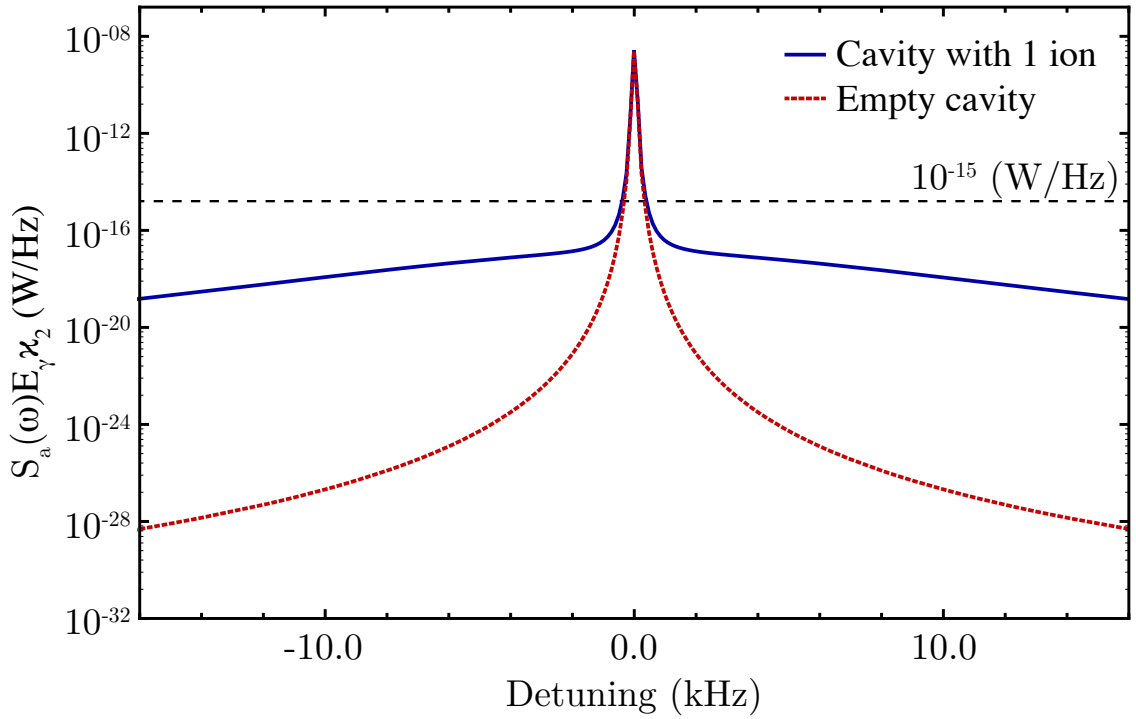

Figure 8.6: Cavity response as a function of detuning for an empty cavity (dashed) and a cavity with 1 ion (solid) driven with a input power of 1 mW.

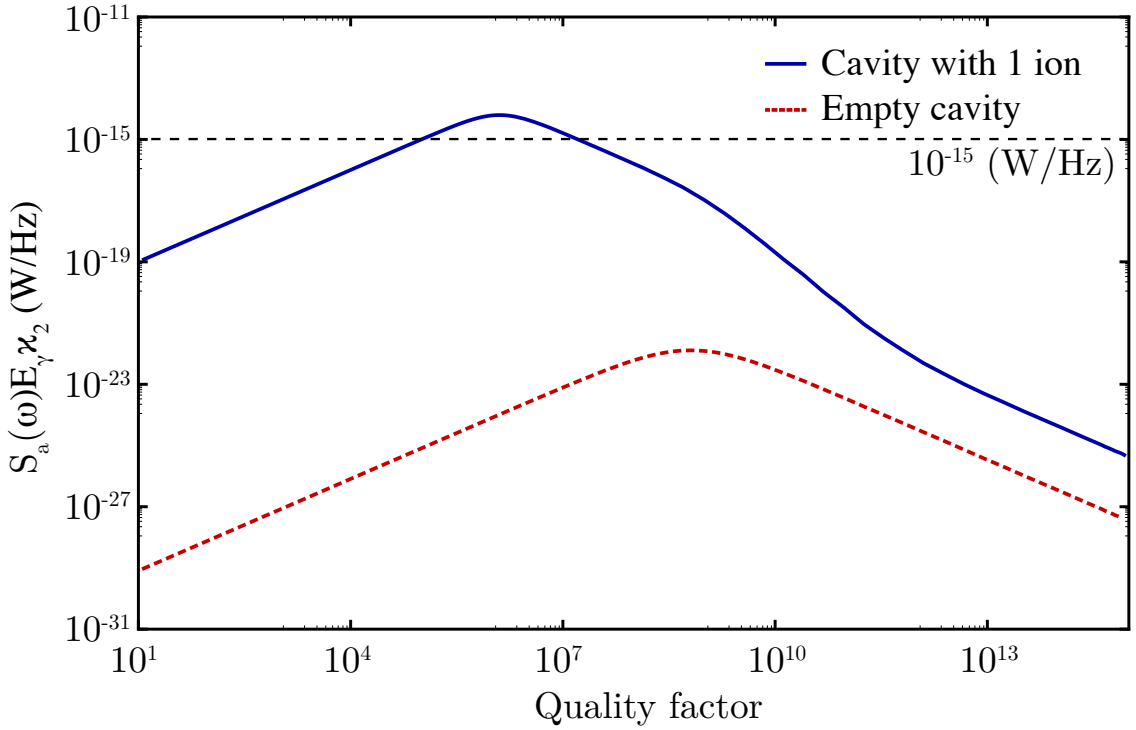

Figure 8.7: Cavity response at a 2 kHz detuning from 12.6 GHz for an empty cavity (dashed) and a cavity with 1 ion (solid) driven with a input power of 1 mW.

input power and also by probing the cavity output closer to the 12.6 GHz resonance. We can observe the effect of probing the cavity at different frequencies by looking at the effects

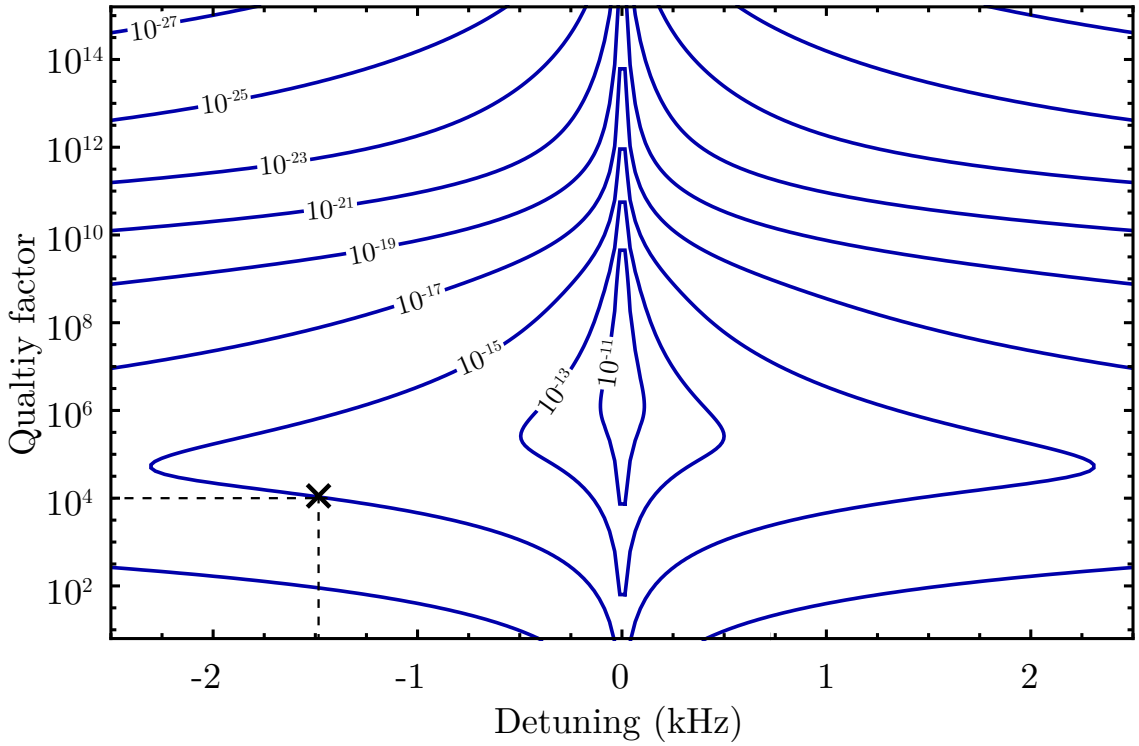

Figure 8.8: Maximum power of the cavity emission spectrum (W/Hz), with each contour showing an order of magnitude, as a function of frequency detuning and cavity quality factor for an input voltage of 500 V and an ion height of 30 μm. The 'X' denotes the maximum detuning while maintaining a signal strength of 10^{-15} W/Hz for the high-Q cavity designed in this thesis, where a quality factor of $Q \sim 10^4$ was obtained.

of figure 8.7 as a function of frequency.

Figure 8.8 shows a contour plot of the maximum power of the cavity emission spectrum as a function of frequency detuning and cavity quality factor for an input voltage of 500 V and an ion height of 30 μm. The plot can be used to determine the regime where a measurable cavity emission is possible for a cavity with an arbitrary quality factor. It also allows the determination of the maximum detuning, to help distinguish between the cavity signal for an empty cavity and a cavity with one ion, for a given quality factor. For the high-Q cavity presented in this thesis, where a quality factor of $Q \sim 10^4$ was obtained, we can reach a maximum detuning of $\sim$1.5 kHz while maintaining a signal strength of 10^{-15} W/Hz. At a detuning of 1.5 kHz, the corresponding cavity signal for an empty cavity is $\sim 10^{-18}$ W/Hz. Therefore, for the detection limit given, we could be capable of measuring the presence of a single ion using this cavity.

Conclusion

In this thesis I have described the development of cryogenic ion trapping technology towards scalable quantum computing and quantum hybrid systems. Firstly, I began by outlining the fundamental principles underlining the operation of radio frequency Paul traps and described how specific isotopes of ytterbium can be used as an ion for quantum information experiments. I then described the experimental setup, including lasers, laser stabilisation and the operation of an ultra-high vacuum system at room temperature. The optical imaging setups are then presented in detail for both room temperature and cryogenic vacuum systems with a critical discussion given on both setups. An experimental demonstration is then presented for ion trapping on an ion trap with a novel ring based electrode architecture.

Once the foundation and demonstration of ion trapping have been presented, a core body of work in the development of a cryogenic vacuum system for ion trapping at $\sim$4 K was presented. This includes an in depth discussion on the benefits of the cryogenic regime for trapped ions, including the attainment of ultra-high vacuum pressures from cryopumping, the reduction in ion heating and the utilization of superconducting materials within the system. The closed cycle Gifford McMahon cryocooler is described along with a custom built vacuum system for operation in a cryogenic environment. A helium buffered ultra-low vibration interface is then presented to mechanically decouple the cryocooler from the experiment. Ancillary technologies are also described such as an in-vacuum superconducting rf resonator with additional dc electronics. A low power dissipation ceramic based atomic source oven for cryogenic ion trapping is then described along side an ion trap mounting scheme for efficient trap cooling with the ability for mounting permanent magnets to perform long-wavelength based quantum logic. The description of the cryogenic setup concludes with the characterization of the system and its operation.

After the cryogenic system has been described, the design and simulation of microfab-

ricated surface ion traps toward quantum hybrid technologies are described. First, the design for a superconducting ion trap with an integrated high quality factor microwave cavity is presented. The trap design also incorporates vertical ion shuttling capabilities, allowing for trapping at larger ion heights and shuttling to lower ion heights for ion-cavity interactions. The experimental demonstration of the cavity is also presented with quality factors of Q$\sim$6 000 and Q$\sim$15 000 for superconducting niobium nitride and gold respectively, which are the highest demonstrated for microwave cavities integrated within ion trapping electrode architectures. An ion trap with a multipole electrode geometry is then presented, which is capable of trapping a large number of ions simultaneously. The homogeneity of five individual linear trapping regions are optimized and the design for the principle axis rotation of each linear region is presented.

An overview of microfabrication techniques used for fabricating surface electrode ion traps was then presented. This includes the detailed microfabrication procedure for ion traps, including those designed within this thesis, using a gold based electrode process and a superconducting niobium nitride based electrode process. The results of the fabrication are then presented and discussed.

An experimental design for the integration of ion trapping and superconducting qubit systems as a step towards the realization of a quantum hybrid system is then presented. This scheme addresses two key difficulties in realizing such a system; a combined microfabricated ion trap and superconducting qubit architecture, and the experimental infrastructure to facilitate both technologies. Solutions that can be immediately implemented using current technology are then described in detail. This includes the experimental design for and ion trap with the potential of producing a coupling strength between an ion and a superconducting circuit in the tens of kHz, as well as a detailed scheme for ion trapping in a dilution fridge.

Finally, as a step towards scalability and quantum hybrid systems, the interaction between ions and a microwaves field produced from an on chip microwave cavity is explored. The interaction between a single trapped ion and the high-Q microwave cavity designed in this thesis is presented. A description of the observable transmission from the cavity due to the interaction is described and it is shown that single ions can indeed be observed in the emission spectrum of high-Q microwave cavities even in the weak coupling regime.

Bibliography

[1] A. S. Bell, P. Gill, H. A. Klein, A. P. Levick, Chr. Tamm, and D. Schnier. Laser cooling of trapped ytterbium ions using a four-level optical-excitation scheme. *Phys. Rev. A*, 44:R20–R23, Jul 1991. Cited on xviii, 19

[2] CRC Handbook of chemistry, physics, Charles David Hodgman, and William Reed Veazey. *CRC Handbook of chemistry and physics*. Chemical Rubber Publishing Company, 1977. Cited on xviii, 64

[3] C Day. Basics and applications of cryopumps. 2006. Cited on xxi, 47

[4] Q. A. Turchette, Kielpinski, B. E. King, D. Leibfried, D. M. Meekhof, C. J. Myatt, M. A. Rowe, C. A. Sackett, C. S. Wood, W. M. Itano, C. Monroe, and D. J. Wineland. Heating of trapped ions from the quantum ground state. *Phys. Rev. A*, 61(6):063418, May 2000. Cited on xxi, 49, 50, 51

[5] Louis Deslauriers, S Olmschenk, D Stick, WK Hensinger, J Sterk, and C Monroe. Scaling and suppression of anomalous heating in ion traps. *Physical review letters*, 97(10):103007, 2006. Cited on xxi, 49, 50, 51, 165

[6] F Diedrich, JC Bergquist, Wayne M Itano, and DJ Wineland. Laser cooling to the zero-point energy of motion. *Physical Review Letters*, 62(4):403, 1989. Cited on xxi, 18, 50

[7] Ralph G. DeVoe and Christian Kurtsiefer. Experimental study of anomalous heating and trap instabilities in a microscopic ^{137}ba ion trap. *Phys. Rev. A*, 65(6):063407, Jun 2002. Cited on xxi, 50

[8] Ch. Roos, Th. Zeiger, H. Rohde, H. C. Nägerl, J. Eschner, D. Leibfried, F. Schmidt-Kaler, and R. Blatt. Quantum state engineering on an optical transition and decoherence in a paul trap. *Phys. Rev. Lett.*, 83(23):4713–4716, Dec 1999. Cited on xxi, 50

[9] Stephan A. Schulz, Ulrich Poschinger, Frank Ziesel, and Ferdinand Schmidt-Kaler. Sideband cooling and coherent dynamics in a microchip multi-segmented ion trap. *New J. Phys.*, 10(045007):15, 2008. Cited on xxi, 50

[10] N. Daniilidis, S. Narayanan, S. A. Möller, R. Clark, T. E. Lee, P. J. Leek, A. Wallraff, St. Schulz, F. Schmidt-Kaler, and H. Häffner. Fabrication and heating rate study of microscopic surface electrode ion traps. *New J. Phys.*, 13(013032):17, 2011. Cited on xxi, 50

[11] Chr. Tamm, D. Engelke, and V. Bühner. Spectroscopy of the electric-quadrupole transition ${}^2s_{1/2}(f=0)-{}^2d_{3/2}(f=2)$ in trapped ${}^{171}yb^+$. *Phys. Rev. A*, 61(5):053405, Apr 2000. Cited on xxi, 50

[12] M. A. Rowe, A. Ben-Kish, B. DeMarco, D. Leibfried, V. Meyer, J. Beall, J. Britton, J. Hughes, W. M. Itano, B. Jelenkovic, C. Langer, T. Rosenband, and D. J. Wineland. Transport of quantum states and separation of ions in a dual rf ion trap. *Quant. Inf. Comp.*, 2(4):257–271, 2002. Cited on xxi, 50, 115

[13] J. Britton. *Microfabrication techniques for trapped ion quantum information processing.* Ph.d. thesis, arxiv:1008.2222v1, Boulder, 2008. Cited on xxi, 50

[14] R. J. Epstein, S. Seidelin, D. Leibfried, J. H. Wesenberg, J. J. Bollinger, J. M. Amini, R. B. Blakestad, J. Britton, J. P. Home, W. M. Itano, J. D. Jost, E. Knill, C. Langer, R. Ozeri, N. Shiga, and D. J. Wineland. Simplified motional heating rate measurements of trapped ions. *Phys. Rev. A*, 76(3):033411, Sep 2007. Cited on xxi, 50

[15] Shannon X. Wang, Yufei Ge, Jaroslaw Labaziewicz, Eric Dauler, Karl Berggren, and Isaac L. Chuang. Superconducting microfabricated ion traps. *Appl. Phys. Lett.*, 97:244102, 2010. Cited on xxi, 50

[16] J. Labaziewicz, Y. Ge, P. Antohi, D. Leibrandt, K. R. Brown, and I. L. Chuang. Suppression of heating rates in cryogenic surface-electrode ion traps. *Phys. Rev. Lett.*, 100(1):013001, 2008. Cited on xxi, 5, 50

[17] D. Stick, W. K. Hensinger, S. Olmschenk, M. J. Madsen, K. Schwab, and C. Monroe. Ion trap in a semiconductor chip. *Nature Phys.*, 2:36–39, 2006. Cited on xxi, 5, 50

[18] Signe Seidelin, John Chiaverini, Rainer Reichle, JJ Bollinger, Didi Leibfried, Joe Britton, JH Wesenberg, RB Blakestad, RJ Epstein, DB Hume, et al. Microfabricated

surface-electrode ion trap for scalable quantum information processing. *Physical review letters*, 96(25):253003, 2006. Cited on xxi, 50, 170

[19] V. Letchumanan, G. Wilpers, M. Brownnutt, P. Gill, and A. G. Sinclair. Zero-point cooling and heating-rate measurements of a single $^{88}Sr^{+}$ ion. *Phys. Rev. A*, 75:063425, Jun 2007. Cited on xxi, 50

[20] D. T. C. Allcock, J. A. Sherman, D. N. Stacey, A. H. Burrell, M. J. Curtis, G. Imreh, N. M. Linke, D. J. Szwer, S. C. Webster, A. M. Steane, and D. M. Lucas. Implementation of a symmetric surface-electrode ion trap with field compensation using a modulated raman effect. *New J. Phys.*, 12:053026, 2010. Cited on xxi, 50, 141

[21] J. Britton, D. Leibfried, J. A. Beall, R. B. Blakestad, J. H. Wesenberg, and D. J. Wineland. Scalable arrays of rf paul traps in degenerate si. *Appl. Phys. Lett.*, 95:173102, Oct 2009. Cited on xxi, 50

[22] J. M. Amini, H. Uys, J. H. Wesenberg, S. Seidelin, J. Britton, J. J. Bollinger, D. Leibfried, C. Ospelkaus, A. P. VanDevender, and D. J. Wineland. Toward scalable ion traps for quantum information processing. *New J. Phys.*, 12:033031, 2010. Cited on xxi, 50

[23] James J. McLoughlin, Altaf H. Nizamani, James D. Siverns, Robin C. Sterling, Marcus D. Hughes, Bjoern Lekitsch, Björn Stein, Seb Weidt, and Winfried K. Hensinger. Versatile ytterbium ion trap experiment for operation of scalable ion-trap chips with motional heating and transition-frequency measurements. *Phys. Rev. A*, 83(1):013406, Jan 2011. Cited on xxi, 50

[24] S Weidt, J Randall, SC Webster, ED Standing, A Rodriguez, AE Webb, B Lekitsch, and WK Hensinger. Ground-state cooling of a trapped ion using long-wavelength radiation. *arXiv preprint arXiv:1501.01562*, 2015. Cited on xxi, 18, 50

[25] SHI Cryogenics Group. Cryocoolers product catalogue, 2010. Cited on xxi, 56

[26] Ltd Precision Equipment Group Sumitomo Heavy Industries. External magnetic field data for 4kgm cold head motor. Technical report, Sumitomo Heavy Industries, Ltd, 2012. Cited on xxi, 58

[27] Lake Shore Cryotronics. Cryogenic reference tables. Technical report, Lake Shore Cryotronics, Inc, 2010. Cited on xxii, 68

[28] D Gandolfi, M Niedermayr, M Kumph, M Brownnutt, and R Blatt. Compact radio-frequency resonator for cryogenic ion traps. *Review of Scientific Instruments*, 83(8):084705, 2012. Cited on xxiv, 54, 83, 84, 85

[29] Todd Karin, Isabela Le Bras, Andreas Kehlberger, Kilian Singer, Nikos Daniilidis, and Hartmut Häffner. Transport of charged particles by adjusting rf voltage amplitudes. *Applied Physics B*, 106(1):117–125, 2012. Cited on xxv, 112

[30] M Göppl, A Fragner, M Baur, R Bianchetti, S Filipp, JM Fink, PJ Leek, G Puebla, L Steffen, and Andreas Wallraff. Coplanar waveguide resonators for circuit quantum electrodynamics. *Journal of Applied Physics*, 104(11):113904, 2008. Cited on xxvi, 121, 122, 124, 125

[31] Tomonori Arakawa, Yoshitaka Nishihara, Masahiro Maeda, Shota Norimoto, and Kensuke Kobayashi. Cryogenic amplifier for shot noise measurement at 20 mk. *Applied Physics Letters*, 103(17):172104, 2013. Cited on xxx, 182

[32] Alan Mathison Turing. On computable numbers, with an application to the entscheidungsproblem. *J. of Math*, 58(345-363):5, 1936. Cited on 2

[33] Richard P Feynman. Simulating physics with computers. *International journal of theoretical physics*, 21(6/7):467–488, 1982. Cited on 3

[34] David Deutsch. Quantum theory, the church-turing principle and the universal quantum computer. In *Proceedings of the Royal Society of London A: Mathematical, Physical and Engineering Sciences*, volume 400, pages 97–117. The Royal Society, 1985. Cited on 3

[35] Lov K. Grover. Quantum mechanics helps in searching for a needle in a haystack. *Phys. Rev. Lett.*, 79:325–328, Jul 1997. Cited on 4

[36] P. W. Shor. Algorithms for quantum computation: Discrete logarithms and factoring. *In Proceedings, 35th Annual Symposium on Foundations of Computer Science, IEEE Computer Soc. Press*, pages 124–134, 1994. Cited on 4

[37] Chris Cesare. Online security braces for quantum revolution. *Nature*, 525(7568):167–168, 2015. Cited on 4

[38] R Barends, A Shabani, L Lamata, J Kelly, A Mezzacapo, U Las Heras, R Babbush, AG Fowler, B Campbell, Yu Chen, et al. Digitized adiabatic quantum computing with a superconducting circuit. *Nature*, 534(7606):222–226, 2016. Cited on 4

[39] S Poletto, Jay M Gambetta, Seth T Merkel, John A Smolin, Jerry M Chow, AD Córcoles, George A Keefe, Mary B Rothwell, JR Rozen, DW Abraham, et al. Entanglement of two superconducting qubits in a waveguide cavity via monochromatic two-photon excitation. *Physical review letters*, 109(24):240505, 2012. Cited on 4

[40] Dave Wecker, Matthew B Hastings, Nathan Wiebe, Bryan K Clark, Chetan Nayak, and Matthias Troyer. Solving strongly correlated electron models on a quantum computer. *Physical Review A*, 92(6):062318, 2015. Cited on 4

[41] Lieven MK Vandersypen, Matthias Steffen, Gregory Breyta, Costantino S Yannoni, Richard Cleve, and Isaac L Chuang. Experimental realization of an order-finding algorithm with an nmr quantum computer. *Physical Review Letters*, 85(25):5452, 2000. Cited on 4, 163

[42] Ivan H. Deutsch, Gavin K. Brennen, and Poul S. Jessen. Quantum computing with neutral atoms in an optical lattice. *Fortschritte der Physik*, 48(9-11):925–943, 2000. Cited on 4, 163

[43] Yu Nakamura, Yu A Pashkin, and JS Tsai. Coherent control of macroscopic quantum states in a single-cooper-pair box. *Nature*, 398(6730):786–788, 1999. Cited on 4, 54, 163

[44] Daniel Loss and David P. DiVincenzo. Quantum computation with quantum dots. *Phys. Rev. A*, 57:120–126, Jan 1998. Cited on 4, 163

[45] Jörg Wrachtrup and Fedor Jelezko. Processing quantum information in diamond. *Journal of Physics: Condensed Matter*, 18(21):S807, 2006. Cited on 4, 163

[46] Klaus M Gheri, Klaus Ellinger, Thomas Pellizari, and Peter Zoller. Photon-wavepackets as flying quantum bits. *Fortschritte der Physik*, 46(4):401–416, 1998. Cited on 4, 163

[47] C Ospelkaus, U Warring, Y Colombe, KR Brown, JM Amini, D Leibfried, and DJ Wineland. Microwave quantum logic gates for trapped ions. *Nature*, 476(7359):181–184, 2011. Cited on 4, 5, 163, 165, 166, 170

[48] J. I. Cirac and P. Zoller. Quantum computations with cold trapped ions. *Phys. Rev. Lett.*, 74:4091–4094, May 1995. Cited on 4, 7, 17

[49] Chris Monroe, DM Meekhof, BE King, WM Itano, and DJ Wineland. Demonstration of a fundamental quantum logic gate. *Physical Review Letters*, 75(25):4714, 1995. Cited on 4, 164

[50] Ferdinand Schmidt-Kaler, Hartmut Häffner, Mark Riebe, Stephan Gulde, Gavin PT Lancaster, Thomas Deuschle, Christoph Becher, Christian F Roos, Jürgen Eschner, and Rainer Blatt. Realization of the cirac-zoller controlled-not quantum gate. *Nature*, 422(6930):408–411, 2003. Cited on 4, 94, 141

[51] D. P. DiVincenzo. Quantum computation. *Science*, 270:255–261, 13 October 1995. Cited on 4

[52] D. Leibfried, D. M. Meekhof, B. E. King, C. Monroe, W. M. Itano, and D. J. Wineland. Experimental determination of the motional quantum state of a trapped atom. *Phys. Rev. Lett.*, 77(21):4281–4285, Nov 1996. Cited on 5

[53] D. Leibfried, B. DeMarco, V. Meyer, D. Lucas, M. Barrett, J. Britton, W. M. Itano, B. Jelenkovic, C. Langer, T. Rosenband, and D. J. Wineland. Experimental demonstration of a robust, high-fidelity geometric two ion-qubit phase gate. *Nature*, 422:412–415, 2003. Cited on 5, 48, 141

[54] J. Benhelm, G. Kirchmair, C. F. Roos, and Rainer Blatt. Towards fault-tolerant quantum computing with trapped ions. *Nature Phys.*, 4:463–466, 2008. Cited on 5

[55] A. H. Myerson, D. J. Szwer, S. C. Webster, D. T. C. Allcock, M. J. Curtis, G. Imreh, J. A. Sherman, D. N. Stacey, A. M. Steane, and D. M. Lucas. High-fidelity readout of trapped-ion qubits. *Phys. Rev. Lett.*, 100(20):200502, May 2008. Cited on 5

[56] D. M. Lucas, B. C. Keitch, J. P. Home, G. Imreh, M. J. McDonnell, D. N. Stacey, D. J. Szwer, and A. M. Steane. A long-lived memory qubit on a low-decoherence quantum bus. *arXiv:0710.4421v1*, 2007. Cited on 5

[57] TP Harty, DTC Allcock, CJ Ballance, L Guidoni, HA Janacek, NM Linke, DN Stacey, and DM Lucas. High-fidelity preparation, gates, memory, and readout of a trapped-ion quantum bit. *Physical review letters*, 113(22):220501, 2014. Cited on 5, 164

[58] R. B. Blakestad, C. Ospelkaus, A. P. VanDevender, J. M. Amini, J. Britton, D. Leibfried, and D. J. Wineland. High-fidelity transport of trapped-ion qubits

through an x-junction trap array. *Phys. Rev. Lett.*, 102(15):153002, Apr 2009. Cited on 5, 115

[59] B Lekitsch, S Weidt, AG Fowler, K Mølmer, SJ Devitt, Ch Wunderlich, and WK Hensinger. Blueprint for a microwave ion trap quantum computer. *arXiv preprint arXiv:1508.00420*, 2015. Cited on 5, 171

[60] S. Seidelin, J. Chiaverini, R. Reichle, J. J. Bollinger, D. Leibfried, J. Britton, J. H. Wesenberg, R. B. Blakestad, R. J. Epstein, D. B. Hume, W. M. Itano, J. D. Jost, C. Langer, R. Ozeri, N. Shiga, and D. J. Wineland. Microfabricated surface-electrode ion trap for scalable quantum information processing. *Phys. Rev. Lett.*, 96(25):253003, Jun 2006. Cited on 5

[61] J. Britton, D. Leibfried, J. A. Beall, R. B. Blakestad, J. J. Bollinger, J. Chiaverini, R. J. Epstein, J. D. Jost, D. Kielpinski, C. Langer, R. Ozeri, R. Reichle, S. Seidelin, N. Shiga, J. H. Wesenberg, and D. J. Wineland. A microfabricated surface-electrode ion trap in silicon. *arXiv:quant-ph/0605170v1*, Feb 2008. Cited on 5

[62] D. Stick, K. M. Fortier, R. Haltli, C. Highstrete, D. L. Moehring, C. Tigges, and M. G. Blain. Demonstration of a microfabricated surface electrode ion trap. *arXiv:1008.0990v2*, Aug 2010. Cited on 5

[63] R. C. Sterling, H. Rattanasonti, S. Weidt, K. Lake, P. Srinivasan, M. Kraft, and W. K. Hensinger. Trapping and shuttling in a microfabricated two-dimensional ion trap lattice array. *in preparation*, 2011. Cited on 5, 44

[64] M. J. Madsen, W. K. Hensinger, D. Stick, J. A. Rabchuk, and C. Monroe. Planar ion trap geometry for microfabrictaion. *App. Phys. B*, (78):639–651, 2004. Cited on 5

[65] Marcus D Hughes, Bjoern Lekitsch, Jiddu A Broersma, and Winfried K Hensinger. Microfabricated ion traps. *Contemporary Physics*, 52(6):505–529, 2011. Cited on 5, 170

[66] PB Antohi, D Schuster, GM Akselrod, J Labaziewicz, Y Ge, Z Lin, WS Bakr, and IL Chuang. Cryogenic ion trapping systems with surface-electrode traps. *Review of Scientific Instruments*, 80(1):013103, 2009. Cited on 5, 181, 184

[67] Shannon X Wang, Yufei Ge, Jaroslaw Labaziewicz, Eric Dauler, Karl Berggren, and Isaac L Chuang. Superconducting microfabricated ion traps. *Applied Physics Letters*, 97(24):244102, 2010. Cited on 5, 131, 170

[68] David Kielpinski, D Kafri, MJ Woolley, GJ Milburn, and JM Taylor. Quantum interface between an electrical circuit and a single atom. *Physical review letters*, 108(13):130504, 2012. Cited on 5, 166, 167, 168, 170, 174, 176

[69] Margareta Wallquist, Klemens Hammerer, Peter Rabl, Mikhail Lukin, and Peter Zoller. Hybrid quantum devices and quantum engineering. *Physica Scripta*, 2009(T137):014001, 2009. Cited on 5, 53, 163, 164

[70] Ze-Liang Xiang, Sahel Ashhab, JQ You, and Franco Nori. Hybrid quantum circuits: Superconducting circuits interacting with other quantum systems. *Reviews of Modern Physics*, 85(2):623, 2013. Cited on 5

[71] DJ Wineland, RE Drullinger, and FL Walls. Radiation-pressure cooling of bound resonant absorbers. *Physical Review Letters*, 40(25):1639, 1978. Cited on 7

[72] W. Neuhauser, M. Hohenstatt, P. Toschek, and H. Dehmelt. Optical-sideband cooling of visible atom cloud confined in parabolic well. *Phys. Rev. Lett.*, 41:233–236, Jul 1978. Cited on 7

[73] S. A. Webster, P. Taylor, M. Roberts, G. P. Barwood, and P. Gill. Kilohertz-resolution spectroscopy of the $^2s_{1/2} -^2 f_{7/2}$ electric octupole transition in a single $^{171}yb^+$ ion. *Phys. Rev. A*, 65(5):052501, Apr 2002. Cited on 7

[74] M. Chwalla, J. Benhelm, K. Kim, G. Kirchmair, T. Monz, M. Riebe, P. Schindler, A. S. Villar, W. Hänsel, C. F. Roos, R. Blatt, M. Abgrall, G. Santarelli, G. D. Rovera, and Ph. Laurent. Absolute frequency measurement of the $^{40}ca^+$ $4s\,^2s_{1/2} - 3d\,^2d_{5/2}$ clock transition. *Phys. Rev. Lett.*, 102(2):023002, Jan 2009. Cited on 7

[75] Th. Udem, S. A. Diddams, K. R. Vogel, C. W. Oates, E. A. Curtis, W. D. Lee, W. M. Itano, R. E. Drullinger, J. C. Bergquist, and L. Hollberg. Absolute frequency measurements of the hg^+ and ca optical clock transitions with a femtosecond laser. *Phys. Rev. Lett.*, 86(22):4996–4999, May 2001. Cited on 7

[76] Chr. Tamm, S. Weyers, B. Lipphardt, and E. Peik. Stray-field-induced quadrupole shift and absolute frequency of the 688-thz $^{171}yb^+$ single-ion optical frequency standard. *Phys. Rev. A*, 80(4):043403, Oct 2009. Cited on 7

[77] PJ Blythe, SA Webster, HS Margolis, SN Lea, G Huang, S-K Choi, WRC Rowley, P Gill, and RS Windeler. Subkilohertz absolute-frequency measurement of the 467-nm electric octupole transition inˆ{171} ybˆ{+}. *Physical Review A*, 67(2):020501, 2003. Cited on 7

[78] M. Keller, B. Lange, K. Hayasaka, W. Lange, and H. Walther. Deterministic cavity quantum electrodynamics with trapped ions. *J. Phys. B: At. Mol. Opt. Phys.*, 36(3):613–622, 2003. Cited on 7

[79] Juan I Cirac, Peter Zoller, et al. Quantum computations with cold trapped ions. *Physical review letters*, 74(20):4091–4094, 1995. Cited on 7, 48, 94

[80] Rainer Blatt, H Häffner, CF Roos, C Becher, and F Schmidt-Kaler. Ion trap quantum computing with ca+ ions. In *Experimental Aspects of Quantum Computing*, pages 61–73. Springer, 2005. Cited on 7

[81] Andrew Steane. The ion trap quantum information processor. *Applied Physics B: Lasers and Optics*, 64(6):623–643, 1997. Cited on 7

[82] Rainer Blatt and David Wineland. Entangled states of trapped atomic ions. *Nature*, 453:1008–1015, June 2008. Cited on 7

[83] H. Häffner, C. F. Roos, and R. Blatt. Quantum computing with trapped ions. *Physical Reports*, 469:155–203, 2008. Cited on 7

[84] David Kielpinski, Chris Monroe, and David J Wineland. Architecture for a large-scale ion-trap quantum computer. *Nature*, 417(6890):709–711, 2002. Cited on 7, 141

[85] H G Dehmelt. Radiofrequency spectroscopy of stored ions i: Storage. *Adv. At. Mol. Phys.*, 3:53, 1967. Cited on 10

[86] N Abramovitch and LA Stegun. Handbook of mathematical functions dover publications inc. *New York*, 1965. Cited on 12

[87] U Warring, C Ospelkaus, Y Colombe, R Jördens, D Leibfried, and DJ Wineland. Individual-ion addressing with microwave field gradients. *Physical review letters*, 110(17):173002, 2013. Cited on 12

[88] Nir Navon, Shlomi Kotler, Nitzan Akerman, Yinnon Glickman, Ido Almog, and Roee Ozeri. Addressing two-level systems variably coupled to an oscillating field. *Physical review letters*, 111(7):073001, 2013. Cited on 12

[89] M. G. House. Analytic model for electrostatic fields in surface-electrode ion traps. *Phys. Rev. A*, 78(3):033402, Sep 2008. Cited on 13

[90] J Verdú, S Kreim, K Blaum, H Kracke, W Quint, S Ulmer, and J Walz. Calculation of electrostatic fields using quasi-green's functions: application to the hybrid penning trap. *New Journal of Physics*, 10(10):103009, 2008. Cited on 14

[91] D. Hucul, M. Yeo, W. K. Hensinger, J. Rabchuk, S. Olmschenk, and C. Monroe. On the transport of atomic ions in linear and multidimensional ion trap arrays. *Quant. Inf. Comp.*, 8:501–578, 2008. Cited on 14

[92] D. J. Griffiths. Benjamin Cummings, 3rd edition, 1999. Cited on 16

[93] Kilian Singer, Ulrich Poschinger, Michael Murphy, Peter Ivanov, Frank Ziesel, Tommaso Calarco, and Ferdinand Schmidt-Kaler. Colloquium: Trapped ions as quantum bits: Essential numerical tools. *Reviews of Modern Physics*, 82(3):2609, 2010. Cited on 16

[94] Anders Sørensen and Klaus Mølmer. Quantum computation with ions in thermal motion. *Phys. Rev. Lett.*, 82(9):1971–1974, Mar 1999. Cited on 17, 48, 94

[95] Pierre Meystre. *Atom optics*, volume 33. Springer Science & Business Media, 2001. Cited on 17

[96] Harold J. Metcalf and Peter Van Der Straten. Springer-Verlag New York, Inc., 1999. Cited on 17, 18

[97] J. D. Siverns. *Yb ion trap experimental set-up and two-dimensional ion trap surface array design towards analogue quantum simulations.* PhD thesis, University of Sussex, 2011. Cited on 18

[98] M. Johanning, A. Braun, D. Eiteneuer, C. Paape, C. Balzer, W. Neuhauser, and C. Wunderlich. Resonance-enhanced isotope-selective photoionization of ybi for ion trap loading. *Applied Physics B: Lasers and Optics*, 103:327–338, 2011. 10.1007/s00340-011-4502-7. Cited on 20

[99] Altaf H. Nizamani, James J. McLoughlin, and Winfried K. Hensinger. Doppler-free yb spectroscopy with the fluorescence spot technique. *Phys. Rev. A*, 82:043408, Oct 2010. Cited on 21

[100] L Ricci, M Weidemüller, T Esslinger, A Hemmerich, C Zimmermann, V Vuletic, W König, and Th W Hänsch. A compact grating-stabilized diode laser system for atomic physics. *Optics Communications*, 117(5):541–549, 1995. Cited on 25

[101] TW Hansch and B Couillaud. Laser frequency stabilization by polarization spectroscopy of a reflecting reference cavity. *Optics communications*, 35(3):441–444, 1980. Cited on 28

[102] James McLoughlin. *Development and Implementation of an Yb^+ Ion Trap Experiment Towards Coherent Manipulation and Entanglement.* PhD thesis, University of Sussex, 2011. Cited on 30

[103] A. H. Nizamani. *Yb^+ ion trapping and optimum planar trap geometries for scalable quantum technology.* Ph.d. thesis, Brighton, 2011. Cited on 34, 89

[104] QA Turchette, BE King, D Leibfried, DM Meekhof, CJ Myatt, MA Rowe, CA Sackett, CS Wood, WM Itano, C Monroe, et al. Heating of trapped ions from the quantum ground state. *Physical Review A*, 61(6):063418, 2000. Cited on 34, 50, 51, 89

[105] JD Siverns, LR Simkins, S Weidt, and WK Hensinger. On the application of radio frequency voltages to ion traps via helical resonators. *Applied Physics B*, 107(4):921–934, 2012. Cited on 36, 82

[106] Marcus Hughes. *The development of microfabricated ion traps towards quantum information and simulation.* PhD thesis, University of Sussex, 2012. Cited on 37, 42, 45

[107] Christian Schneider. *Entwicklung eines Objektivs hoher numerischer Apertur zum Nachweis der Resonanzfluoreszenz einzelner gespeicherter Ionen.* PhD thesis, University of Siegen, 2007. Cited on 37

[108] Shmuel Fishman, Gabriele De Chiara, Tommaso Calarco, and Giovanna Morigi. Structural phase transitions in low-dimensional ion crystals. *Physical Review B*, 77(6):064111, 2008. Cited on 42

[109] B. Horstmann, B. Reznik, S. Fagnocchi, and J. I. Cirac. Hawking radiation from an acoustic black hole on an ion ring. *Phys. Rev. Lett.*, 104:250403, Jun 2010. Cited on 42

[110] Tongcang Li, Zhe-Xuan Gong, Zhang-Qi Yin, HT Quan, Xiaobo Yin, Peng Zhang, L-M Duan, and Xiang Zhang. Space-time crystals of trapped ions. *Physical review letters*, 109(16):163001, 2012. Cited on 42

[111] R. C. Sterling, M. D. Hughes, C. J. Mellor, and W. K. Hensinger. Increased surface flashover voltage in microfabricated devices. *arXiv:1208.5672*, 2012. Cited on 45

[112] Adam L Woodcraft, Adam Gray, Betty Young, Blas Cabrera, and Aaron Miller. A low temperature thermal conductivity database. In *AIP Conference Proceedings*, volume 31, page 681, 2009. Cited on 48

[113] ED Marquardt, JP Le, and Ray Radebaugh. Cryogenic material properties database cryogenic material properties database. 2000. Cited on 48

[114] Klaus Mølmer and Anders Sørensen. Multiparticle entanglement of hot trapped ions. *Phys. Rev. Lett.*, 82(9):1835–1838, Mar 1999. Cited on 48

[115] Anders Sorensen and Klaus Molmer. Entanglement and quantum computation with ions in thermal motion. *arXiv preprint quant-ph/0002024*, 2000. Cited on 48, 94

[116] GJ Milburn, S Schneider, and DFV James. Ion trap quantum computing with warm ions. *Fortschritte der Physik*, 48(9-11):801–810, 2000. Cited on 48

[117] PC Haljan, K-A Brickman, L Deslauriers, PJ Lee, and C Monroe. Spin-dependent forces on trapped ions for phase-stable quantum gates and entangled states of spin and motion. *Physical review letters*, 94(15):153602, 2005. Cited on 48

[118] John Bertrand Johnson. Thermal agitation of electricity in conductors. *Physical review*, 32(1):97, 1928. Cited on 49

[119] David R. Leibrandt, Bernard Yurke, and Richart E. Slusher. Modeling ion trap thermal noise decoherence. *Quantum Information & Computation*, 7(1):52–72, 2007. Cited on 49

[120] Harry Nyquist. Thermal agitation of electric charge in conductors. *Physical review*, 32(1):110–113, 1928. Cited on 49

[121] M Brownnutt, M Kumph, P Rabl, and R Blatt. Ion-trap measurements of electric-field noise near surfaces. *Reviews of Modern Physics*, 87(4):1419, 2015. Cited on 49

[122] JB Camp, TW Darling, and Ronald E Brown. Macroscopic variations of surface potentials of conductors. *Journal of applied physics*, 69(10):7126–7129, 1991. Cited on 49

[123] F Rossi and GI Opat. Observations of the effects of adsorbates on patch potentials. *Journal of Physics D: Applied Physics*, 25(9):1349, 1992. Cited on 49

[124] Taylor and Francis. *CRC Handbook of Chemistry and Physics, 89th ed.* Oxford, 2008. Cited on 50

[125] Diego Dalvit, Peter Milonni, David Roberts, and Felipe da Rosa. *Casimir Physics*, volume 834. Springer Science & Business Media, 2011. Cited on 50

[126] Woo-Joong Kim, AO Sushkov, Diego AR Dalvit, and Steve K Lamoreaux. Surface contact potential patches and casimir force measurements. *Physical Review A*, 81(2):022505, 2010. Cited on 50

[127] Romain Dubessy, Thomas Coudreau, and Luca Guidoni. Electric field noise above surfaces: A model for heating-rate scaling law in ion traps. *Physical Review A*, 80(3):031402, 2009. Cited on 50

[128] D. J. Wineland, C. Monroe, W. M. Itano, D. Leibfried, B. E. King, and D. M. Meekhof. Experimental issues in coherent quantum-state manipulation of trapped atomic ions. *J. Res. Nat. Inst. Stand. Tech.*, 103(3):259–328, 1998. Cited on 51

[129] J Bardeen. Cooper ln and schrieffer jr. *Phys. Rev*, 108:1175, 1957. Cited on 51

[130] P Monthoux, AV Balatsky, and D Pines. Toward a theory of high-temperature superconductivity in the antiferromagnetically correlated cuprate oxides. *Physical review letters*, 67(24):3448, 1991. Cited on 52

[131] David Pines. The spin fluctuation model for high temperature superconductivity: progress and prospects. In *The Gap Symmetry and Fluctuations in High-Tc Superconductors*, pages 111–142. Springer, 2002. Cited on 52

[132] Adam Mann. Still in suspense, 2011. Cited on 52

[133] Martin E Poitzsch, James C Bergquist, Wayne M Itano, and David J Wineland. Cryogenic linear ion trap for accurate spectroscopy. *Review of scientific instruments*, 67(1):129–134, 1996. Cited on 53

[134] Kunihiro Okada, Michiharu Wada, Takashi Nakamura, Ichiro Katayama, Ludwig Boesten, and Shunsuke Ohtani. Cryogenic ion trap for minimization of trapped ion loss. *Japanese Journal of Applied Physics*, 40(6R):4221, 2001. Cited on 53

[135] PB Antohi, D Schuster, GM Akselrod, J Labaziewicz, Y Ge, Z Lin, WS Bakr, and IL Chuang. Cryogenic ion trapping systems with surface-electrode traps. *Review of Scientific Instruments*, 80(1):013103, 2009. Cited on 53, 54, 59, 90

[136] Grahame Vittorini, Kenneth Wright, Kenneth R Brown, Alexa W Harter, and S Charles Doret. Modular cryostat for ion trapping with surface-electrode ion traps. *Review of Scientific Instruments*, 84(4):043112, 2013. Cited on 54

[137] Maria Schwarz, OO Versolato, Alexander Windberger, FR Brunner, Tim Ballance, SN Eberle, Joachim Ullrich, PO Schmidt, Anders Kragh Hansen, Alexander David Gingell, et al. Cryogenic linear paul trap for cold highly charged ion experiments. *Review of Scientific Instruments*, 83(8):083115, 2012. Cited on 54

[138] Matteo Fadel. Cryogenic setup for fast manipulation of the quantum motional states of trapped ions. Master's thesis, ETH Zurich, 2013. Cited on 54, 82

[139] Frank Pobell. *Matter and methods at low temperatures*. Springer Science & Business Media, 2007. Cited on 54

[140] OV Lounasmaa. Dilution refrigeration. *Journal of Physics E: Scientific Instruments*, 12(8):668, 1979. Cited on 54

[141] Matthias Steffen, M Ansmann, Radoslaw C Bialczak, Nadav Katz, Erik Lucero, R McDermott, Matthew Neeley, Eva Maria Weig, Andrew N Cleland, and John M Martinis. Measurement of the entanglement of two superconducting qubits via state tomography. *Science*, 313(5792):1423–1425, 2006. Cited on 54

[142] Yu Chen, C Neill, P Roushan, N Leung, M Fang, R Barends, J Kelly, B Campbell, Z Chen, B Chiaro, et al. Qubit architecture with high coherence and fast tunable coupling. *arXiv preprint arXiv:1402.7367*, 2014. Cited on 54, 164

[143] William E Gifford and RC Longsworth. Pulse-tube refrigeration. *Journal of Manufacturing Science and Engineering*, 86(3):264–268, 1964. Cited on 55

[144] ColdEdge Technologies T. Rufer. Private communication, January 2012. Cited on 55

[145] ETH Zurich J. Alonso. Private communication, May 2012. Cited on 55

[146] Imperial College London R. Hendricks. Private communication, July 2012. Cited on 55

[147] T Trollier, A Ravex, C Aubry, A Seidel, H Stephan, L De Parolis, A Sirbi, and R Kujala. Trade-off between thermal link solutions for the cryosystem cryocooler on-board the international space station. In *ADVANCES IN CRYOGENIC ENGEINEERING: Transactions of the Cryogenic Engineering Conference-CEC*, volume 710, pages 1187–1196. AIP Publishing, 2004. Cited on 59

[148] GK White and PJ Meeson. Experimental techniques in low-temperature physics clarendon. *Oxford*, 19792:318, 1979. Cited on 67

[149] H Rutt. The thermal conductivity of macor at intermediate cryogenic temperatures. Technical report, Technical Note, 2002. Cited on 75

[150] F Teyssandier and D Prêle. Commercially available capacitors at cryogenic temperatures. In *Ninth International Workshop on Low Temperature Electronics-WOLTE9*, 2010. Cited on 76

[151] Rogers Corporation. Ro4000 series high frequency circuit materials. Technical report, Rogers Corporation, 2014. Cited on 76

[152] Steffen Kahra. *Trapping and cooling of single molecular ions for time resolved experiments.* PhD thesis, Ludwig-Maximilians-Universitat Munchen, 2010. Cited on 89

[153] Guenther Leschhorn. *Time-resolved measurements on a single molecular target and Discrete Kink Solitons in Ion traps.* PhD thesis, Ludwig-Maximilians-Universitat Munchen, 2011. Cited on 89

[154] Nitzan Akerman. *Trapped ions and free photons.* PhD thesis, Wiezmann Institute of Science, 2012. Cited on 89

[155] Daniel Rotter. *Quantum feedback and quantum correlation measurements with a single Barium ion.* PhD thesis, Universitat Innsbruck, 2008. Cited on 89

[156] Paul Bogdan Antohi. *Cryogenic surface electrode ion traps with integrated superconducting microwave resonators for polar molecular ion spectroscopy.* PhD thesis, Massachusetts Institute of Technology, 2011. Cited on 90, 184

[157] Chris Monroe, DM Meekhof, BE King, WM Itano, and DJ Wineland. Demonstration of a fundamental quantum logic gate. *Physical Review Letters*, 75(25):4714, 1995. Cited on 94, 141

[158] Thomas Monz, Philipp Schindler, Julio T Barreiro, Michael Chwalla, Daniel Nigg, William A Coish, Maximilian Harlander, Wolfgang Hänsel, Markus Hennrich, and Rainer Blatt. 14-qubit entanglement: Creation and coherence. *Physical Review Letters*, 106(13):130506, 2011. Cited on 94, 141, 164

[159] R Ozeri, WM Itano, RB Blakestad, J Britton, J Chiaverini, JD Jost, C Langer, D Leibfried, R Reichle, S Seidelin, et al. Errors in trapped-ion quantum gates due to spontaneous photon scattering. *Physical Review A*, 75(4):042329, 2007. Cited on 94

[160] Florian Mintert and Christof Wunderlich. Ion-trap quantum logic using long-wavelength radiation. *Phys. Rev. Lett.*, 87:257904, Nov 2001. Cited on 94

[161] M. Johanning, A. Braun, N. Timoney, V. Elman, W. Neuhauser, and Chr. Wunderlich. Individual addressing of trapped ions and coupling of motional and spin states using rf radiation. *Phys. Rev. Lett.*, 102:073004, Feb 2009. Cited on 95

[162] A Khromova, Ch Piltz, B Scharfenberger, TF Gloger, M Johanning, AF Varón, and Ch Wunderlich. Designer spin pseudomolecule implemented with trapped ions in a magnetic gradient. *Physical review letters*, 108(22):220502, 2012. Cited on 95

[163] N Timoney, I Baumgart, M Johanning, AF Varón, MB Plenio, A Retzker, and Ch Wunderlich. Quantum gates and memory using microwave-dressed states. *Nature*, 476(7359):185–188, 2011. Cited on 95

[164] SC Webster, S Weidt, K Lake, JJ McLoughlin, and WK Hensinger. Simple manipulation of a microwave dressed-state ion qubit. *Physical review letters*, 111(14):140501, 2013. Cited on 95

[165] K Lake, S Weidt, J Randall, ED Standing, SC Webster, and WK Hensinger. Generation of spin-motion entanglement in a trapped ion using long-wavelength radiation. *Physical Review A*, 91(1):012319, 2015. Cited on 95, 166

[166] Valéria Hrabovcova, Tapani Jokinen, and J Pyrhonen. Design of rotating electrical machines, 2008. Cited on 95, 96

[167] Harold J Metcalf and Peter Van der Straten. *Laser cooling and trapping.* Springer Science & Business Media, 1999. Cited on 96, 97

[168] Gregory Breit and II Rabi. Measurement of nuclear spin. *Physical Review*, 38(11):2082, 1931. Cited on 97, 98

[169] Altaf H. Nizamani and Winfried K. Hensinger. Optimum electrode configurations for fast ion separation in microfabricated surface ion traps. *Appl Phys B*, 106(2):327–338, 2012. Cited on 110, 111

[170] M. D. Barrett, J. Chiaverini, T. Schaetz, J. Britton, W. M. Itano, J. D. Jost, E. Knill, C. Langer, D. Leibfried, R. Ozeri, and D. J. Wineland. Deterministic quantum teleportation of atomic qubits. *Nature*, 429:737–739, 2004. Cited on 115

[171] R. B Blakestad, C. Ospelkaus, A. P VanDevender, J. H Wesenberg, M. J Biercuk, D. Leibfried, and D. J Wineland. Near-ground-state transport of trapped-ion qubits through a multidimensional array. *Phys. Rev. A*, 84:032314, Sep 2011. Cited on 115

[172] Andreas Wallraff, David I Schuster, Alexandre Blais, L Frunzio, R-S Huang, J Majer, S Kumar, Steven M Girvin, and Robert J Schoelkopf. Strong coupling of a single photon to a superconducting qubit using circuit quantum electrodynamics. *Nature*, 431(7005):162–167, 2004. Cited on 121

[173] Luigi Frunzio, Andreas Wallraff, David Schuster, Johannes Majer, and Robert Schoelkopf. Fabrication and characterization of superconducting circuit qed devices for quantum computation. *Applied Superconductivity, IEEE Transactions on*, 15(2):860–863, 2005. Cited on 121

[174] Mika A Sillanpää, Jae I Park, and Raymond W Simmonds. Coherent quantum state storage and transfer between two phase qubits via a resonant cavity. *Nature*, 449(7161):438–442, 2007. Cited on 121

[175] David M Pozar. *Microwave engineering.* John Wiley & Sons, 2009. Cited on 121

[176] David Isaac Schuster. *Circuit quantum electrodynamics.* 2007. Cited on 121

[177] Luigi Frunzio, Andreas Wallraff, David Schuster, Johannes Majer, and Robert Schoelkopf. Fabrication and characterization of superconducting circuit qed devices for quantum computation. *Applied Superconductivity, IEEE Transactions on*, 15(2):860–863, 2005. Cited on 122

[178] WA Phillips. Tunneling states in amorphous solids. *Journal of Low Temperature Physics*, 7(3-4):351–360, 1972. Cited on 122

[179] Rick Sturdivant. *Microwave and Millimeter-wave Electronic Packaging.* Artech House, 2013. Cited on 123

[180] J Oldenburg. What is a microstrip transmission line and how do you design one? *Course Material, Obtained from http://www. csus. edu/indiv/o/oldenburgj/EEE*, 20161, 2014. Cited on 126, 127

[181] R. N Simons. *Coplanar Waveguide Circuits, Components, and Systems.* John Wiley and Sons, 2001. Cited on 128

[182] D. M. Pozar. *Microwave Engineering 4th ed.* John Wiley and Sons, 2012. Cited on 128

[183] SP Chockalingam, Madhavi Chand, John Jesudasan, Vikram Tripathi, and Pratap Raychaudhuri. Superconducting properties and hall effect of epitaxial nbn thin films. *Physical Review B*, 77(21):214503, 2008. Cited on 129

[184] W Słysz, M Guziewicz, M Borysiewicz, JZ Domagała, I Pasternak, K Hejduk, W Rzodkiewicz, J Ratajczak, J Bar, M Wegrzecki, et al. Ultrathin nbn films for superconducting single-photon detectors. *Acta Physica Polonica A*, 120(1):200–203, 2011. Cited on 129

[185] Jeremy M Sage, Andrew J Kerman, and John Chiaverini. Loading of a surface-electrode ion trap from a remote, precooled source. *Physical Review A*, 86(1):013417, 2012. Cited on 131, 184

[186] Robert H Dicke. Coherence in spontaneous radiation processes. *Physical Review*, 93(1):99, 1954. Cited on 134, 165

[187] James D Siverns, Seb Weidt, Kim Lake, Bjoern Lekitsch, Marcus D Hughes, and Winfried K Hensinger. Optimization of two-dimensional ion trap arrays for quantum simulation. *New Journal of Physics*, 14(8):085009, 2012. Cited on 136, 137

[188] C. Ospelkaus, U. Warring, Y. Colombe, K. R. Brown, J. M. Amini, D. Leibfried, and D. J. Wineland. Microwave quantum logic gates for trapped ions. *Nature*, 476:181Â–184, 2011. Cited on 141, 194

[189] PJ Kunert, D Georgen, L Bogunia, MT Baig, MA Baggash, M Johanning, and Ch Wunderlich. A planar ion trap chip with integrated structures for an adjustable magnetic field gradient. *Applied Physics B*, 114(1-2):27–36, 2014. Cited on 141

[190] Grigoriĭ Samsonov. Nitrides. Technical report. Cited on 148

[191] Teer Coatings Ltd. Joanne Hampshire. Private communications, 2013. Cited on 148

[192] Manchester Metropolitan University. Peter Kelly. Private communications, 2013. Cited on 148

[193] Alexandre Blais, Ren-Shou Huang, Andreas Wallraff, SM Girvin, and R Jun Schoelkopf. Cavity quantum electrodynamics for superconducting electrical circuits: An architecture for quantum computation. *Physical Review A*, 69(6):062320, 2004. Cited on 164

[194] Thomas Niemczyk, F Deppe, H Huebl, EP Menzel, F Hocke, MJ Schwarz, JJ Garcia-Ripoll, D Zueco, T Hümmer, E Solano, et al. Circuit quantum electrodynamics in the ultrastrong-coupling regime. *Nature Physics*, 6(10):772–776, 2010. Cited on 164

[195] Jonathan P Home, David Hanneke, John D Jost, Jason M Amini, Dietrich Leibfried, and David J Wineland. Complete methods set for scalable ion trap quantum information processing. *Science*, 325(5945):1227–1230, 2009. Cited on 164

[196] Dietrich Leibfried, Brian DeMarco, Volker Meyer, David Lucas, Murray Barrett, Joe Britton, WM Itano, B Jelenković, Chris Langer, Till Rosenband, et al. Experimental demonstration of a robust, high-fidelity geometric two ion-qubit phase gate. *Nature*, 422(6930):412–415, 2003. Cited on 164

[197] Chr Wunderlich, Th Hannemann, T Körber, H Häffner, Ch Roos, W Hänsel, R Blatt, and F Schmidt-Kaler. Robust state preparation of a single trapped ion by adiabatic passage. *Journal of Modern Optics*, 54(11):1541–1549, 2007. Cited on 164

[198] Peter TH Fisk, Matthew J Sellars, Malcolm A Lawn, and Colin Coles. Accurate measurement of the 12.6 ghz" clock" transition in trapped/sup 171/yb/sup+/ions. *Ultrasonics, Ferroelectrics and Frequency Control, IEEE Transactions on*, 44(2):344–354, 1997. Cited on 164

[199] CA Sackett, David Kielpinski, BE King, C Langer, V Meyer, CJ Myatt, M Rowe, QA Turchette, WM Itano, DJ Wineland, et al. Experimental entanglement of four particles. *Nature*, 404(6775):256–259, 2000. Cited on 164

[200] J Chiaverini, D Leibfried, T Schaetz, MD Barrett, RB Blakestad, J Britton, WM Itano, JD Jost, E Knill, C Langer, et al. Realization of quantum error correction. *Nature*, 432(7017):602–605, 2004. Cited on 164

[201] TR Tan, JP Gaebler, R Bowler, Y Lin, JD Jost, D Leibfried, and DJ Wineland. Demonstration of a dressed-state phase gate for trapped ions. *Physical review letters*, 110(26):263002, 2013. Cited on 164

[202] J Verdú, H Zoubi, Ch Koller, J Majer, H Ritsch, and J Schmiedmayer. Strong magnetic coupling of an ultracold gas to a superconducting waveguide cavity. *Physical review letters*, 103(4):043603, 2009. Cited on 165, 197

[203] Z Kim, CP Vlahacos, JE Hoffman, JA Grover, KD Voigt, BK Cooper, CJ Ballard, BS Palmer, M Hafezi, JM Taylor, et al. Thin-film superconducting resonator tunable to the ground-state hyperfine splitting of 87rb. *AIP Advances*, 1(4):042107, 2011. Cited on 166

[204] Anders S Sørensen, Caspar H van der Wal, Lilian I Childress, and Mikhail D Lukin. Capacitive coupling of atomic systems to mesoscopic conductors. *Physical review letters*, 92(6):063601, 2004. Cited on 166

[205] D. Leibfried, R. Blatt, C. Monroe, and D. Wineland. Quantum dynamics of single trapped ions. *Rev. Mod. Phys.*, 75(1):281–324, Mar 2003. Cited on 166

[206] Oxford Instruments. Triton specification sheet. Technical report, Oxford Instruments, 2015. Cited on 168

[207] Altaf H Nizamani and Winfried K Hensinger. Optimum electrode configurations for fast ion separation in microfabricated surface ion traps. *Applied Physics B*, 106(2):327–338, 2012. Cited on 169, 171

[208] Robert Aigner. Mems in rf-filter applications: thin film bulk-acoustic-wave technology. In *Solid-State Sensors, Actuators and Microsystems, 2005. Digest of Technical Papers. TRANSDUCERS'05. The 13th International Conference on*, volume 1, pages 5–8. IEEE, 2005. Cited on 169

[209] Matthew L Johnston, Ioannis Kymissis, and Kenneth L Shepard. Fbar-cmos oscillator array for mass-sensing applications. *Sensors Journal, IEEE*, 10(6):1042–1047, 2010. Cited on 169

[210] D Petit, E Cesar, P Bar, S Joblot, G Parat, O Berchaud, D Barbier, and JF Carpentier. Thermally stable oscillator at 2.5 ghz using temperature compensated baw resonator and its integrated temperature sensor. In *Ultrasonics Symposium, 2008. IUS 2008. IEEE*, pages 895–898. IEEE, 2008. Cited on 169

[211] Tatsuya Omori, KY Hashimoto, and Masatsune Yamaguchi. Pzt thin films for saw and baw devices. In *International symposium on acoustic wave devices for future mobile communication systems*, 2001. Cited on 170

[212] Zhihong Wang, Yingbang Yao, Xianbin Wang, Weisheng Yue, Longqing Chen, and Xi Xiang Zhang. Bending-induced electromechanical coupling and large piezoelectric response in a micromachined diaphragm. *Scientific reports*, 3, 2013. Cited on 170

[213] RC Sterling, MD Hughes, CJ Mellor, and WK Hensinger. Increased surface flashover voltage in microfabricated devices. *Applied Physics Letters*, 103(14):143504, 2013. Cited on 170, 195

[214] John Chiaverini, R Brad Blakestad, Joe Britton, John D Jost, Chris Langer, Dietrich Leibfried, Roee Ozeri, and David J Wineland. Surface-electrode architecture for ion-trap quantum information processing. *arXiv preprint quant-ph/0501147*, 2005. Cited on 170

[215] PB Antohi, D Schuster, GM Akselrod, J Labaziewicz, Y Ge, Z Lin, WS Bakr, and IL Chuang. Cryogenic ion trapping systems with surface-electrode traps. *Review of Scientific Instruments*, 80(1):013103, 2009. Cited on 170

[216] Jaroslaw Labaziewicz, Yufei Ge, Paul Antohi, David Leibrandt, Kenneth R Brown, and Isaac L Chuang. Suppression of heating rates in cryogenic surface-electrode ion traps. *Physical review letters*, 100(1):013001, 2008. Cited on 170

[217] Rudeger HT Wilke, Raegan L Johnson-Wilke, Vincenzo Cotroneo, William N Davis, Paul B Reid, Daniel A Schwartz, and Susan Trolier-McKinstry. Sputter deposition of pzt piezoelectric films on thin glass substrates for adjustable x-ray optics. *Applied optics*, 52(14):3412–3419, 2013. Cited on 171, 179

[218] Ville Kaajakari, Tomi Mattila, Aarne Oja, and Heikki Seppä. Nonlinear limits for single-crystal silicon microresonators. *Microelectromechanical Systems, Journal of*, 13(5):715–724, 2004. Cited on 171

[219] EM Yeatman, MM Ahmad, and RRA Syms. Piezoelectric films in silicon-based microactuation structures. 1995. Cited on 172

[220] K_D Budd, SK Key, and DA Payne. Sol-gel processing of pbtio 3, pbzro 3, pzt and plzt thin films. In *BR. CERAM. PROC. Br. Ceram. Proc.*, number 36, page 107, 1985. Cited on 179

[221] Takeshi Morita, Minoru Kuribayashi Kurosawa, and Toshiro Higuchi. A cylindrical micro ultrasonic motor using pzt thin film deposited by single process hydrothermal method (/spl phi/2.4 mm, l= 10 mm stator transducer). *Ultrasonics, Ferroelectrics, and Frequency Control, IEEE Transactions on*, 45(5):1178–1187, 1998. Cited on 179

[222] Erik S Thiele, Dragan Damjanovic, and Nava Setter. Processing and properties of screen-printed lead zirconate titanate piezoelectric thick films on electroded silicon. *Journal of the American Ceramic Society*, 84(12):2863–2868, 2001. Cited on 179

[223] Xuan-Yu Wang, Chi-Yuan Lee, Pei-Yen Chen, Cheng-Jien Peng, and Pei-Zen Chang. Microfabrication process of pzt thick film by aerosol deposition method. In *Nano/Micro Engineered and Molecular Systems, 2006. NEMS'06. 1st IEEE International Conference on*, pages 1288–1291. IEEE, 2006. Cited on 179

[224] Michael J Renn, D Montgomery, O Vdovin, DZ Anderson, CE Wieman, and EA Cornell. Laser-guided atoms in hollow-core optical fibers. *Physical review letters*, 75(18):3253, 1995. Cited on 181, 184, 185

[225] BA Mazin, SR Meeker, MJ Strader, B Bumble, K O'Brien, P Szypryt, D Marsden, JC van Eyken, GE Duggan, G Ulbricht, et al. Arcons: A 2024 pixel optical through near-ir cryogenic imaging spectrophotometer. *arXiv preprint arXiv:1306.4674*, 2013. Cited on 181, 185, 186

[226] D.E. Dean, C.J. Ginfrida, S.T. Mansell, T.M. Nixon, D.A. Purgill, and M.J. Radziun. Cryocooler vibration isolation and noise reduction in magnetic resonance imaging, January 26 1999. US Patent 5,864,273. Cited on 182

[227] F Jessen, M Knufinke, SC Bell, P Vergien, H Hattermann, P Weiss, M Rudolph, M Reinschmidt, K Meyer, T Gaber, et al. Trapping of ultracold atoms in a 3he/4he dilution refrigerator. *Applied Physics B*, pages 1–7, 2013. Cited on 182

[228] Jack W Ekin. *Experimental techniques for low-temperature measurements*. Oxford Univ. Press, 2006. Cited on 183

[229] John Bertrand Johnson. Thermal agitation of electricity in conductors. *Physical review*, 32(1):97, 1928. Cited on 183

[230] Harry Nyquist. Thermal agitation of electric charge in conductors. *Physical review*, 32(1):110–113, 1928. Cited on 183

[231] Altaf H. Nizamani. *Yb^+ ion trapping and optimum planar trap geometries for scalable quantum technology.* PhD thesis, University of Sussex, 2011. Cited on 184

[232] HARUHIKO Ito, T Nakata, K Sakaki, M Ohtsu, KI Lee, and W Jhe. Laser spectroscopy of atoms guided by evanescent waves in micron-sized hollow optical fibers. *Physical review letters*, 76(24):4500, 1996. Cited on 184

[233] MA Ol'Shanii, Yu B Ovchinnikov, and VS Letokhov. Laser guiding of atoms in a hollow optical fiber. *Optics communications*, 98(1):77–79, 1993. Cited on 184

[234] RF Cregan, BJ Mangan, JC Knight, TA Birks, P St J Russell, PJ Roberts, and DC Allan. Single-mode photonic band gap guidance of light in air. *science*, 285(5433):1537–1539, 1999. Cited on 185

[235] Caleb A Christensen, Sebastian Will, Michele Saba, Gyu-Boong Jo, Yong-Il Shin, Wolfgang Ketterle, and David Pritchard. Trapping of ultracold atoms in a hollow-core photonic crystal fiber. *Physical Review A*, 78(3):033429, 2008. Cited on 185

[236] Hyatt M Gibbs and Eugene D Commins. Large aperture, high efficiency ion detector. *Review of Scientific Instruments*, 37(10):1385–1390, 1966. Cited on 185

[237] BA Mazin, SR Meeker, MJ Strader, B Bumble, K O'Brien, P Szypryt, D Marsden, JC van Eyken, GE Duggan, G Ulbricht, et al. Arcons: A 2024 pixel optical through near-ir cryogenic imaging spectrophotometer. *arXiv preprint arXiv:1306.4674*, 2013. Cited on 185, 186, 187

[238] DC Mattis and John Bardeen. Theory of the anomalous skin effect in normal and superconducting metals. *Physical Review*, 111(2):412, 1958. Cited on 185, 186

[239] Sean McHugh, Benjamin A Mazin, Bruno Serfass, Seth Meeker, Kieran O'Brien, Ran Duan, Rick Raffanti, and Dan Werthimer. A readout for large arrays of microwave kinetic inductance detectors. *Review of Scientific Instruments*, 83(4):044702, 2012. Cited on 185, 187

[240] M Roesch, L Swenson, A Bideaud, A Benoit, S Doyle, KF Schuster, and A Monfardini. Development, fabrication and characterization of lumped element kinetic inductance detectors for nika. In *Twenty-First International Symposium on Space Terahertz Technology*, volume 1, pages 72–75, 2010. Cited on 185, 187

[241] M Roesch, A Benoit, A Bideaud, N Boudou, M Calvo, A Cruciani, S Doyle, HG Leduc, A Monfardini, L Swenson, et al. Development of lumped element kinetic inductance detectors for nika. *arXiv preprint arXiv:1212.4585*, 2012. Cited on 185, 187

[242] S Friedrich, K Segall, MC Gaidis, CM Wilson, DE Prober, AE Szymkowiak, and SH Moseley. Experimental quasiparticle dynamics in a superconducting, imaging x-ray spectrometer. *Applied physics letters*, 71(26):3901–3903, 1997. Cited on 186

[243] Gustavo. Cancelo and Juan Estrada. A readout architecture for 100,000 pixel microwave kinetic inductance detector array. *Manuscript*, 2013. Cited on 187

[244] G Vardulakis, S Withington, DJ Goldie, and DM Glowacka. Superconducting kinetic inductance detectors for astrophysics. *Measurement Science and Technology*, 19(1):015509, 2008. Cited on 187

[245] A Bosotti, R Paparella, and F Puricelli. Pi piezolifetime test report. Technical report, INFN Milan Internal Report, 2005. Cited on 188

[246] Mohammed Fouaidy, G Martinet, N Hammoudi, F Chatelet, Sebastien Blivet, A Olivier, and Herve Saugnac. Full characterization at low temperature of piezoelectric actuators used for srf cavities active tuning. In *Particle Accelerator Conference, 2005. PAC 2005. Proceedings of the*, pages 728–730. IEEE, 2005. Cited on 188, 189

[247] M Fouaidy, N Hammoudi, and IPN Orsay. Characterization of piezoelectric actuators used for srf cavities active tuning at low temperature. In *Proceedings of the 11 th Superconducting Radio Frequency workshop (SRF 2003)*, 2003. Cited on 188

[248] M Fouaidy, G Martinet, N Hammoudi, F Chatelet, and A Olivier. Characterization at cryogenic temperatures of piezostacks dedicated to fast tuners for srf cavities. In *Mixed Design of Integrated Circuits and Systems, 2007. MIXDES'07. 14th International Conference on*, pages 17–22. IEEE, 2007. Cited on 188

[249] Brian Julsgaard and Klaus Mølmer. Reflectivity and transmissivity of an optical cavity coupled to two-level atoms: Coherence properties and the influence of atomic phase noise. *arXiv preprint arXiv:1110.3610*, 2011. Cited on 190, 191, 192, 193

[250] Rainee Navin Simons and Rajendra K Arora. Coupled slot line field components. *IEEE Transactions on Microwave Theory and Techniques*, 7(30):1094–1099, 1982. Cited on 194

[251] James William Rohlf. Modern physics from aalpha to z0. *Modern Physics from aalpha to Z0, by James William Rohlf, pp. 664. ISBN 0-471-57270-5. Wiley-VCH, March 1994.*, 1, 1994. Cited on 194

[252] J Britton, D Leibfried, JA Beall, RB Blakestad, JH Wesenberg, and DJ Wineland. Scalable arrays of rf paul traps in degenerate si. *Applied Physics Letters*, 95(17):173102, 2009. Cited on 195

[253] Robin C Sterling, Hwanjit Rattanasonti, Sebastian Weidt, Kim Lake, Prasanna Srinivasan, SC Webster, Michaël Kraft, and Winfried K Hensinger. Fabrication and operation of a two-dimensional ion-trap lattice on a high-voltage microchip. *Nature communications*, 5, 2014. Cited on 195

Appendix A

Mask designs

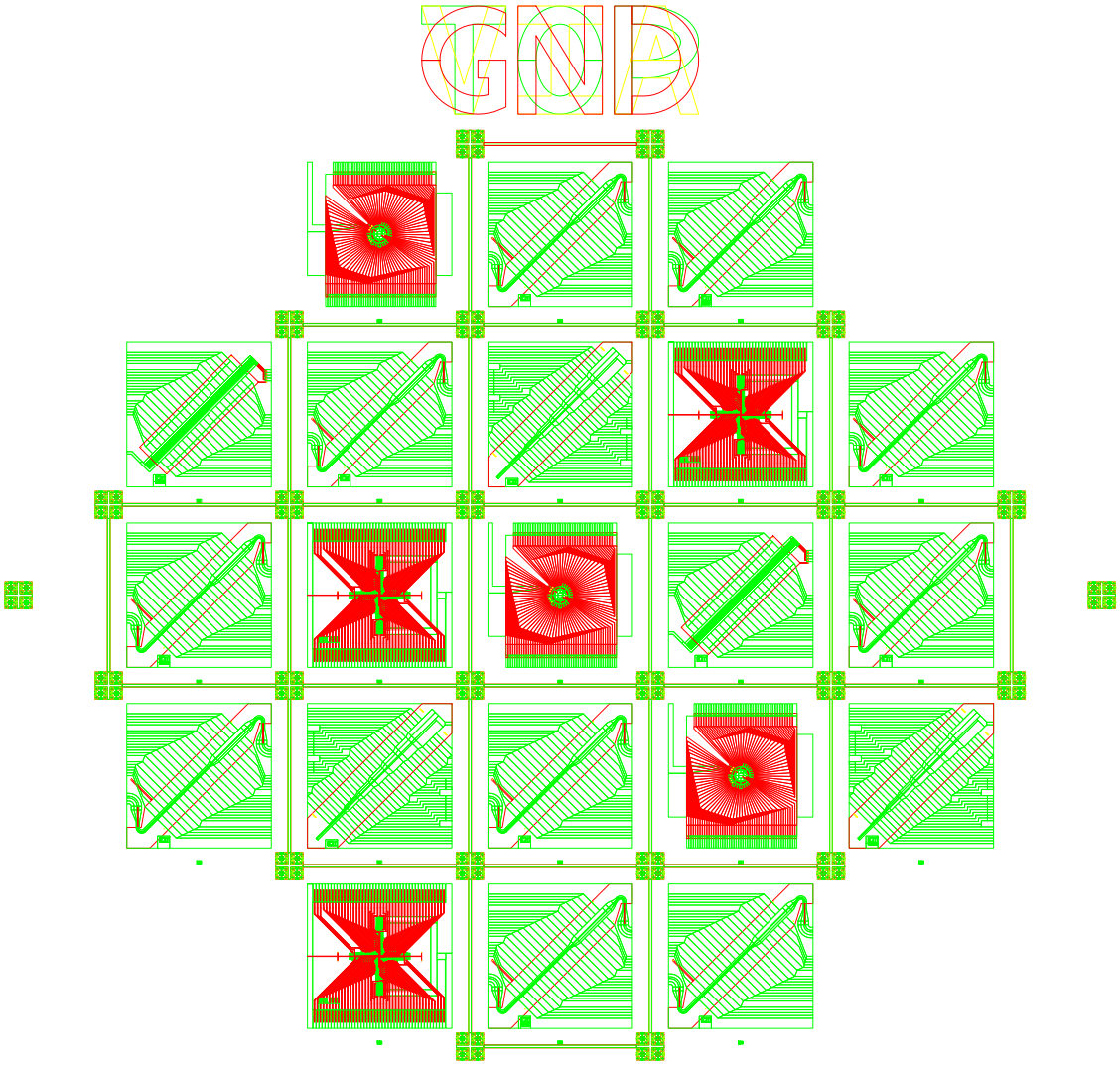

Figure A.1: Combined masks for the top electrode layer, the ground layer and the via layer.

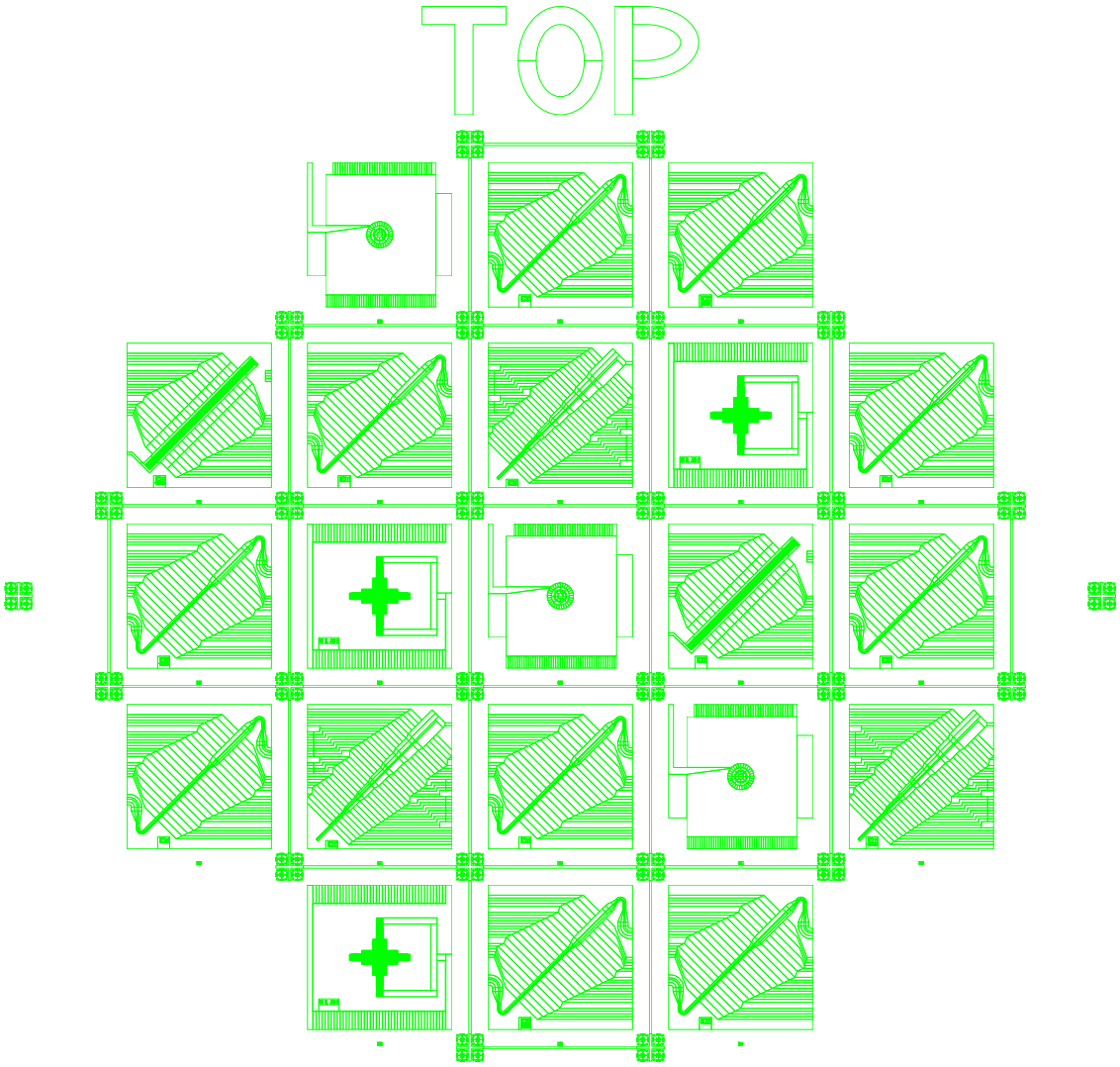

Figure A.2: Mask for the top electrode layer.

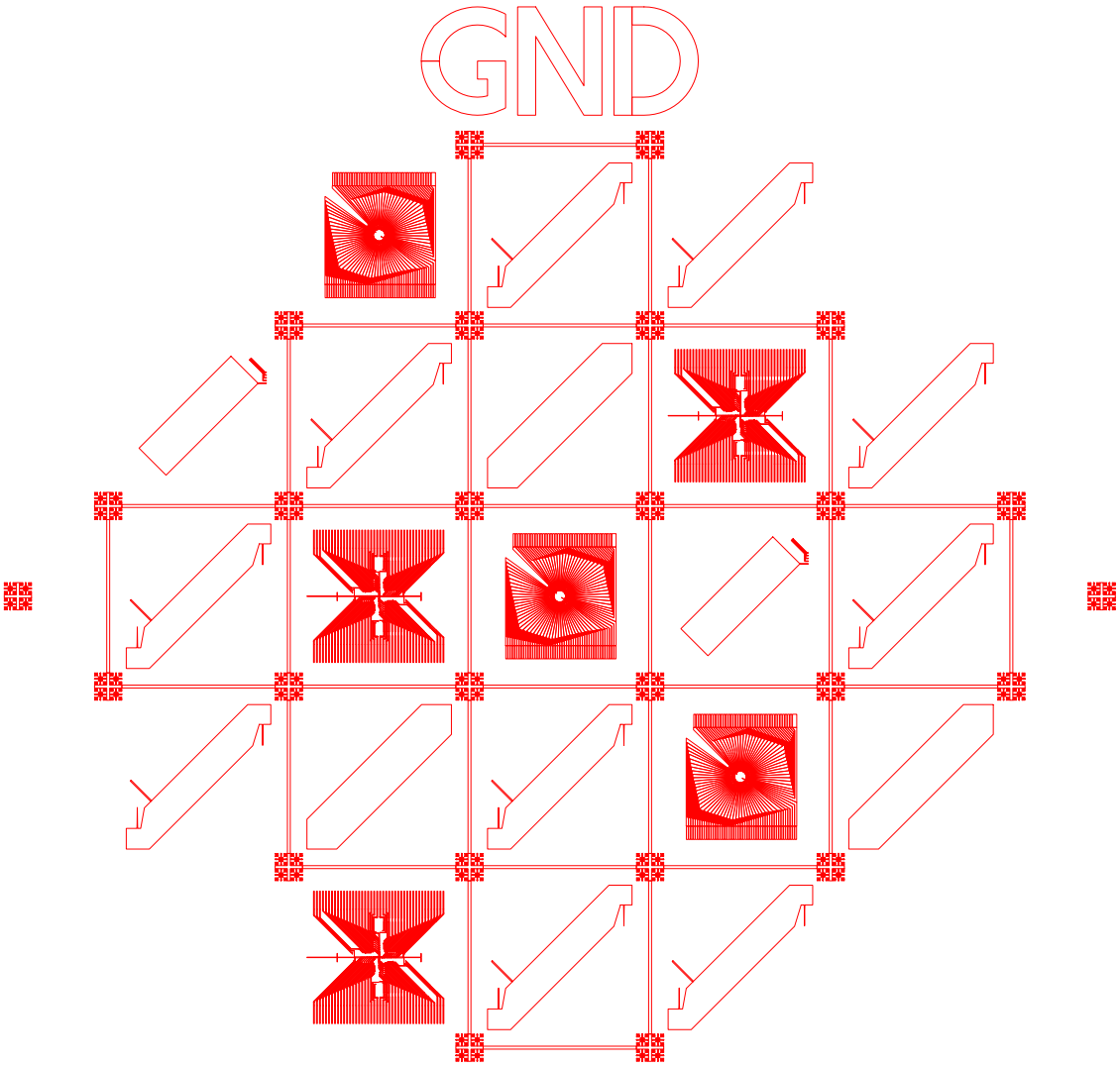

Figure A.3: Mask for the top electrode layer.

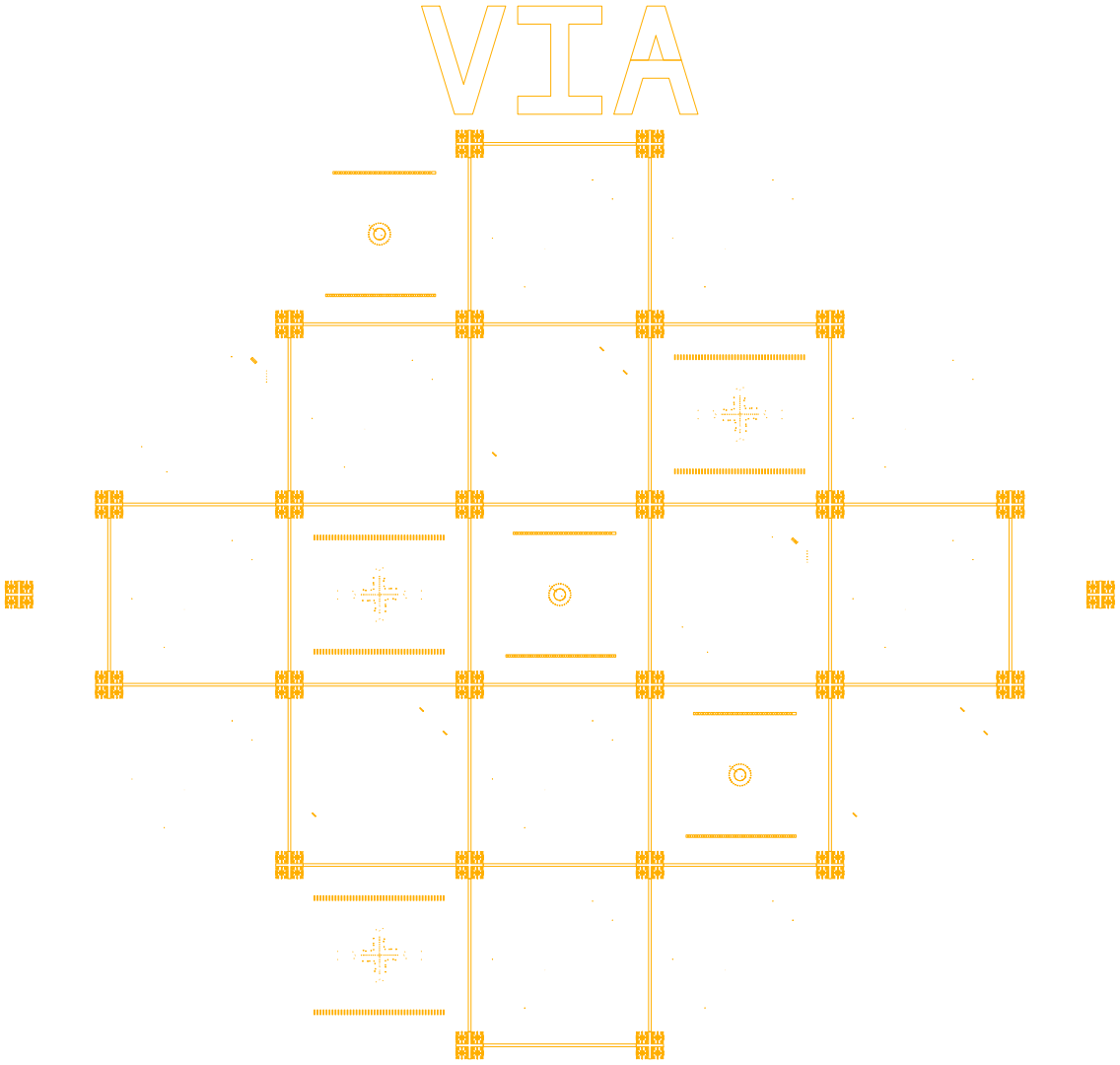

Figure A.4: Mask for the top electrode layer.

Appendix B

Technical drawings

This section lists a selection technical drawings used to design various areas of the cryogenic system and which would be useful for its future development and improvement. All length measurements are given in mm.

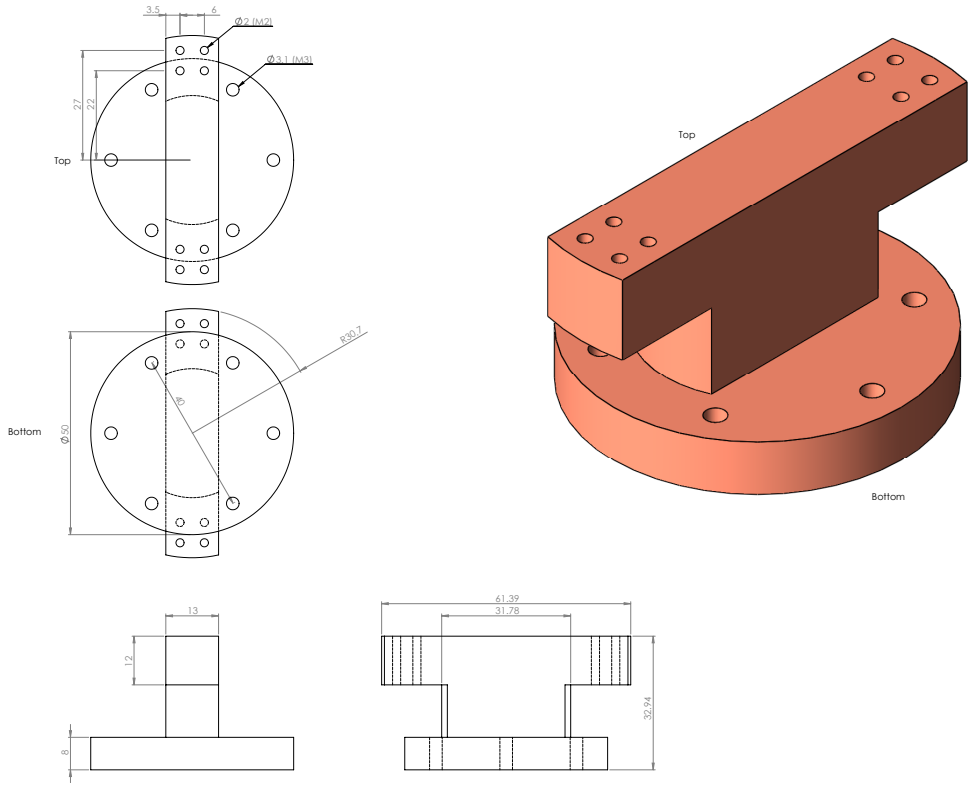

Figure B.1: OFHC copper base mount.

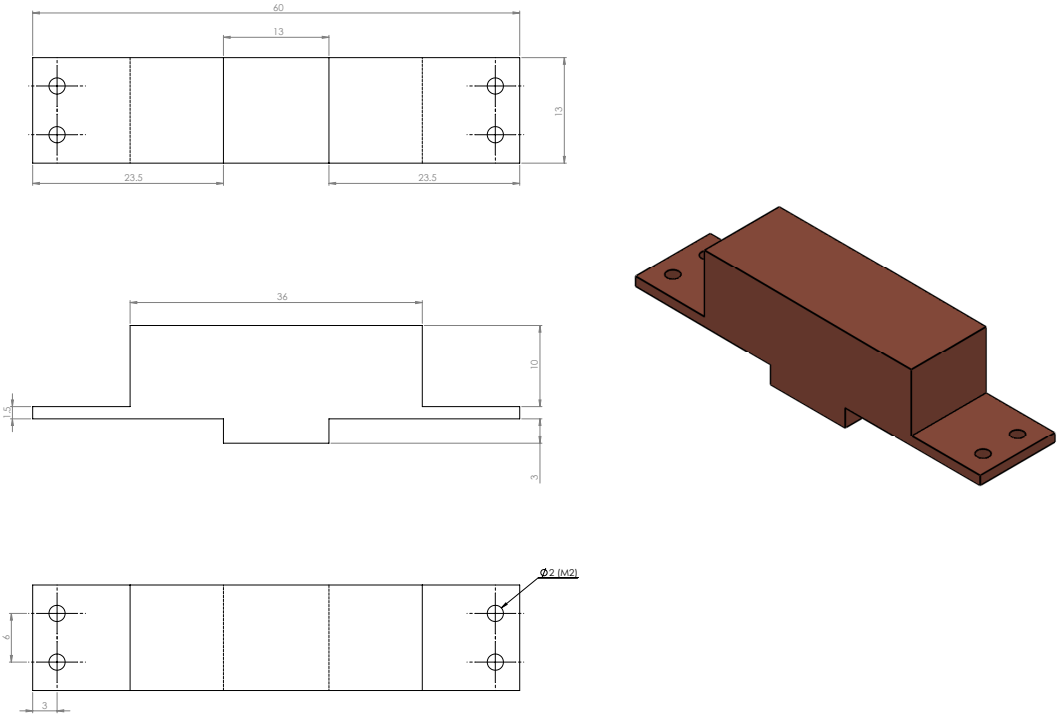

Figure B.2: OFHC copper chip mount.

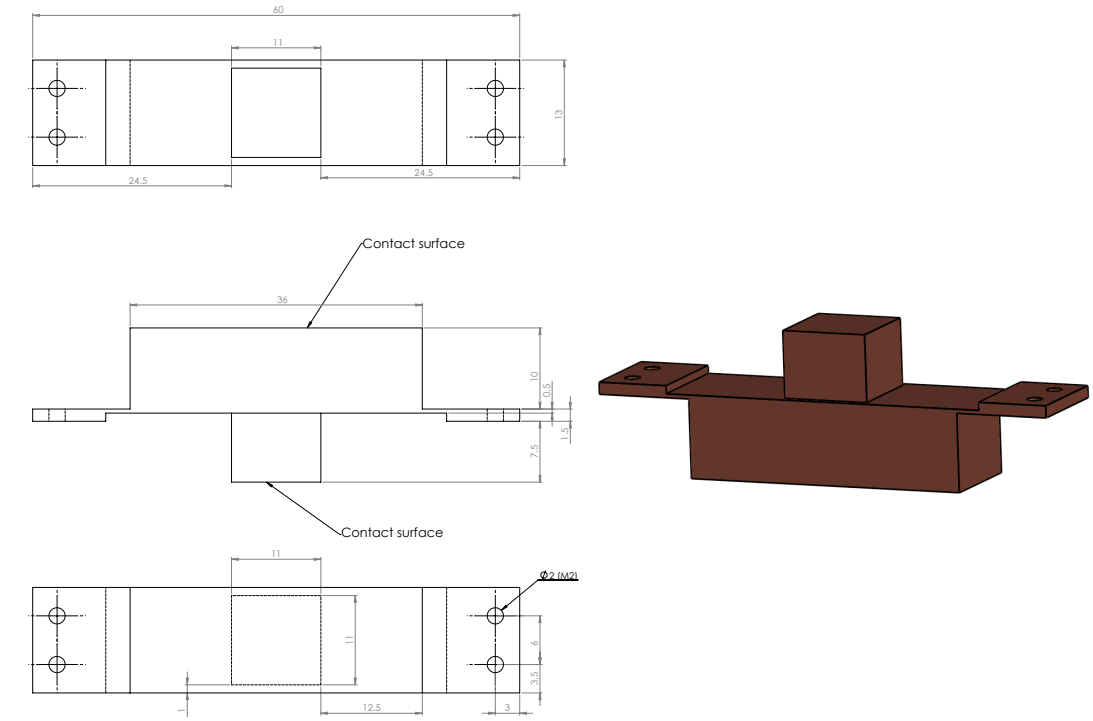

Figure B.3: OFHC copper chip mount with raised chip platform to be used with permanent magnets.

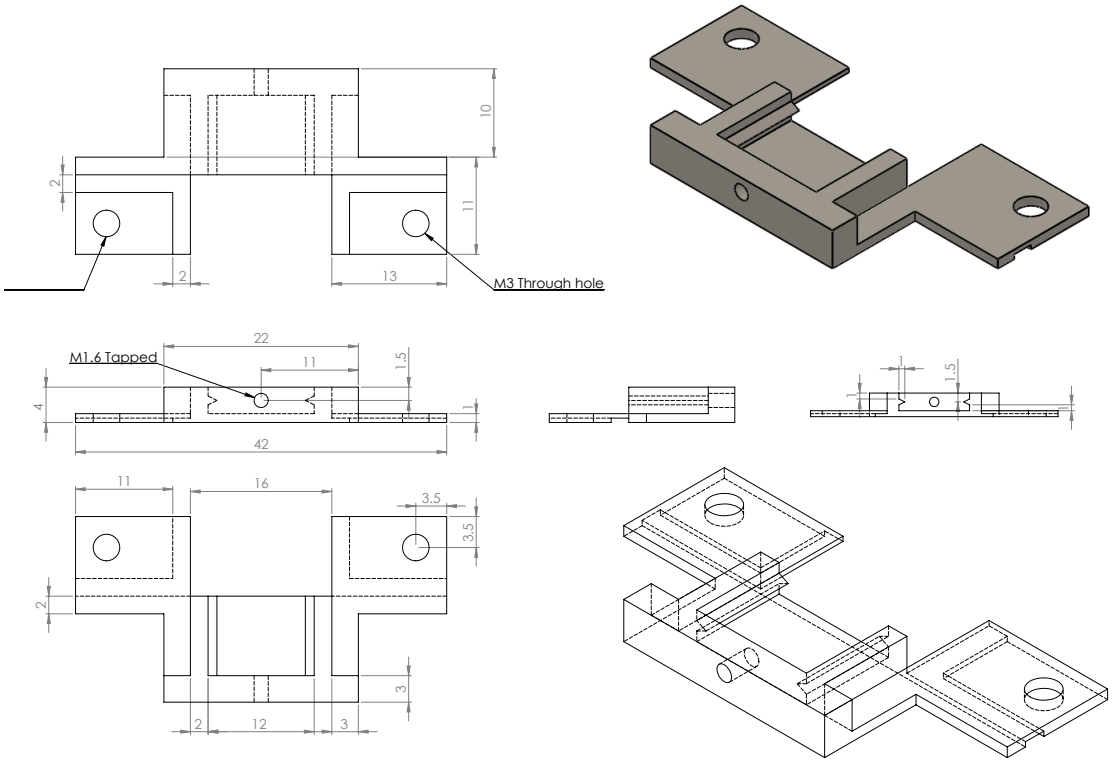

Figure B.4: In vacuum permanent magnet mount: Magnet clamp x-axis stage.

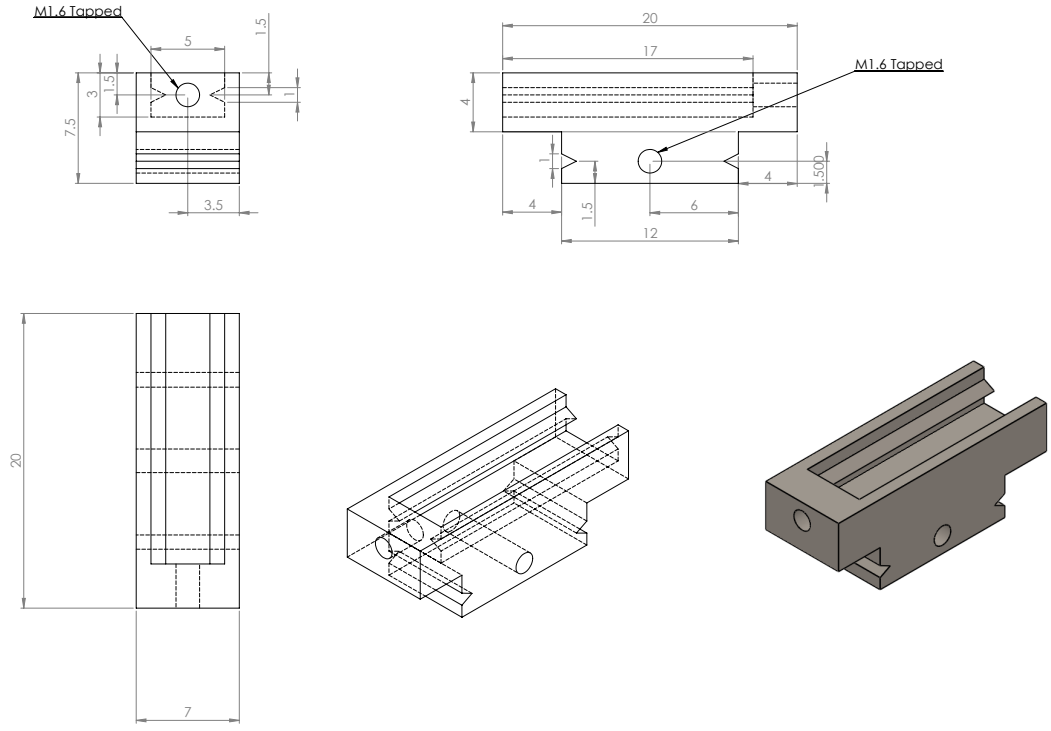

Figure B.5: In vacuum permanent magnet mount: Magnet clamp y-axis stage.

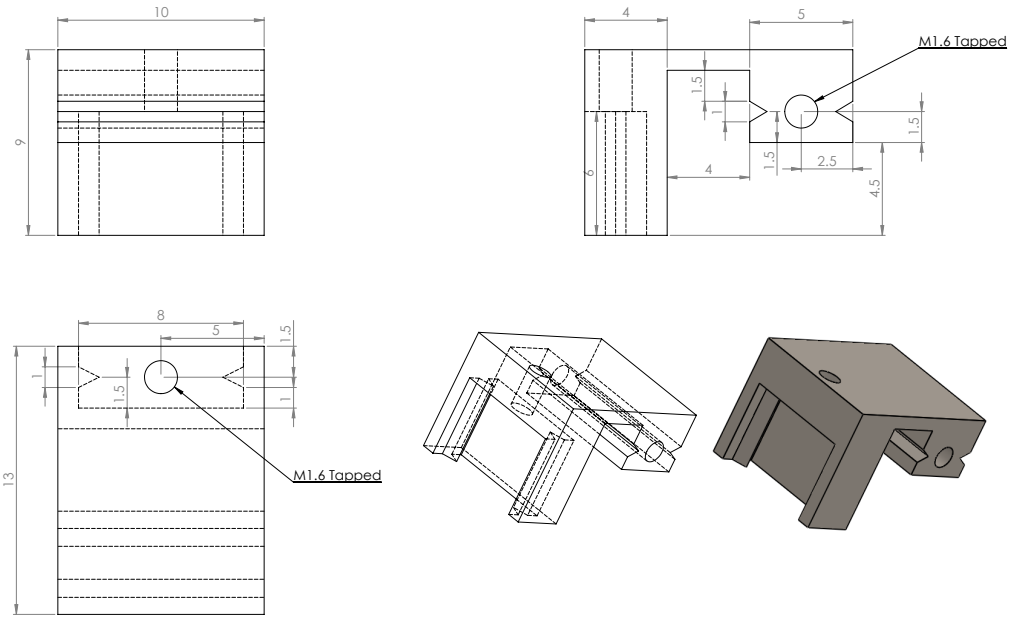

Figure B.6: In vacuum permanent magnet mount: Magnet clamp z-axis stage.

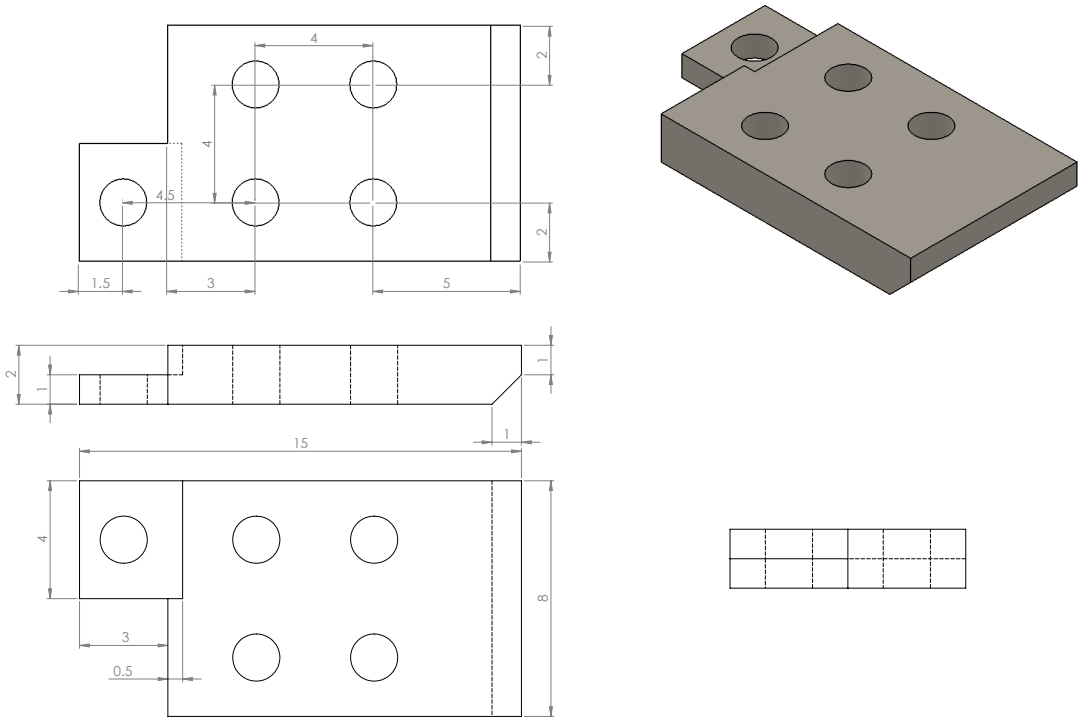

Figure B.7: In vacuum permanent magnet mount: Magnet clamp right side.

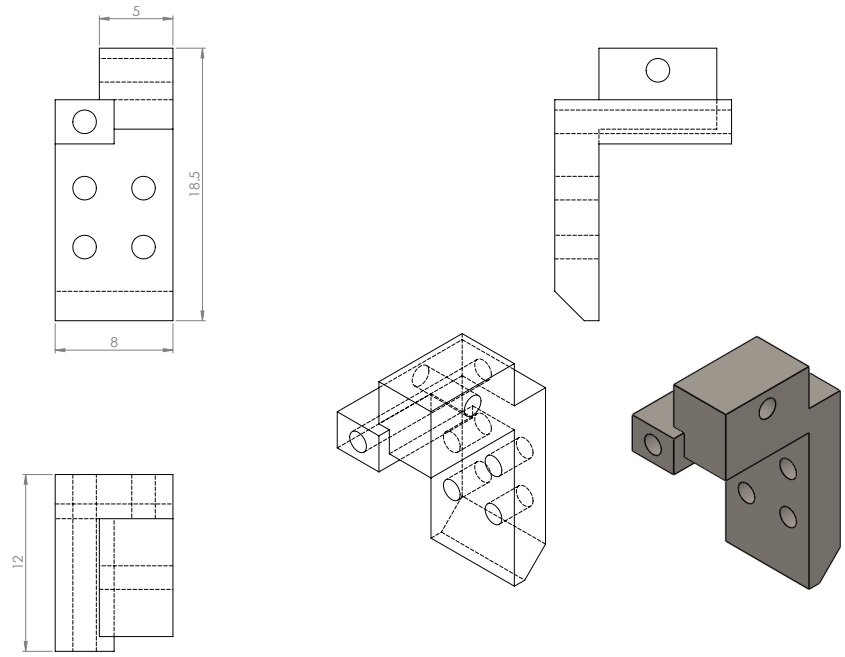

Figure B.8: In vacuum permanent magnet mount: Magnet clamp left side.

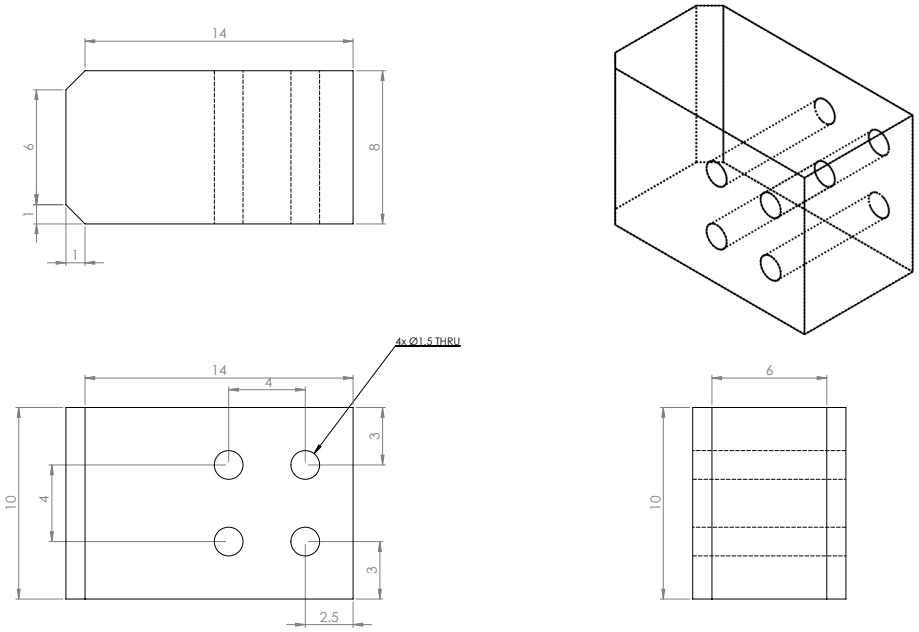

Figure B.9: Dimensions for in-vacuum permanent magnets.

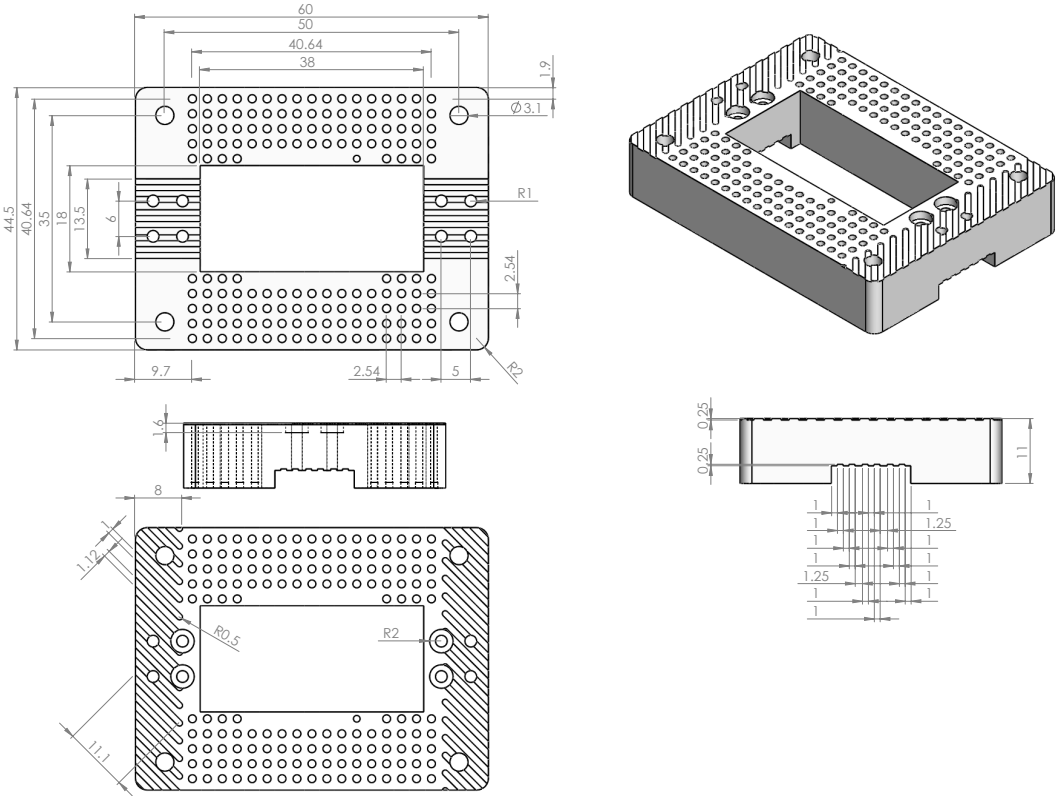

Figure B.10: Middle PEEK plate for housing pin receptacles and backside dc filtering.

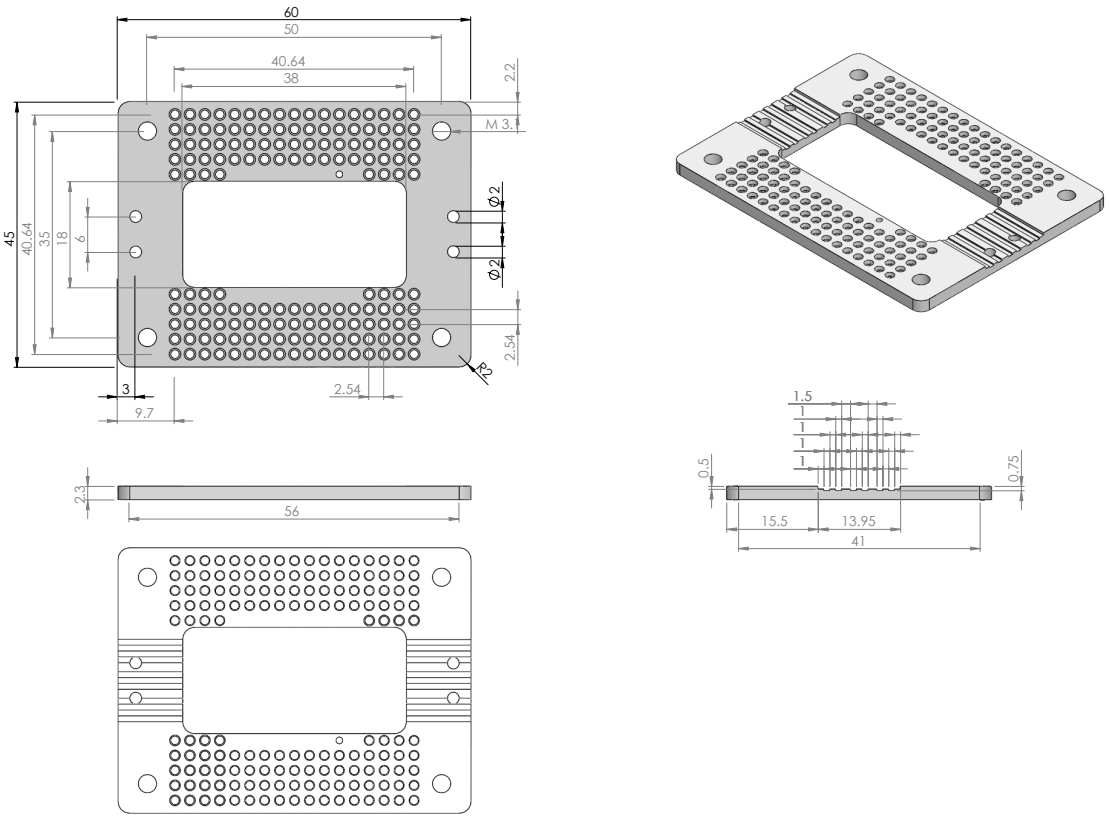

Figure B.11: Top PEEK plate for housing pin receptacles and backside dc filtering.

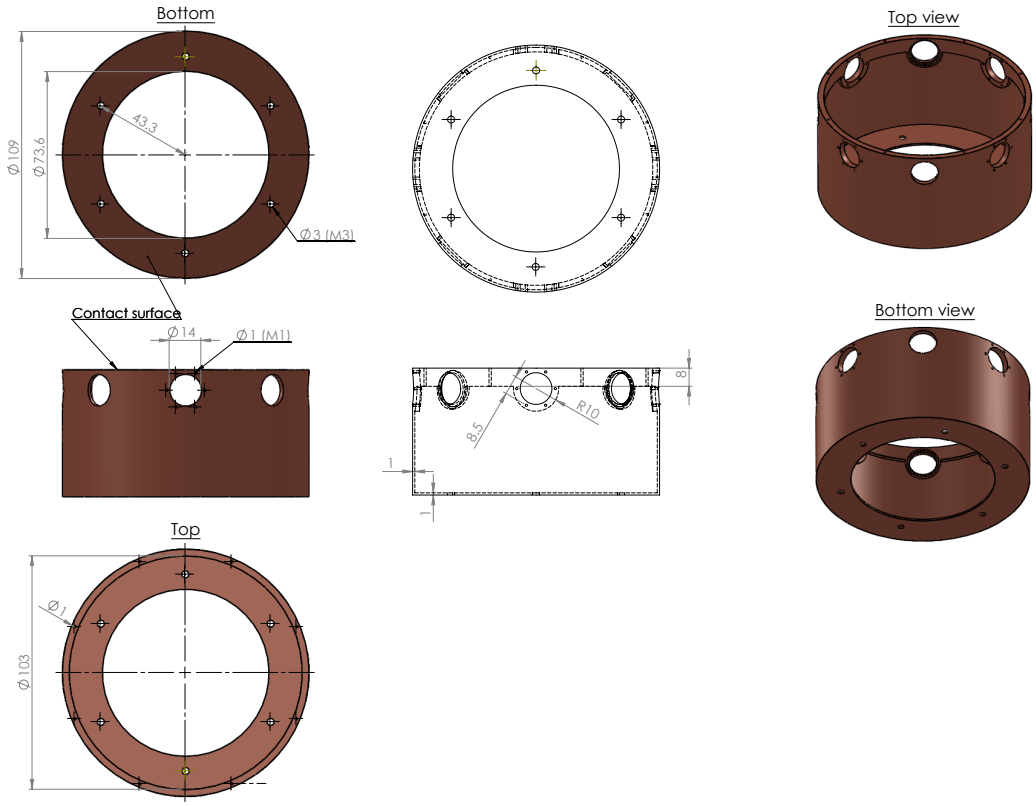

Figure B.12: OFHC copper 4 K radiation shield.

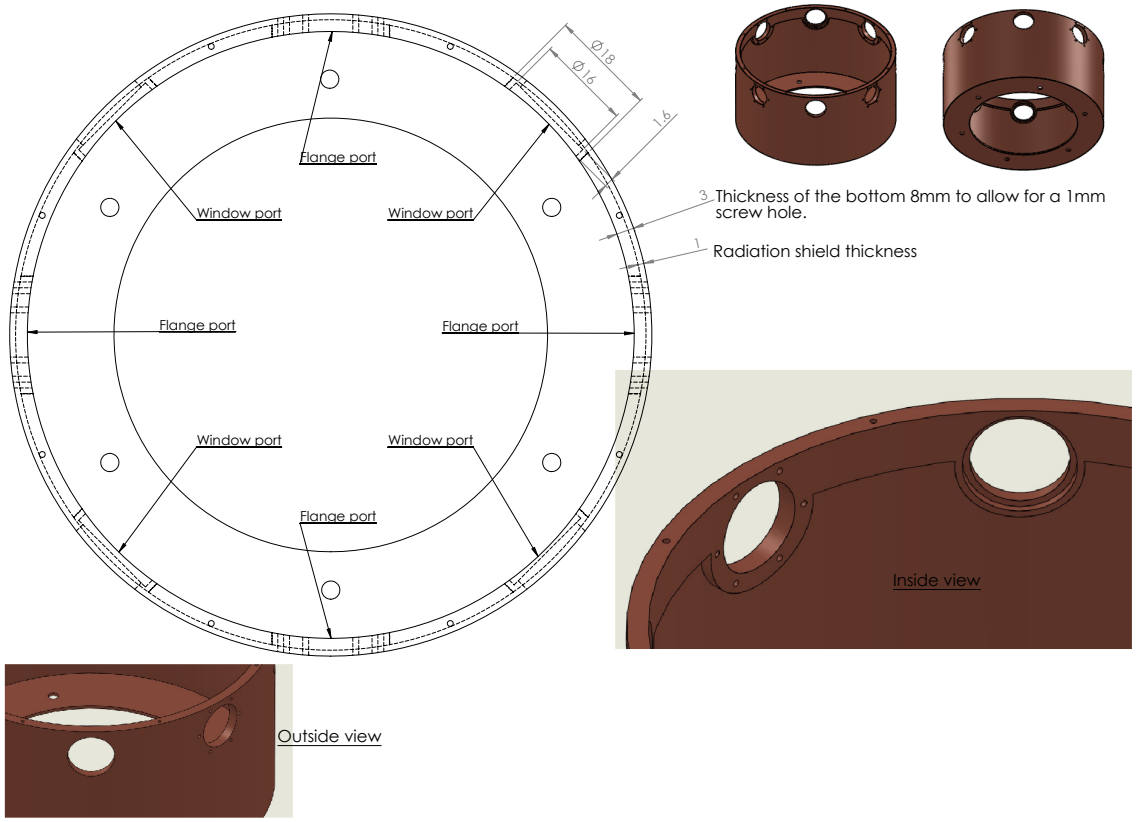

Figure B.13: Detailed view of the OFHC copper 4 K radiation shield.

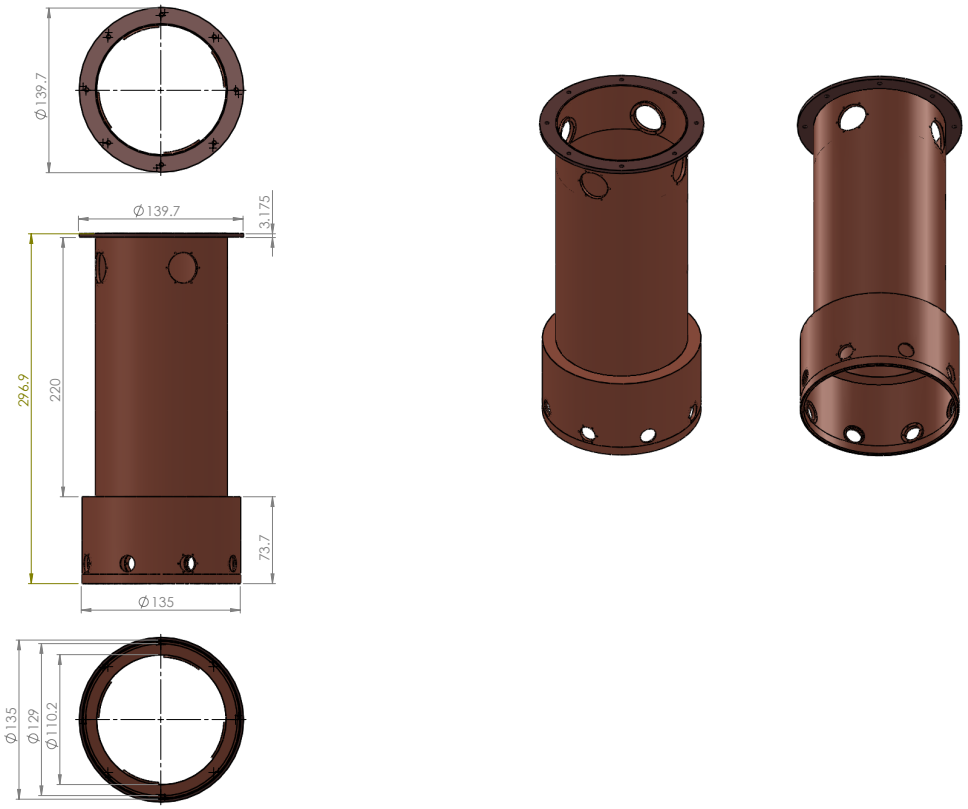

Figure B.14: OFHC copper 40 K radiation shield.

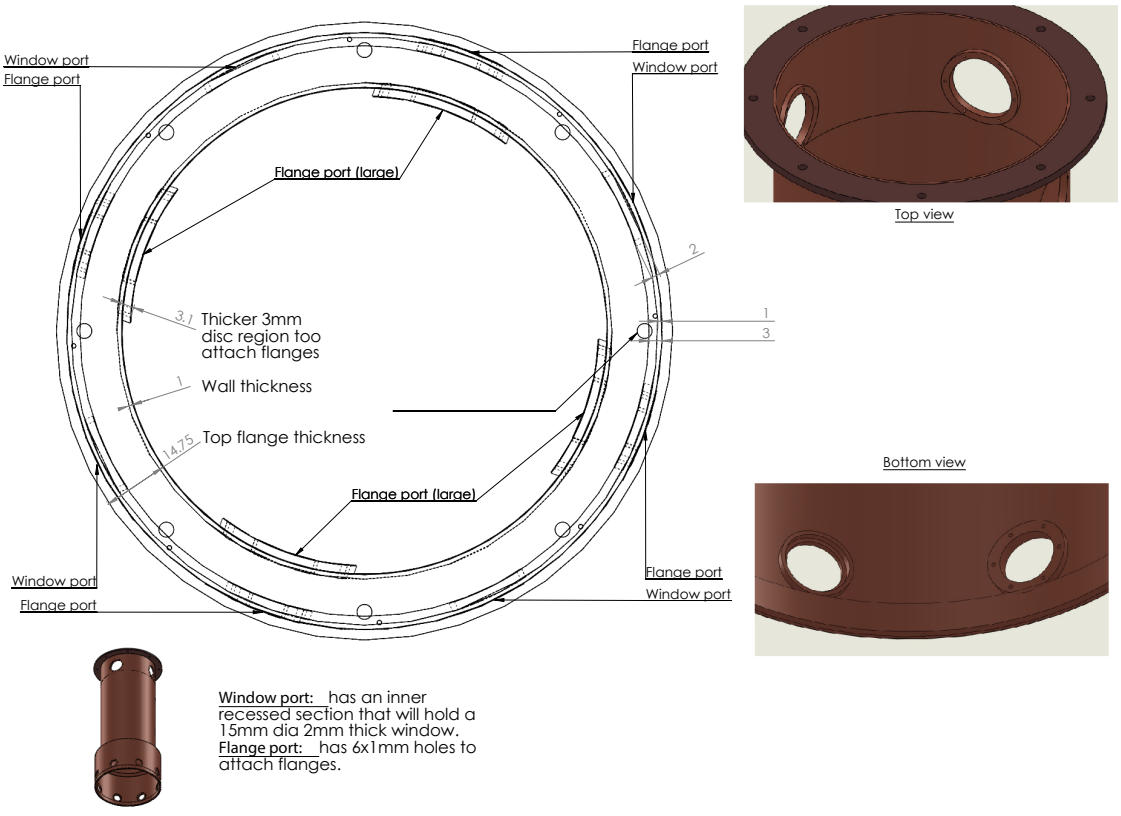

Figure B.15: OFHC copper 40 K radiation shield.

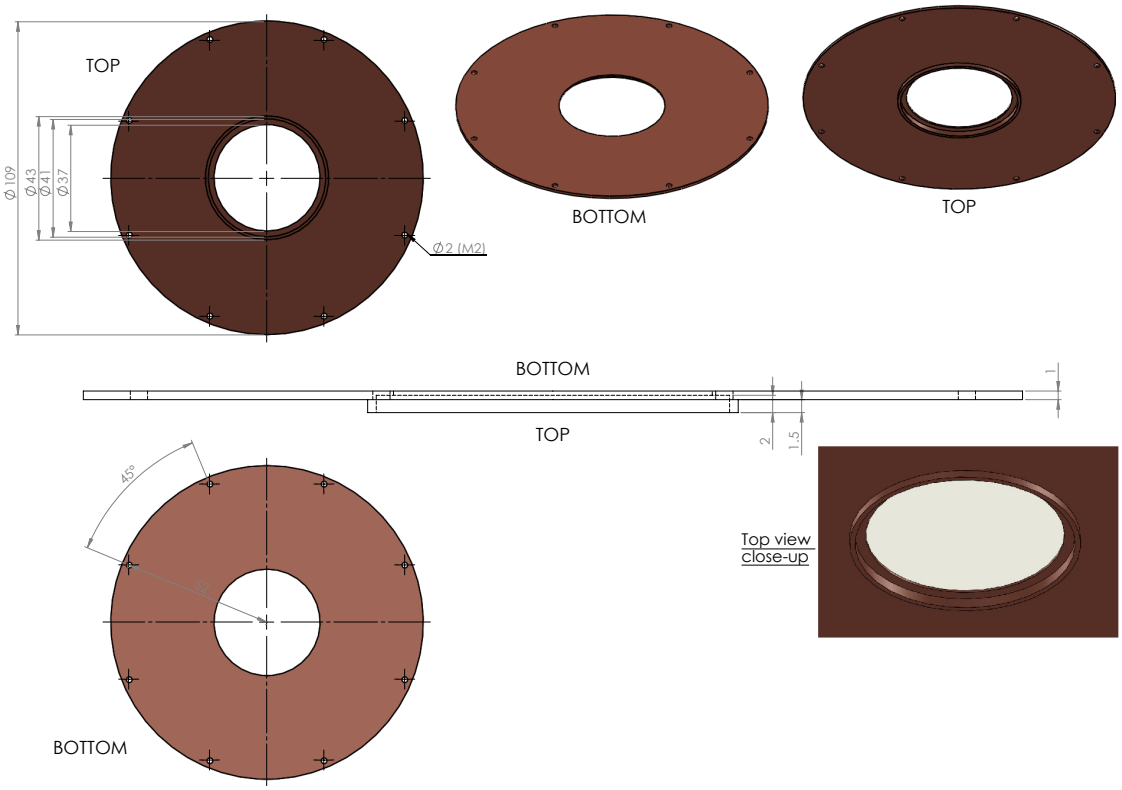

Figure B.16: OFHC copper 4 K radiation shield base plate.

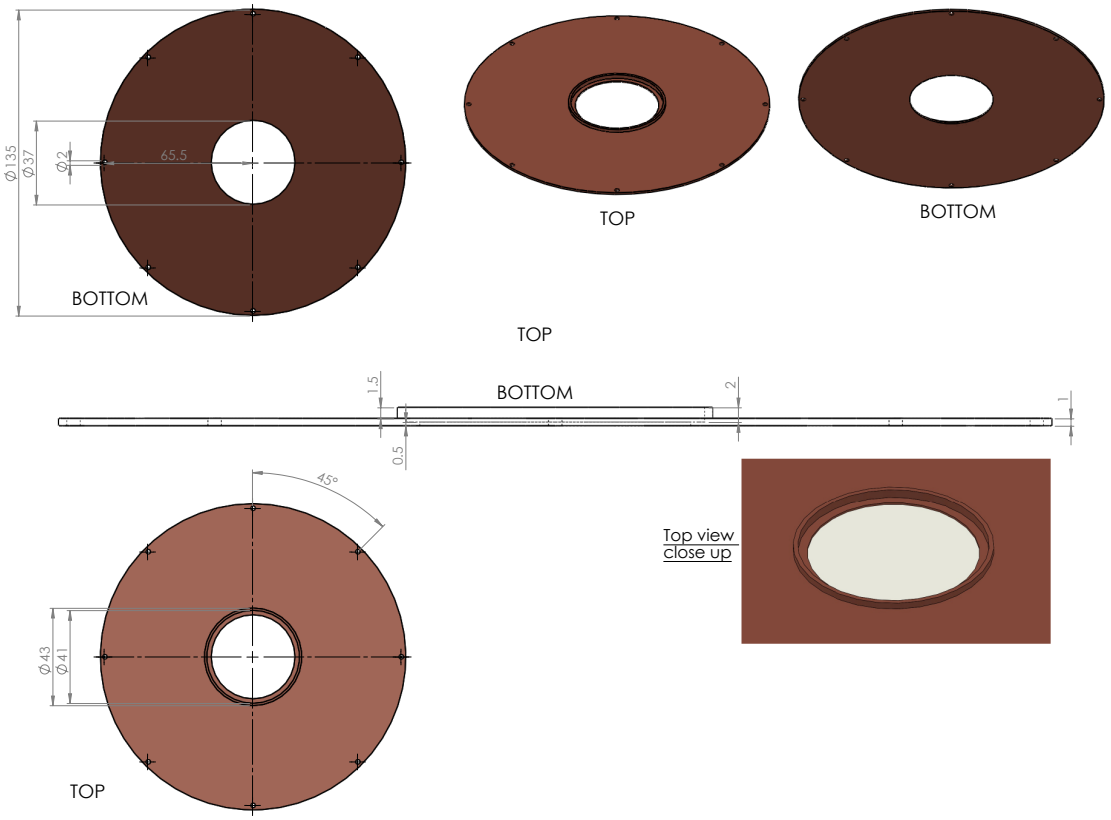

Figure B.17: OFHC copper 40 K radiation shield base plate.

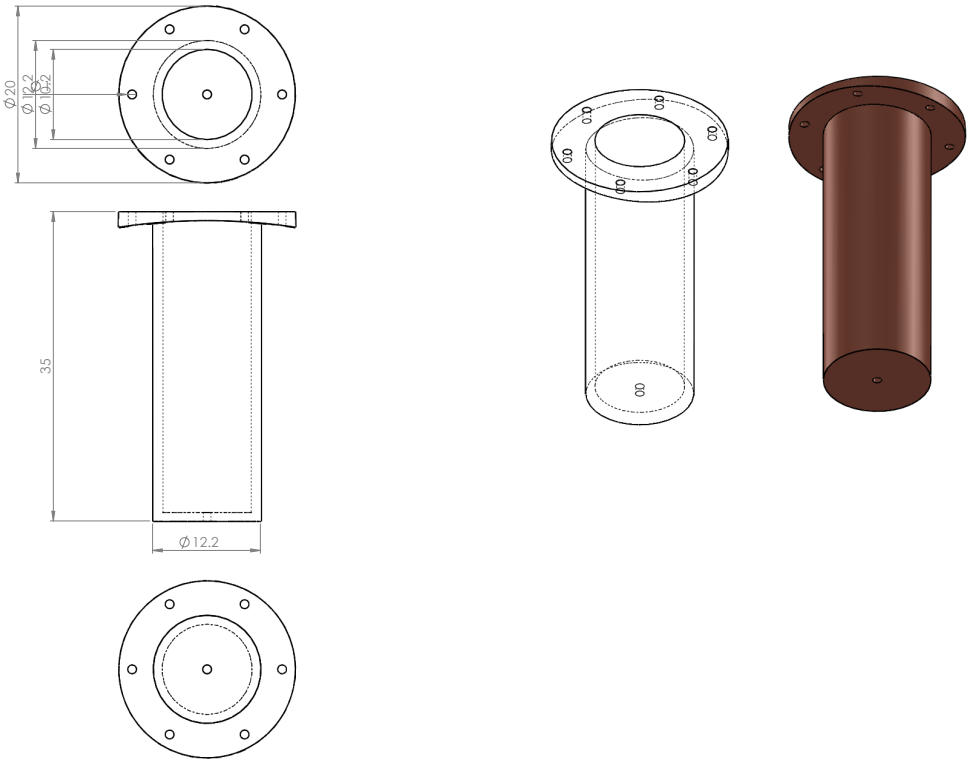

Figure B.18: OFHC copper low power dissipation ceramic based oven mount.